University of Rhode Island

DigitalCommons@URI

2014

REDOX STATUS OF FE IN SERPENTINITES OF THE COAST RANGE AND ZAMBALES OPHIOLITES

Amy Stander
University of Rhode Island, astander1@gmail.com

REDOX STATUS OF FE IN SERPENTINITES OF THE COAST RANGE AND

ZAMBALES OPHIOLITES

BY

AMY STANDER

A THESIS SUBMITTED IN PARTIAL FULFILLMENT OF THE REQUIRMENTS

FOR THE DEGREE OF

MASTER OF SCIENCE

IN

BIOLOGICAL AND ENVIRONMENTAL SCIENCES

WITH A SPECIALIZATION IN ENVIRONMENTAL AND EARTH SCIENCES

UNIVERSITY OF RHODE ISLAND

2014

MASTER OF BIOLOGICAL AND ENVIRONMENTAL SCIENCES

WITH A SPECIALIZATION IN ENVIRONMENTAL AND EARTH SCIENCES

THESIS

OF

AMY STANDER

APPROVED:

Thesis Committee:

Major Professor   Dawn Cardace

Katherine Kelley

Mark Stolt

Nasser H. Zawia
DEAN OF THE GRADUATE SCHOOL

UNIVERSITY OF RHODE ISLAND

2014

ABSTRACT

Although, the reduced status of the Earth's upper mantle is a possible controller of the deep, rock-hosted biosphere, knowledge of the redox state of the mantle is incomplete. Peridotites (mantle rocks) are composed of ultramafic (Fe, Mg-rich) minerals such as olivine and pyroxene. During serpentinization, water and ultramafic minerals react, generating a package of secondary minerals dominated by serpentine. This releases hydrogen gas in amounts dependent on system geochemistry and largely controlled by the Fe(II) budget in the protolith, as well as other products. Microbial life can be fueled by the hydrogen produced by serpentinization in environments that are generally not regarded as hospitable to life—cool, dark, low energy, subseafloor settings. Peridotite-hosted vents in the seabed and springs in continental ophiolites reveal active microbial communities at work in these distinctive serpentinization-associated waters.

In this study, 16 variably serpentinized peridotite samples from the Coast Range Ophiolite (CRO) (11 core samples and one hand sample) and Zambales Ophiolite (ZO) (four hand samples) were selected for study based on mineralogy. The objective of this study was to understand better the redox status of Fe in these rocks and produce possible H_2 generation values for the CRO and ZO. Each sample was analyzed using X-ray diffraction and thin sections (when available) to identify possible Fe bearing minerals (olivine, spinel, serpentine, pyroxene, magnetite, other Fe-oxides). X-ray fluorescence was used to obtain the bulk concentration of Fe in each sample (~28,000 to 51,000 ppm (~3.7 to 6.5 wt% FeO)). Mössbauer spectroscopy was used to determine the percentage of total Fe that is Fe^{2+} (~23 to 70%), Fe^{3+} (~14 to

65%), and magnetite (~0 to 63%), which is a combination of Fe^{2+} and Fe^{3+}. The data sets were integrated into a hydrogen generation model. I assumed that each sample was representative of the peridotite units of the corresponding ophiolite. This permitted computation of a range of total hydrogen production possible by the peridotite considered, until serpentinization is complete (~900 to 4800 Tmol H_2 or ~2000 to 12,735 Tmol H_2 if density is factored into the calculation). The CRO can produce less H_2 per rock volume than the ZO because the CRO samples generally have a lower Fe concentration, but the CRO has a greater volume and can produce a larger total amount of H_2.

Variability in bulk rock Fe concentration and Fe valence states in samples taken in close proximity indicate diverse serpentinization reaction paths even in a single ultramafic unit. Tectonics, emplacement history, age, climate, composition, and hydrology of the ophiolite all influence the redox status in the modern, ophiolite-hosted ultramafics.

And last, but not least, thank you to my wonderful family and other friends for believing in me, praying for me, and knowing that I could get it all done.

I couldn't have done it without y'all. Thanks a million!

PREFACE

This thesis is written in manuscript format for the American Geophysical

Union's (AGU) peer-reviewed journal *Geochemistry, Geophysics, Geosystems*

(G^3).

TABLE OF CONTENTS

LIST OF FIGURES

LIST OF ACRONYMS

BSE ....Backscattered electron (image)

CRO ....Coast Range Ophiolite

CROMO .... Coast Range Ophiolite Microbial Observatory

DSDP .... Deep Sea Drilling Project

GSA..Geologic Society of America

IS ....Isomer shift

ODP... Ocean Drilling Project

PPL...Plane-polarized light

MOSS..Mössbauer spectroscopy

QS... Quadrupole splitting

SEM-EDS...............Scanning Electron Microscope with an energy-dispersive detector

SSZ...Supra-subduction zone

TS ....Thin section microscopy

USGS .... United States Geological Survey

XPL...Cross-polarized light

XRD .... X-ray diffraction

XRF...X-ray fluorescence

ZO ....Zambales Ophiolite

MANUSCRIPT

This manuscript is prepared for submission to the American Geophysical Union's (AGU) peer-reviewed journal *Geochemistry, Geophysics, Geosystems* (G^3).

1. Introduction

As the search for the deep extent of life on Earth and other planets progresses, it fuels the need to better understand life on Earth and the extreme environments in which life is found. Water-rock chemical reactions often provide the energy source(s) these extremophile microbes need. As peridotite is serpentinized, Fe can be oxidized by water, releasing hydrogen gas, which can be used by microorganisms as an energy source.

The objective of this study was to determine the redox status of the Coast Range Ophiolite (CRO) and Zambales Ophiolite (ZO), based on iron speciation in selected mineral phases. Serpentinized peridotite samples were collected from the CRO and ZO, their general mineralogy was identified, Fe concentration data were obtained, and Mössbauer spectroscopy was utilized. Fe was used as the redox status indicator because of its general abundance in the rocks, its multiple valence states, and its participation in energy production during serpentinization. Possible energy yield in the form of hydrogen released during serpentinization was also calculated.

1.1 Deep life can be fueled by serpentinization

Hydrogen is an energy source for various forms of life from man to microbes. It can be produced naturally through water-rock reactions by rusting or oxidizing the Fe within ultramafic (Mg, Fe-rich) rocks. Serpentinization at its most fundamental level is the hydration of Fe^{2+} minerals in ultramafic rocks in an overall reducing, anoxic environment. This process can be represented by a redox transformation of mineral-hosted Fe from Fe^{2+} to Fe^{3+}:

$$(1)\ 2(\text{Fe}^{2+}\text{O})_{rock} + \text{H}_2\text{O} \rightarrow (\text{Fe}^{3+}_2\text{O}_3)_{rock} + \text{H}_2$$
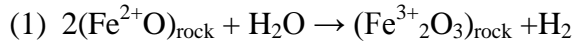
The hydrogen so generated can be utilized by microbes as hydrogen gas (H_2), often with metabolic reactions coupled to cycling of methane (CH_4) other hydrocarbons, and/or complex organic compounds that are also produced in this environment [Ophan and Hoehler, 2011; Charlou *et al.*, 2010; McCollom and Seewald, 2013; Schrenk *et al.*, 2013].

Chemosynthetic ecosystems that are fueled at least in part from hydrogen produced by serpentinization have been discovered in/around sites where there is active serpentinization occurring, including submarine seeps from fault-bounded peridotite blocks like the Lost City hydrothermal field on the Atlantis Massif near the Mid-Atlantic Ridge [Kelley *et al.*, 2005]; within ophiolite groundwater and/or groundwater springs including the Cedars [Morrill *et al.*, 2013] and CROMO wells [Cardace *et al.*, 2013] in California, USA, various locations within the Oman ophiolite [Neal and Stranger, 1983; Paukert *et al.* 2012; Sano *et al.*, 1993], the Tablelands ophiolite in Newfoundland [Szponar *et al.*, 2013], the Leka Ophiolite complex in Norway [Okland *et al.*, 2012], and Gruppo di Voltri in Italy [Cipolli *et al.*, 2003] to name a few. Serpentinization tied to plate convergence and aqueous alteration of mantle wedge material also fosters submarine mud volcanoes such as the Kumano Mud Volcano, Nankai Trough, Japan [Case *et al.*, 2013] and the South Chamorro Seamount near the Marianas Trench, and mud diapirs. See appendix for a brief overview of microbiological diversity of serpentinization-related fluids.

Because the oxidation of available Fe and attendant H_2 production is expected in serpentinization, the redox status of the upper mantle can be considered an indicator

of a deep rock-biosphere, at least until temperatures of 121°C, and perhaps 150°C, are reached [Kashefi and Lovley, 2003]. Serpentinites are thus one promising environment for studying endolithic extremophiles [Schrenk *et al.*, 2013; McCollom and Seewald, 2013; Takai *et al.*, 2006;] (microbes that live in rocks and off the energy released as the rocks weather). Subsurface lithoautotrophic microbial ecosystems (SLiMES) [Nealson *et al.*, 2005; Takai *et al.*, 2006] can be fueled by the hydrogen produced during serpentization in an environment that is generally not regarded as hospitable to life—cold, dark, possibly high pressure (compared to surface pressure), anaerobic, and extremely alkaline with high pH (8-12) formation fluids and potentially high levels of metals like Fe, Ni, As and Cr.

1.2 Serpentinization as a geologic process

Mantle rocks of the subseafloor can be sampled where exposed by fault action or tectonics; diverse dredged peridotite samples from oceanographic expeditions and many seafloor drilling projects have also sampled peridotite. However, drilling through stratigraphically complete lithosphere to mantle peridotite is exceedingly difficult due to the depths (generally 5+ km) of rock that would need to be drilled, generally submarine, where there are additional complications and pressure and temperature constraints. Geoscientists often rely also on specimens delivered from great depth by magma streams as xenoliths [e.g., Pearson *et al.*, 2014]. In this study, variably serpentinized (hydrated and altered) peridotite samples from two ophiolites—Coast Range Ophiolite (CRO) in Northern California, USA, and the Zambales Ophiolite (ZO) in the Philippines (Figure 1)—are characterized and compared. The peridotite units in ophiolite bodies are mantle rocks that have been uplifted by

tectonics. In a naturally reducing environment, ultramafic minerals can react with water, a process that often starts on the ocean floor, and alter to serpentine assemblages that are stable at the lower temperatures and pressures of Earth's surface.

Serpentinization is the process in which hydrous fluids react with ultramafic rocks to produce serpentine and other alteration minerals, and is a volume increasing (which can further fracture rocks and expose fresh surfaces), exothermic (adds heat energy back into the system to further catalyze the reaction), and, therefore, can be a self-sustaining (positive feedback) reaction. For equation 1 to be viable, the environment needs to be oxygen-depleted and reducing so that Fe is oxidized by oxygen from water while the hydrogen is released. Ultramafic minerals formed at high temperatures and pressures undergo chemical weathering (serpentinization) to re-equilibrate with lower temperatures and pressures. Having a heat source (such as magma) nearby, can expedite the serpentinization process, but serpentinization itself is exothermic, thus heating and priming regionally associated rocks for further serpentinization.

Serpentinization is coupled to plate tectonics. Ophiolites that are or were on plate boundaries (Figure 2) can record subduction-related plate flexure or regions of tension that yield fractured areas with deep faults that allow sea water access to ultramafic rocks. For example, ophiolites may result from obduction near the trench of oceanic lithosphere formed at a mid-ocean ridge (MOR) [Dickinson *et al.*, 1996]. Ophiolites may also form in supra-subduction zone(s) (SSZ) in environments similar to nascent spreading centers in backarc or fore-arc settings, which have distinct oceanic lithosphere geochemical signatures [McLaughlin *et al.*, 1988; Coleman, 2000;

Dickinson *et al*., 1996; Shervais and Kimbrough, 1985]. All formation mechanisms allow for complete or partial ophiolite sequences to be exposed at Earth's surface.

According to the 1972 GSA Penrose Conference, an ophiolite consists of a partial or complete sequence consisting of, from bottom to top, an ultramafic complex (variably serpentinized mantle peridotite), a gabbroic complex, mafic sheeted dike complex, and mafic volcanic complex dominated by pillow basalt overlain by various sedimentary rocks (see Figure 3) [Dilek, 2003]. This definition holds true, whatever the tectono-magmatic origin may be. Seawater is also mineral-bound within the ophiolite when it is uplifted, and continues to serpentinize the ultramafic units, slowly exiting through vents/springs, and variably mixing with meteoric surface and groundwater.

1.3 Means of inferring serpentinite redox status and relevance to H$_2$ yield

The redox status of Fe in variably serpentinized peridotite can give clues to the possible hydrogen yield that has occurred and still has the potential to occur because Fe is oxidized by the oxygen in water (equation 1) and the hydrogen is released. Mössbauer spectroscopy (MOSS) of Fe is one way to determine the redox status of multivalent elements in minerals. MOSS determines the proportions of Fe^{2+}, Fe^{3+}, and mixed valence states like magnetite (with both Fe^{2+}, Fe^{3+} present in the mineral, see Table 1). A stoichiometric conversion can be calculated from concentration of Fe^{3+} to quantify possible hydrogen yield over the lifetime of the rock. The larger the quantity of Fe^{2+} in the ultramafic protolith, the greater the chance of hydrogen production when ultramafic minerals react with water.

The Earth's mantle is solid and composed primarily of olivine group, pyroxene group, spinel, and/or garnet, accompanied by diamond and other minerals that are stable at high temperatures and pressures. In the anhydrous upper mantle, Fe^{2+} is expected to be found in ultramafic minerals, like olivine, pyroxene, and spinel, because it will substitute for Mg in mineral structures (see Table 1). Molecular water in the mantle is possibly located mostly in the transition zone between the upper and lower mantle [Hirschmann *et al.*, 2005; Pearson, 2014] and the mantle wedge in subduction zones where the subducting oceanic slab is releasing water into the mantle.

1.4 Importance of Al-rich phases, spinels, in H_2 production

Serpentinization can be catalyzed by spinels and is a complicated and highly variable process that depends on the starting composition of the rock and primary minerals, fluid composition, substitutions between Fe, Mg, and other elements [Evans, 2008], if and how much Al is present in the system [Andreani *et al.*, 2013; Mayhew *et al.*, 2013], system pressure and/or temperature [Mayhew *et al.*, 2013], and even the presence of microbes could encourage one mineral to form over another [Nealson *et al.*, 2005; Takai *et al.*, 2006]. For example, serpentinization needs olivine and water, and responds to additional mineral phases such as spinel and pyroxene. Different forms of serpentine can be created along with magnetite, hydrogen, spinel, and other minerals. Equation 2 and 3 below provide examples of possible parent and alteration mineral combinations. Equation 3 is provided in both mineral names and general chemical formulas (Table 1), which help illustrate the complex chemistry observed in some serpentinization systems.

(2) Olivine + hydrous fluids ± spinel ± pyroxene ↔ serpentine ± brucite ± magnetite ± free hydrogen ± other spinel(s) ± quartz ± albite

Or

(3) Olivine ± pyroxene + hydrous fluids = serpentine ± magnetite ± other clays ± free hydrogen

and in chemical formulas:
$(Mg, Fe)_2SiO_4 \pm (Mg, Fe, Al, Mn, Ti, Cr, Ca)_2Si_2O_6 \pm (H_2O + dissolved\ ions) = (Mg,Fe)_3Si_2O_5(OH)_4 \pm Fe_3O_4 \pm [Ca_{0.17}(Al,Mg,Fe)_2(Si,Al)_4O_{10}(OH)_2 \cdot nH_2O \pm (Mg,Fe,Al)_3(Si,Al)_4O_{10}(OH)_2 \cdot (Mg,Fe,Al)_3(OH)_6 \pm (Mg,Ca)_{0.3}(Mg,Fe^{2+},Fe^{3+},Al)_3(Si,Al)_4O_{10}(OH)_6] \pm H_2$
[Bach *et al.*, 2006; Sleep *et al.*, 2004].
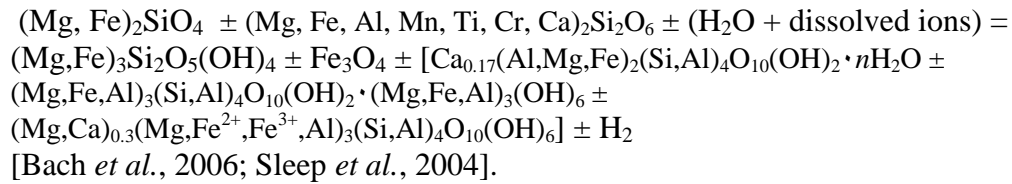
Spinel group minerals, especially Al-bearing spinels, can act as catalysts for hydrogen production. Mayhew *et al.* [2013] saw a correlation between the quantity and surface area of spinel phases (mainly magnetite, chromite, and gahnite) and the amount of hydrogen generated, especially at lower temperatures (100 and 55°C) where microbes can live. Spinels are metal oxide minerals ($M^{2+}M^{3+}_2O_4$; see Table 1), and Mayhew *et al.* [2013] suspect that they encourage H_2 generation by acting as an electron transfer shuttle surface for aqueous Fe^{2+} and hydrogen/protrons.

Spinels can include aluminum in their structures. When Andreani *et al.* [2013] conducted diamond-anvil experiments with olivine, saline water, and aluminum, the rate of olivine alteration increased 1-2 orders of magnitude when Al was included at natural hydrothermal environment temperatures (200 and 300°C) and pressures (200 MPa). Al seemed to enhance the solubility of the olivine in their experiments allowing serpentine to form within ~2 hours of beginning the experiment. The rate of H_2 production could also increase with the increased rate of serpentinization, which may allow for economic gain from serpentinization [Andreani *et al.*, 2013].

The minerals in this study include olivine, pyroxene (cpx and opx), serpentine, brucite, spinel, and magnetite (Table 1) in altering peridotites of the Coast Range Ophiolite and Zambales Ophiolite. A general serpentinization reaction including these minerals is below:

(4) olivine ± pyroxene ± spinel ± hydrous fluids ↔ serpentine ± brucite ± spinel ± magnetite ± hydrogen gas
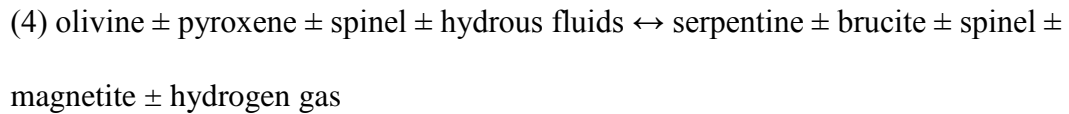
1.5 Geologic Setting

Ophiolites are generally structurally intact blocks of the oceanic lithosphere (ocean crust and upper mantle, see Figure 3) that are uplifted and deposited on continental crust, or form (essentially in situ) in extensional environments in the back arc. Partial, segmented, and/or mélange ophiolite sequences are common because the emplacement can be complex. The Coast Range Ophiolite is located on modern tectonic plate boundries as illustrated by Figure 2.

1.5.1 Coast Range Ophiolite (CRO)

The Coast Range Ophiolite (CRO) is exposed at various locations in the mid-western portion of California, USA (Figure 1). The CRO exposures and sampling locations in this study are near Lower Lake (junction of Lake, Napa, and Yolo Counties) on the University of California-Davis, McLaughlin Natural Reserve, and near Stonyford (Colusa County) in the confluence of the Hyphus Creek and Little Stony Creek. See the appendix Figure A1 for a geologic map of the CRO. The CRO formed in a supra-subduction zone (SSZ) setting [Shervais, 2001]. SSZ tectonic

settings may include backarc and forearc basins, and arc volcanism in an intra-oceanic plate convergent margin [Hawkins, 2003]. The CRO formation (rock age and emplacement) is ~163-170 Ma [Coleman, 2000; Shervais *et al.*, 2005; McLaughlin, 1988] and was associated with an oceanic plate back-arc basin and continent collision in a convergent margin. The CRO units are often found between the Franciscan Complex (Middle Jurassic or older peridotite wedges [Coleman, 2000]) to the west and the Great Valley Sequence (Middle Jurassic calc-alkalic and mafic pillow lava, sheeted dikes, and gabbro [Coleman, 2000] to the east. The CRO sequence includes mafic rocks, pyroclastic rocks, gabbro, and peridotite [Coleman, 2000]. It is often found as mélange.

The McLaughlin Natural Reserve is now a research and education-focused space, administered by the UC-Davis and supported by a joint initiative between the Homestake Mining Inc. Co. (currently engaged in closure of a gold mining operation at the site) and local conservation groups.

1.5.2 Zambales Ophiolite (ZO)

The Philippine Islands are a mixture of island arcs and continental fragments [Hall *et al.*, 1995]. They are bordered by oppositely-dipping subduction trenches (Manila Trench to the west and Philippines Trench to the east) and have a complicated history of uplift and faulting. The Zambales Ophiolite (ZO), Zambales Range, Luzon, Philippines (Figure 1) is a SSZ ophiolite and was derived from interactions of an island arc system and back-arc basin [Yumul, 2007; Hawkins and Evans, 1983] during the Cenozoic era [Karig *et al.*, 1986], Eocene epoch (33-56Ma) [Yumul, 2007]), which implies that the rock and emplacement age are roughly the same.

The ZO is broadly composed of two blocks of uplifted, tilted, and strike-slip fault shifted lithosphere that have complete Penrose ophiolite sequences [Yumul, 2007] and vary in geochemistry and thickness of the crustal section [Hawkins and Evans, 1983]. The (1) Acoje block to the north is accreted tholeiitic intraoceanic island arc material, while the (2) Coto block to the south is a typical back-arc basin rock series [Hawkins and Evans, 1983]. See the appendix Figure A2 for a geologic map of the ZO.

2. Methods

2.1 Sample descriptions

Samples include serpentinite cores and hand samples from the Coast Range Ophiolite (CRO) in Northern CA and hand samples obtained from serpentinites from the Zambales (ZO) Ophiolite in the Philippines. Table 2 gives a summary of sample locations, depths, and approximate elevations. Figure 4 presents pictures of each sample following collection. Samples collected ranged in mineralogy, depth (surface and core samples), and locations within the sampling area. X-ray diffraction analysis was performed first on each sample to indentify the main component minerals. Many samples of the CRO and ZO were analyzed; however, only variably serpentinized peridotite samples' data are reported here. Chlorite-rich samples are not reported as they were interpreted as being from weathered basalt units and not peridotite units [Wetzel and Shock, 2000]. Additional data and sample information are reported in the appendix.

2.1.1 Coast Range Ophiolite Samples

Coast Range Ophiolite Microbial Observatory (CROMO) wells were drilled and cores dominated by serpentinite were collected in 2011 [Cardace, *et al.*, 2013]. The CROMO 2 well located in the Quarry Valley area of the McLaughlin Reserve bottoms out at ~45.7 m (~152 ft) depth from surface in a serpentinized peridotite layer [Cardace, *et al.*, 2013]. CROMO 2 core samples were taken from ~44.5 m (~148 ft) to ~45.7 m (bottom of hole). CROMO samples were vibrated in distilled/DI water. The water and suspended clay minerals were poured into an Al-foil boat. The bulk of the samples (not suspended in the water), were also placed on an Al-foil boat. Both parts

of the samples were dried at 60°C over night and were analyzed with XRD, XRF, and MOSS. See appendix for data on the suspended clays.

Additionally, the McLaughlin Natural Reserve has archived cores from when Homestake Mining Company was surveying the area. Some of the boreholes passed through hundreds of feet of variably-serpentinized peridotite, some of which were found to contain relict olivine grains. Samples were collected from 3 cores: M81-167, M81-309, and M81-313 at various depths (see Table 2).

Hand samples from the Stonyford Volcanic Complex [Shervais, *et al.*, 2005] were collected as float (cobbles in the creek and not collected in situ) located in the Hyphus-Little Stony Creek confluence near Stonyford, California.

2.1.2 Zambales Ophiolite Samples

Serpentinized peridotite hand samples were collected in September 2012 from the Poon Bato region of the ZO and were analyzed. See Table 2 for latitude and longitude data, and Figure 4 for pictures of the samples before being powdered for analysis.

2.2 XRD

X-ray Diffraction (XRD) analysis determined the bulk mineralogy of the samples. A portable Olympus (formerly InXitu) Terra field XRD instrument, with the specifications equivalent to the CheMin tool developed for Mars exploration as described in Blake *et al.*, [2012], was used for all XRD analyses. The Terra engages a Co X-ray source and a cooled charge-coupled device (CCD) detector arranged in

transmission geometry with the sample, with angular range of 5° to 50° 2θ with <

0.35° 2θ resolution [Blake *et al.*, 2012]. X-ray tube voltage is typically 30 kV, with a

power of 10 W, a step size of 0.05°, and an exposure time of 10 s per step. Default

settings were used except the number of exposures was 1000 (total run time is about

70 min) and the piezo volume was 70.

Samples were powdered using a percussion mortar and/or agate mortar and

pestle; when necessary a Dremel manual drill was used to subsample grains of

interest. A total of ~9 g of the focus samples were powdered. Powders were passed

through a standard 150 μm sieve (100-mesh) prior to analysis. The portions of each

sample selected for analysis were not always completely powdered to ≥150 μm, so

some of the harder minerals may be under represented in all experiments that required

a powdered sample. About 15 mg of powdered material was transferred with a spatula

to the inlet hopper of the standard sample vibration chamber, which continuously

mixes the powdered sample for the duration of the analysis. Rotation disks (sample is

rotated instead of vibrated) were also used for some samples and all the standards.

The resulting diffractograms were interpreted using XPowder software, which

is a commercially available peak search-and-match program that queries the PDF2

database for reference mineral peak information. XPowder allows for identification

only (not quantification) of major minerals and trace minerals can be easily missed

and/or masked by peaks of other minerals. Diffractograms have °2θ on the *x*-axis and

intensity on the *y*-axis. An intensity peak is the result of constructive interference

when Bragg's law ($n\lambda=2d \sin\theta$, where n is the "order" of reflection, λ is the incident

14

X-rays wavelength, d is spacing between atomic planes in a crystal structure, and θ is the incidence angle) is fulfilled by the incoming X-rays.

2.3 Thin section microscopy

Thin section (TS) petrography was used to identify relic, accessory, and trace minerals, confirm XRD analysis, and observe relationships between minerals at the micro-scale. Thin sections (30 μm-thick, standard slides) available of select samples were viewed at various magnifications (2-10X) in both plane-polarized (ppl) and cross-polarized (xpl) light and photographed (Figures 9-12, 14-21, and 23) using an Olympus BH-2 polarizing light microscope, an Olympus DP73 digital color microscope camera, and Stream Essentials 1.8 image analysis software.

2.4 XRF

X-ray fluorescence (XRF) and scanning electron microscopy (SEM) were used to constrain elemental, especially Fe, concentrations in bulk rock and individual grains, respectively. Fe concentrations (see Appendix for additional element concentrations) were obtained from selected bulk samples (see section 2.1 for sampling bias).

A Thermo Scientific Niton XL3t portable XRF analyzer desktop laboratory unit was used for element analysis. Because the Niton XL3t is a handheld device and was used without vacuum conditions, elements lighter than Mg were not detected [Rollinson, 1993; Wirth and Barth, 2012; EPA Method 6200, 2007]. An adapted EPA Method 6200 was used. Samples were analyzed using soils mode, which is tuned for

quantification of elements common in soils and is biased toward those of specific interest to the lab analyzing soils. There are other modes (metal, mining, consumer goods) generally used with the hand held XRF, but they were not available at time of analysis.

Samples were sieved to 150 μm (#100 sieve) and ~2 mL of bulk sample was analyzed. Samples were run for 200 s and analyzed three times with the sample being shaken/agitated between each run. The three values were averaged and the mean was normalized using USGS standards described below.

Fe precision and accuracy were estimated from replicate sample runs and utilizing USGS standards Dunite, Twin Sisters (DTS-1), Dunite, Twin Sisters Mountain DTS-2B (DTS-2), and Peridotite, Cedars CA Ultramafic Mass (PCC-1) which indicate accuracy within ~24-64% and precision with a standard deviation between 170-770ppm.

To obtain the normalization factor (Table 5), each standard's reference value was divided by the average observed value (REF/OBS). When REF/OBS was calculated, DTS-1 was 0.6133, DTS-2 was 0.8045, and PCC-1 was 0.6096. See calculations below used to obtain the normalization factor:

$$\frac{\textbf{\textit{Reference}}}{\textbf{\textit{Observed}}} =$$

$$\frac{\textbf{\textit{DTS}} - \textbf{1}\,published\,average}{(average\,of\,4\,sample\,runs)} = \frac{\sim 60710 ppm}{\sim 98979\,ppm} = \sim 0.61$$

$$\frac{\textbf{\textit{DTS}} - \textbf{2}\,published\,average}{(average\,of\,4\,sample\,runs)} = \frac{\sim 54300 ppm}{\sim 67489\,ppm} = \sim 0.80$$

$$\frac{\textbf{\textit{PCC}} - \textbf{1}\,published\,average}{(average\,of\,4\,sample\,runs)} = \frac{\sim 58402 ppm}{\sim 95798\,ppm} = \sim 0.61$$

Sample values were normalized to DTS-1 because it had a similar percentage difference between the observed value and the published value of PCC-1 which is a serpentinized peridotite similar to the samples. See calculations below used to obtain general accuracy error:

$$\frac{Observed}{Reference} =$$

$$\frac{DTS-1 \; average \; of \; 4 \; sample \; runs}{published \; average} = \frac{\sim 98979 \; ppm}{\sim 60710 ppm} = \sim 1.63 \rightarrow \sim 63\% \; error$$

$$\frac{DTS-2 \; average \; of \; 4 \; sample \; runs}{published \; average} = \frac{\sim 67489 \; ppm}{\sim 54300 ppm} = \sim 1.24 \rightarrow \sim 24\% \; error$$

$$\frac{PCC-1 \; average \; of \; 4 \; sample \; runs}{published \; average} = \frac{\sim 95798 \; ppm}{\sim 58402 ppm} = \sim 1.64 \rightarrow \sim 64\% \; error$$

The error for XRF is ±24% based on the discrepancy of DTS-2 after normalizing to DTS-1 (Table 5). Additional error could come from samples not being homogeneous, so the Fe is not equally distributed resulting in over or under exaggerating the concentrations. Standards were run four times and samples were run three times. The samples and standards were shaken/agitated between each run to try and get a more accurate account of the Fe present.

Additional error between reference and observed could occur if the average used for the reference data incorporated values that oven dried the samples prior to analysis and, therefore, has loss on ignition (LOI). The USGS certificate of analysis for DTS-1 and DTS-2 does not include LOI values. The GeoReM database [Jochum *et al.*, 2005] reports that the LOI for DTS-1 is 0.2%m/m, DTS-2 is 0.36%m/m, and PCC-1 is 4.91%m/m. There are more than 100 data sets for PCC-1; however, only two

report LOI (4.91 and 5.12%m/m). DTS-1 has more than 80 data sets and only one reports LOI (0.2%m/m). DTS-2 only has 22 data sets with only one reporting LOI (0.36%m/m). The data sets that report LOI do not always report Fe concentration, so it is difficult to gauge how Fe concentration would vary with less water in the samples; however, it stands to reason that if concentration data are normalized to 100%, then low water contents could result in relatively higher reported concentrations of FeO. For instance, the observed Fe concentrations in this case were higher than the reference values. The main source of error was probably instrumental.

The CROMO 1, CROMO 2, and PHL samples in this study were dried in an incubator oven set at $60^{o}C$ ($140^{o}F$). Other CRO samples were air dried at generally less than $37^{o}F$ ($95^{o}F$). Standards were transferred directly from original container to sample holders. They were not dried in an oven before analysis.

Most of the samples were powdered using a steel percussion mortar, so it is possible that the samples were contaminated resulting in higher Fe concentrations. This would not account for the higher values of the USGS standards as they were already powdered.

2.5 SEM-EDS

SEM-EDS was used to measure the concentration of most major elements in weight percent (wt%) in specific mineral grains from the thin section of sample 313_329. A JEOL 5900 scanning electron microscope (SEM) with Energy Dispersive X-ray Spectroscopy (SEM-EDS) was used on thin sections to obtain high resolution imagery (Figures 13, 18, 20, 22, and 25-29) and spot analysis compositions of major

elements in wt% oxides (Tables 7-11) in individual mineral grains and within the groundmass.

The detection limit for SEM-EDS is 0.5wt%, so the elements with lower concentrations have lower accuracy. The SEM-EDS also has limited sensitivity for elements with atomic numbers below 11 (Na) [Goldstein, 2003], so the oxygen present is not accounted for. The SEM-EDS instrument was set to do a spot analysis for 30 s for each spot. With more time (e.g., 5 min instead of 30 s) dedicated to data analysis for each spot, the accuracy increases for low concentration elements. Wt% are calculated from the area under the curve created from intensity peaks. SEM-EDS data are reported in Tables 7-10 and corresponding area images are in Figures 13, and 25-29.

2.6 Mössbauer spectroscopy (MOSS)

The redox status of a system can be broadly determined from the valence state of Fe—Fe^{2+} is reduced and Fe^{3+} is oxidized—and MOSS data provide Fe^{2+} and Fe^{3+} as percentages of total Fe. There are limitations to MOSS: it can't distinguish between similar minerals, and results vary as a function of cation substitution and temperature. There is better peak resolution at colder temperatures with a recommended temperature of 40 K and the magnetic properties can change at temperatures below ~24 K [Dyar, *et al.*, 2008]).

Often MOSS is performed on individual minerals, which will only give the redox status of individual mineral types within the sample. In this study, a bulk analysis was done to gauge better the redox status of the whole sample. It is also very

difficult to hand-pick minerals found in a highly serpentinized rock. Bulk rock

samples were again powdered and sieved to 150 μm. Samples were prepared,

analyzed, and modeled similar to the methods used in Evans, *et al.* [2012], which are

briefly outlined here. About 40-100 mg of sample were mixed with a sucrose filler and

mounted in a sample holder confined by Kapton polyimide film tape. Samples were

run at room temperature (~295 K) using a source of 100-60mCi ^{57}Co in Rh on a WEB

Research Co. model WT302 spectrometer at Mt. Holyoke College (South Hadley,

MA) for periods of time from 2-24 hours. More time is needed for lower Fe

concentrations. Spectra were collected over a velocity range of ±4 mm s^{-1} for samples

without oxides and/or ±10mm/s if Fe oxides, like magnetite, were present. A ±10 mm

s^{-1} velocity scale is needed to show the magnetite peaks resulting from additional

quadrupole splitting from the magnetic properties of the Fe.

Spectra were processed using two software packages from the University of

Ghent. Simple paramagnetic doublet (Fe^{2+} and Fe^{3+}) spectra were modeled using the

Dist3e program. More complex spectra with sextets (magnetite) and doublets were

modeled using the MEX FielDD program. While modeling, isomer shifts (IS) and

quadrupole splitting (QS) were allowed to vary in unison. Peak widths for doublet sets

were allowed to vary in unison with IS and QS [Evans, *et al.* 2012] in most cases.

Some widths were fixed to guarantee a ≥0.23mm/s. Dyar *et al.* [2008] discusses

sources of error (low number of recoil-free emissions, temperature and its influence on

QS, IS, and resulting Fe valence state percentages, etc.) of MOSS measurements

associated with phyllosilicates (clay minerals), which applies to serpentine minerals

(and other alteration minerals like chlorite), which are clay minerals. MOSS results are

given as area under the curve corresponding to percentages Fe^{2+} and Fe^{3+} (doublets), and magnetite (sextet), if present, of the total Fe. Table 3 gives general parameters for MOSS data fitting.

Some samples for MOSS do not contain magnetite; however, TS and XRD indicate that magnetite is present in every sample. For samples with MOSS spectra without magnetite, it is assumed that magnetite is less than 1% of the total Fe. It is possible that the XRD and TS splits were more magnetite-rich than the powder analyzed by MOSS and/or the magnetite indicated by the XRD was actually a different spinel.

2.7 H$_2$ modeling

For simplicity, in this model, it is assumed that all the Fe is originally Fe^{2+}, that the Fe concentration has not changed over time [Adreani *et al.*, 2013B], and that the simplified serpentinization reaction (equation 1) holds true. Peridotite can contain opx, cpx, and/or spinel which can house Fe^{3+} (Table 1), so it is basically assumed that the samples started out as 100% olivine (only Fe^{2+}) (dunite peridotite) or that the Fe in other minerals is also only in the 2+ valence state and/or minerals, like spinel, are present in trace amounts which are lost within the error of XRF measurements (see section 2.4).

Using MOSS results, the approximate volume of the CRO or ZO peridotite, the Fe concentration, the simplified serpentinization reaction (Eq. 1), and stoichometry, the hydrogen yield of the CRO and ZO can be estimated for the life time of the peridotite unit. It was estimated using two different conversion factors: one of which

was density (g/cm^3) and mg/kg to convert from ppm to g; the other used mg/L to

convert from ppm to g. See section 3.4 for worked-out examples.

3. Results and Discussion

In general, data from XRD, TS, XRF, SEM-EDS, and MOSS analyses confirm there are important differences in the proportions of mineral phases and Fe valence state in those phases, within a geographic region and also across all samples.

3.1 XRD & Thin section petrography

Minerals identified using XRD and/or TS include serpentine, magnetite, other spinel group minerals, pyroxenes, olivine, chlorite, other unidentified clay minerals, brucite, amphibole, and garnet. On XRD diffractograms, brucite and spinels, including magnetite, have overlapping and/or closely spaced intensity peaks that vary in position depending on chemical composition, which can make differentiating these minerals challenging. Spinels (spinel, magnetite, chromite) and brucite look different under a polarizing light microscope. The spinel series in these samples are often reddish-brown or dark brown to black. Spinel is most often in individual, isolated grains that are reddish brown and semi-transparent (Figure 12, 15, 20, among others). Magnetite and chromite are opaque and appear black (Figure 9, 11, 14, 15, etc…). They were not distinguished from each other and assumed to be magnetite in thin sections. Individual mineral elemental analysis would be needed to distinguish them. Brucite is often colorless or yellowish and found intermixed with serpentine and/or in veins (Figure 11, 19). Therefore, thin sections were used to confirm XRD analysis, and identify trace or relict minerals that (1) may not have been included in the ~15 mg of powdered rock used in XRD and/or (2) were present in amounts too small to be detected by the

XRD. Thin sections also allow petrographic study of the spatial distribution of mineral grains and textures.

3.1.1 Diffractograms

The main two serpentine phases available for peak comparisons in reference databases were antigorite and lizardite. While each sample had peaks corresponding to one or both of these phases, it is also highly likely that other phases of serpentine like chrysotile and greenalite were also present. The serpentine peaks (Figures 5-8) generally have the highest intensity in the samples followed by peaks for magnetite, spinel, and olivine near 39 to 44°2θ. The intensity indicates diffraction caused by mineral crystallinity and helps in mineral identification because each mineral has a unique diffraction pattern. Figure 6 is the stacked diffractogram for ZO samples. PHL_3 has the strongest peaks for olivine found in any of the samples. Figure 7 is the stacked diffractogram for CRO CROMO2 samples. CROMO2_3 has an unknown peak with a 2θ of ~31° (*i.e.*, d-spacing of 3.3471Å). The variation of peaks with a 2θ of ~40-45° is from magnetite and spinel variations.

Overall, XRD data indicate that serpentine, magnetite and/or other spinel are present in all the samples. Pyroxene, olivine, chlorite, brucite, amphibole, garnet, and/or other clay minerals such as smectite are identified in various samples.

3.1.2 Thin section and SEM images

Serpentine is the most abundant mineral based on qualitative assessment of mineral abundance in thin sections. Serpentine often forms a square-like mesh or net-

like texture on the micro- and macro-scale; interlocking veins of serpentine surround

fractured relict (or variably serpentinized) olivine and/or pyroxene, as seen especially

in Figures 12, 16, 19, 20, and 23. This mesh texture is often more easily visible in xpl

with the grey serpentine surrounding the more brightly colored (higher birefringence)

olivine/pyroxenes. Serpentine is also found in larger veins that show variations in

color, texture, and/or composition (TS Figures 11a, 16a, and 23a, and SEM-EDS

Figures 13a & d) from the center to edge of the vein. The dissolution of olivine can

also be seen in SEM-EDS images (Figure 22) that show olivine grains with irregular

grain boundaries (jagged dendritic wedges on the edges), giving the appearance of

micro-scale reaction zone.

3.1.3 Mineralogical results summary

Documenting site-specific mineral assemblages is a first step in characterizing

the redox status of Fe because Fe occurs in different valence states in different

minerals (Table 1). The mineral assemblages in the samples are similar to those

predicted [Wetzel and Shock, 2000; Moody, 1976; McCollom and Seewald, 2013;

Sleep *et al.*, 2004] and similar to those found in serpentinite cores from Ocean Drilling

Project (ODP) sites [Bach *et al.*, 2006; Beard *et al.*, 2009 also found plagioclase; Klein

et al., 2014].

All of the target samples contain serpentine (lizardite and/or antigorite, and

probably greenalite and/or chrysotile) and spinel group minerals such as magnetite

(Fe), chromite (Fe & Cr), gahnite (Zn & Al), and/or galaxite (Mn, Mg, Al, and/or Fe).

Different minerals indicate different compositions and temperature and pressure

conditions. Olivine and pyroxenes were identified in samples that appear to be less serpentinized. Olivine was identified in all the ZO samples and three of the four samples from McLaughlin borehole 313, which had hundreds of feet of variably serpentinized peridotite recorded on the core log.

Chlorite was found in small quantities in samples 313_210 and maybe 313_356, indicating that there were, at least locally, variations in composition of the fluid and/or rock, temperature, and/or pressure that encouraged chlorite instead of serpentine to form. From a thermodynamic viewpoint, peridotite alteration modeled in the subseafloor at ~350 to 400°C yields much less chlorite than serpentine, but chlorite is expected, to some extent, in these ophiolite samples (Wetzel and Shock, 2000).

Garnet was found in samples HLSC_1, 313_356, and maybe PHL_3, indicating possible high pressure/temperature conditions, likely in a subduction zone subsurface environment in the mantle wedge [Liou *et al.*, 2007] and/or during emplacement at the continental margin. Andradite garnet ($Ca_3Fe^{3+}_2(SiO_4)_3$) was identified by XRD in HLSC_1 and 313_356. Andradite garnet can be formed at low pressure and high temperatures [Huckenholz and Yoder, 1971; Gustafson, 1974]. Chemical analysis is needed to confirm the XRD analysis. The garnet grains in 313_356 do not appear to be the well-formed, geometric crystals expected if the garnets were neoformed minerals, instead suggesting that they may have started to undergo dissolution and/or other alteration since their original formation. It is possible that these samples were in a relatively shallow area in a subduction zone but still exposed to high temperatures (prograde metamorphism), and then uplifted (retrograde metamorphism) and emplaced. Sample 313_356 seems to have a more complicated

history than some of the other samples as indicated by the garnet and lack of serpentine veins or classic serpentinite mesh textures.

The brucite group mineral identified by XRD is portlandite, which is a Ca-rich hydroxide instead of the expected Mg-rich ($Mg(OH)_2$) brucite, predicted by McCollom and Bach [2009] and references therein. Portlandite was identified in samples also containing pyroxene (cpx—hedenbergite and johannsenite—and opx—enstatite group), which could account for the Ca. However, the Ca could have also come from entrapped seawater and/or the sedimentary rock units of the CRO and ZO. It is also possible that Fe and Mg-rich brucite is present in the samples.

The minerals most likely to contain Fe are magnetite, spinel, olivine, pyroxenes, and serpentine.

3. 2 XRF & SEM-EDS

In general, the Fe concentrations found in the samples are similar to those found in other variably serpentinized peridotite (see Table 6, Figure 24, Table A2 for data from literature, and Table A8 for raw XRF data collected). CRO core 313 and the ZO samples have the highest concentrations of Fe (Figure 24). They are also the samples with more abundant relict olivine and, therefore, are less serpentinized (see Figures 10-12, 14, 16-21, 23). This leads to the conclusion that Fe is reapportioned into different host minerals through water-rock reaction, may have left the system in fluid phases (Fe^{2+}) during serpentinization, and/or CRO core 313 and the ZO samples parent rocks had more Fe than the other samples. It is possible that Fe^{2+} could have been oxidized, precipitated, and accumulated in areas other than where the samples

were collected, perhaps in the more hydrothermal areas of the ophiolites where Au, Ag, S, and other metals also accumulate. CRO core 313 was located in what was a pit mine, so maybe, it was more Fe-rich because more Fe was being deposited, which may also account for the higher percent of Fe^{3+} reported in MOSS.

Sample 313_210 has the highest bulk concentration of Fe across all samples. It also contains large grains of possible Fe-oxide(s) (and/or hydroxides) (Figure 10), which may account for the larger bulk concentration of Fe.

HLSC_1 has the lowest concentration of Fe and most of the Fe is in magnetite instead of the silicates. The TS for HLSC_1 also shows Fe-oxide zones similar to 313_210 and magnetite scattered throughout (Figure 9). HLSC_1 may be a case of under exaggeration of the bulk sample concentration, or the thin section could be an over exaggeration and just happens to be a Fe-oxide rich section.

SEM-EDS data for sample 313_329 (Tables 7-10, Figures A19-23) indicate that the Fe concentration in the minerals analyzed is ≤0.02wt% (200 ppm) (see section 2.5 for detection limit discussion—0.5 wt%) for olivine (Tables 7, 9, and 10), ≤11.1wt% (111,000 ppm) for an alteration mineral (probably serpentine) (Table 8) next to an olivine grain (Table 7) that had ≤0.02 wt% Fe at its center. The fractured spinel (Table 11) had ≤33.3 wt% Fe (332,500 ppm) with the median being 0.03 wt% (300 ppm) (of the 10 spots analyzed on the spinel, seven had Fe wt % of 0.03, one with 0.02, one with 26.6, and one with 33.3 wt%). According to these numbers and mineral observations, the bulk of the Fe is concentrated in spinel group minerals including magnetite and other Fe-oxides. There is also Fe in serpentine, possibly greenalite, with smaller contributions from olivine.

Spinel also contains large quantities of Al (22.7 to 80.3 wt % or 332,500 to 803,100 ppm). The smallest concentration of Al occurred at the spot where Fe was also the highest. The Al and the spinels could be a catalyst for hydrogen generation [Andreani *et al.*, 2013]. Besides spinels, Al can also be hosted in olivine, serpentine, pyroxene, and other clay minerals. Al was identified in olivine by SEM-EDS as having ≤5.89 wt% (589,000 ppm), which was surprising because olivine is not usually thought of as incorporating elements with a 3+ valence state into a 2+ slot.

3. 3 MOSS

MOSS parameters (IS, QS, W, A, and B_{hf}), chi-squared (X^2), and areas under the curve (Table 12) are similar to those of serpentine and other minerals reported by others (Table 3, Table A2) . Within each MOSS plot (Figures 30-45), the best-fit curve (red) can be seen as a combination of Fe^{2+}, Fe^{3+}, and magnetite ($Fe_2^{3+}Fe^{2+}O_4$) curves. In practice, curve fitting parameters determine the % area under the curves that is tied to Fe^{2+}, Fe^{3+}, or magnetite. For samples from CRO and ZO, percentages of total iron found as Fe^{2+}, Fe^{3+}, and magnetite-hosted Fe are stacked in Figure 46. Magnetite has distinct fit, sextet patterns and curves that are distinguishable from other minerals in the sample such as Fe-oxides like hematite. The silicates (serpentine, olivine, pyroxene, chlorite, and amphibole), other clay minerals, hydroxides, and/or other spinel group minerals account for the Fe^{2+} and Fe^{3+} doublet curves. Each the Fe^{2+} and Fe^{3+} doublet curve could account for a different mineral.

3.3.1 MOSS analysis of bulk sample

The amount of magnetite in each sample is just a random chance from sampling and the magnetite peaks are fit so they can be removed and look more directly at the silicates, especially serpentine. Magnetite, however, will be discussed in this section in the attempt to gauge the status of the whole bulk rock and not just the silicates, which will be discussed in the next section (3.3.2). The $\%Fe^{3+}$ and $\%Fe^{2+}$ values that include divided up %magnetite are also utilized in the H_2 generation calculations.

HLSC_1 has the most Fe attributed to magnetite: ~63%. Samples 309_105_A, 313_210, 313_318, 313_329, 313_356, and PHL_3 have the least Fe attributed to magnetite (<1%) and generally have the least visible magnetite in TS. When %magnetite is divided up into Fe^{2+} and Fe^{3+} (see Figure 47) and added to $\%Fe^{3+}$ and $\%Fe^{2+}$, the average Fe^{2+} for CRO is 54% Fe^{2+} (~30% range from 40-70%) and ZO averages less at 37% Fe^{2+} (~6% range from 34-40%). In other words, ZO averages more Fe^{3+} (~63%, 6% range from 60-66) than the CRO (~46% Fe^{3+}, 30% range from 30-60%). The wide range for CRO samples may largely be due to the larger number of samples (12 vs. 4 for ZO).

Samples from CRO core 313 had the most variation with ~18% range (~36% Fe^{3+} in sample 313_210 to 54% Fe^{3+} in sample 313_356). ZO samples had a smaller range (6% from 60-66 $\%Fe^{3+}$), but also fewer samples to compare. I suspect, however, that even with a similar spread of hand and core samples, the ZO would have closer percentages (*i.e.*, tighter range) than the CRO because the ZO rocks have a less complicated tectonic history; the CRO, however, is often found reworked in mélanges

or mixtures of the classic ophiolite sequence. The ZO hand samples were collected at the surface, so it is possible that less serpentinized and weathered samples could be found deeper below the surface, which would cause more variation in Fe valence state percentages. The CRO was a mix of surface samples, shallow cores, and deep cores (>300ft). When all surface and core samples are compared together, there is not a direct correlation between depth and %Fe^{3+}, possibly due to the mixing and/or additional oxidation at the surface when exposed to O_2. When cores samples only are compared, especially 309 and 313, there is a slight positive correlation between depth and %Fe^{3+} (Figure A39).

3.3.2 MOSS analysis of silicates

To better understand the redox state of the system, the magnetite was factored out (Table 12, Figure 48) to get a Fe^{3+}/Fe_{tot} in other minerals, especially silicates like serpentine.

When comparing ZO samples to CRO core 313 samples that still had relict olivine, it seems like the more olivine there is, the more Fe^{3+} there is. In other words, ZO samples have the highest %Fe^{3+} average (~63%). CRO core 313 samples had ~45% average). Some samples with little to no olivine, such as CROMO2 samples 1A and 4A, and 313_356, actually hover around 50 % Fe^{3+}. Sample167_238 has the expected higher %Fe^{3+} (57%), which may have relict olivine and/or pyroxenes similar to ZO and 313 samples. HLSC_1, CROMO2 _2, CROMO2_3A, 309_105_A, and 309_150 have <40 %Fe^{3+}.

Variations in Fe valence states were expected because of the varying degree of serpentinization, the mineral contents, and environments even within a few feet. It was assumed that the Fe would be oxidized during serpentinization, so it was expected that samples with trace amounts of olivine would have a higher percentage of Fe^{3+} than Fe^{2+}; however, the general trend where the more olivine-rich or the less serpentinized rocks had higher $\%Fe^{3+}$. The Fe^{3+} could be within the pyroxenes, spinel, and serpentine and/or it is possible that when the Fe^{2+} was mobilized, it was carried away in the fluid while the Fe^{3+} was deposited (recall that Fe^{3+} is not soluble in water at high pH, which would apply in this case). As discussed in section 2.7, Adreani *et al.* [2013B] did not see a change in Fe concentration over time, so the Fe is probably staying within close proximity to its parent mineral.

O'Hanley and Dyar [1993; 1998] (Table A2) analyzed ~35 lizardite and chrysotile specimens from Canada with MOSS and found a range of 22-100% Fe^{3+} (most between 30 and 88 $\%Fe^{3+}$ and chrysotile generally had less $\%Fe^{3+}$ than lizardite). Klein *et al.* [2014] analyzed 12 samples from the Ocean Drilling Program (ODP) and Deep Sea Drilling Project (DSDP) of variably serpentinized peridotites (harzburgites and dunites). They found a range from 14-66 $\%Fe^{3+}$ and ~54% average without factoring in magnetite. The samples also ranged from magnetite-rich to magnetite-poor. Canil *et al.* [1994] found <5 $\%Fe^{3+}$ in various African peridotites that included garnet harzburgite and iherzolite, and spinel iherzolite.

3. 4 H$_2$ modeling

Hydrogen generation was calculated using the normalized average Fe concentrations, the estimated volumes of the ZO and CRO, the valence states of Fe

obtained from MOSS with %magnetite divided into $\%Fe^{3+}$ and $\%Fe^{2+}$ values, and the

simplified serpentinization reaction equation (1). For each sample's hydrogen yield, it

is assumed that the Fe concentration for that sample was the same for all of the

peridotite units of the CRO or ZO. Table 13 and 14 (utilizes density into conversion

from ppm Fe to possible Tmol H_2 (T, Tera=10^{12})) are summaries of normalized Fe

concentration in ppm (see appendix Table A7 for FeO wt%), Fe valence states in

percent from MOSS, and possible hydrogen gas yield per 1km^3 of rock and per the

total volume of the peridotite units of the corresponding ophiolite. The estimated

volume of the peridotite units in the CRO is 7730km^3 [Area (~3865km^2)—Carnevale,

2013; depth (~2km)—Coleman, 2000] and 1455 in the ZO [Area (~485km^2)—

Abrajano and Pasteris, 1989; depth (~3km)—Hawkins and Evans, 1983]. Average

density (g/cm^3) of variably (40-100%) serpentinized hazburgites and dunites taken

from Andreani *et al.* [2013B] and Klein *et al.* [2013].

Explanations and example calculations starting with CRO sample 167_238 Fe

concentration (ppm) to possible H_2 (Tmol) already released (total $\%Fe^{3+}$) are below.

Calculation using mg/L to convert ppm to g:

$$
\left(\begin{array}{c} Concentration\ of\ Fe\ in\ ppm \\ \dfrac{29910 ppm\ Fe}{1} \end{array} \right) \times \left(\begin{array}{c} Convert\ ppm\ to\ \frac{mass\ (mg)}{volume} \\ \dfrac{1\frac{mg}{L}}{1ppm} \end{array} \right) \times
$$

$$
\left(\begin{array}{c} convert\ mg\ to\ g \\ \dfrac{1g}{1000mg} \end{array} \right) \times \left(\begin{array}{c} convert\ g\ Fe\ to\ mol\ Fe \\ \dfrac{1\ mol\ Fe}{55.85g\ Fe} \end{array} \right) \times
$$

$$
\left(\begin{array}{c} Convert\ mol\ Fe\ to\ mol\ H_2 \\ \dfrac{1\ mol\ H_2}{1\ mol\ Fe^{2+}} \end{array} \right) \times \left(\begin{array}{c} multiply\ total\ \%\ Fe^{2+}\ or\ Fe^{3+} \\ 40\%Fe^{3+} + \left(\frac{2}{3} \times 30\%Mag\right) \end{array} \right) \times
$$

$$\begin{pmatrix} \textit{muliply the volume of the ophiolite} \\ \dfrac{7730km^3}{1} \end{pmatrix} \times$$

$$\begin{pmatrix} \textit{convert } km^3 \textit{ to L or L to } km^3 \\ \left(\dfrac{1000m}{1\ km}\right)^3 \times \left(\dfrac{100cm}{1\ m}\right)^3 \times \dfrac{1mL}{1cm^3} \times \dfrac{1L}{1000mL} \end{pmatrix} = \begin{pmatrix} \textit{Leaving only moles of } H_2 \\ 2.48x10^{15}mol\ H_2\ (\ 2480\ Tmol) \end{pmatrix}$$

The same conversion, only using mg/kg and density (g/cm^3):

$$\begin{pmatrix} \textit{Concentration of Fe in ppm} \\ \dfrac{29910ppm\ Fe}{1} \end{pmatrix} \times \begin{pmatrix} \textit{Convert ppm to } \dfrac{mass}{volume} \\ \dfrac{1\frac{mg}{kg}}{1ppm} \end{pmatrix} \times$$

$$\begin{pmatrix} \textit{convert mg to g} \\ \dfrac{1g}{1000mg} \end{pmatrix} \times \begin{pmatrix} \textit{convert g Fe to mol Fe} \\ \dfrac{1\ mol\ Fe}{55.85g\ Fe} \end{pmatrix} \times$$

$$\begin{pmatrix} \textit{Convert mol Fe to mol } H_2 \\ \dfrac{1\ mol\ H_2}{1\ mol\ Fe^{2+}} \end{pmatrix} \times \begin{pmatrix} \textit{multiply total \% Fe }^{2+}\textit{or Fe }^{3+} \\ 40\%Fe^{2+} + \left(\dfrac{2}{3} \times 30\%Mag\right) \end{pmatrix} \times$$

$$\begin{pmatrix} \textit{Multiply by average density and convert it to } \dfrac{kg}{km^3} \\ \left(\dfrac{2.68g}{cm^3}\right) \times \left(\dfrac{100cm}{1\ m}\right)^3 \times \left(\dfrac{1000m}{1\ km}\right)^3 \times \dfrac{1kg}{1000g} \end{pmatrix} \times$$

$$\begin{pmatrix} \textit{muliply the volume of the ophiolite} \\ \dfrac{7730km^3}{1} \end{pmatrix} = \begin{pmatrix} \textit{Leaving only moles of } H_2 \\ 6.65x10^{15}mol\ H_2\ (\ 6650\ Tmol) \end{pmatrix}$$

The total possible hydrogen production (Tmol) normalized to a volume of one

1km^3 (Figure 49 and 51) illustrates that even though the overall volume of the ZO is

smaller, it can produce more hydrogen per unit volume than the CRO due to the

generally higher concentration of Fe (Figure 24). The average total hydrogen that

could be produced-per 1km^3, given the present Fe valence status of the bulk rock, is

0.46 Tmol $H_{2(g)}$ for the CRO and 0.64Tmol $H_{2(g)}$ for the ZO. Core 313 samples had the

highest average for a CRO location at 0.53 Tmol $H_{2(g)}$, followed by 167_238 and

CROMO2 (0.43 Tmol $H_{2(g)}$), and HLSC_1 and core 309 (0.40 Tmol $H_{2(g)}$). When density is used in the calculation, the averages in Tmol are ZO-1.70, CRO-1.22, 313 core-1.41, and CROMO 1.15.

Figure 50 and 51 show hydrogen generation in Tmol using the estimated volumes of the ZO and CRO peridotite, as reported in the literature. Due to its total smaller volume, the ZO is estimated to produce less hydrogen than the CRO. The average hydrogen production for the CRO is 3511 Tmol and 923 Tmol for the ZO. The highest CRO site average is 4058 Tmol for core 313 samples, followed by CROMO1 (3327 Tmol), 167_328 (3310 Tmol), HLSC_1 (3107 Tmol), and core 309 (3086 Tmol). When density is used in the calculation, the averages in Tmol are ZO-2475, CRO-9410, core 313-10,877, and CROMO 8918.

3.5 Implications of rock data and modeling outputs

Possible hydrogen yield over the lifetime of the ultramafic peridotite blocks considered range from ~2848 Tmol to ~4752 Tmol for the CRO and ~908 Tmol to 1029 Tmol for the ZO (when density is use it is ~2028 to 2758 for ZO and ~7634 to 12735 for CRO), and is modeled here as largely controlled by Fe concentration and the volume of the ophiolite. The likelihood of water causing oxidization of Fe^{2+} to Fe^{3+} and releasing hydrogen is also a factor, but not directly tied into the calculations. The range of samples with their different Fe concentrations may give an upper and a lower limit of the total hydrogen generation possible from the peridotite units. It is also possible to have hydrogen produced from other mafic and ultramafic layers such as basalt and gabbros, so the actual hydrogen generation from the entire ophiolite could be higher than the simplified model predicts.

Fe is not uniformly distributed and sample concentrations (normalized) range from ~28741 to 50673ppm in the CRO and ~58364 to 78265 in the ZO. The valence states of the Fe also vary with each sample; the %magnetite ranges from ~0-63%, Fe^{3+} from ~14 to 65%, and Fe^{2+} from ~23 to 70 %. When magnetite is separated into its Fe^{2+} and Fe^{3+} components, total Fe^{2+} ranges from ~34 to 70% and Fe^{3+} ranges from ~30 to 66%. The range for silicates and factoring out magnetite ranges from 24 to 66%Fe^{3+}. Variation in concentration and valence states indicates different reaction histories. On the other hand, if we assume that the olivine had similar starting Fe compositions, then the variation in observed concentrations shows that the Fe is not constant in the system(s).

The more Al-rich a sample is the more hydrogen can be yielded via serpentinization [Andreani *et al.*, 2013]. Additional analysis of the bulk samples considered in this work and separated mineral grains is required to constrain where and how much Al is in the system at the time, to constrain the relative volumes of minerals (% serpentine, olivine, chlorite, magnetite, spinel, etc...) to help gage the extent of serpentinization (parent vs. alteration minerals), to better identify minerals including trace minerals to understand better the chemistry of the system, and to analyze fluid data, if possible, of current fluids in the system including dissolved gases like hydrogen.

Based on TS, XRD, and MOSS, the CRO and ZO are still reactive as both ophiolites still have budgets of Fe^{2+} and serpentinization is not complete. However, in areas that are mostly serpentinized, the remaining Fe^{2+} budget has been partitioned into minerals like spinel, serpentine, and magnetite that are generally chemically stable

at surface conditions and based on the sample set, $\%Fe^{2+}$ could stay near 50% of the

total Fe.

4. Conclusion

Serpentinites evolve complexly in the natural environment. Tectonics, emplacement history, age, climate, composition, unit hydrology, etc…all influence the redox status of a given ophiolite. The samples presented here give a glimpse into the variability of the redox status of ophiolite-hosted ultramafic peridotites, at ZO and CRO localities.

In general, the ZO has higher Fe concentrations and greater modern Fe^{3+}, thus could produce more hydrogen per unit volume than the CRO because of the higher Fe content in the system. The larger area and volume extent (though poorly constrained) of the CRO does mean that the lower hydrogen productivity per unit volume might yet yield greater hydrogen in total, if integrated over the entire ultramafic volume, over the alteration lifetime of the ultramafic block. Taken together, this work indicatesthat geologically long term support of a H_2-fueled deep biosphere by serpentinization is feasible, and shows that the ultramafic subsurfaces of the CRO and ZO are not yet depleted in Fe^{2+}.

Serpentinizing systems on Earth can be used as an analog for other terrestrial planets as we continue to search for the limits of life both on Earth and in the universe.

5. Implications for future research

A more thorough and accurate chemical (XRF, Mg concentration data for both bulk sample and individual minerals) and mineralogical analysis of the samples presented here, along with additional samples, are needed to better (1) constrain the possible hydrogen generation of the CRO and ZO, (2) understand the Fe and Mg concentration, their relationship within the contexts of peridotites, serpentinized or not, and which minerals they are partitioned into, (3) differentiate between spinel group minerals such as spinel, magnetite, and chromite, (4) obtain mineral specific redox status and possible zoning as a marker of the changes the mineral(s) has undergone as the rock and ophiolite unit were formed, and (5) provide markers to look for as we continue the search for life on Earth and other terrestrial planets.

References Cited

Abrajano, T. A. and J. D. Pasteris (1989), Zambales ophiolite, Philippines II. Sulfide petrology of the critical zone of the Acoje Massif, *Tectonophysics, 103*, 64-77.

Andreani, M., I. Daniel, and M. Pollet-Villard (2013), Aluminum speeds up the hydrothermal alteration of olivine, *Am. Mineral., 98*(10), 1738-1744.

Andreani, M., M. Muñoz, C. Marcaillou, and A. Delacour (2013B), µXANES study of iron redox state in serpentine during oceanic serpentinization, *Lithos, 178*(0), 70-83, doi: http://dx.doi.org/10.1016/j.lithos.2013.04.008.

Bach, W., H. Paulick, C. J. Garrido, B. Ildefonse, W. P. Meurer, and S. E. Humphris (2006), Unraveling the sequence of serpentinization reactions: petrography, mineral chemistry, and petrophysics of serpentinites from MAR 15 N (ODP Leg 209, Site 1274), *Geophys. Res. Lett., 33*(13).

Beard, J. S., B. R. Frost, P. Fryer, A. McCaig, R. Searle, B. Ildefonse, P. Zinin, and S. K. Sharma (2009), Onset and progression of serpentinization and magnetite formation in olivine-rich troctolite from IODP Hole U1309D, *J. Petrol., 50*(3), 387-403.

Blake, D., D. Vaniman, C. Achilles, R. Anderson, D. Bish, T. Bristow, C. Chen, S. Chipera, J. Crisp, and D. Des Marais (2012), Characterization and calibration of the CheMin mineralogical instrument on Mars Science Laboratory, *Space science reviews, 170*(1-4), 341-399.

Brazelton, W. J., B. Nelson, and M. O. Schrenk (2012), Metagenomic evidence for H_2 oxidation and H_2 production by serpentinite-hosted subsurface microbial communities, *Frontiers inMicrobiology, 2*, 268, doi: 10.3389/fmicb.2011.00268; 10.3389/fmicb.2011.00268.

Brazelton, W. J., M. O. Schrenk, D. S. Kelley, and J. A. Baross (2006), Methane- and sulfur-metabolizing microbial communities dominate the Lost City hydrothermal field ecosystem, *Appl. Environ. Microbiol., 72*(9), 6257-6270, doi: 72/9/6257 [pii].

Bryndzia, L. T. and B. J. Wood (1990), Oxygen thermobarometry of abyssal spinel peridotites: the redox state and C–O–H volatile composition of the Earth's sub-oceanic upper mantle, *Am. J. Sci., 290*(10), 1093-1116.

Canil, D., H. S. C. O'Neill, D. Pearson, R. Rudnick, W. McDonough, and D. Carswell (1994), Ferric iron in peridotites and mantle oxidation states, *Earth Planet. Sci. Lett., 123*(1), 205-220.

Cardace, D., T. Hoehler, T. McCollom, M. Schrenk, D. Carnevale, and M. Kubo (2013), Establishment of the Coast Range ophiolite microbial observatory (CROMO): drilling objectives and preliminary outcomes., *Scientific Drilling*(16).

Carnevale, D. C. (2013), Carbon sequestration potential of the Coast Range Ophiolite in California, Masters of Science thesis, 15 pp., The University of Rhode Island.

Case, D. H., A. Ijiri , Y. Morono , V. J. Orphan, and F. Inagaki (2013), Microbiological and Geochemical Characterization of the Deep Subsurface Environment: Kumano Mud Volcano, Nankai Trough, Japan*, Abstract B13C-0483 presented at 2013 Fall Meeting, AGU, San Francisco, Calif. , 9-13 Dec.*

Charlou, J. L., J. P. Donval, C. Konn, H. Ondréas, Y. Fouquet, P. Jean-Baptiste, and E. Fourré (2010), High production and fluxes of H2 and CH4 and evidence of abiotic hydrocarbon synthesis by serpentinization in ultramafic-hosted hydrothermal systems on the Mid-Atlantic Ridge*, Geophysical Monograph Series, 188*, 265-296, doi: 10.1029/2008GM000752.

Cipolli, F., B. Gambardella, L. Marini, G. Ottonello, and M. Vetuschi Zuccolini (2004), Geochemistry of high-pH waters from serpentinites of the Gruppo di Voltri (Genova, Italy) and reaction path modeling of CO_2 sequestration in serpentinite aquifers*, Appl. Geochem., 19*(5), 787-802.

Coleman, R. G. (1981), *Tectonic setting for ophiolite obduction in Oman, Journal of Geophysical Research, 86*, 2497-2508.

Coleman, R. G. (2000), Prospecting for ophiolites along the California continental margin*, Special Papers-Geological Society of America*, 351-364.

Deschamps, F., M. Godard, S. Guillot, and K. Hattori (2013), Geochemistry of subduction zone serpentinites: A review*, Lithos, 178*, 96-127.

Dickinson, W. R., C. A. Hopson, J. B. Saleeby, R. Schweickert, R. Ingersoll, E. Pessagno Jr, J. Mattinson, B. Luyendyk, W. Beebe, and D. Hull (1996), Alternate origins of the Coast Range ophiolite (California): Introduction and implications*, GSA today, 6*(2), 1-10.

Dilek, Y. (2003), Ophiolite concept and its evolution*, Special Papers-Geological Society of America*, 1-16.

Dyar, M. D., D. G. Agresti, M. W. Schaefer, C. A. Grant, and E. C. Sklute (2006), Mössbauer spectroscopy of Earth and planetary materials*, Annu. Rev. Earth Planet. Sci., 34*, 83-125.

Dyar, M., M. Schaefer, E. Sklute, and J. Bishop (2008), Mössbauer spectroscopy of phyllosilicates: Effects of fitting models on recoil-free fractions and redox ratios*, Clay Miner., 43*(1), 3-33.

Ehlmann, B., J. Mustard, and S. Murchie (2010), Geologic setting of serpentine deposits on Mars*, Geophys. Res. Lett., 37*(6).

EPA (2007), Method 6200: Field portable x-ray fluorescence spectrometry for the determination of elemental concentrations in soil and sediment.

Evans, B. W. (2008), Control of the products of serpentinization by the Fe2 Mg− 1 exchange potential of olivine and orthopyroxene, *J. Petrol., 49*(10), 1873-1887.

Evans, B. W., M. D. Dyar, and S. M. Kuehner (2012), Implications of ferrous and ferric iron in antigorite, *Am. Mineral., 97*(1), 184-196.

Flanagan, F. J. (1976), Descriptions and Analyses of Eight New USGS Rock Standards: Twenty-eight papers present analytical data on new and previously described whole-rock standards, *United States Geologic Survey Professional Paper, 840*, 171.

Fuchs, Y., J. Linares, and M. Mellini (1998), Mössbauer and infrared spectrometry of lizardite-1T from Monte Fico, Elba, *Physics and Chemistry of Minerals, 26*(2), 111-115.

Goldstein, J., D. E. Newbury, D. C. Joy, C. E. Lyman, P. Echlin, E. Lifshin, L. Sawyer, and J. R. Michael (2003), *Scanning Electron Microscopy and X-Ray Microanalysis*, 3rd ed., 689-350 pp., Springer, United States of America.

Goncharov, A., D. Ionov, L. Doucet, and L. Pokhilenko (2012), Thermal state, oxygen fugacity and C-O-H fluid speciation in cratonic lithospheric mantle: New data on peridotite xenoliths from the Udachnaya kimberlite, Siberia, *Earth Planet. Sci. Lett., 357*, 99-110.

GUSTAFSON, W. I. (1974), The Stability of Andradite, Hedenbergite, and Related Minerals in the System Ca—Fe—Si—O—H, *J. Petrol., 15*(3), 455-496.

Hall, R., J. R. Ali, C. D. Anderson, and S. J. Baker (1995), Origin and motion history of the Philippine Sea Plate, *Tectonophysics, 251*(1), 229-250.

Hawkins, J. W. and C. A. Evans (1983), Geology of the Zambales Range, Luzon, Philippine Islands: ophiolite derived from an island arc-back arc basin pair, *Geophysical Monograph Series, 27*, 95-123.

Hawkins, J. (2003), Geology of supra-subduction zones: Implications for the origin of ophiolites, *Ophiolite Concept and the Evolution of Geological Thought: Boulder, Colorado.Geological Society of America Special Paper, 373*, 227-268.

Hirschmann, M. M., C. Aubaud, and A. C. Withers (2005), Storage capacity of H_2O in nominally anhydrous minerals in the upper mantle, *Earth Planet. Sci. Lett., 236*(1), 167-181, doi: 10.1016/j.epsl.2005.04.022.

Huckenholz, H. and H. Yoder Jr (1971), Andradite stability relations in the CaSiO 3-Fe 2 O 3 join up to 30 kb, *Neues Jahrb.Mineral.Abhandl, 114*, 246-280.

Jochum, K. P., U. Nohl, K. Herwig, E. Lammel, B. Stoll, and A. W. Hofmann (2005), GeoReM: A New Geochemical Database for Reference Materials and Isotopic Standards, *Geostandards and Geoanalytical Research, 29*(3), 333-338, doi: 10.1111/j.1751-908X.2005.tb00904.x.

Karig, D., D. Sarewitz, and G. Haeck (1986), Role of strike-slip faulting in the evolution of allochthonous terranes in the Philippines, *Geology, 14*(10), 852-855.

Kashefi, K. and D. R. Lovley (2003), Extending the upper temperature limit for life, *Science, 301*(5635), 934, doi: 10.1126/science.1086823 [doi].

Kelley, D. S., G. L. Fruh-Green, J. A. Karson, and K. A. Ludwig (2007), The Lost City hydrothermal field revisited, *Oceanography, 20*(4), 90-99.

Kelley, D. S. et al. (2005), A serpentinite-hosted ecosystem: the Lost City hydrothermal field, *Science, 307*(5714), 1428-1434, doi: 307/5714/1428 [pii].

Klein, F., W. Bach, S. E. Humphris, W. Kahl, N. Jöns, B. Moskowitz, and T. S. Berquó (2013), Magnetite in seafloor serpentinite—Some like it hot, *Geology, 42*(2), 135-138.

Liou, J. G., R. Y. Zhang, and W. G. Ernst (2007), Very high-pressure orogenic garnet peridotites, *Proc. Natl. Acad. Sci. U. S. A., 104*(22), 9116-9121, doi: 0607300104 [pii].

Mallmann, G. and H. S. C. O'Neill (2009), The crystal/melt partitioning of V during mantle melting as a function of oxygen fugacity compared with some other elements (Al, P, Ca, Sc, Ti, Cr, Fe, Ga, Y, Zr and Nb), *J. Petrol., 50*(9), 1765-1794.

Mayhew, L., E. Ellison, T. McCollom, T. Trainor, and A. Templeton (2013), Hydrogen generation from low-temperature water-rock reactions, *Nature Geoscience, 6*(6), 478-484.

McCollom, T. M. and W. Bach (2009), Thermodynamic constraints on hydrogen generation during serpentinization of ultramafic rocks, *Geochim. Cosmochim. Acta, 73*(3), 856-875.

McCollom, T. M. and J. S. Seewald (2013), Serpentinites, hydrogen, and life, *Elements, 9*(2), 129-134.

McLaughlin, R., M. Blake Jr, A. Griscom, C. Blome, and B. Murchey (1988), Tectonics of formation, translation, and dispersal of the Coast Range ophiolite of California, *Tectonics, 7*(5), 1033-1056.

Moody, J. B. (1976), Serpentinization: a review, *Lithos, 9*(2), 125-138, doi: 10.1016/0024-4937(76)90030-X.

Morrill, P. L., J. G. Kuenen, O. J. Johnson, S. Suzuki, A. Rietze, A. L. Sessions, M. L. Fogel, and K. H. Nealson (2013), Geochemistry and geobiology of a present-day serpentinization site in California: The Cedars, *Geochim. Cosmochim. Acta, 109*, 222-240.

Neal, C. and G. Stanger (1983), Hydrogen generation from mantle source rocks in Oman, *Earth Planet. Sci. Lett., 66*, 315-320.

Nealson, K. H., F. Inagaki, and K. Takai (2005), Hydrogen-driven subsurface lithoautotrophic microbial ecosystems (SLiMEs): do they exist and why should we care?, *Trends Microbiol., 13*(9), 405-410.

Nesse, W. D. (2000), *Introduction to Mineralogy*, 1st ed., Oxford University Press, Inc.

O'Hanley, D. S., and M. D. Dyar (1993), The composition of lizardite 1T and, the formation of magnetite in serpentinites, *American Mineralogist, 78*, 391-404.

O'Hanley, D. S. and M. D. Dyar (1998), The composition of chrysotile and its relationship with lizardite, *Canadian mineralogist, 36*, 727-740.

Okland, I., S. Huang, H. Dahle, I. H. Thorseth, and R. B. Pedersen (2012), Low temperature alteration of serpentinized ultramafic rock and implications for microbial life, *Chem. Geol., 318*, 75-87.

Orphan, V. J. and T. M. Hoehler (2011), Microbiology: hydrogen for dinner, *Nature, 476*(7359), 154-155.

Paukert, A. N., J. M. Matter, P. B. Kelemen, E. L. Shock, and J. R. Havig (2012), Reaction path modeling of enhanced in situ CO2 mineralization for carbon sequestration in the peridotite of the Samail Ophiolite, Sultanate of Oman, *Chem. Geol., 330–331*(0), 86-100, doi: http://dx.doi.org/10.1016/j.chemgeo.2012.08.013.

Pearson, D., F. Brenker, F. Nestola, J. McNeill, L. Nasdala, M. Hutchison, S. Matveev, K. Mather, G. Silversmit, and S. Schmitz (2014), Hydrous mantle transition zone indicated by ringwoodite included within diamond, *Nature, 507*(7491), 221-224.

Peslier, A. H., J. F. Luhr, and J. Post (2002), Low water contents in pyroxenes from spinel-peridotites of the oxidized, sub-arc mantle wedge, *Earth Planet. Sci. Lett., 201*(1), 69-86.

Rollinson, H. (1993), *Using Geochemical Data: Evaluation, Presentation, Interpretation*, 1st ed., 9-16 pp., Longman Scientific & Technical.

Sano, Y., A. Urabe, H. Wakita, and H. Wushiki (1993), Origin of hydrogen-nitrogen gas seeps, Oman, *Appl. Geochem., 8*(1), 1-8.

Schrenk, M. O., D. S. Kelley, S. Bolton, and J. D. Baross (2004), Low archaeal diversity linked to sub-seafloor geochemical processes at the Lost City Hydrothermal Field, Mid-Atlantic Ridge, *Environmental Microbiology, 6(10)*, 1,086-1,095.

Schrenk, M. O., W. J. Brazelton, and S. Q. Lang (2013), Serpentinization, carbon, and deep life, *Rev Mineral Geochem, 75*, 575-606.

Shervais, J. W. (2001), Birth, death, and resurrection: The life cycle of suprasubduction zone ophiolites, *Geochem. Geophys. Geosyst., 2*(1).

Shervais, J. W., B. L. Murchey, D. L. Kimbrough, P. R. Renne, and B. Hanan (2005), Radioisotopic and biostratigraphic age relations in the Coast Range Ophiolite, northern California: Implications for the tectonic evolution of the Western Cordillera, *Geological Society of America Bulletin, 117*(5-6), 633-653.

Shervais, J. W. and D. L. Kimbrough (January, 1985), Geochemical evidence for the tectonic setting of the Coast Range ophiolite: A composite island arc–oceanic crust terrane in western California, *Geology, 13*(1), 35-38, doi: 10.1130/0091-7613(1985)13<35:GEFTTS>2.0.CO;2.

Sleep, N., A. Meibom, T. Fridriksson, R. Coleman, and D. Bird (2004), H2-rich fluids from serpentinization: Geochemical and biotic implications, *Proc. Natl. Acad. Sci. U. S. A., 101*(35), 12818-12823.

State of California (2010), California geologic map, Copyright 2007, http://www.quake.ca.gov/gmaps/GMC/stategeologicmap.html, accessed September 2014.

Szponar, N., W. J. Brazelton, M. O. Schrenk, D. M. Bower, A. Steele, and P. L. Morrill (2013), Geochemistry of a continental site of serpentinization, the Tablelands Ophiolite, Gros Morne National Park: A Mars analogue, *Icarus, 224*(2), 286-296.

Takai, K., K. Nakamura, K. Suzuki, F. Inagaki, K. H. Nealson, and H. Kumagai (2006), Ultramafics-Hydrothermalism-Hydrogenesis-HyperSLiME (UltraH3) linkage: a key insight into early microbial ecosystem in the Archean deep-sea hydrothermal systems, *Paleontological research, 10*(4), 269-282.

USGS (2011), tectonic plate boundary graphic, http://pubs.usgs.gov/publications/text/slabs.html, accessed September 2014.

Vaughan, A. P. M. and J. H. Scarrow (2003), Ophiolite obduction pulses as a proxy indicator of superplume events?, *Earth Planet. Sci. Lett., 213*(3), 407-416.

Wedepohl, K. H. and Y. Muramatsu (1979), Proceedings of the Second International Kimberlite Conference.

Wetzel, L. R. and E. L. Shock (2000), Distinguishing ultramafic-from basalt-hosted submarine hydrothermal systems by comparing calculated vent fluid compositions, *Journal of Geophysical Research: Solid Earth (1978–2012), 105*(B4), 8319-8340.

Winter, J. D. (2010), *Principles of Igneous and Metamorphic Petrology*, 2nd ed., 647-652 pp., Pearson Education, Inc.

Wirth, K. and A. Barth (2012), X-Ray Fluorescence (XRF), *Science Education Resource Center (SERC) at Carleton College, 2013*.

Yumul, G. P. (2007), Westward younging disposition of Philippine ophiolites and its implication for arc evolution, *Island Arc, 16*(2), 306-317.

Table 1: Some of the possible minerals involved/created during serpentinization [Winter, 2010; Nesse, 2000; Sleep *et al.*, 2004; Mindat.org; webmineral.com].

Mineral Group	Mineral name	Chemical Formula	Fe valence state
Olivine	Olivine	$(Mg, Fe)_2SiO_4$	2+
	Forsterite (Fo)	Mg_2SiO_4	2+
	Fayalite (Fa)	Fe_2SiO_4	2+
Orthopyroxene (opx)	Orthopyroxene	$(Mg, Fe)_2Si_2O_6$	2+
	ferrosilite	$FeSiO_3$ $(Fe_2Si_2O_6)$	2+
Clinopyroxene (cpx)	Pigeonite	$(Mg, Fe^{2+},Ca)Si_2O_6$	2+
	Hedenbergite	$(CaFeSi_2O_6)$	2+
	Augite	$(Ca, Mg, Fe^{2+}, Fe^{3+}, Al)_2(Si,Al)_2O_6)$	Both
	Aegirine-augite	$(Na,Ca)(Fe^{3+},Fe^{2+},Mg)Si_2O_6$	Both
	Omphacite	$(Ca,Na)(Mg,Fe^{2+},Fe^{3+},Al)\ Si_2O_6$	Both
Amphibole	Tremolite to ferro-actinolite	$Ca_2(Mg, Fe)_5Si_8O_{22}(OH)_2$	2+
	Richterite	$NaCa_2(Mg, Fe)_5Si_8O_{22}(OH)_2$	2+
	Hornblende	$(Na,K)_{0-1}Ca_2(Mg, Fe^{2+}, Fe^{3+}, Al)_5(Si,Al)_8O_{22}(OH)_2$	Both
	Pargasite-hornblend	$NaCa_2(Mg, Fe^{2+})_4AlSi_6Al_2O_{22}(OH)_2$	2+
Spinel	Spinel Spinel group	$MgAl_2O_4$ $(Mg, Fe^{2+}, Zn, Mn)(Fe^{3+}, Al)_2O_4$	Both
	Magnetite	Fe_3O_4 $(Fe^{2+}Fe^{3+}{}_2O_4)$	Both
	Chromite	$FeCr_2O_4$	Both
	Gahnite	$ZnAl_2O_4$	
	Galaxite	$(Mn,Mg)(Al,Fe^{3+})_2O_4$	3+
Serpentine	Antigorite	$Mg_3Si_2O_5(OH)_4$ $(Fe, Mg)_3Si_2O_5(OH)_4$	2+
	Chrysotile		2+
	Lizardite		2+
	Greenalite	$(Fe^{2+}, Fe^{3+})_{2-3}(Si_2O_5)(OH)_4$	Both
Other clay minerals	Smectite	$\sim Ca_{0.17}(Al,Mg,Fe)_2(Si,Al)_4O_{10}(OH)_2 \cdot nH_2O$	2+
	Chlorite	$(Mg,Fe,Al)_3(Si,Al)_4O_{10}(OH)_2 \cdot (Mg,Fe,Al)_3(OH)_6$	2+
	Vermiculite	$\sim (Mg,Ca)_{0.3}(Mg,Fe^{2+},Fe^{3+},Al)_3(Si,Al)_4O_{10}(OH)_6$	Both
	Talc	$Mg_3Si_4O_{10}(OH)_2$ also $(Mg,Fe)_3Si_4O_{10}(OH)_2$	2+
Hydroxides	Brucite	$Mg(OH)_2$, also $(Mg,Fe,Ca)(OH)_2$	2+
	Portlandite	$Ca(OH)_2$	
Fe Oxides	Wüstite	FeO	2+
	Magnetite	Fe_3O_4 $(FeFe_2O_4)$	Both
	Hematite	Fe_2O_3	3+
Limonite/ Fe oxyhydroxides	Goethite	$FeO(OH)$	2+
	Lepidocrocite	$FeO(OH)$	2+
Metals	awaruite	$Ni_{2-3}Fe$	Both

Table 2: Approximate locations, elevations, and depths of samples collected from Hyphus-Little Stoney Creek confluence in northern CA, CROMO2 well in Lower Lake, CA, and Zambales Ophiolite sites, Philippines. Homestake Mining Co. drill core sample locations, depths, and elevations.

Sample	Approx. Depth		Collar Elevation (ft above sea level)	Drill Hole	Total depth of well		Coordinates		Grid Coordinates	
	ft	m			ft	m	North	East	N.W.	N.E/S.W
167_238	238-BOH	73	2019.5	M81-167	249.0	~75.9	107458.91'	104156.78	125+96.7'	9+34.6' NW
309_105_A	105	32	1890.3	M81-309	330	~100.6	104118.95'	104022.53'	101+24.4'	13+15.1' SW
309_150	150	32								
309_84	84	46								
313_210	210	64	1776.2	M81-313	370	~112.8	103533.86'	105296.39'	88+57.4'	7+15.4' SW
313_318	318	97								
313_329	329	100								
313_356	356	109								

Sample	Approx. Depth		Collar Elevation (ft above sea level)	Drill Hole	Total depth of well		Latitude	Longitude
	ft	m			ft	m		
HLSC_1	0	0	~1230	na	0	0	N 39.32401°	W 122.52460°
CROMO2_1A	144-BOH	44-45.7	~2120	QV 2, 1	~150	45.7	N 38°51.724'	W 122°25.827'
CROMO2_2								
CROMO2_3A								
CROMO2_4A								
PHL_1	0	0	~590	na	0	0	N 15° 19.333'	E 120° 04.306'
PHL_2B	0	0		na	0	0		
PHL_3	0	0		na	0	0		
PHL_5	0	0		na	0	0		

Bottom of hole (BOH).

Table 3: Typical 295K Mössbauer spectroscopy (MOSS) data fitting parameters for some minerals found in Coast Range Ophiolite and Zambales Ophiolite taken from Dyar *et al.*, [2006].

Valence state or mineral	Doublet/sextet	IS (mm/s)	QS (mm/s)	Site occupancy or B_{hf} (tesla)
Ferric [Fe^{3+}]	Doublet	0.2-0.5	0.3-1.3	
Ferrous [Fe^{2+}]	Doublet	1.0-1.5	1.5-4.0	
Magnetite	Sextet	0.26	-0.02	~ 490
	Sextet	0.67	0.0	~ 460
Hematite	Sextet	0.37	-0.02	518
Spinel	Doublet	1.11	1.75	M
	Doublet	0.90	0.96	T
	Doublet	0.86	1.63	T
	Doublet	0.31	0.79	M
Chromite	Doublet	0.32	0.44	
	Doublet	0.22	0.91	
	Doublet	0.96	0.50	
	Doublet	0.90	1.15	
Olivine (Fa)	Doublet	1.14	3.10	M
Olivine (Fo)	Doublet	1.14	2.93	M
Ferrosilite (opx)	Doublet	1.18	2.49	M1
	Doublet	1.13	1.91	M2
Hedenbergite (opx)	Doublet	1.18	2.21	M1
	Doublet	0.34	0.68	M1
Diopside (cpx)	Doublet	1.16	1.87	M1
	Doublet	1.15	2.14	M2
Amphibole: Tremolite-actinolite	Doublet	1.11	2.85	M1
	Doublet	1.12	1.80	M2
	Doublet	1.11	2.40	M3
Serpentine: Lizardite	Doublet	1.14	2.70	M
	Doublet	0.40	0.70	M
	Doublet	0.24	0.39	T
Serpentine: Chrysotile	Doublet	1.13	2.75	M
	Doublet	0.31	0.86	M
	Doublet	0.18	0.33	T

Isomer shift (IS) is the shift up or down of nuclear levels that results from the overlap of nuclear and s-electron charge distributions, [Dyar *et al.*, 2006]. Quadrupole splitting (QS) is the separation between two component peaks or the difference between two transition energies [Dyar *et al.*, 2006]. The magnetic hyperfine field (B_{hf}) accounts for the magnetic field created by the Fe. All peaks had a width ≥0.23 mm/s. Tetrahedral site (T) and octahedral site (M) for molecular structure site occupancies.

Table 4: Minerals identified using XRD and TS spectroscopy. Bold uppercase **X** indicates mineral identified in both XRD and TS; small x, XRD only; small italicized *x*, TS only.

Sample	Serpentine	Magnetite	Spinel Group	cpx	opx	Olivine	Chlorite	Other clays (d-spacing 14-16 Å)	Brucite	Amphibole	Garnet
HLSC_1	**X**	**X**	x						**X**		x
167_238*	x	x	x					x			
309_105_A*‡	x	x	x					x			
309_150*	x	x	x					x	x?		
313_210‡	**X**	**X**	**X**			*x*	**X**	x		**X**	
313_318‡	**X**	**X**	x	**X**	**X**	*x*			**X**?		
313_329‡	**X**	**X**	**X**	*x*	*x*	**X**		x	**X**		
313_356‡	**X**	**X**	**X**		*x*		*x?*	x	**X**?		**X**
CROMO2_1A**	x	x	x					x			
CROMO2_2**	x	x	x					x			
CROMO2_3A**	x	x	x					x			
CROMO2_4A**	x	x	x					x			
PHL_1	**X**	*x*	*x*	*x?*	*x*	**X**					
PHL_2B	**X**	x	**X**	*x*	x	**X**		x	**X**?		
PHL_3‡	**X**	**X**	**X**	*x*	**X**	**X**		x	**X**?	x?	x?
PHL_5	**X**	**X**	**X**	*x?*	*x?*	*x*		x	**X**		

Shading used to group drill holes and localities; (?) indicates minerals may be present; cpx is clinopyroxene; opx is orthopyroxene; the most common form of brucite identified by XRD was portlandite, which substitutes Ca for Mg.
*No thin section for comparison.
**No thin section for direct comparison. Thin section from shallower depths (~2-3m) confirms serpentine, magnetite, and other spinel group minerals.
‡MOSS indicates that the Fe is contained in magnetite <1%, which means that in the portion of sample analyzed by MOSS, there was little to no magnetite and the magnetite indicated by XRD could actually be another spinel group mineral.

Table 5: USGS standards DTS-1, DTS-2, and PCC-1 were used to determine accuracy and precision of the Thermo Scientific Niton XL3t and to normalize the Fe concentrations.

SAMPLE	Published	Total Fe as Fe$_2$O$_3$ Wt%	Fe$_2$O$_3$ ±	Fe ppm	± ppm
	Std value	8.68	0.24	60710	1679
			Run 1	102595	857
			Run 2	91366	758
			Run 3	107423	886
			Run 4	94530	785
			Run 5	94878	786
			Run 6	94693	786
				Precision	Accuracy
Dunite, Twin Sisters, DTS-1*			MEAN	94701	98979
			STDEV	174	7351
			RSD%	0.18	7.43
			OBS/REF		1.63
		normalizing factor (normalized to DTS-1)			0.613
		normalized result			60710
		normalized OBS/REF			1.00
SAMPLE	Published	Total Fe as Fe$_2$O$_3$ Wt%	Fe ±	Fe ppm	± ppm
	Std value	7.76	0.21	54275	1469
			Run 1	61917	560
			Run 2	71788	641
			Run 3	63397	575
			Run 4	72856	658
			Run 5	72427	619
			Run 6	73922	660
				Precision	Accuracy
Dunite, Twin Sisters Mountain DTS-2*			MEAN	73069	67489
			STDEV	770	5629
			RSD%	1.05	8.34
			OBS/REF		1.24
		normalizing factor (normalized to DTS-1)			0.613
		normalized result			41396
		normalized OBS/REF			0.76
SAMPLE	Published	Total Fe as Fe$_2$O$_3$ Wt%	Fe$_2$O$_3$ ±	Fe ppm	± ppm
	Std value	8.35	5	58402	34971
			Run 1	74439	627
			Run 2	126579	1084
			Run 3	73596	618
			Run 4	108576	916
			Run 5	108790	913
			Run 6	108119	916
				Precision	Accuracy
Peridotite, Cedars CA Ultramafic Mass, PCC-1 ‡			MEAN	108495	95798
			STDEV	343	26203
			RSD%	0.32	27.35
			OBS/REF		1.64
		normalizing factor (normalized to DTS-1)			0.613
		normalized result			58759
		normalized OBS/REF			1.01

Precision mean is calculated using runs 4-5 because the sample containers were not moved between runs. Accuracy mean was based on runs 1-4 because the sample containers were shaken between each run. *Values taken from published USGS powdered standard reference values. ‡Flanagan [1976] mean values did not include error values, so an overestimated ±5% error was assigned.

Table 6: XRF Fe concentrations and normalized averages in ppm.

Sample name	Run	Fe (ppm)	Fe Error (ppm)	Avg. Conc. (ppm)	Std Dev	Avg Error (ppm)	Normalized Avg. (ppm)
		Original data					
HLSC_1	1	46779	442	46885	1600	445	28741
	2	45341	439				
	3	48536	454				
167_238	1	47496	422	48793	2599	430	29910
	2	51786	455				
	3	47099	414				
309_105_A	1	52935	456	51721	1626	463	31705
	2	52355	477				
	3	49874	455				
309_105_B	1	48973	463	59039	8827	552	36191
	2	62686	583				
	3	65458	612				
309_150	1	54727	498	56527	4022	513	34651
	2	61135	553				
	3	53719	488				
313_210	1	93367	729	82664	12004	664	50673
	2	69685	574				
	3	84939	687				
313_318	1	51081	486	53564	3735	507	32835
	2	57860	543				
	3	51752	493				
313_329	1	73110	666	68497	3851	838	41989
	2	73426	676				
	3	66604	611				
	4	60849	1398				
313_356	1	75456	687	60906	13442	570	37335
	2	58312	551				
	3	48949	472				

Table 6 *continued*

Sample name	Run	Original data		Avg. Conc. (ppm)	Std Dev	Avg Error (ppm)	Normalized Avg. (ppm)
		Fe (ppm)	Fe Error (ppm)				
CROMO2_1A	1	51628	509	50250	1560	498	30803
	2	48557	478				
	3	50565	507				
CROMO2_2	1	46999	443	50515	3292	473	30966
	2	53526	497				
	3	51020	480				
CROMO2_3A	1	75864	653	61810	12459	535	37889
	2	52121	453				
	3	57444	498				
CROMO2_4A	1	50800	483	49412	1288	463	30290
	2	49182	455				
	3	48255	450				
PHL_1	1	80763	614	78265	2566	585	47976
	2	78395	597				
	3	75637	545				
PHL_2B	1	58751	519	58364	1006	517	35777
	2	57222	509				
	3	59120	523				
PHL_3	1	77208	637	77887	5112	638	47745
	2	73148	597				
	3	83305	680				
PHL_5	1	68477	540	68465	2298	538	41969
	2	66161	523				
	3	70757	550				

Table 7: SEM-EDS elemental concentrations for interior of olivine grains (1) in 313_329. See Figure 25 for larger image.
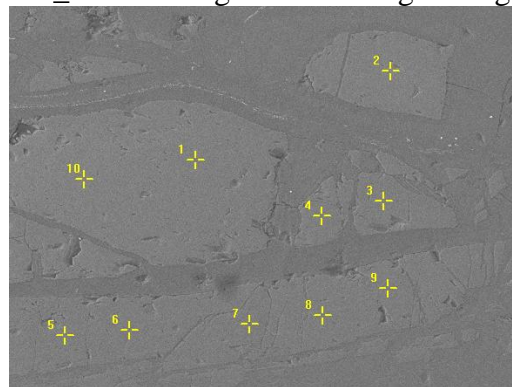
313_329, mag 250X_BSE_ROI2_SEI								
Spot	Element	Wt%	X^2	Z Corr	A Corr	F Corr	Calculated ppm	*Element present?
1	Si	63.06	2.41	1.01	1.426	1	630600	yes
	Mg	36.93	0.67	0.984	1.096	0.982	369300	yes
	Fe	0.01	1.05	1.136	1.016	1	100	yes
	Total	**100**	**1.17**					
2	Si	61.81	2.81	1.01	1.441	1	618100	yes
	Mg	38.18	1.44	0.984	1.094	0.982	381800	yes
	Fe	0.01	1.06	1.137	1.016	1	100	yes
	Total	**100**	**0.98**					
3	Si	63.58	1.26	1.01	1.419	1	635800	yes
	Mg	36.4	0.4	0.984	1.097	0.982	364000	yes
	Fe	0.01	0.34	1.136	1.016	1	100	yes
	Total	**100**	**1.02**					
4	Mg	36.01	1.02	0.983	1.097	0.981	360100	yes
	Fe	0.01	0.05	1.136	1.016	1	100	yes
	Si	63.98	1.89	1.009	1.414	1	639800	yes
	Total	**100**	**0.84**					
5	Si	71.95	1.1	1.007	1.329	1	719500	yes
	Mg	23.12	1.04	0.981	1.112	0.975	231200	yes
	Al	4.92	0.25	0.994	1.443	0.964	49200	yes
	Fe	0.01	0.77	1.133	1.018	1	100	yes
	Total	**100**	**1.09**					
6	Mg	22.64	0.37	0.981	1.112	0.975	226400	yes
	Fe	0.01	0.39	1.133	1.018	1	100	yes
	Si	71.46	3.76	1.007	1.337	1	714600	yes
	Al	5.89	0.46	0.994	1.434	0.964	58900	yes
	Total	**100**	**1**					
7	Mg	23.89	0.58	0.98	1.115	0.974	238900	yes
	Si	76.1	2.97	1.006	1.27	1	761000	yes
	Fe	0.01	2.25	1.133	1.019	1	100	yes
	Al						Not included in sum but present similar intensity peaks to other spots (5-9) in this grain.	
	Total	**100**	**1.87**					

Table 7 *continued.*

Spot	Element	Wt%	X^2	Z Corr	A Corr	F Corr	Calculated ppm	*Element present?
313_329, mag 250X_BSE_ROI2_SEI								
8	Mg	22.54	0.22	0.98	1.114	0.974	225400	yes
	Si	73.48	0.93	1.006	1.309	1	734800	yes
	Fe	0.01	1.48	1.133	1.018	1	100	yes
	Al	3.97	0.32	0.994	1.433	0.962	39700	yes
	Total	**100**	**1.06**					
9	Mg	22.73	0.74	0.981	1.113	0.975	227300	yes
	Si	72.22	3.96	1.007	1.326	1	722200	yes
	Fe	0.01	0.24	1.133	1.018	1	100	yes
	Al	5.05	0.31	0.994	1.436	0.964	50500	yes
	Total	**100**	**1.13**					
10	Mg	37.95	1.08	0.984	1.094	0.982	379500	yes
	Si	62.04	1.34	1.01	1.438	1	620400	yes
	Fe	0.02	0.89	1.137	1.016	1	200	yes
	Total	**100**	**1.13**					

*Element present is based on a second look at the intensity peaks. Elements labeled as no, did not actually have a peak and the values reported are often zero. Those labeled as "not likely" or "maybe" may have a presence, but the peaks could be counted as noise between other peaks. Those labeled as yes have distinguished intensity peaks. See appendix Figure A19 for peak images.

Table 8: SEM-EDS elemental concentrations for the alteration mineral along the exterior of the olivine grains in Table 7 in 313_329. See Figure 26 for larger image.
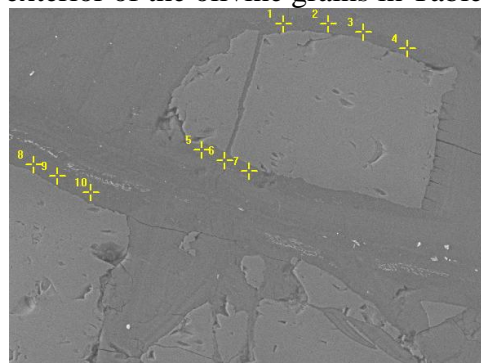
313_329_500Xzoom_BSE_extgrain								
Spot	Element	Wt%	X^2	Z Corr	A Corr	F Corr	Calculated ppm	*Element present?
1	Mg	32.3	0.63	0.983	1.103	0.979	323300	yes
	Fe	0.01	1.97	1.135	1.017	1	100	yes
	Si	67.7	1.15	1.009	1.37	1	676700	yes
	Total	**100**	**0.99**					
2	Mg	33.8	0.01	0.983	1.099	0.98	337700	yes
	Fe	0	0.97	1.136	1.017	1	0	yes
	Si	64.9	3.16	1.009	1.406	1	648800	yes
	Al	1.35	1.3	0.996	1.636	0.971	13500	not likely
	Total	**100**	**1.15**					
3	Mg	33.3	0.22	0.983	1.1	0.98	332700	yes
	Fe	0.01	0.31	1.136	1.017	1	100	yes
	Al	1.79	0.58	0.996	1.627	0.971	17900	not likely
	Si	64.9	3.22	1.009	1.407	1	649300	yes
	Total	**100**	**0.96**					
4	Mg	97.2	0.08	1	1.002	0.999	971700	yes
	Fe	0.01	1.51	1.154	1.005	1	100	yes
	Al	2.81	3.66	1.013	2.973	1	28100	not likely
	Si						Not included in wt%, but present similar to other spots (1-3 & 5-7)	
	Total	**100**	**10.72**					
5	Mg	34	0.36	0.983	1.1	0.98	339600	yes
	Fe	0	1	1.136	1.017	1	0	yes
	Al	0	0.3	0.996	1.641	0.97	0	not likely
	Si	66	4.99	1.009	1.389	1	660300	yes
	Total	**100**	**0.75**					
6	Mg	33	1.16	0.983	1.101	0.98	329500	yes
	Fe	0	2.46	1.135	1.017	1	0	yes
	Al	0.59	2.64	0.996	1.622	0.97	5900	not likely
	Si	66.5	2.89	1.009	1.386	1	664600	yes
	Total	**100**	**0.86**					

Table 8 *continued*.

Spot	Element	Wt%	x^2	Z Corr	A Corr	F Corr	Calculated ppm	*Element present?
313_329_500Xzoom_BSE_extgrain								
7	Mg	34.3	1.33	0.983	1.1	0.98	342600	yes
	Fe	0	0.83	1.136	1.017	1	0	yes
	Al	0.19	0.68	0.996	1.646	0.971	1900	not likely
	Si	65.5	4.73	1.009	1.396	1	655400	yes
	Total	**100**	**1.01**					
8	Si	54.8	3.62	0.999	1.498	1	548400	yes
	Mg	35.6	1.57	0.973	1.286	0.986	356000	yes
	Fe	9.56	0.34	1.124	1.014	1	95600	yes
	Total	**100**	**1.24**					
9	Fe	11.1	0.9	1.122	1.014	1	111000	yes
	Si	54.2	0.29	0.996	1.507	1	541700	yes
	Mg	34.7	0.4	0.97	1.326	0.987	347200	yes
	Total	**100**	**1.01**					
10	Si	66.7	1.25	1.009	1.381	1	667200	yes
	Mg	33.3	0.92	0.983	1.101	0.98	332700	yes
	Fe	0.01	0.91	1.135	1.017	1	100	yes
	Total	**100**	**1.11**					

*Element present is based on a second look at the intensity peaks. Elements labeled as no, did not actually have a peak and the values reported are often zero. Those labeled as "not likely" or "maybe" may have a presence, but the peaks could be counted as noise between other peaks. Those labeled as yes have distinguished intensity peaks. See appendix Figure A20 for peak images.

Table 9: SEM-EDS elemental concentrations for olivine in 313_329. Image is at 250x shows serpentine and magnetite in veins and olivine grains. Pit is from ICPMS laser oblation (data in appendix). See Figure 27 for larger image.
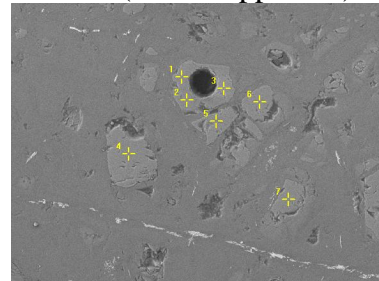
313_239_250X_BSE_poss_olv_1_SEI								
Spot	Element	Wt%	x^2	Z Corr	A Corr	F Corr	Calculated ppm	*Element present?
1	Mg	37.5	0.24	0.984	1.094	0.982	374500	yes
	Ca	0		1.079	1.165	1	0	no
	Cr	0		1.119	1.039	1	0	no
	Mn	0		1.128	1.026	1	0	no
	Fe	0.01	0.43	1.137	1.016	1	100	yes
	Si	61.1	0.2	1.01	1.453	1	610700	yes
	Al	1.48	3.12	0.997	1.705	0.974	14800	yes
	Total	**100**	**0.85**					
2	Mg	37.8	0.43	0.984	1.097	0.983	378200	yes
	Ca	0.42		1.079	1.164	1	4200	no
	Cr	0		1.118	1.039	1	0	no
	Mn	0		1.128	1.026	1	0	no
	Fe	0.01	1.94	1.136	1.016	1	100	yes
	Si	60.6	1.2	1.01	1.455	1	605900	yes
	Al	1.16	0.32	0.997	1.714	0.975	11600	yes
	Total	**100**	**0.81**					
3	Mg	40.3	1.7	0.985	1.091	0.983	403400	yes
	Ca	0		1.08	1.164	1	0	no
	Cr	0		1.119	1.038	1	0	no
	Mn	0		1.128	1.025	1	0	no
	Fe	0.01	0.51	1.137	1.016	1	100	yes
	Si	59.7	3.63	1.011	1.467	1	596600	yes
	Al	0	6.1	0.998	1.76	0.976	0	not likely
	Total	**100**	**0.97**					
4	Mg	39.6	0.48	0.984	1.093	0.983	395800	yes
	Ca	0.26		1.08	1.163	1	2600	no
	Cr	0		1.119	1.038	1	0	no
	Mn	0		1.128	1.026	1	0	no
	Fe	0.01	1.17	1.137	1.016	1	100	yes
	Si	59	0.5	1.01	1.476	1	589500	yes
	Al	1.21	1.56	0.998	1.746	0.976	12100	not likely
	Total	**100**	**0.79**					

Table 9 *continued*

Spot	Element	Wt%	X²	Z Corr	A Corr	F Corr	Calculated ppm	*Element present?
313_239_250X_BSE_poss_olv_1_SEI								
5	Mg	39.1	0.18	0.984	1.092	0.983	391300	yes
	Ca	0		1.08	1.165	1	0	no
	Cr	0		1.119	1.038	1	0	no
	Mn	0		1.128	1.026	1	0	no
	Fe	0.01	1.43	1.137	1.016	1	100	yes
	Si	60.5	0.21	1.01	1.458	1	604900	yes
	Al	0.37	0.8	0.998	1.737	0.975	3700	not likely
	Total	**100**	**0.63**					
6	Mg	37.8	0.84	0.984	1.098	0.983	377900	yes
	Ca	0.55		1.079	1.164	1	5500	no
	Cr	0		1.118	1.039	1	0	no
	Mn	0		1.127	1.026	1	0	no
	Fe	0.01	1.37	1.136	1.016	1	100	yes
	Si	60.8	0.25	1.01	1.451	1	607900	yes
	Al	0.86	0.6	0.997	1.715	0.975	8600	yes
	Total	**100**	**0.95**					
7	Mg	38.7	0.22	0.984	1.093	0.983	387400	yes
	Ca	0.1		1.079	1.164	1	1000	no
	Cr	0.02	1.14	1.119	1.038	1	200	no
	Mn	0		1.128	1.026	1	0	no
	Fe	0.01	0.71	1.137	1.016	1	100	yes
	Si	59.8	3.99	1.01	1.468	1	597700	yes
	Al	1.37	1.76	0.997	1.73	0.975	13700	not likely
	Total	**100**	**1.08**					

*Element present is based on a second look at the intensity peaks. Elements labeled as no, did not actually have a peak and the values reported are often zero. Those labeled as "not likely" or "maybe" may have a presence, but the peaks could be counted as noise between other peaks. Those labeled as yes have distinguished intensity peaks. See appendix Figure A21 for peak images.

Table 10: SEM-EDS elemental concentrations of pyroxene grains in 313_329. See Figure 28 for large image.
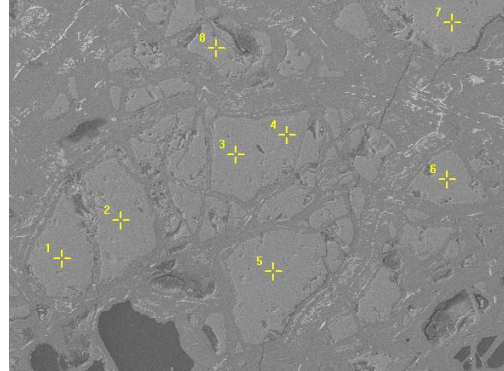
313_239_150X_BSE_poss_olv_6_SEI								
Spot	Element	Wt%	X^2	Z Corr	A Corr	F Corr	Calculated ppm	*Element present?
1	Si	60.2	0.18	1.01	1.462	1	602100	yes
	Al	0.62	1.25	0.998	1.737	0.975	6200	not likely
	Ca	0		1.08	1.164	1	0	no
	Mg	39.2	1.51	0.984	1.092	0.983	391600	yes
	Cr	0		1.119	1.038	1	0	no
	Mn	0		1.128	1.026	1	0	no
	Fe	0.01	0.49	1.137	1.016	1	100	yes
	Total	**100**	**0.6**					
2	Mg	38.6	0.62	0.984	1.094	0.983	385800	yes
	Ca	0.02		1.079	1.165	1	200	no
	Cr	0		1.119	1.038	1	0	no
	Mn	0		1.128	1.026	1	0	no
	Fe	0.01	0.8	1.137	1.016	1	100	yes
	Si	61.4	0.34	1.01	1.446	1	613900	yes
	Al	0	1.3	0.997	1.727	0.974	0	not likely
	Total	**100**	**0.62**					
3	Mg	38.6	0.83	0.984	1.094	0.983	385900	yes
	Ca	0.2		1.079	1.164	1	2000	no
	Cr	0		1.119	1.039	1	0	no
	Mn	0		1.128	1.026	1	0	no
	Fe	0.01	0.41	1.137	1.016	1	100	yes
	Si	60.2	4.29	1.01	1.461	1	602400	yes
	Al	0.96	1.75	0.997	1.728	0.975	9600	not likely
	Total	**100**	**0.66**					
4	Mg	36.2	0.47	0.984	1.097	0.982	362400	yes
	Ca	0.09		1.079	1.167	1	900	no
	Cr	0		1.118	1.039	1	0	no
	Mn	0		1.127	1.026	1	0	no
	Fe	0.01	1.23	1.136	1.016	1	100	yes
	Si	63.1	5.64	1.01	1.426	1	630600	yes
	Al	0.6	0.5	0.997	1.683	0.973	6000	not likely
	Total	**100**	**0.96**					

Table 10 *continued*.

Spot	Element	Wt%	X^2	Z Corr	A Corr	F Corr	Calculated ppm	*Element present?
313_239_150X_BSE_poss_olv_6_SEI							
5	Mg	37.8	0.13	0.984	1.097	0.983	378100	yes
	Ca	0.49		1.079	1.164	1	4900	no
	Cr	0		1.118	1.039	1	0	no
	Mn	0		1.128	1.026	1	0	no
	Fe	0.01	1.46	1.136	1.016	1	100	yes
	Si	60.1	0.11	1.01	1.461	1	601400	yes
	Al	1.55	1.15	0.997	1.714	0.975	15500	maybe
	Total	**100**	**0.69**					
6	Mg	37.9	0.11	0.984	1.094	0.982	378900	yes
	Ca	0		1.079	1.165	1	0	no
	Cr	0		1.119	1.038	1	0	no
	Mn	0		1.128	1.026	1	0	no
	Fe	0.01	0.29	1.137	1.016	1	100	yes
	Si	61.2	0.18	1.01	1.451	1	611600	yes
	Al	0.93	0.4	0.997	1.713	0.974	9300	not likely
	Total	**100**	**0.52**					
7	Mg	37.9	0.45	0.984	1.097	0.983	379200	yes
	Ca	0.57		1.079	1.164	1	5700	no
	Cr	0		1.119	1.039	1	0	no
	Mn	0		1.128	1.026	1	0	no
	Fe	0.01	0.6	1.137	1.016	1	100	yes
	Si	59.3	0.28	1.01	1.471	1	593300	yes
	Al	2.17	4.36	0.997	1.717	0.976	21700	not likely
	Total	**100**	**0.65**					
8	Mg	37.2	0.31	0.984	1.096	0.982	372000	yes
	Ca	0.09		1.079	1.166	1	900	no
	Cr	0		1.118	1.039	1	0	no
	Mn	0		1.128	1.026	1	0	no
	Fe	0.01	2.49	1.136	1.016	1	100	yes
	Si	62.7	0.55	1.01	1.429	1	627100	yes
	Al	0	1.2	0.997	1.701	0.973	0	no
	Total	**100**	**0.69**					

*Element present is based on a second look at the intensity peaks. Elements labeled as no, did not actually have a peak and the values reported are often zero. Those labeled as "not likely" or "maybe" may have a presence, but the peaks could be counted as noise between other peaks. Those labeled as yes have distinguished intensity peaks. See appendix Figure A22 for peak images.

Table 11: SEM-EDS major element concentrations for a spinel grain in 313_329. Image is at 150x shows a spinel grain surrounded by serpentine and olivine grains. Pit is from ICPMS laser oblation (data in appendix). See Figure 29 for larger image.
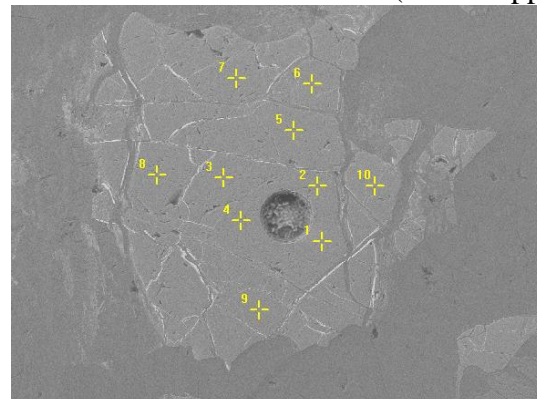
313_239_150X_BSE_spinel4_SEI								
Spot	Element	Wt%	x^2	Z Corr	A Corr	F Corr	Calculated ppm	*Element present?
1	Mg	15.8	0.78	0.988	1.058	0.957	158400	yes
	Fe	0.03	1.09	1.141	1.012	1	300	yes
	Si	5.1	1.55	1.014	2.395	1	51000	yes
	Al	78.9	2.38	1.001	1.275	0.999	789400	yes
	Cr	0.05	2.7	1.123	1.031	1	500	yes
	Mn	0	2.57	1.132	1.02	1	0	not likely
	Ca	0.03		1.084	1.144	1	300	no
	Total	**100**	**0.75**					
2	Mg	17.1	0.16	0.988	1.058	0.96	170900	yes
	Cr	0.06	1.63	1.123	1.031	1	600	yes
	Fe	0.03	1.81	1.141	1.012	1	300	yes
	Si	6	3.95	1.014	2.377	1	60000	yes
	Al	76.8	3.6	1.001	1.298	0.998	768200	yes
	Mn	0	2.86	1.132	1.02	1	0	not likely
	Ca	0		1.084	1.144	1	0	no
	Total	**100**	**1.09**					
3	Mg	16.1	0.52	0.988	1.056	0.957	160800	yes
	Cr	0.07	1.71	1.123	1.031	1	700	no
	Mn	0	1.37	1.133	1.02	1	0	not likely
	Fe	0.03	3.33	1.141	1.012	1	300	yes
	Si	3.52	0.1	1.014	2.423	1	35200	yes
	Al	80.3	1.02	1.002	1.279	0.999	803100	yes
	Ca	0		1.084	1.143	1	0	no
	Total	**100**	**0.62**					
4	Cr	17.4	2.97	1.065	1.02	0.943	174200	yes
	Al	43.1	2.23	0.947	1.776	0.999	431200	yes
	Mg	10.9	0.14	0.934	1.944	0.988	109000	yes
	Si	1.95	1.59	0.959	2.134	0.999	19500	yes
	Fe	26.6	1.29	1.082	1.033	1	266000	yes
	Total	**100**	**1.07**					

Table 11 *continued*

Spot	Element	Wt%	X^2	Z Corr	A Corr	F Corr	Calculated ppm	*Element present?
					313_239_150X_BSE_spinel4_SEI				
5	Mg	14.5	0.99	0.988	1.061	0.957	145400	yes
	Ca	0		1.083	1.146	1	0	no
	Cr	0.05	4.9	1.123	1.032	1	500	yes
	Mn	0	1.54	1.132	1.021	1	0	not likely
	Fe	0.03	0.92	1.141	1.012	1	300	yes
	Si	8.16	2.25	1.014	2.346	1	81600	yes
	Al	77.2	3.24	1.001	1.254	0.998	772200	yes
	Total	**100**	**0.64**					
6	Mg	16.5	0.19	0.988	1.061	0.959	164900	yes
	Ca	0.4		1.083	1.143	1	4000	no
	Cr	0.07	1.84	1.123	1.032	1	700	yes
	Mn	0	3.79	1.132	1.021	1	0	not likely
	Fe	0.03	1.15	1.141	1.012	1	300	yes
	Si	5.3	6.95	1.014	2.385	1	53000	yes
	Al	77.7	4.1	1.001	1.289	0.999	777200	yes
	Total	**100**	**1.05**					
7	Mg	15.8	0.14	0.988	1.059	0.957	158100	yes
	Ca	0		1.084	1.144	1	0	no
	Cr	0.19	129.5	1.123	1.031	1	1900	yes
	Mn	0.01	10.3	1.132	1.02	1	100	not likely
	Fe	0.02	3.92	1.141	1.012	1	200	yes
	Si	4.38	0.7	1.014	2.407	1	43800	yes
	Al	79.6	4.76	1.001	1.276	0.999	795900	yes
	Total	**100**	**2.99**					
8	Mg	17.4	0.03	0.988	1.061	0.96	173700	yes
	Ca	0.44		1.083	1.143	1	4400	no
	Cr	0.06	1.73	1.123	1.032	1	600	yes
	Mn	0	5.73	1.132	1.021	1	0	not likely
	Fe	0.03	0.86	1.141	1.012	1	300	yes
	Si	4.69	0.05	1.014	2.393	1	46900	yes
	Al	77.4	3.03	1.001	1.305	0.999	774100	yes
	Total	**100**	**0.54**					
9	Mg	18.2	0.59	0.988	1.063	0.961	181600	yes
	Ca	0.67		1.083	1.142	1	6700	no
	Cr	0.06	1.78	1.123	1.032	1	600	yes
	Mn	0	2.14	1.132	1.021	1	0	not likely
	Fe	0.03	0.55	1.141	1.012	1	300	yes
	Si	5.42	1.3	1.014	2.375	1	54200	yes
	Al	75.7	3.29	1.001	1.321	0.999	756700	yes
	Total	**100**	**0.52**					

Table 11 *continued*

Spot	Element	Wt%	X^2	Z Corr	A Corr	F Corr	Calculated ppm	*Element present?
313_239_150X_BSE_spinel4_SEI								
10	Cr	17.4	2.17	1.045	1.036	0.939	173700	yes
	Fe	33.3	0.08	1.062	1.043	1	332500	yes
	Al	22.7	1.46	0.928	1.882	0.997	227200	yes
	Si	7.57	0.31	0.941	1.88	0.998	75700	yes
	Mg	7.46	0.09	0.916	2.209	0.993	74600	yes
	Ca	11.6	2.59	1.007	1.088	0.975	116300	yes
	Total	**100**	**1.02**					

*Element present is based on a second look at the intensity peaks. Elements labeled as no, did not actually have a peak and the values reported are often zero. Those labeled as "not likely" or "maybe" may have a presence, but the peaks could be counted as noise between other peaks. Those labeled as yes have distinguished intensity peaks. See appendix Figure A23 for peak images.

Table 12: Mössbauer parameters for Coast Range Ophiolite and Zambales Ophiolite samples.

Sample		HLSC_1‡	167_238‡	309_105_A	309_150	313_210
Sextet 1 Magnetite	IS	0.27	0.27		0.26	
	QS	-0.04	-0.01		-0.01	
	W	0.24	0.230*		0.23	
	A	25	12		12	
	B_{hf}	490.1	490.3		489.6	
Sextet 2 Magnetite	IS	0.67	0.67		0.67	
	QS	-0.01	-0.03		-0.02	
	W	0.28	0.26		0.30	
	A	38	18		22	
	B_{hf}	459.2	459.7		459.7	
Ferric 1 Silicate	IS	0.33	0.25	0.38	0.38	0.37
	QS	0.69	0.47	0.71	0.64	0.71
	W	0.72	0.51	0.41	0.56	0.67
	A	14	40	18	16	36
Ferric 2 Silicate	IS			0.45		
	QS			1.16		
	W			0.81		
	A			11		
Ferrous 1 Silicate	IS	1.16	1.14	1.14	1.15	1.14
	QS	2.67	2.72	2.73	2.71	2.70
	W	0.37	0.31	0.25	0.33	0.24
	A	23	9	70	50	65
Ferrous 2 Silicate	IS		1.45			
	QS		1.20			
	W		0.46			
	A		21			
X^2		849.88	1690.49	484.52	2096.67	1228.27
$\|X^2\|$		1.6593	3.3028	0.9456	4.0934	2.3749
Sum areas		100	100	100	100	100
Magnetite		63	30	0	34	0
%Fe^{3+}		14	40	30	16	36
%Fe^{2+}		23	30	70	50	65
%Fe^{3+} excluding magnetite		39	57	30	24	36

65

Table 12 *continued*

Sample		313_318	313_329	313_356	CROMO2_1A‡	CROMO2_2‡
Sextet 1 Magnetite	**IS**				0.25	0.24
	QS				-0.02	-0.04
	W				0.30	0.30
	A				11	10
	B_{hf}				488.9	489.3
Sextet 2 Magnetite	**IS**				0.69	0.67
	QS				-0.01	-0.02
	W				0.32	0.30
	A				16	12
	B_{hf}				459.6	459.7
Ferric 1 Silicate	**IS**	0.36	0.35	0.37	0.35	0.34
	QS	0.68	0.52	0.64	0.69	0.66
	W	0.56	0.40	0.45	0.60	0.56
	A	49	25	41	35	28
Ferric 2 Silicate	**IS**		0.36	0.47		
	QS		1.24	1.17		
	W		0.65	0.61		
	A		17	13		
Ferrous 1 Silicate	**IS**	1.14	1.14	1.14	1.14	1.14
	QS	2.71	2.71	2.62	2.69	2.67
	W	0.23*	0.23*	0.33	0.30	0.31
	A	51	58	28	38	50
Ferrous 2 Silicate	**IS**			1.13		
	QS			2.78		
	W			0.25		
	A			19		
X²		512.83	483.88	1283.09	1284.9	953.84
|X²|		1.0018	0.9459	2.499	2.5003	1.8534
Sum areas		100	100	100	100	100
Magnetite		0	0	0	26	22
%Fe $^{3+}$		49	42	54	35	28
%Fe $^{2+}$		51	58	46	38	50
%Fe $^{3+}$ excluding magnetite		49	42	54	48	36

Table 12 *continued*

Sample		CROMO2_3A‡	CROMO2_4A‡	PHL_1‡	PHL_2B‡	PHL_3	PHL_5‡
Sextet 1 Magnetite	IS	0.28	0.27	0.30	0.33		0.29
	QS	0.00	-0.01	-0.02	-0.01		-0.02
	W	0.30	0.23	0.35	0.35		0.35
	A	10	12	19	6		21
	B_{hf}	489.9	489.4	498.6	501.5		495.5
Sextet 2 Magnetite	IS	0.67	0.67	0.88	1.07		0.72
	QS	-0.01	0.00	0.16	0.23		-0.03
	W	0.30	0.30	0.30	0.30		0.30
	A	12	21	8	6		9
	B_{hf}	458.5	459.0	476.1	499.5		464.3
Ferric 1 Silicate	IS	0.35	0.36	0.34	0.35	0.35	0.35
	QS	0.65	0.67	0.66	0.68	0.56	0.65
	W	0.55	0.61	0.59	0.63	0.36	0.59
	A	29	32	42	54	45	47
Ferric 2 Silicate	IS					0.42	
	QS					1.25	
	W					0.66	
	A					20	
Ferrous 1 Silicate	IS	1.14	1.13	1.15	1.14	1.14	1.14
	QS	2.66	2.69	2.82	2.69	2.13	2.69
	W	0.31	0.31	0.37	0.37	0.26	0.32
	A	49	35	31	34	10	24
Ferrous 2 Silicate	IS					1.13	
	QS					2.78	
	W					0.23*	
	A					24	
X^2		1334.05	15229.04	1218.41	2457.07	577.59	1395.6
$|X^2|$		2.5859	29.1855	2.3508	0.7119	1.1233	2.6954
Sum areas		100	100	100	100	100	100
Magnetite		22	33	27	12	0	30
%Fe $^{3+}$		29	32	42	54	65	47
%Fe $^{2+}$		49	35	31	34	35	24
%Fe $^{3+}$ excluding magnetite		37	47	57	62	65	66

Isomer shift (IS) is in mm/s; Quadrupole splitting (QS) is in mm/s; Peak width (W) is in mm/s; magnetic hyperfine field (B_{hf}) is in tesla; % Area (A) under the curve; CHI-squared (X^2), and normalized CHI-squared ($|X^2|$). Silicates are serpentine, pyroxene, and/or chlorite. *Indicates restricted (fixed) parameter. ‡MOSS curves fit by M.Nelms in Dyar Lab at Mout Holyoke College and rest were fit by A.Stander.

Table 13: Summary table of Fe concentration (ppm), Fe valence states in percent from MOSS, and possible hydrogen gas yield per $1km^3$ of rock and per the total volume of the peridotite units of the ophiolite.

| Sample | Normalized Fe average conc (ppm) | Mössbauer results | | | H_{gas} (Tmoles) per 1 km^3 | | Volume ophiolite peridotite (km^3)** | H_{gas} (Tmoles) per volume oph. | |
		% Magnetite	% Ferric (Fe^{3+})	% Ferrous (Fe^{2+})	Released ($\ddagger Fe^{3+}$)*	To be released ($\dagger Fe^{2+}$)*		Released ($\ddagger Fe^{3+}$)	To be released ($\dagger Fe^{2+}$)
HLSC_1	28741	63	14	23	0.29	0.11	7730	2235	872
167_238	29910	30	40	30	0.32	0.11	7730	2481	829
309_105_A	31705	0	30	70	0.17	0.20	7730	1308	1540
309_150	34651	34	16	50	0.24	0.19	7730	1850	1473
313_210	50673	0	36	65	0.32	0.29	7730	2490	2262
313_318	32835	0	49	51	0.29	0.15	7730	2223	1161
313_329	41989	0	42	58	0.32	0.22	7730	2450	1681
313_356	37335	0	54	46	0.36	0.16	7730	2767	1200
CROMO2_1A	30803	26	35	38	0.29	0.13	7730	2261	1001
CROMO2_2	30966	22	28	50	0.24	0.16	7730	1825	1231
CROMO2_3A	37889	22	29	49	0.30	0.19	7730	2289	1478
CROMO2_4A	30290	33	32	35	0.29	0.13	7730	2258	967
PHL_1	47976	27	42	31	0.51	0.17	1455	747	251
PHL_2B	35777	12	54	34	0.40	0.12	1455	581	175
PHL_3	47745	0	65	35	0.56	0.15	1455	814	215
PHL_5	41969	30	47	24	0.50	0.13	1455	724	184

Hydrogen values are calculated assuming that all of the peridotite units of the ophiolite have the same composition as the sample. Tmoles (10^{12} = tera T)
$\dagger$ To be released values use the total % Fe^{2+} in sample (calculated using MOSS Fe^{2+} + 1/3 of the % magnetite), and it is assumed that the Fe(II) in the system can still react with water to produce hydrogen. $\ddagger$ Released values use the total % Fe^{3+} in sample (calculated using MOSS Fe^{3+} + 2/3 of the % magnetite), and that all of the Fe(III) has reacted with water to produce hydrogen. * Normalized volume to 1km^3 to eliminate volume as a controlling factor of hydrogen production from the ZO and CRO. ** Estimated volume of the peridotite units in the CRO [Area (~3865km^2)—Carnevale, 2013; depth (~2km)—Coleman, 2000] and the ZO [Area (~485km^2)—Abrajano and Pasteris, 1989; depth (~3km)—Hawkins and Evans, 1983]. Values in FeO wt% are in the appendix, Table A7.

Table 14: Summary table of Fe concentration (ppm), and possible hydrogen gas yield per 1km^3 of rock calculated using an approximate density (2.68g/cm^3), and per the total volume of the peridotite units of the ophiolite.

Sample	Normalized Fe average conc (ppm)	moles H$_{gas}$ per 1 kg rock		Density (g/cm^3) ***	H$_{gas}$ (Tmoles) per 1 km^3		Volume ophiolite peridotite (km^3)**	H$_{gas}$ (Tmoles) per volume oph.	
		Released (‡Fe^{3+})*	To be released (†Fe^{2+})*		Released (‡Fe^{3+})*	To be released (†Fe^{2+})*		Released (‡Fe^{3+})	To be released (†Fe^{2+})
HLSC_1	28741	0.29	0.11	2.68	0.77	0.30	7730	5989	2336
167_238	29910	0.32	0.11	2.68	0.86	0.29	7730	6650	2222
309_105_A	31705	0.17	0.20	2.68	0.45	0.53	7730	3506	4128
309_150	34651	0.24	0.19	2.68	0.64	0.51	7730	4959	3947
313_210	50673	0.32	0.29	2.68	0.86	0.78	7730	6673	6062
313_318	32835	0.29	0.15	2.68	0.77	0.40	7730	5958	3111
313_329	41989	0.32	0.22	2.68	0.85	0.58	7730	6566	4505
313_356	37335	0.36	0.16	2.68	0.96	0.42	7730	7415	3217
CROMO2_1A	30803	0.29	0.13	2.68	0.78	0.35	7730	6059	2684
CROMO2_2	30966	0.24	0.16	2.68	0.63	0.43	7730	4891	3298
CROMO2_3A	37889	0.30	0.19	2.68	0.79	0.51	7730	6136	3960
CROMO2_4A	30290	0.29	0.13	2.68	0.78	0.34	7730	6051	2592
PHL_1	47976	0.51	0.17	2.68	1.38	0.46	1455	2003	674
PHL_2B	35777	0.40	0.12	2.68	1.07	0.32	1455	1558	470
PHL_3	47745	0.56	0.15	2.68	1.50	0.40	1455	2182	576
PHL_5	41969	0.50	0.13	2.68	1.33	0.34	1455	1941	494

Hydrogen values are calculated assuming that all of the peridotite units of the ophiolite have the same composition as the sample. Tmoles (10^{12} = tera T)
† To be released values use the total % Fe^{2+} in sample (calculated using MOSS Fe^{2+} + 1/3 of the % magnetite), and it is assumed that the Fe(II) in the system can still react with water to produce hydrogen. ‡ Released values use the total % Fe^{3+} in sample (calculated using MOSS Fe^{3+} + 2/3 of the % magnetite), and that all of the Fe(III) has reacted with water to produce hydrogen. * Normalized volume to 1km^3 to eliminate volume as a controlling factor of hydrogen production from the ZO and CRO. ** Estimated volume of the peridotite units in the CRO [Area (~3865km^2)—Carnevale, 2013; depth (~2km)—Coleman, 2000] and the ZO [Area (~485km^2)—Abrajano and Pasteris, 1989; depth (~3km)—Hawkins and Evans, 1983] ***Average density (g/cm^3) of variably serpentinized hazburgites and dunites taken from Andreani *et al.* 2013B and Klein *et al.*, 2013.

Figure 1. Map of field locations in the Philippines and CA, USA (made from images from Google map data [2014] and their image data providers—TerraMetrics and NASA [2014]). Approximate locations for ophiolites (yellow) and field sites (red dots) in the Zambales Ophiolite (ZO) in the Poon Bato region of the Philippines [Yumul, 2007] and the Coast Range Ophiolite (CRO) near Lower Lake, CA, USA [Shervais *et al.*, 2005]. See appendix Figures A1 and A2 for geologic maps.
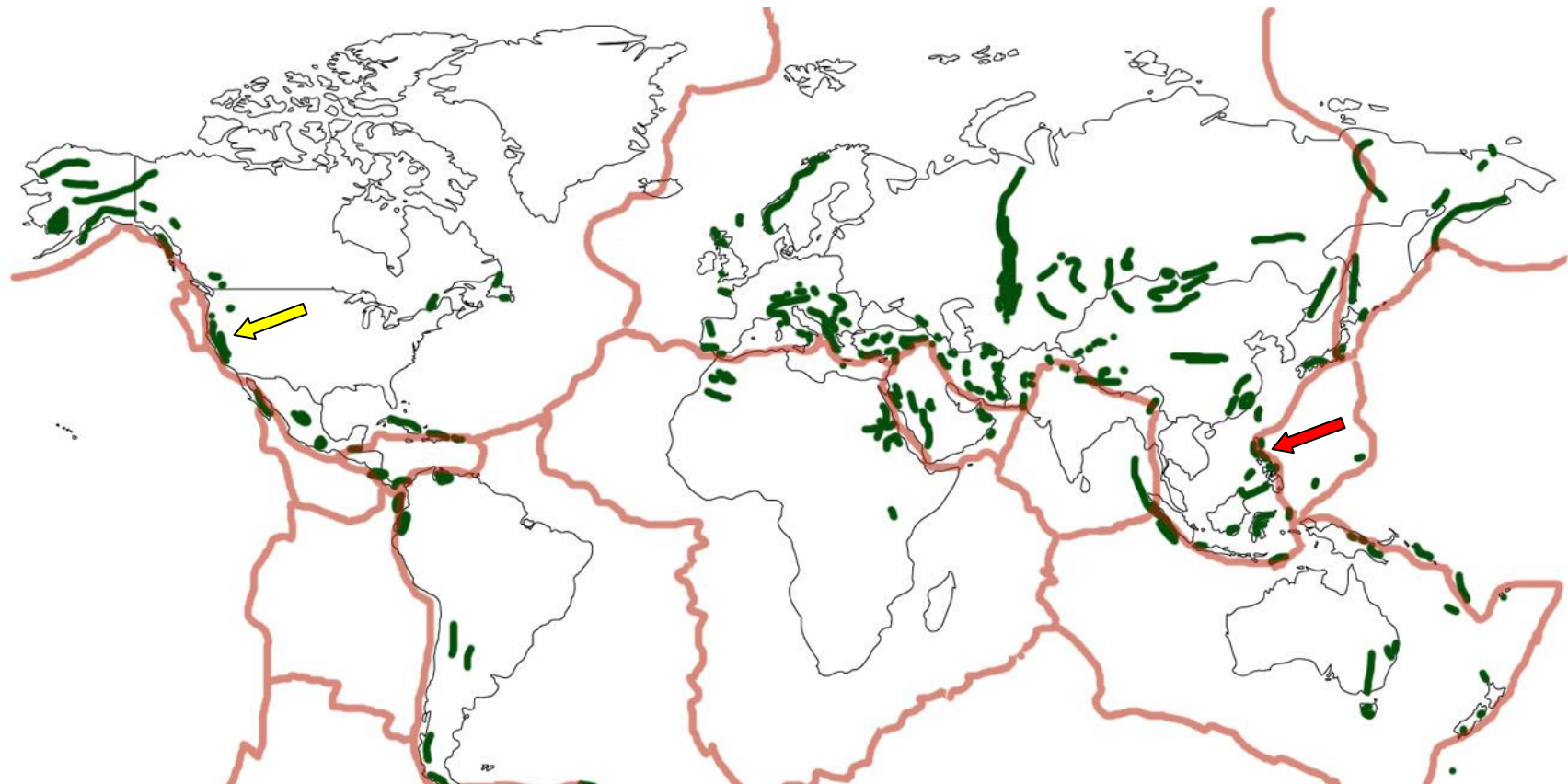
Figure 2. Global ophiolite distribution map adapted from Vaughan and Scarrow [2003]. Green marks are approximate locations of ophiolites Eocene to Cambrian in age (~34-540Ma). Pink lines are approximate locations of modern tectonic plate boundaries [USGS, 2011, tectonic plate boundary graphic]. Arrows indicate locations of the Coast Range Ophiolite (yellow) and Zambales Ophiolite (red). Both ophiolites are located on/very close to modern plate boundries.

	Ocean floor	Ophiolite sequence
Ocean Crust	Sediments	Sedimentary rocks
	Pillow basalt	Mafic volcanic complex
	Dikes	Mafic sheeted dike complex
	Massive Gabbro Sheeted Gabbro	Gabbroic complex
Upper Mantle	Peridotite	Ultramafic complex

Figure 3. Simplified ophiolite sequence adapted from Coleman [1981] and Dilek [2003].

Figure 4. Pictures of samples before being powdered. (a) HLSC_1; (b) 167_238; (c) 309_105_A; (d) 309_150; (e) 313_210; (f) 313_318; (g) 313_329; (h) 313_356; (i) CROMO2_1A; (j) CROMO2_2; (k) CROMO2_3A; (l) CROMO2_4A; (m) PHL_1; (n) PHL_2B; (o) PHL_3; (p) PHL_5. Except for a,d, f, and g, the sample pictured is a smaller piece(s) of sample that was powdered and not the whole sample.
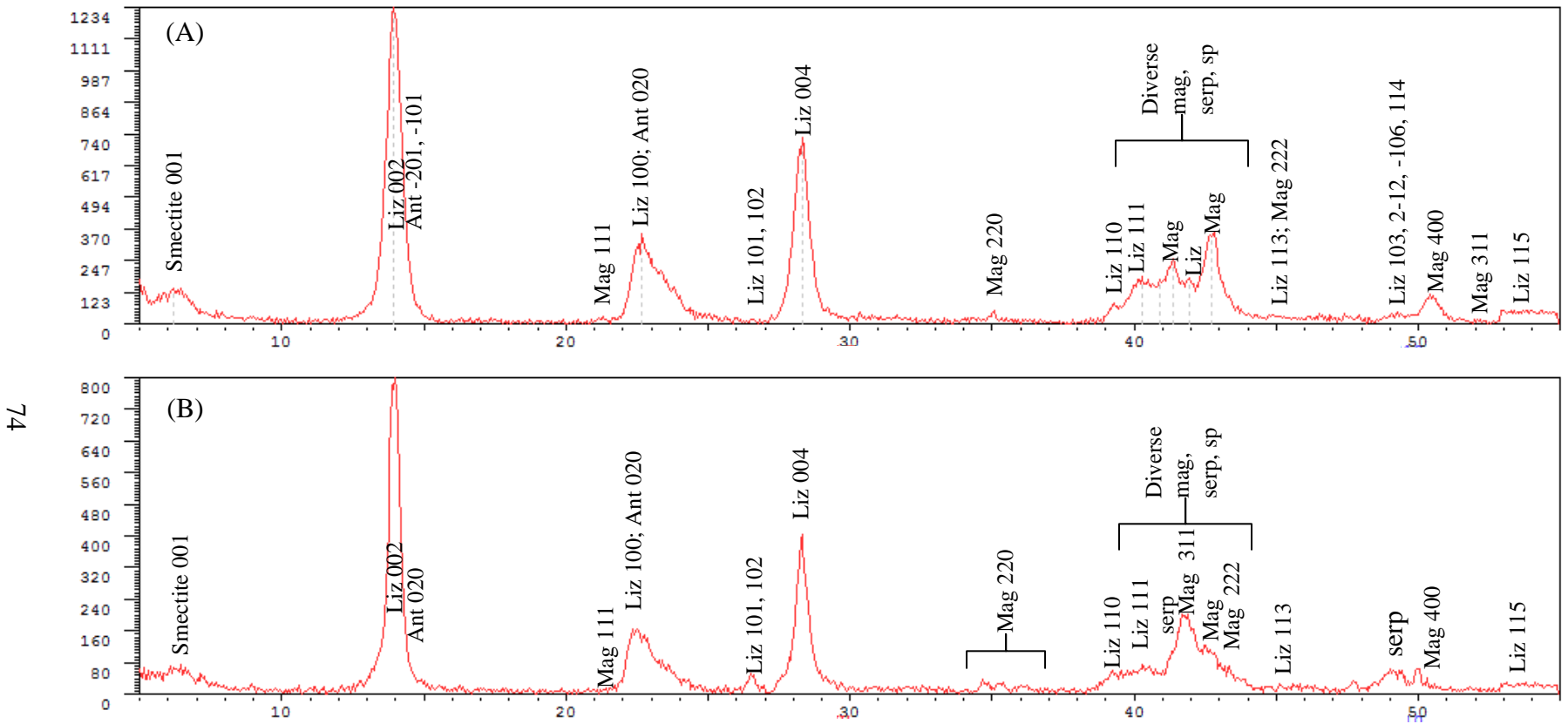
Figure 5. Representative XRD diffractograms with 2θ on the x-axis and intensity on the y-axis and with their peaks labeled according to the mineral constituents and corresponding Miller indices with labeled peaks. **(A)** CRO core sample from CROMO 2_4A and **(B)** ZO hand sample PHL_2 indicate serpentine, magnetite, and other clay mineral. Smectite clays (Smectite), magnetite (mag), serpentine (serp) including lizardite (liz), and antigorite (ant). Numbers (001) indicate the Miller indices associated with that peak.
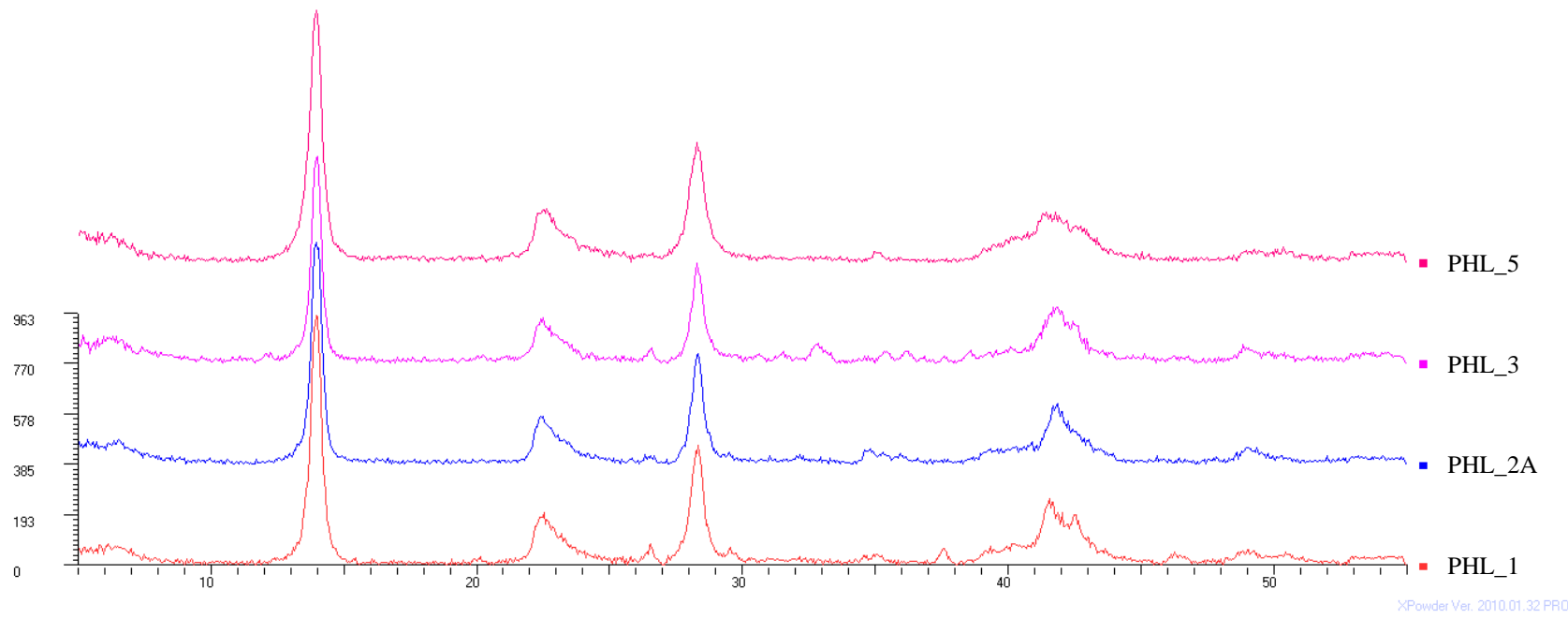
Figure 6. XRD diffractograms with 2θ on the x-axis and intensity on the y-axis for ZO samples showing similarities and small variations in mineral assemblages among samples for a given locality.
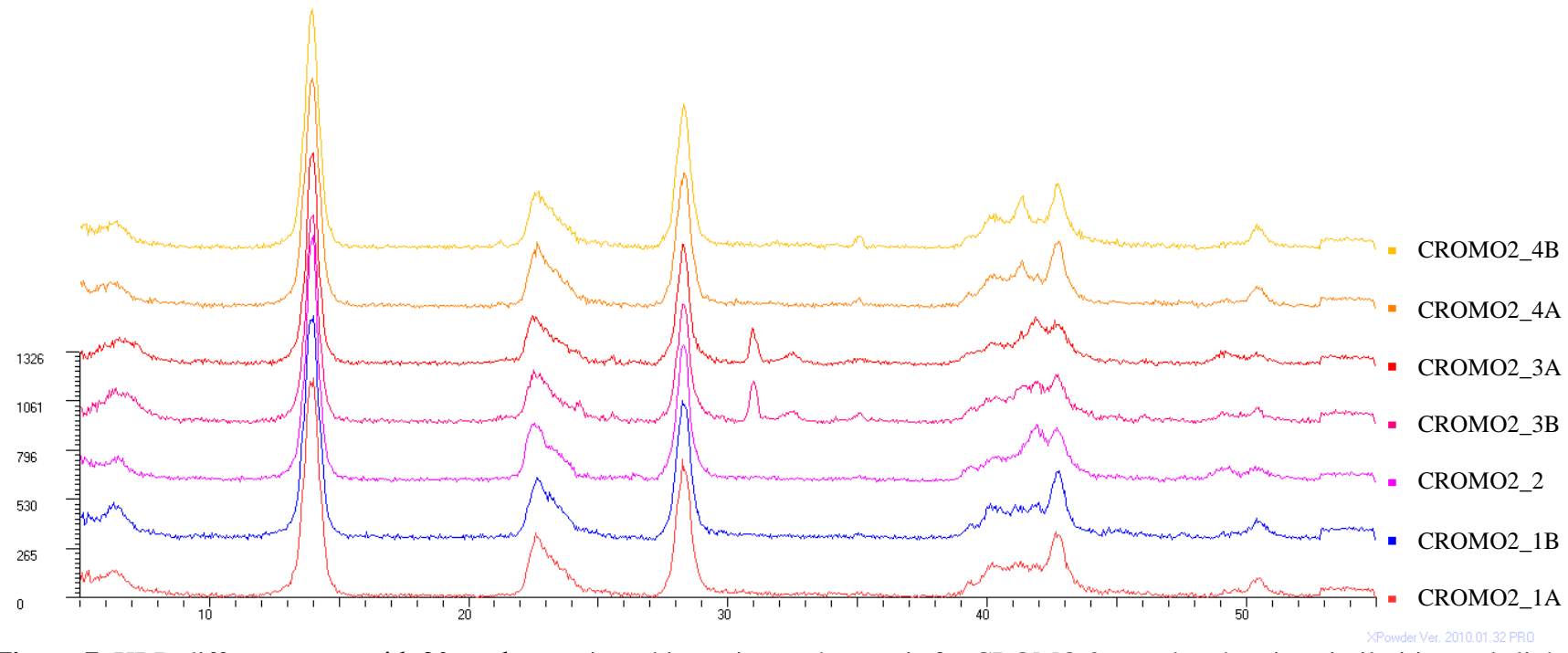
Figure 7. XRD diffractograms with 2θ on the x-axis and intensity on the y-axis for CROMO 2 samples showing similarities and slight differences between samples.
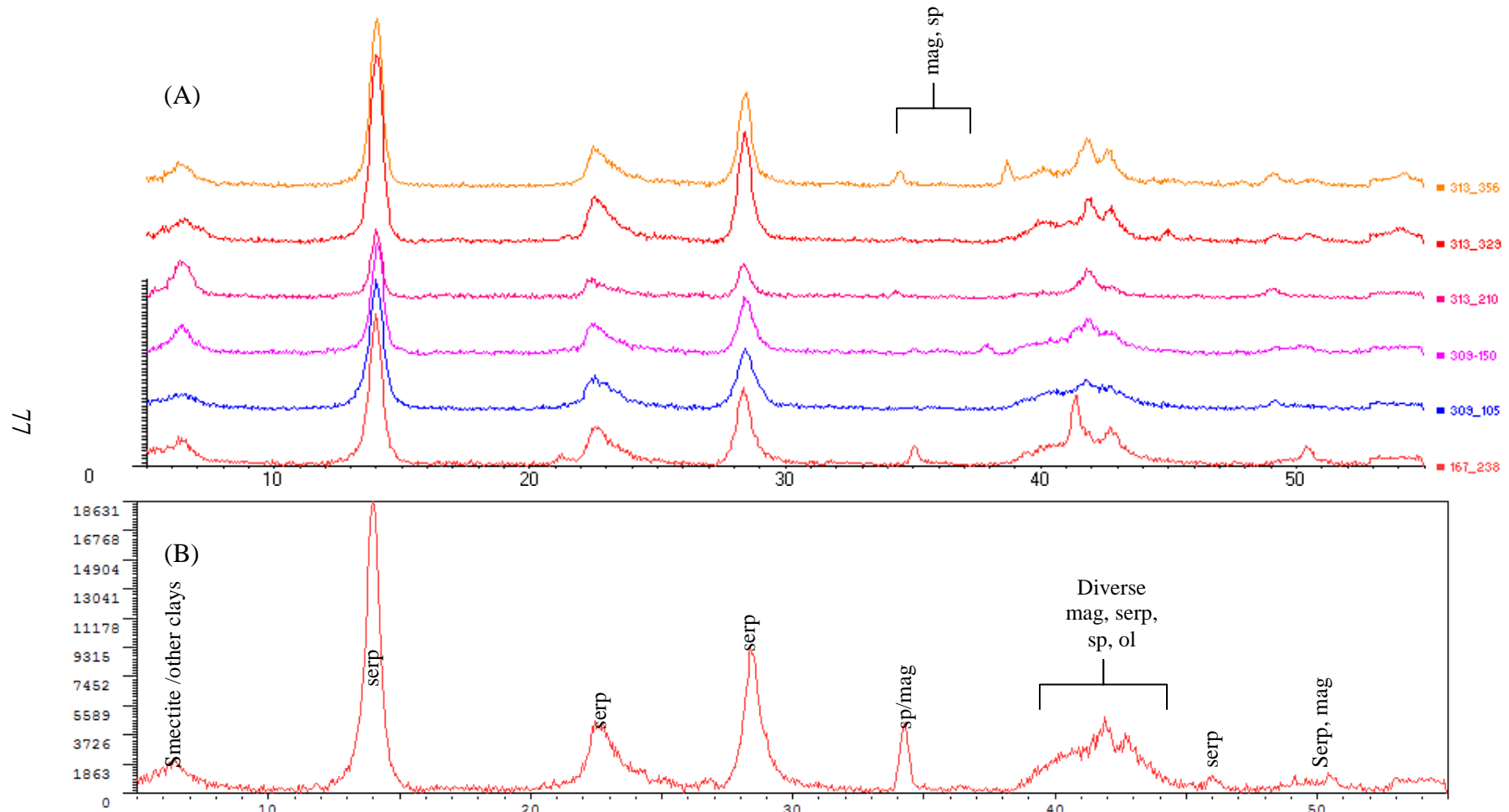
Figure 8. XRD diffractograms with 2θ on the x-axis and intensity on the y-axis for Homestake Mine prospecting cores 309, 313, and 167. (A) Diffractograms for 313_356, 313_329, 313_210, 309_150, 309_105, and 167_238 are stacked. (B) Diffractogram for 313_318 has a greater intensity than the other diffractograms. Serpentine (serp), magnetite (mag), spinel (sp), and possibly olivine (ol).
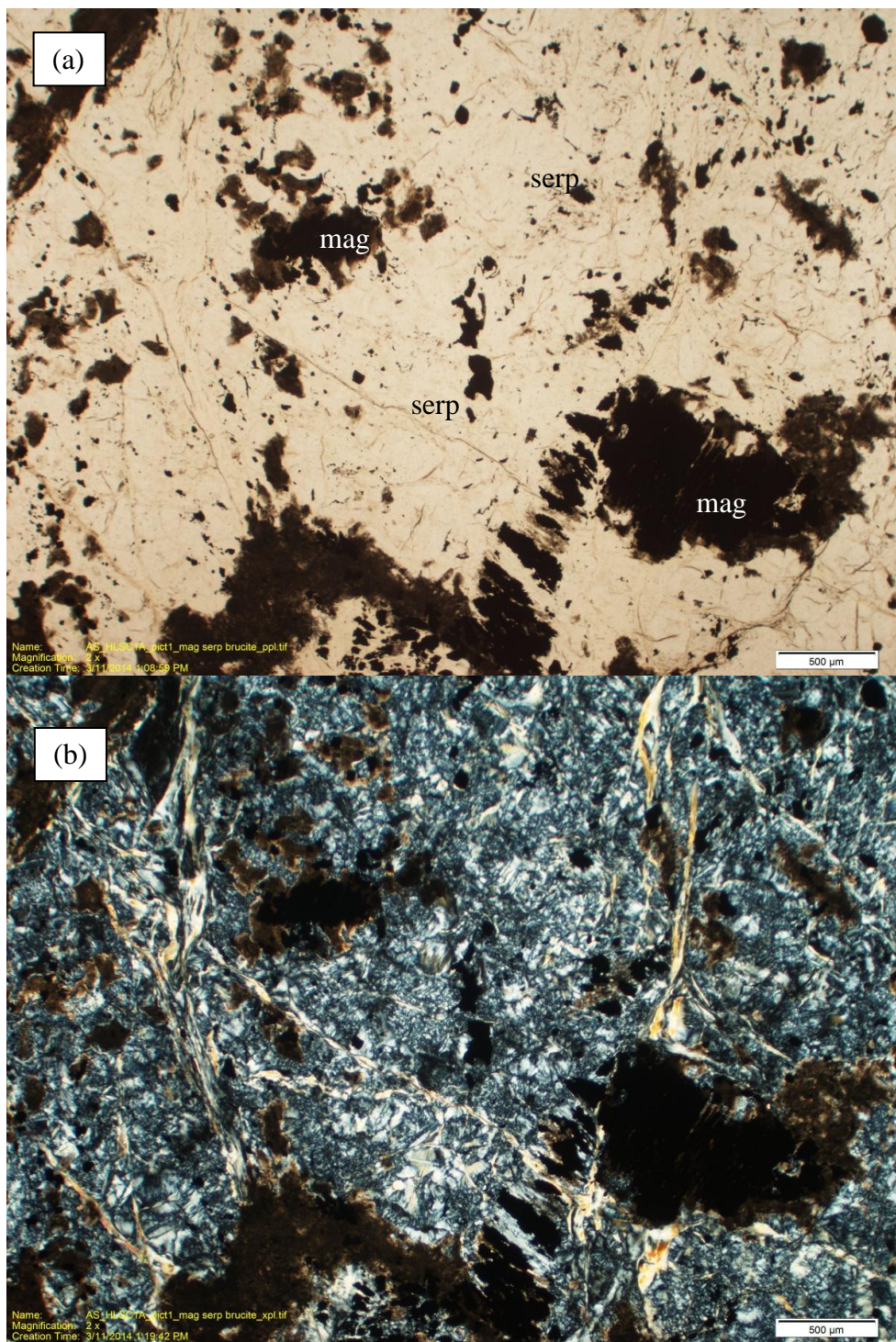
Figure 9. Thin section images of Hyphus-Little Stony Creek confluence float (HLSC_1) in (a) plane polarized light (ppl) and (b) cross polarized light (xpl). Serpentine (serp) (possibly antigorite?), magnetite (mag) and/or other spinel, and possibly brucite (yellow-orange in xpl) veins are visible. The brown "fuzz" around magnetite may be another Fe-oxide such as hematite or clay mineral like smectite. Scale bar represents 500 µm.
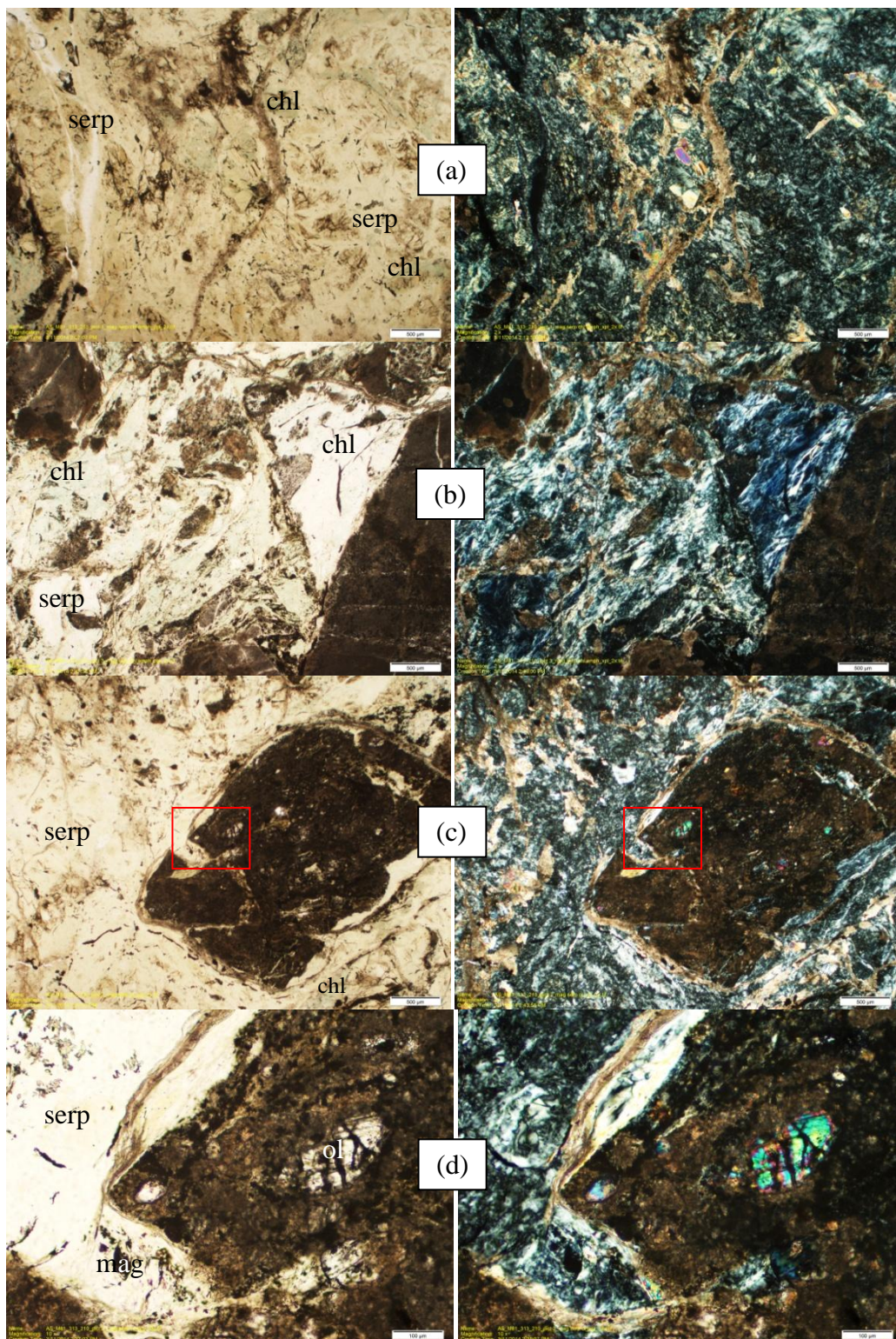
Figure 10. Thin section images 313_210 include serpentine (serp) (a-d), magnetite (mag), chlorite(?) (chl)(a,b), olivine (ol)(c,d) and a brown Fe-oxide (a-d). Sections are in plane-polarized light (left) and cross-polarized light (right). a-c are at 2x (scale bar represents 500μm) and d is a 10x (scale bar 100μm) section of c in the red box. The Fe-oxide phase may be a reaction rind that protected the interior of the large olivine

grain (c) as fluids flowed around it; or it could be further oxidation of the magnetite into hematite. The presence of chlorite in small volumes is not unexpected. Wetzel and Shock [2000] conducted theoretical experiments at 500 bars and 350 and 400°C, which predict that serpentinization should yield 10 to 25 vol% of chlorite, considering peridotites of diverse starting compositions.
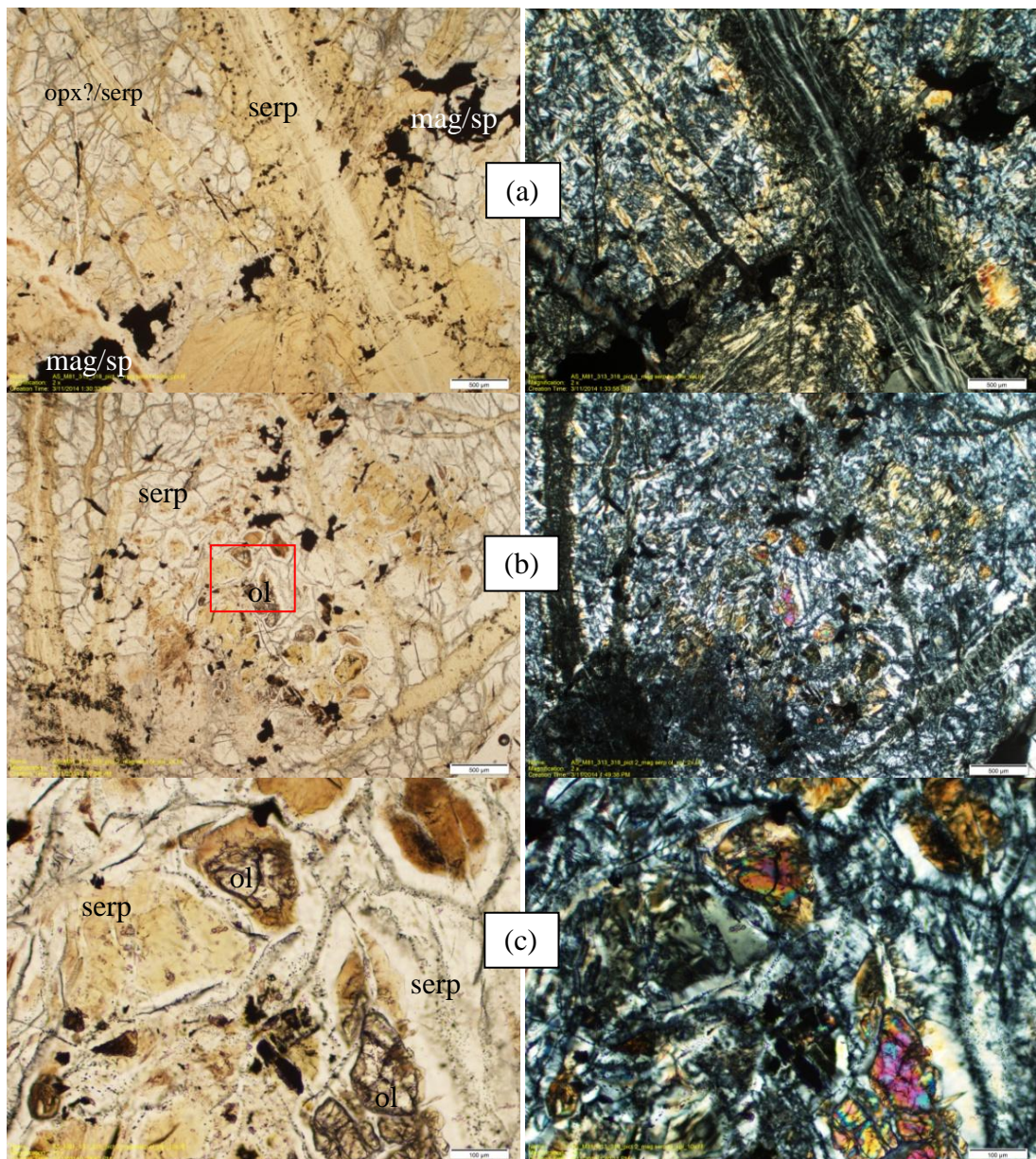
Figure 11. Thin section images of 313_318 include serpentine (serp) (a-c), magnetite (mag), magnetite and/or spinel group (mag/sp) (a-c), and olivine (ol)(b,c). The yellowing of serpentine in ppl may be due to and yellow grains in xpl (a-b) may be brucite. Sections are in plane-polarized light (ppl) (left) and cross-polarized light (xpl)(right). A-b are at 2x (scale bar is 500µm) and c is a 10x (scale bar is 100µm) section of b (red box). The yellow serpenitine veins and mag/sp grain in (a) appear fractured indicating that there were multiple stages of cracking and serpentinization—as would be expected throughout subseafloor serpentinization, during uplift, and post-emplacement alteration. Original mineral grain boundaries are visible as crack-like features in serpentine surrounding the relict olivine in (c).
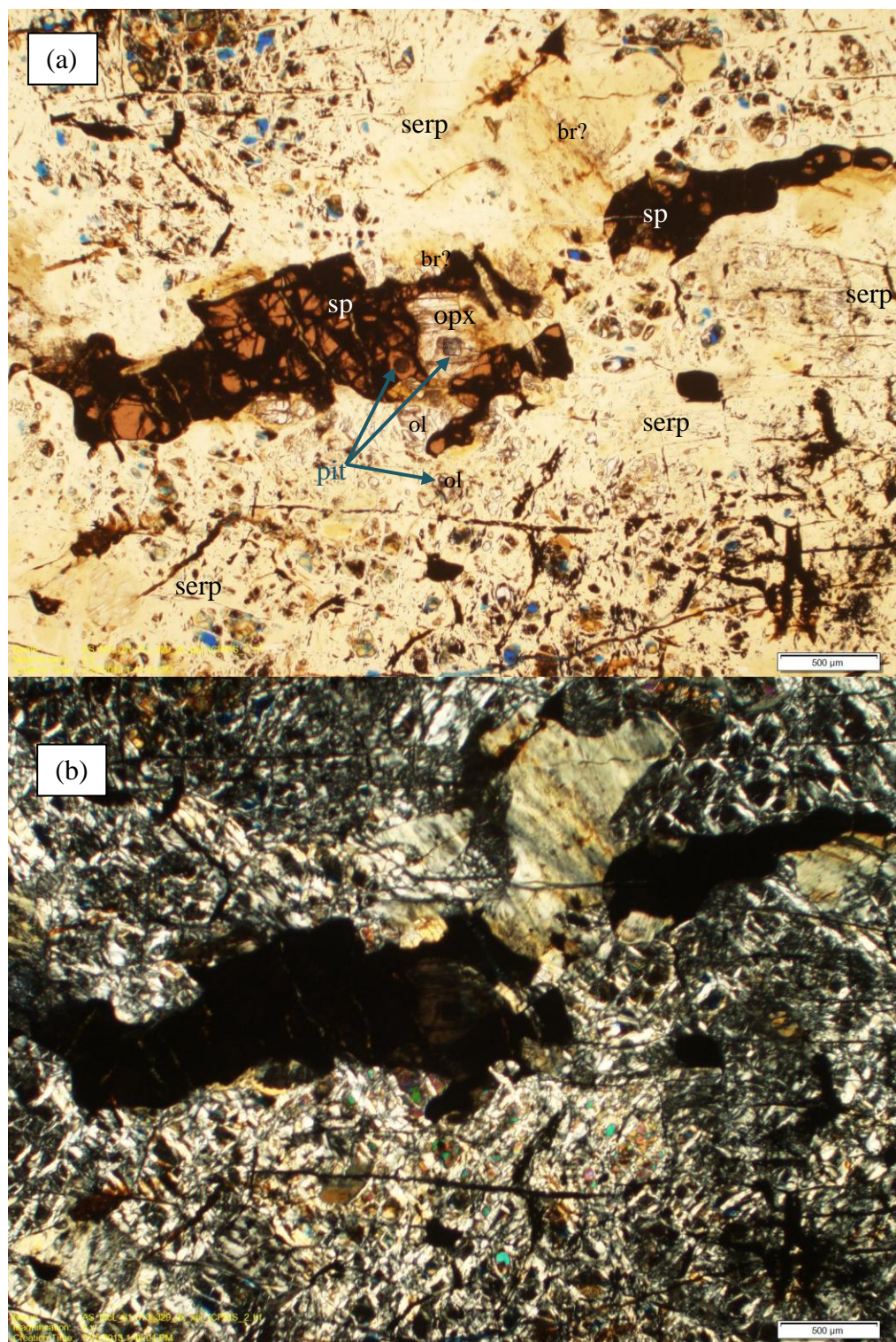
Figure 12. Thin section images of 313_329 in (a) ppl and (b) xpl. Serpentine (serp) mesh texture (possibly lizardite), spinel (sp), orthopyroxene (opx), and olivine (ol) are visible. The yellowing of serpentine in ppl may be due to brucite and yellow grains in xpl may be brucite. Blue spots in ppl are dyed epoxy. 3 pits are visible from ICP-MS laser ablation. Scale bar represents 500μm. Cpx was visible elsewhere on the slide.

(a)

20kV   X250 100μm   URI-SST

(b)

20kV   X150 100μm   URI-SST
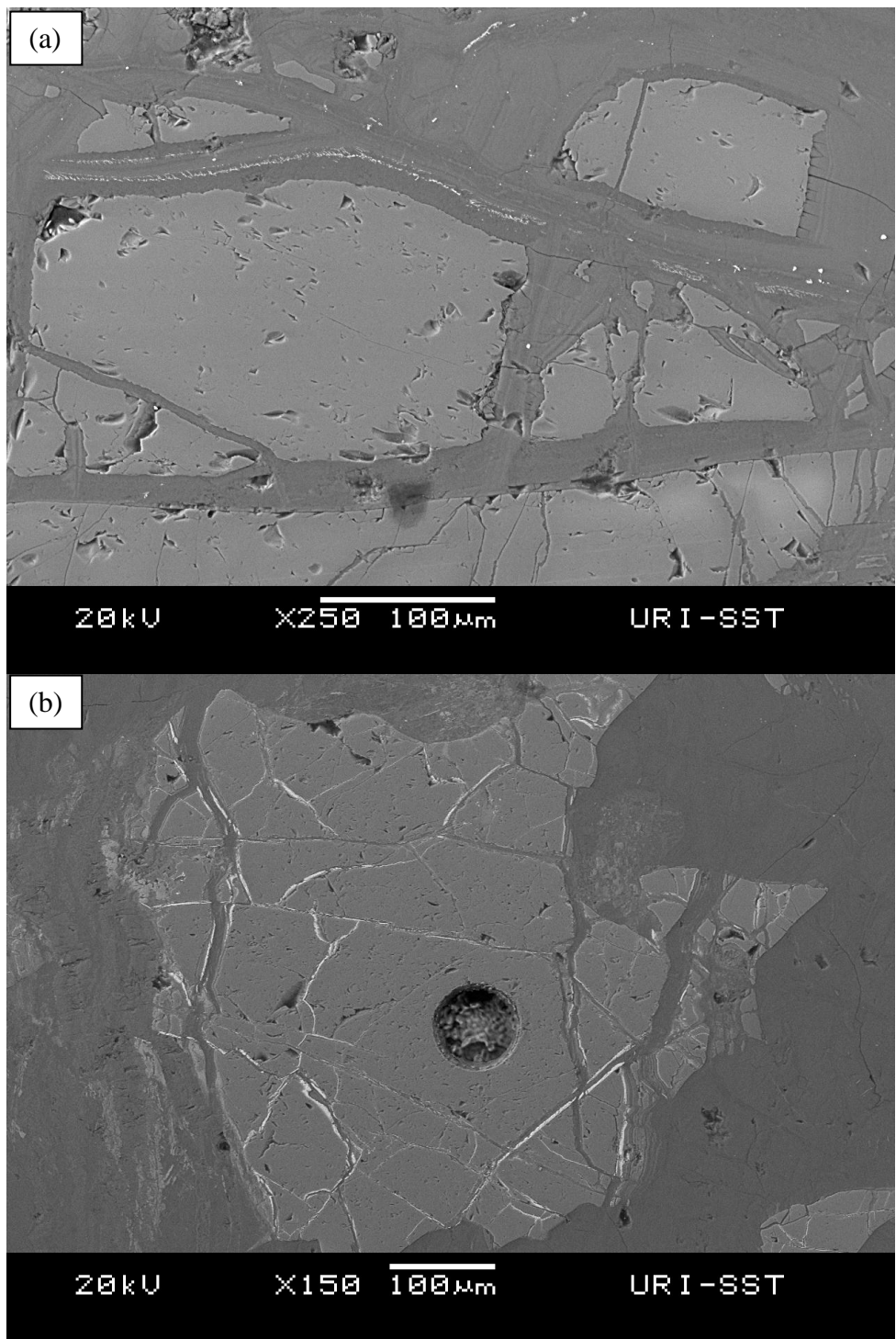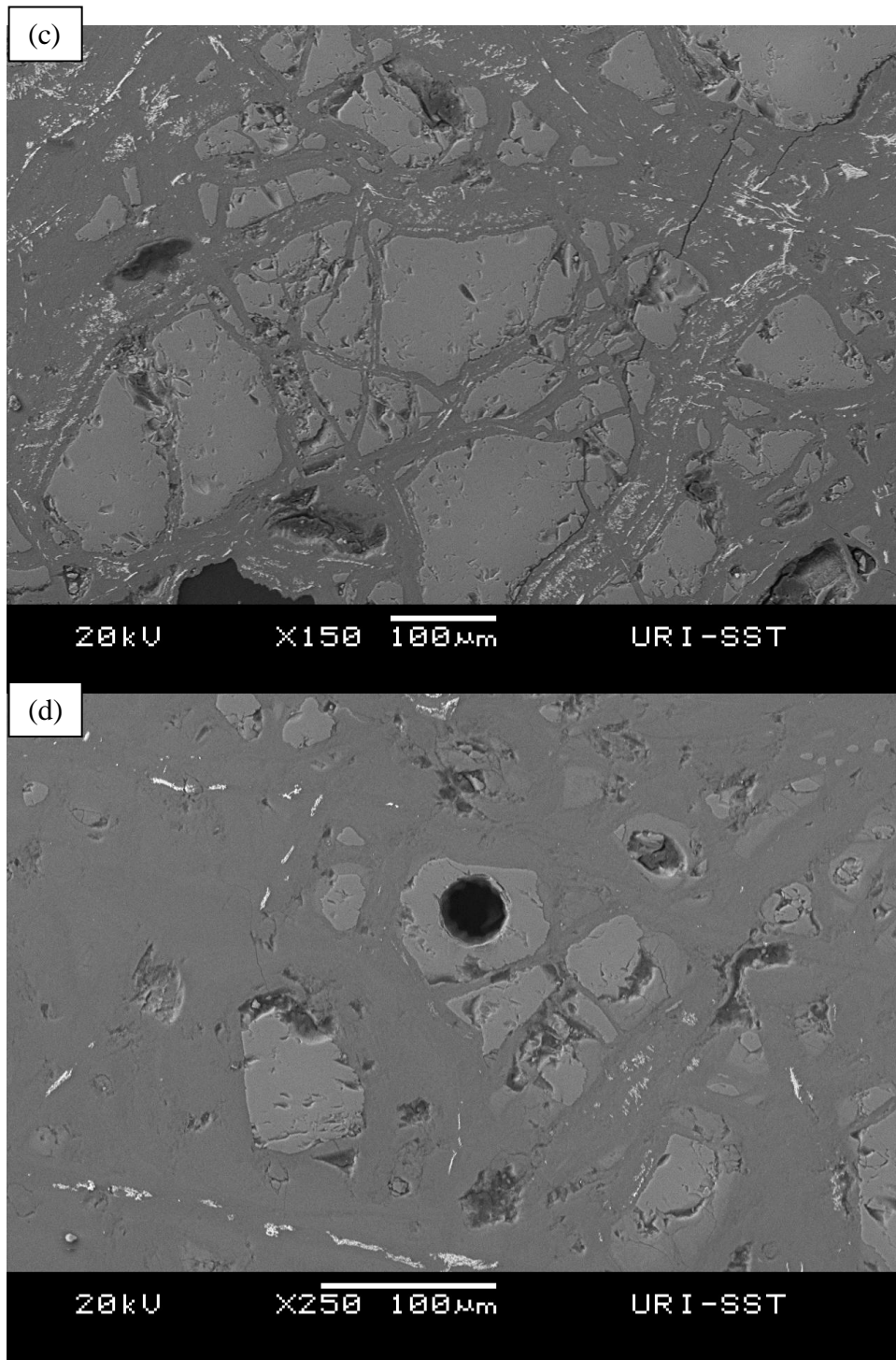
Figure 13. SEM thin section images of 313_329. Serpentine (gray background in a-d) spinel (b), pyroxene (px), and olivine (c-d) are visible. (a) large grains maybe pyroxenes. The light-colored microcrystals ~10μm wide seen in veins are probably magnetite (a, c, d). The light colored areas are more reflective to electrons and more metal-rich. SEM-EDS backscatter images are able to show slight variations in composition (like zoning in veins) that cannot be seen with a light microscope. Pits (b & d) are from ICP-MS laser ablation (Table A12, Figures A40-42). SEM-EDS chemical data for a-d are reported in Tables 7-10.
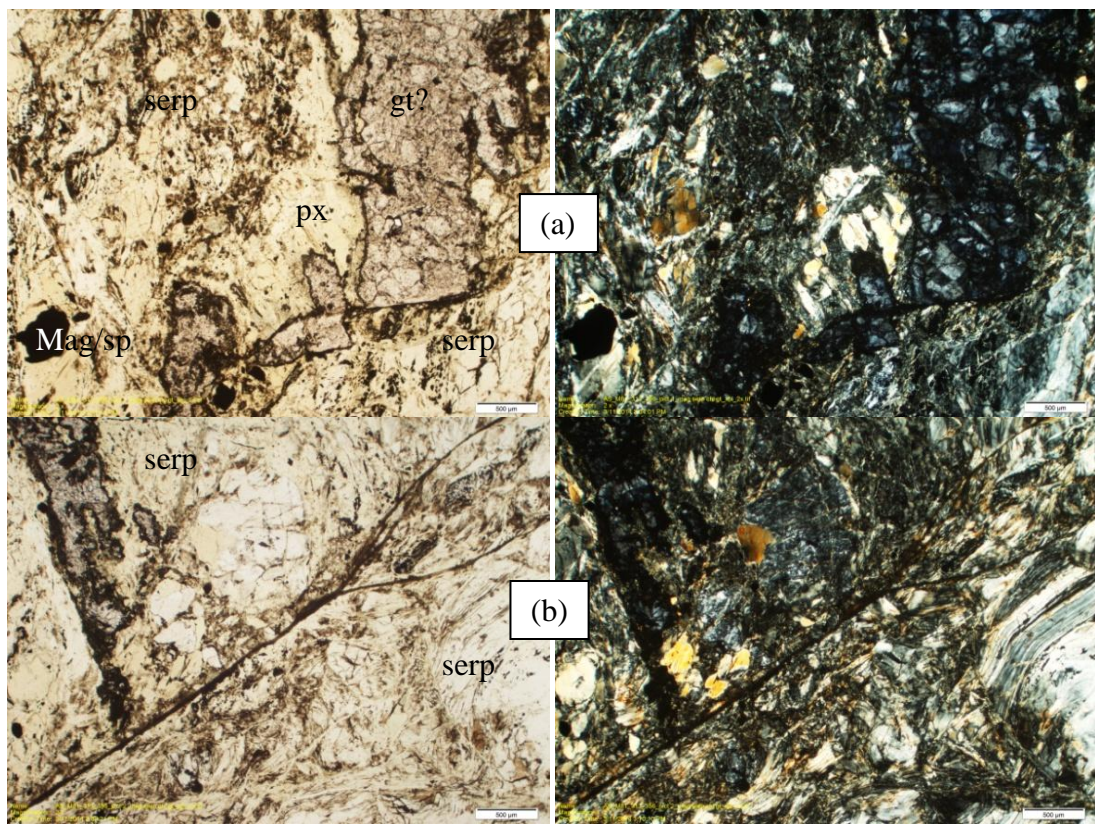
Figure 14. Thin section images of 313_356 in plane polarized light and cross polarized light. Serpentine (serp), magnetite (mag) and/or spinel (sp), pyroxene (px), garnet(?)(gt) and other Fe-oxide veins and around grains are visible. The yellowing of serpentine in ppl may be due to brucite and yellow grains in xpl may be brucite. Scale bar represents 500μm. The garnet (andradite) indicates that this sample may have undergone metamorphism prior to serpentinization because garnet is generally thought of as a higher pressure and temperature mineral. The garnet grains are not well formed crystals, which mean that they could be remnants from the original peridotite body. This sample seems to have a more complicated history than some of the other samples as indicated by the garnet and lack of serpentine veins or classic serpenitinite mesh textures seen in other samples.
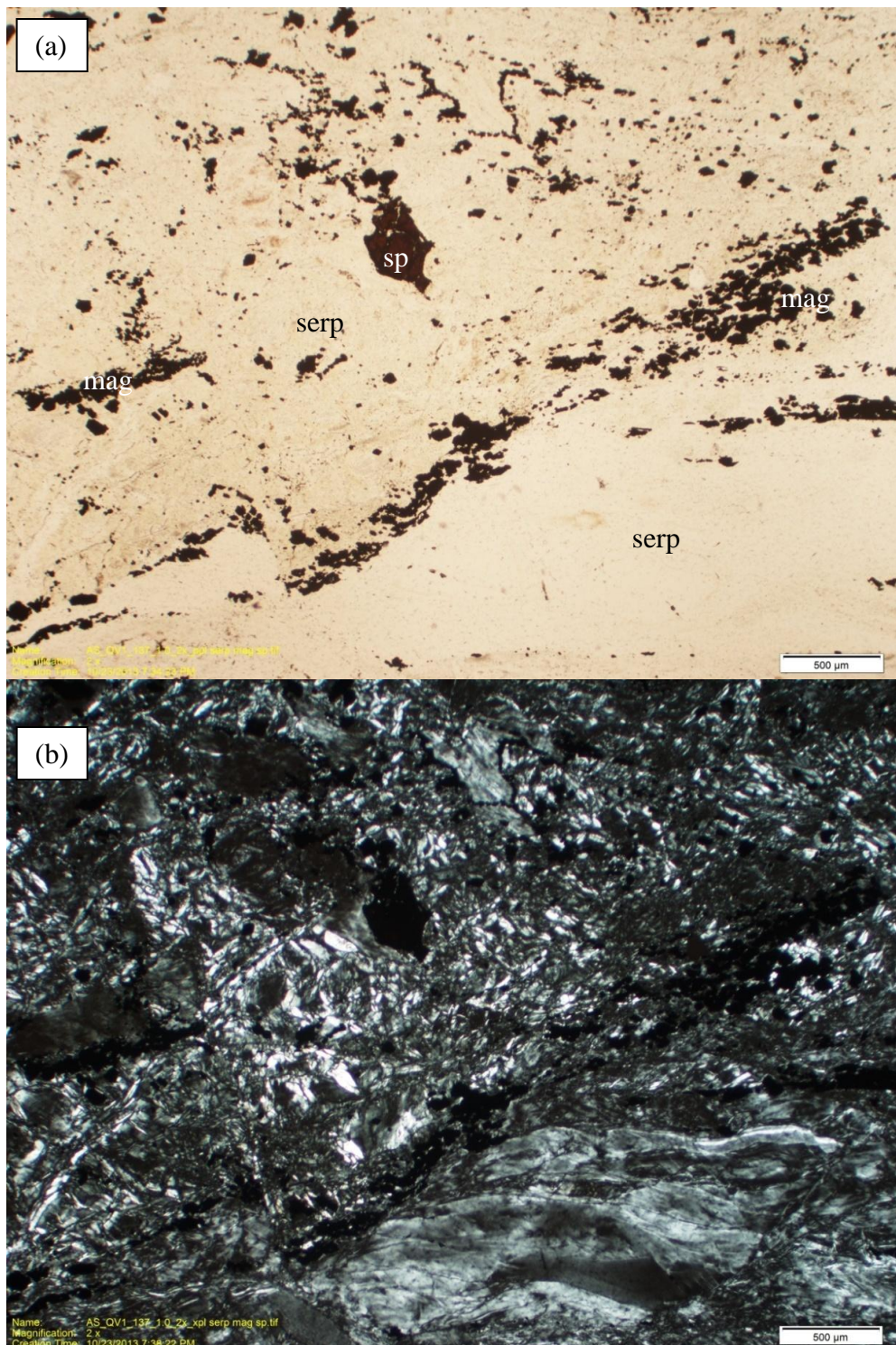
Figure 15. Thin section images of CROMO 2 at shallower depths (~2-3m) than the presented samples confirm the presence of serpentine (possibly antigorite and lizardite), magnetite, and other spinel group minerals. Magnetite seems concentrated on the outside edges of veins and also scattered throughout the other parts of the thin section. (a) plane polarized light and (b) cross polarized light. Serpentine (serp), magnetite (mag), and spinel (sp) are visible. Scale bar represents 500μm
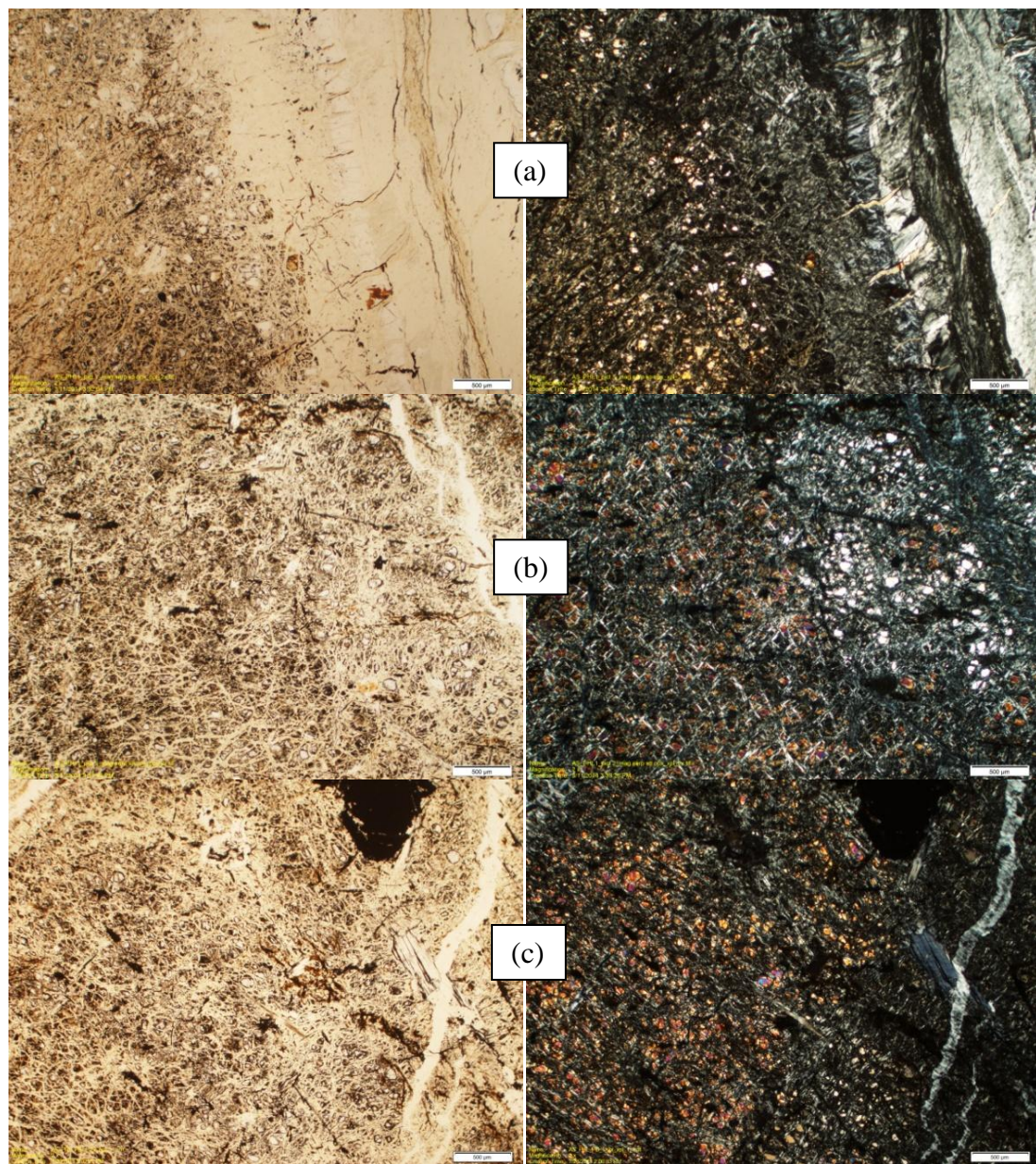
Figure 16. Thin section images of PHL_1 in plane polarized light and cross polarized light. Serpentine (possibly lizardite in the mesh texture and smaller, cross-cutting veins possibly chrysotile) (a-c), olivine (bright and colorful under xpl)(a-c), and spinel (sp)(a-c) are visible. Scale bar represents 500μm.
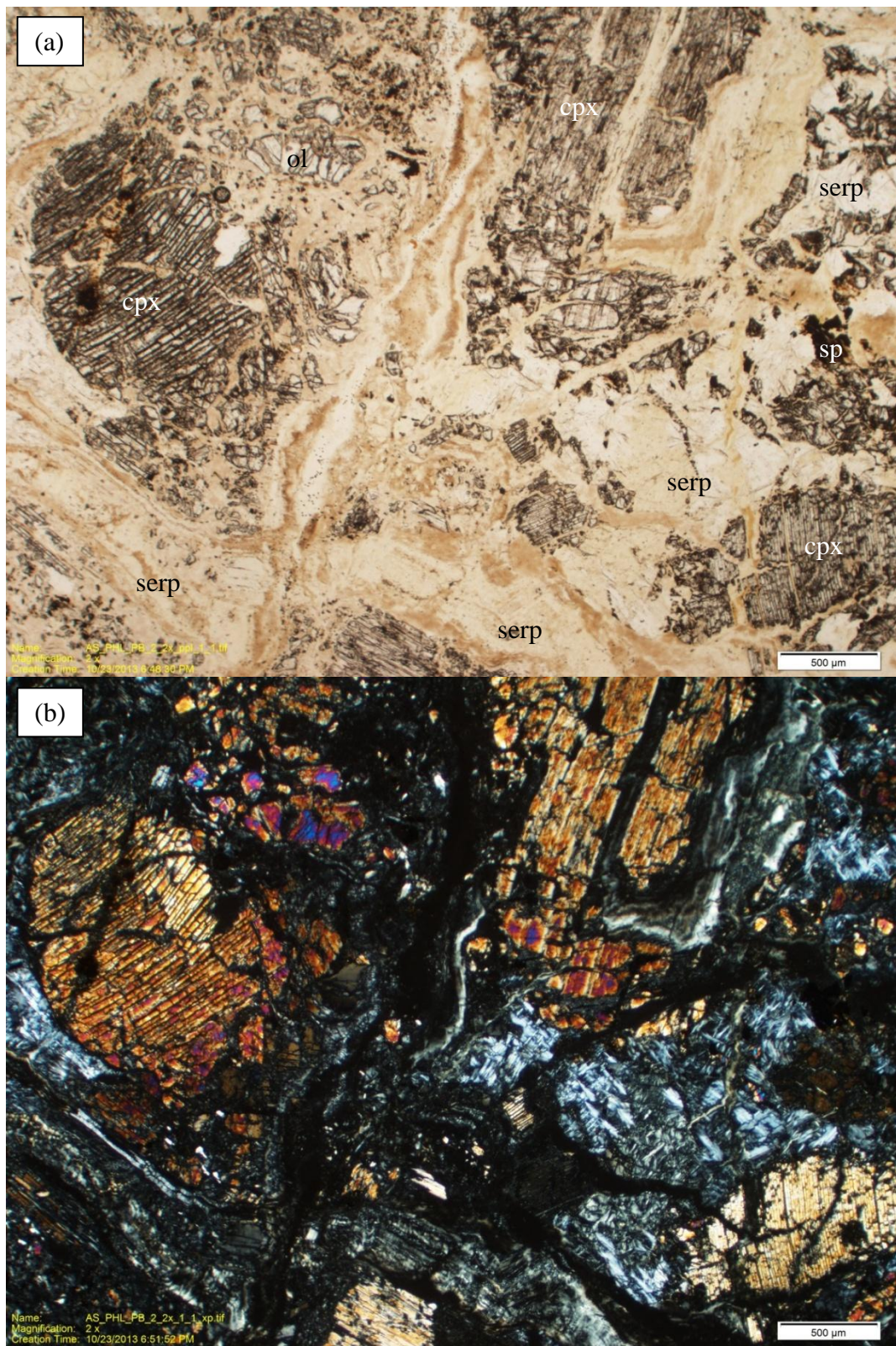
Figure 17. Thin section images of PHL_2 in (a) plane polarized light and (b) cross polarized light. Serpentine (serp), olivine (ol), clinopyroxene (cpx), and spinel (sp) are visible. Scale bar represents 500μm. Cpx grains are larger in size than the olivine

grains and highly fractured. Some of the serpentine veins cut through the cpx grains and show zoning in plane-polarized light between light-colored and rust-colored (Fe-oxide) serpentine. Spinel is often located in veins or on the edges of cpx grains and is likely to be alteration minerals that form as the olivine and cpx serpentinize.
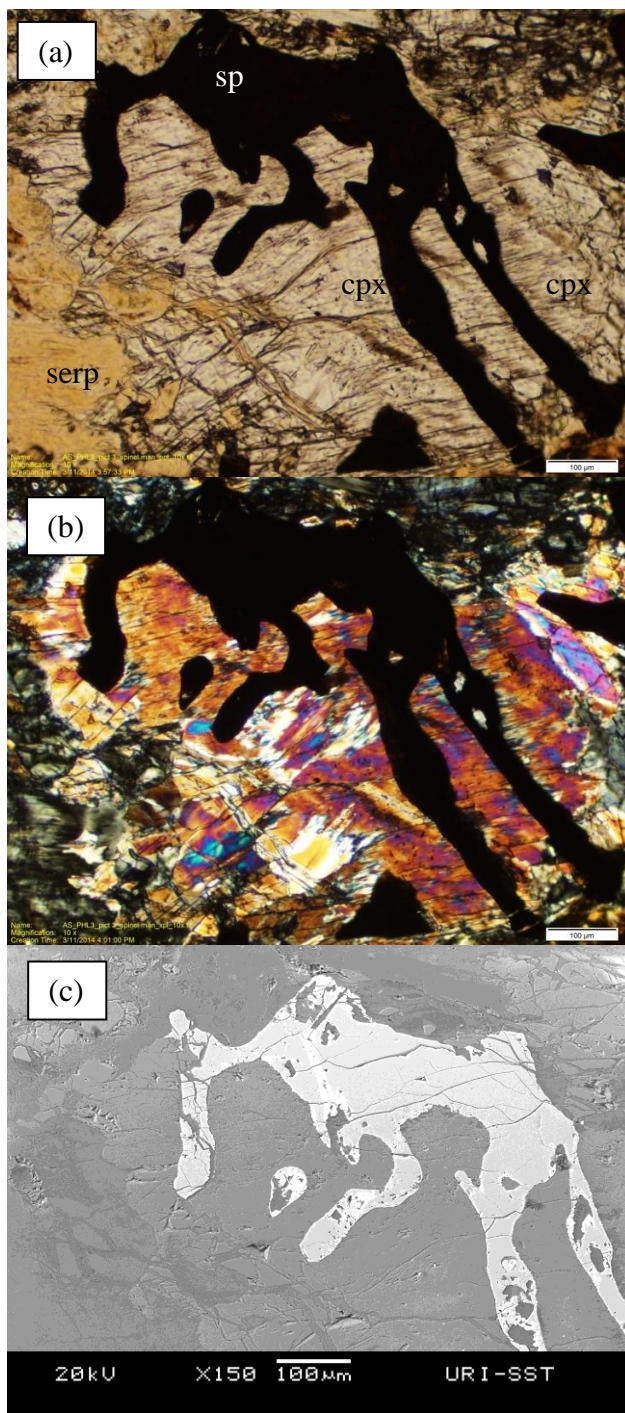
Figure 18. Thin section images of serpentine, cpx, and spinel in PHL_3 in (a) plane polarized light (10x, scale bar represents 100μm.), (b) cross polarized light, and (c) SEM backscatter image. The yellowing of serpentine in ppl may be due to brucite. Detail of a spinel with an interesting shape that appears to be bisecting a cpx grain. The spinel also has inclusions of the cpx grain in legs of the spinel, which indicates that the cpx grain existed before the spinel, which, therefore, is an alteration mineral. The SEM BSE image of the spinel shows micro-cracks in the spinel and variations in its composition (shading differences).

90
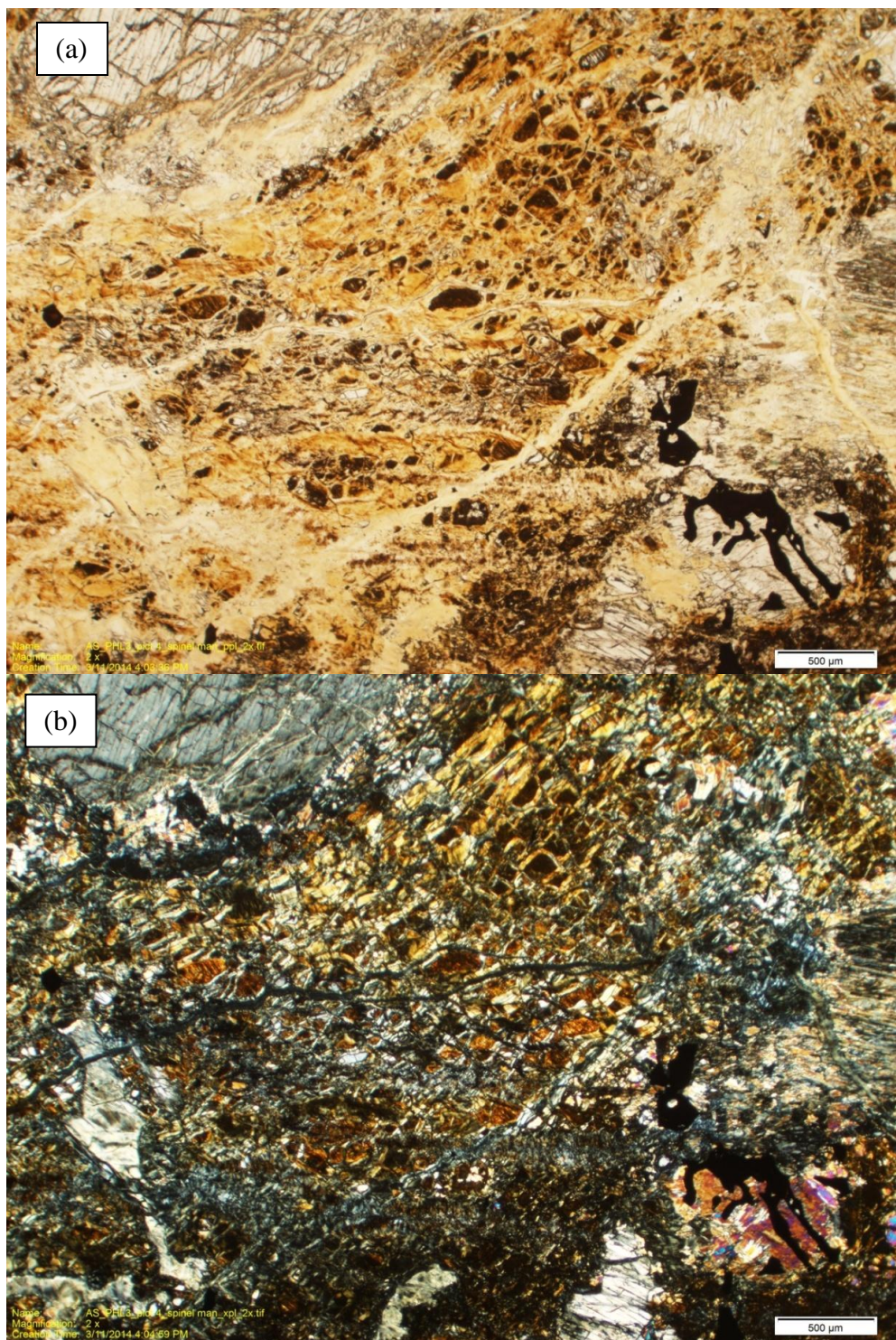
Figure 19. Thin section images of PHL_3 including the spinel in Figure 18 in (a) plane polarized light, (b) cross polarized light, and (c) SEM. Serpentine, cpx, opx, and spinel are visible. Scale bar represents 500μm. The yellowing of serpentine in ppl may be due to brucite and yellow grains in xpl may be brucite. Serpentine mesh and veins (possibly lizardite), cpx, opx, and spinel are visible. There are various Fe-oxides present in this sample indicated by the colors varying from red-orange to dark brown.

91
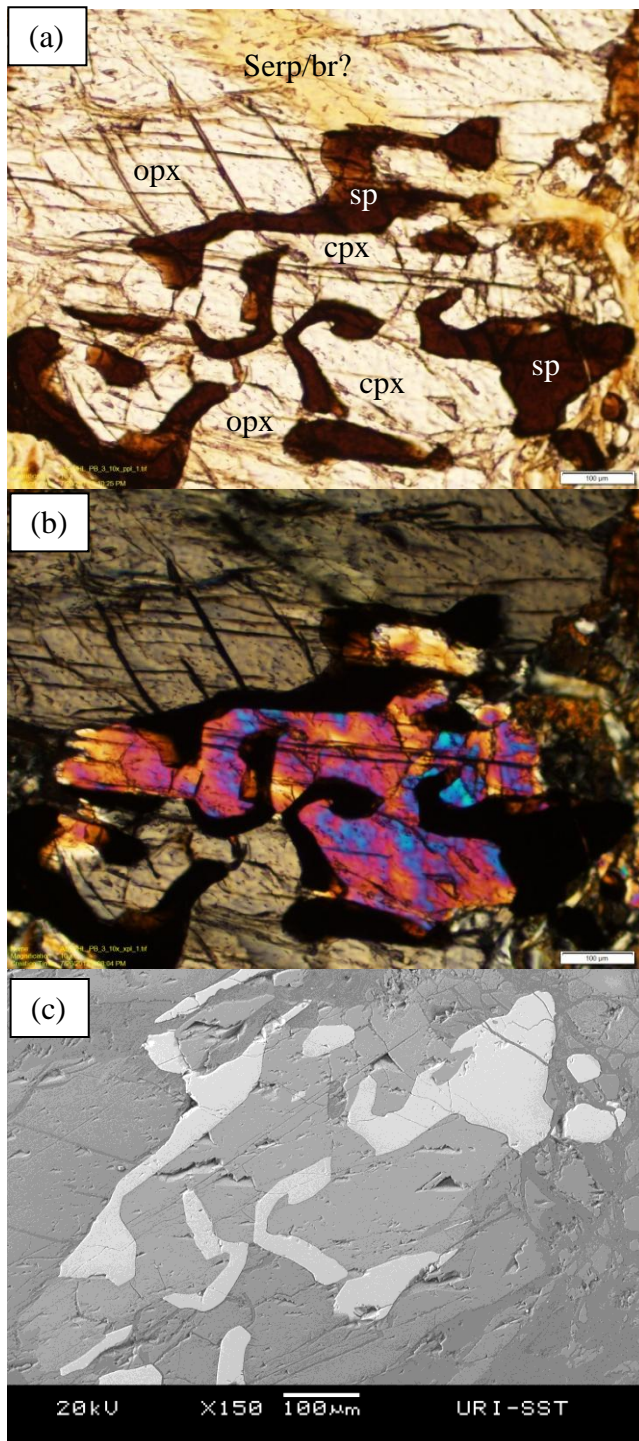
Figure 20. Thin section images of PHL_3 in (a) plane polarized light, (b) cross polarized light, and (c) SEM. Scale bars represent 100μm. Serpentine (serp), pyroxene (opx, cpx), and spinel are visible. (c) shows that the spinel grains are much more rich in metals than the surrounding pyroxene and serpentine. The yellowing of serpentine in ppl may be due to brucite.
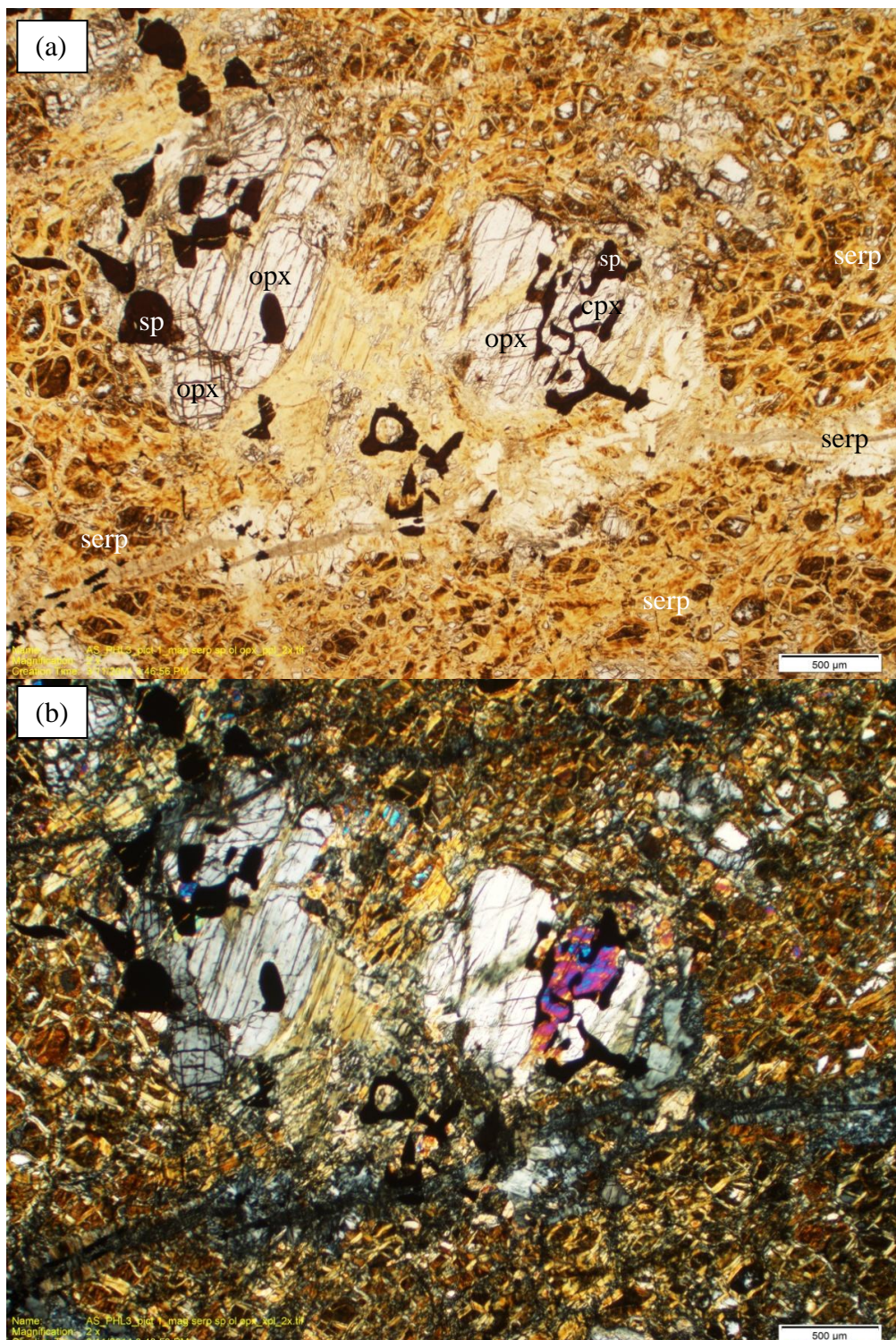
Figure 21. Thin section images of PHL_3 in (a) plane polarized light (scale bar represents 500µm), (b) cross polarized light. Serpentine (serp), pyroxene (opx, cpx), spinel, and relict olivine are visible. The yellowing of serpentine in ppl may be due to brucite. This is a zoomed-out view of Figure 20
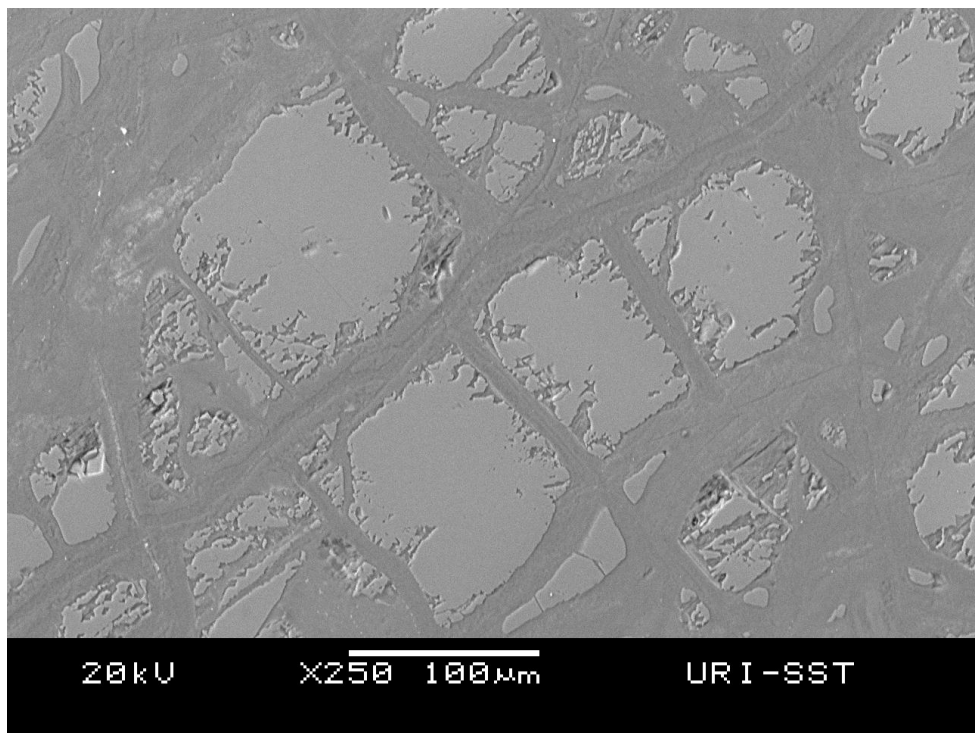
Figure 22. SEM images of thin section of PHL_3 including serpentine and olivine(?) are visible. The serpentine veins show zoning of lighter color near the olivine grains and darker towards the center of veins; and there are areas where the reverse is true. The jagged-edged dissolution of the olivine(?) grains into serpentine are also visible.
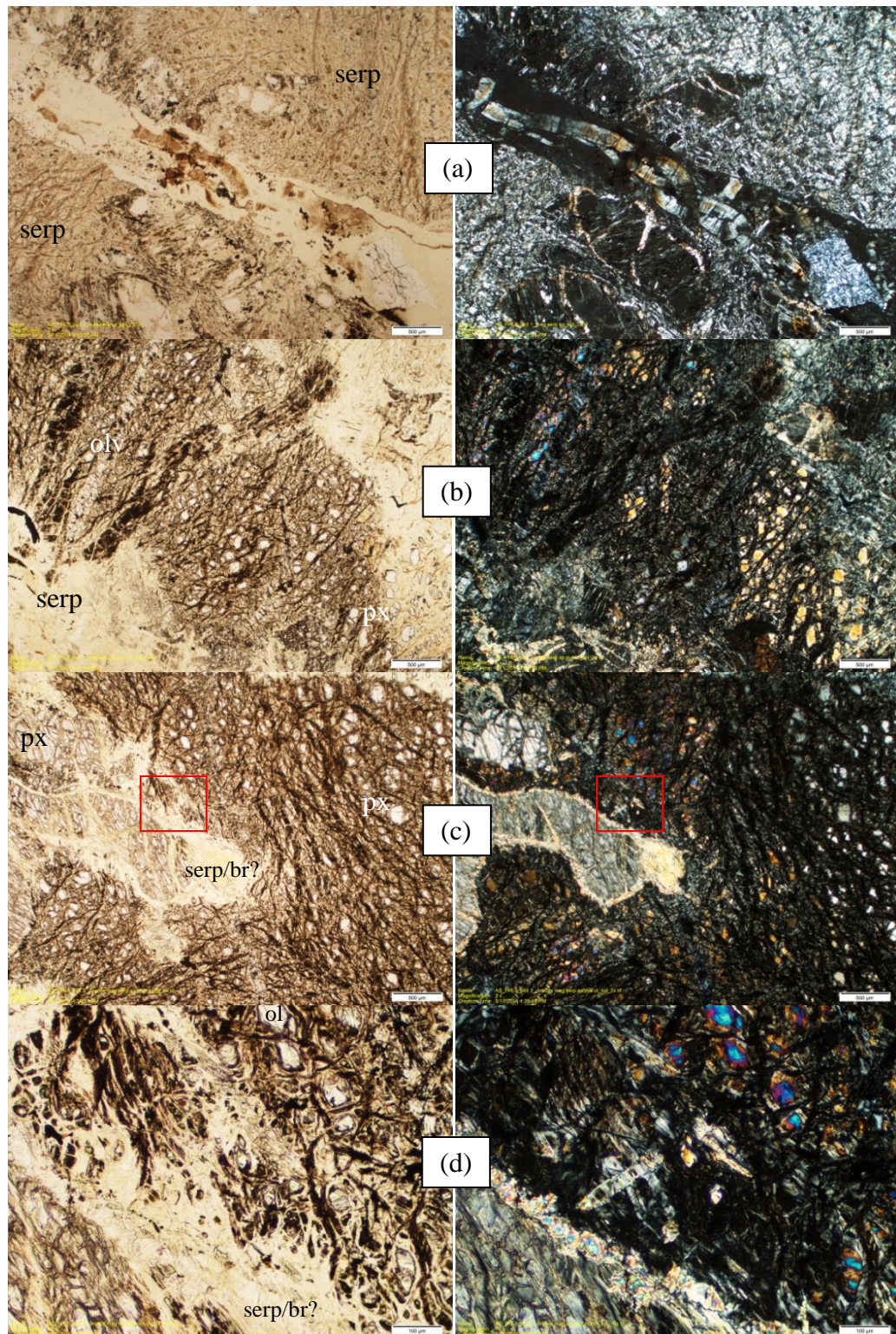
Figure 23. Thin section images of PHL_5 include serpentine (serp) (a-d),
magnetite/Fe oxide (a-d), relict pyroxene (px) (b,c), relict olivine (ol)(b-d), and
brucite(?)(br)(c-d). Sections are in ppl (left) and xpl (right). (a-c) scale bar is 500μm
and (d) scale bar is 100μm. (d) is the section of (c) in the red box. **S**erpentine veins

include a braid-like texture and the mesh is saturated with dark brown Fe-oxides. The yellowing of serpentine in ppl may be due to brucite.
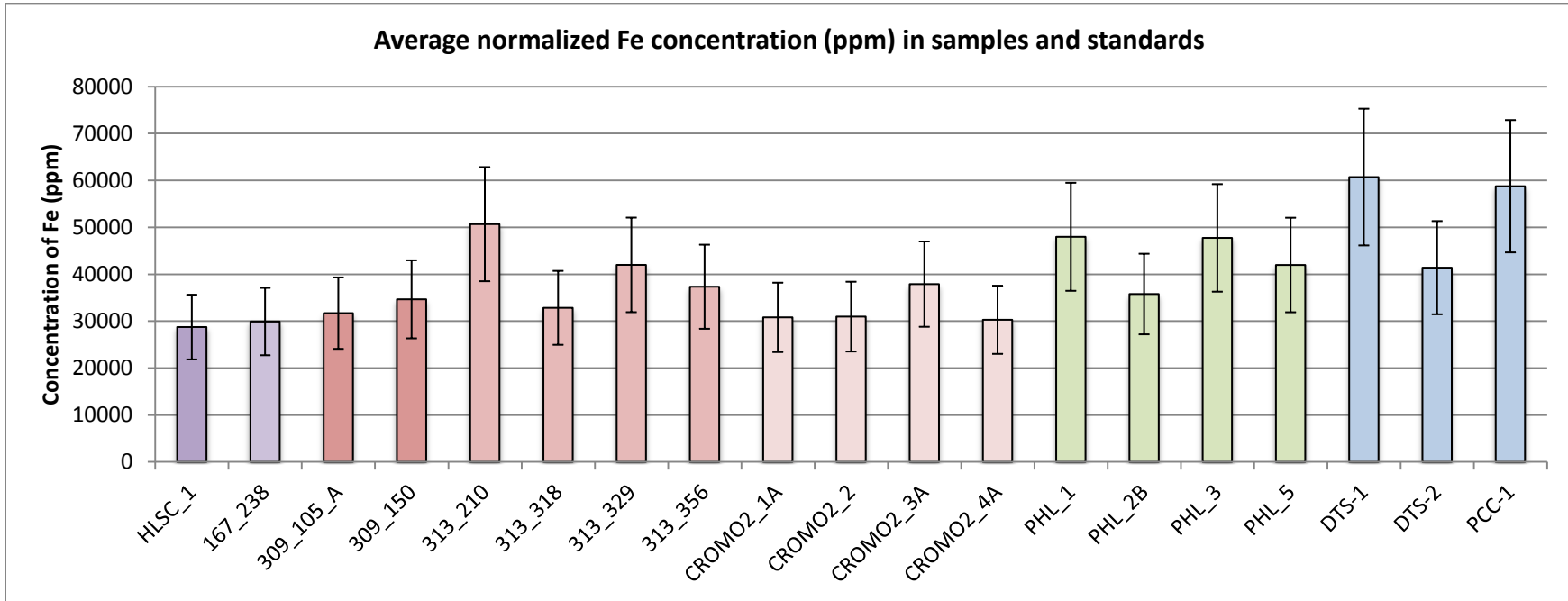
Figure 24. Average normalized Fe concentration (ppm) in standards and samples from CRO and ZO obtained from XRF analysis. Error bars are at 24% to reflect the error after normalizing of DTS-2.
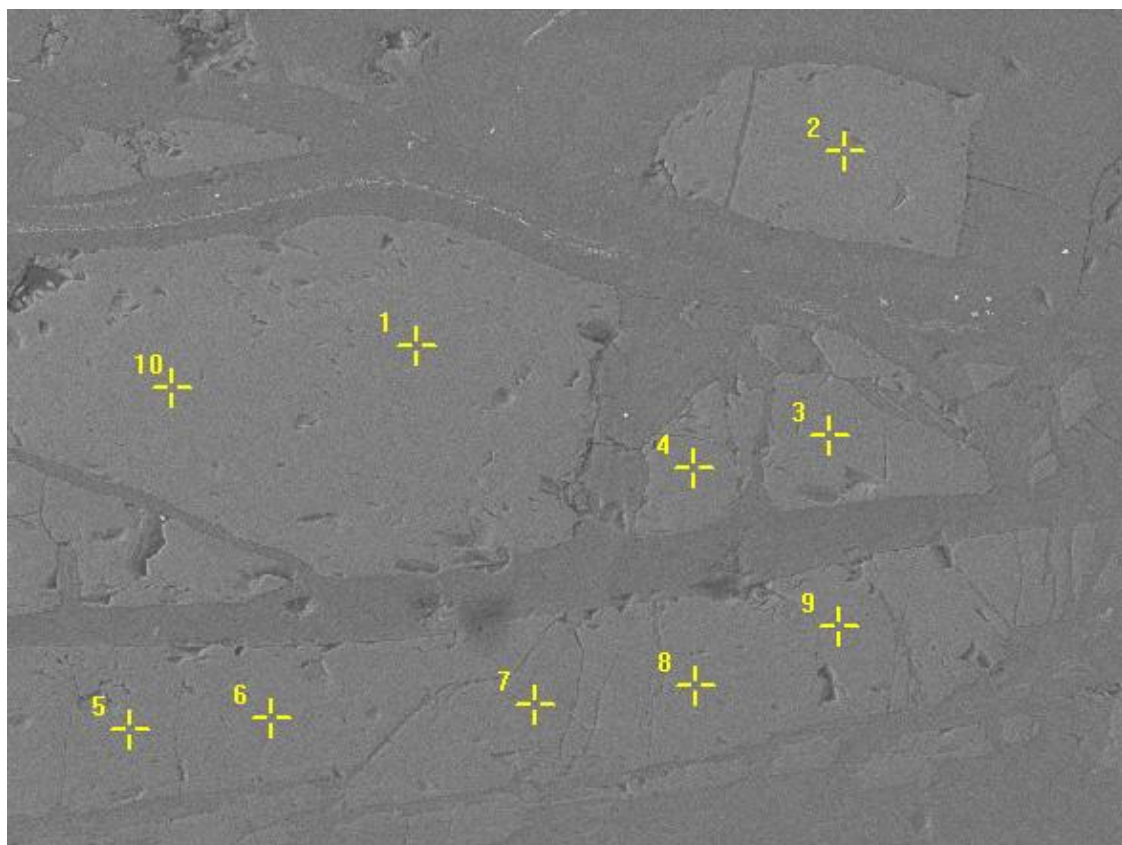
 Figure 25. SEM image showing point locations for SEM-EDS elemental
concentrations for 313_329 Table 7. Image is at 250x shows serpentine veins and
olivine grains.
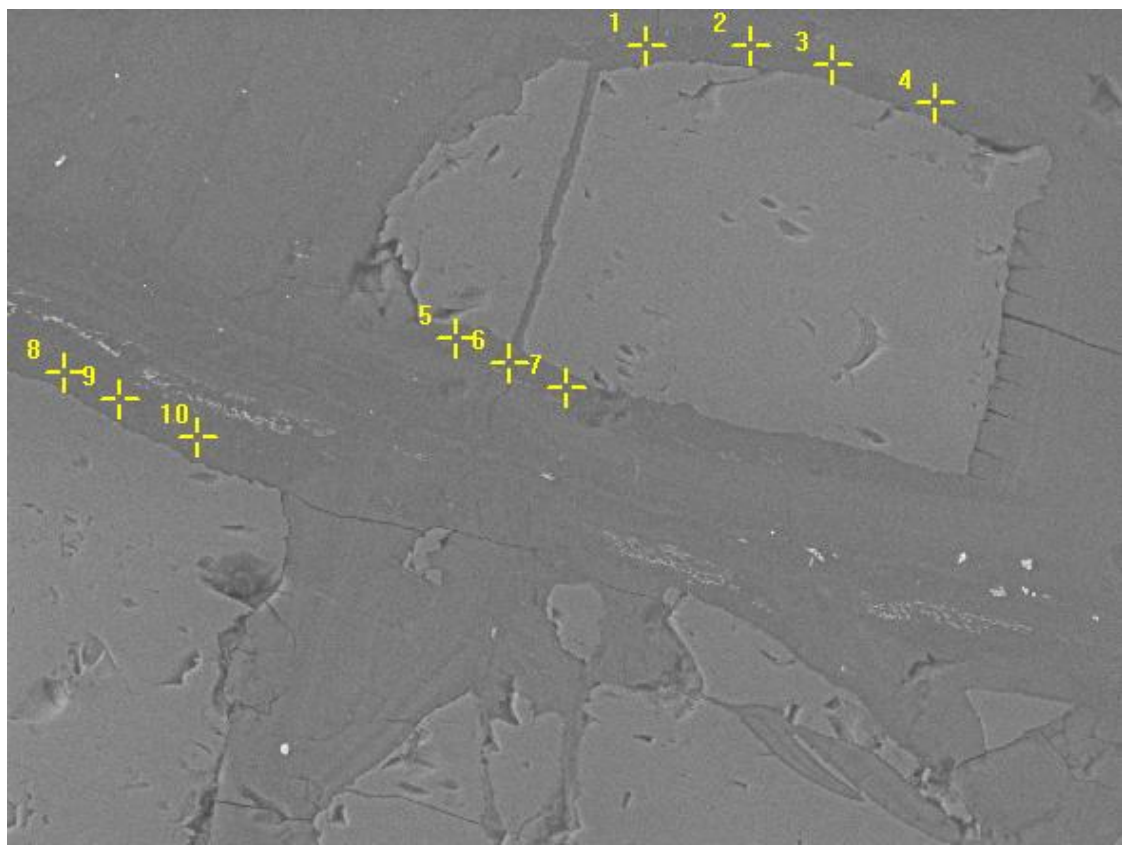
Figure 26. SEM image showing point locations for SEM-EDS elemental concentrations for 313_329 Table 8. It is a 500x detail of image of Figure 25 which shows serpentine veins and olivine grains.
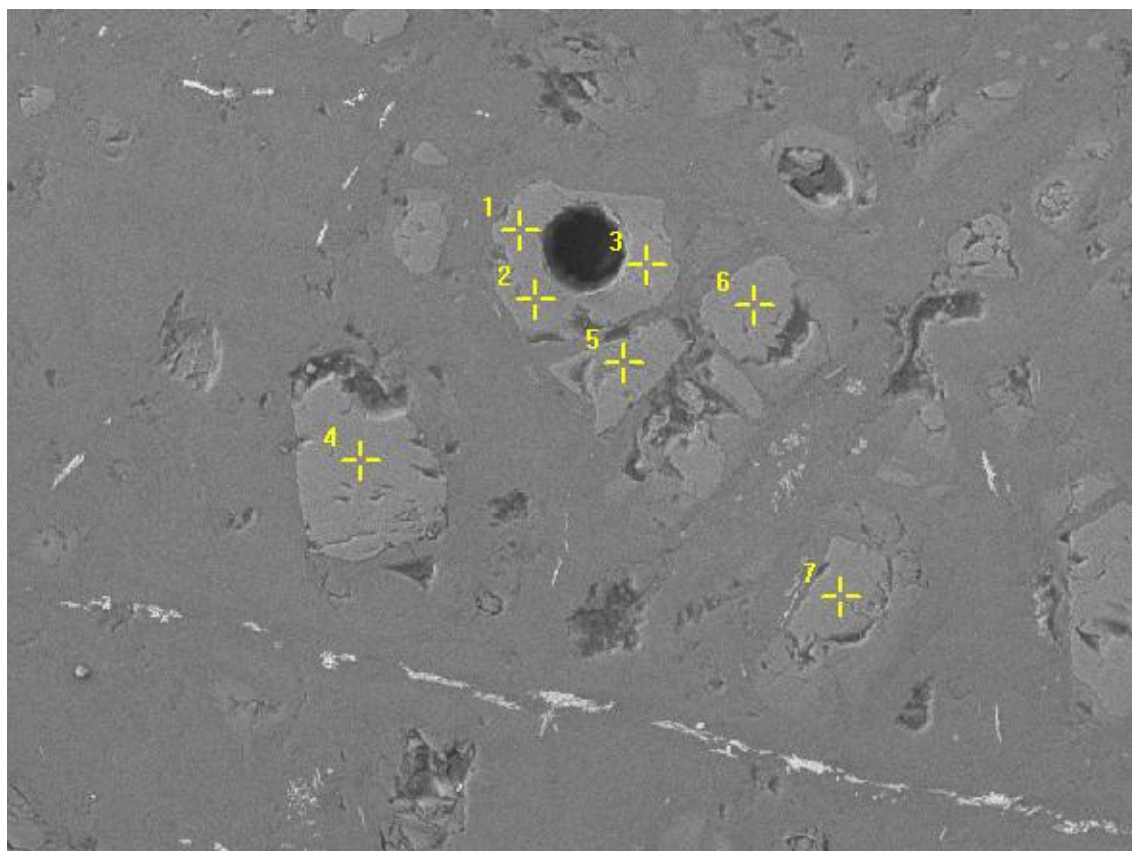
 Figure 27. SEM image showing point locations for SEM-EDS elemental concentrations for 313_329 Table 9. Image is at 250x shows serpentine and magnetite in veins and olivine grains. Pit is from ICPMS laser oblation.
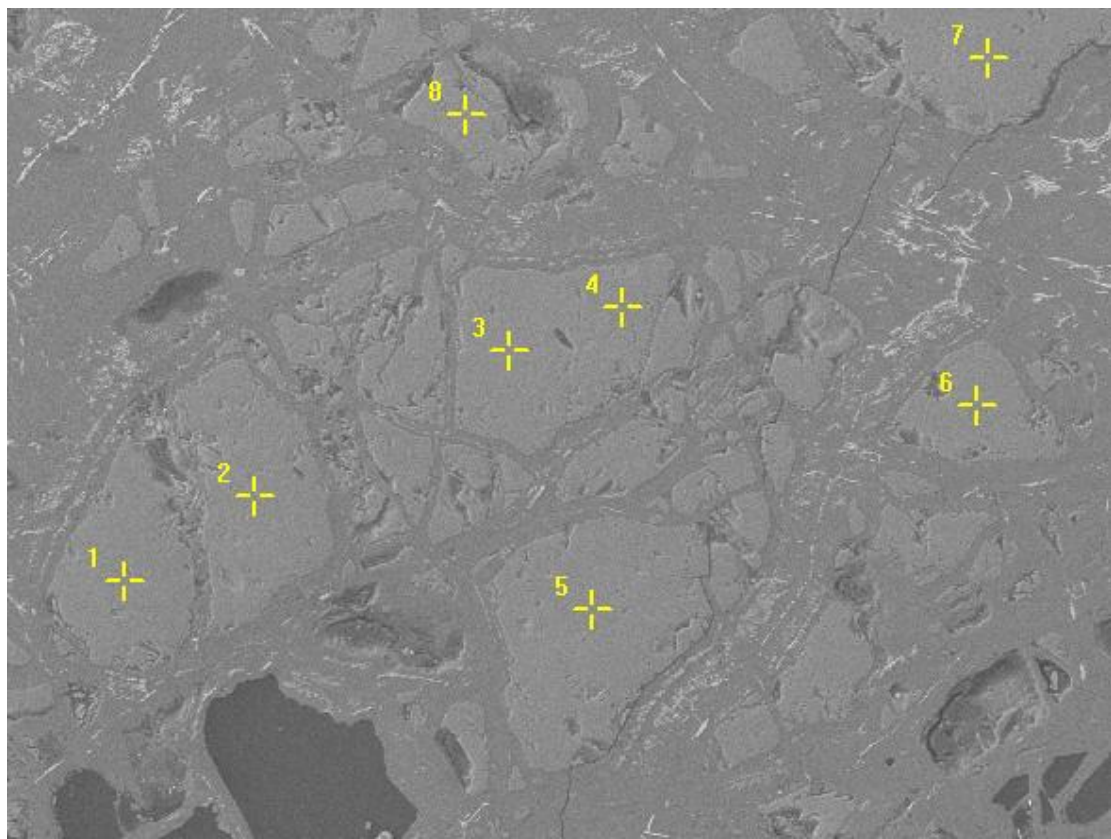
Figure 28. SEM image showing point locations for SEM-EDS elemental concentrations for 313_329 Table 10. Image is at 150x shows serpentine and magnetite in veins and possibly pyroxene grains.
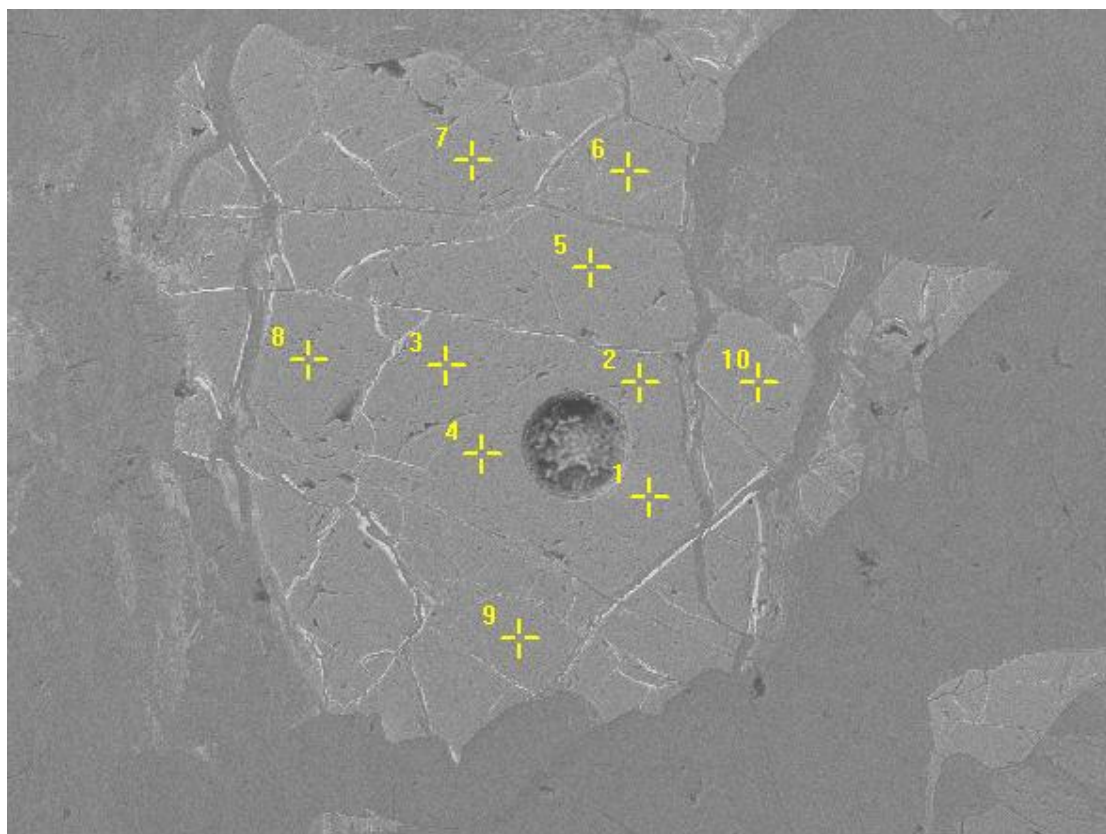
Figure 29. SEM image showing point locations for SEM-EDS elemental concentrations for 313_329 Table 11. Image is at 150x shows a spinel grain surrounded by serpentine and olivine grains. Pit is from ICPMS laser oblation.
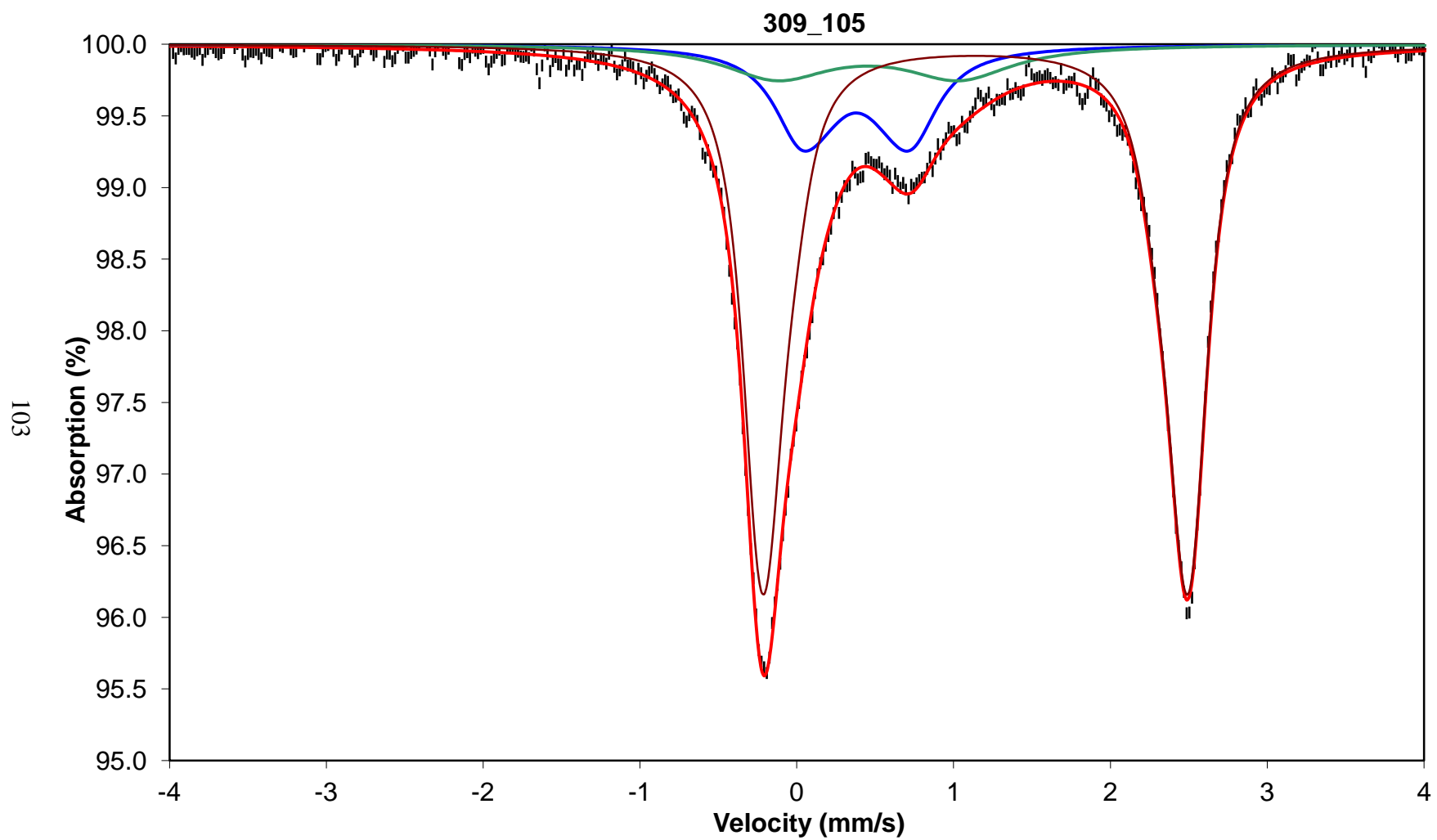
Figure 30. Mössbauer Spectroscopy 309_105_A plot. The data (black dots) were fit using the Ghent program to obtain a best fit curve (red), Fe^{3+} (blue and green) and Fe^{2+} (brown) curves.
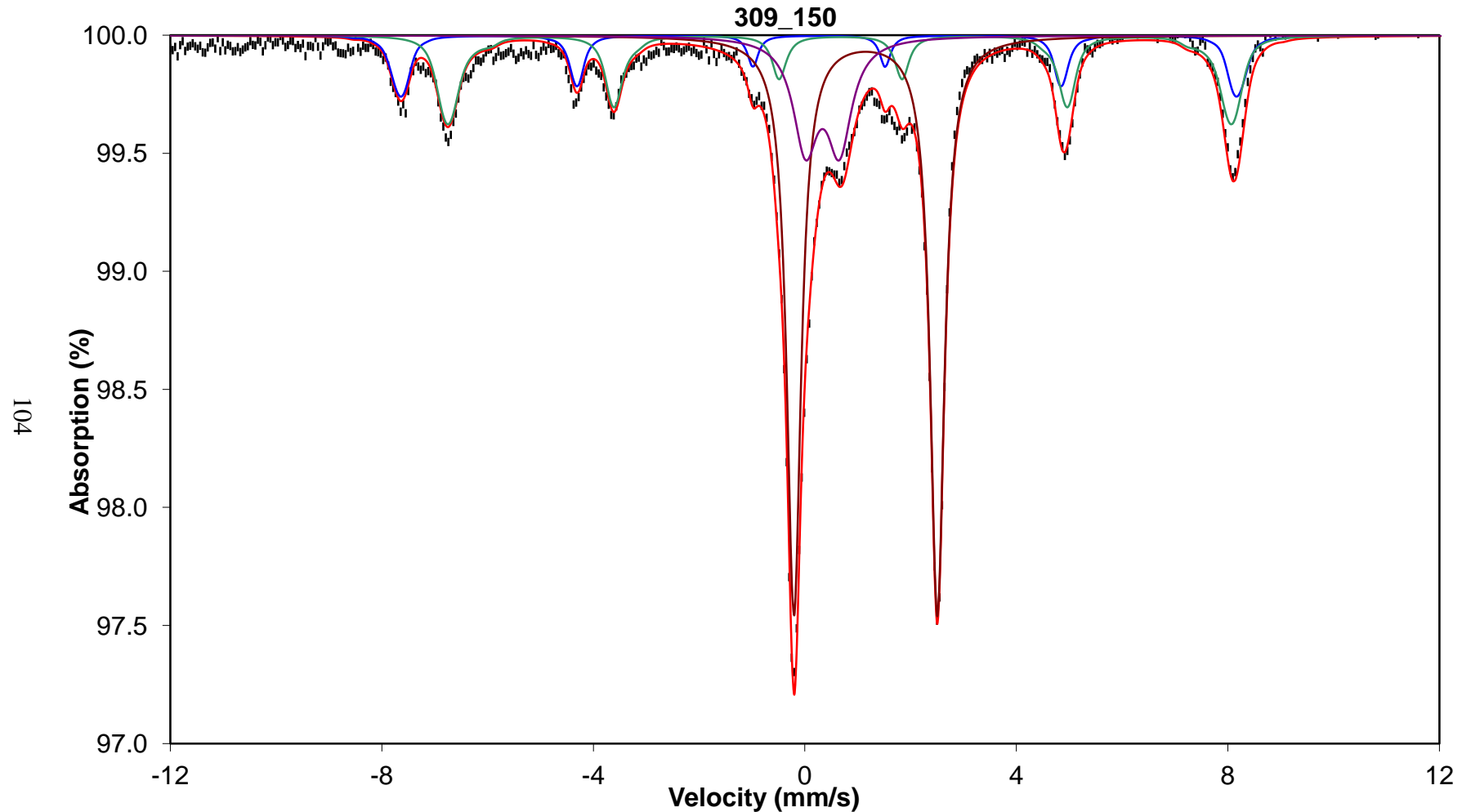
Figure 31. Mössbauer Spectroscopy 309__150 plot. The data (black dots) were fit using the Ghent program to obtain a best fit curve (red) and Fe^{3+} (purple), Fe^{2+} (brown), and magnetite (blue and green) curves.
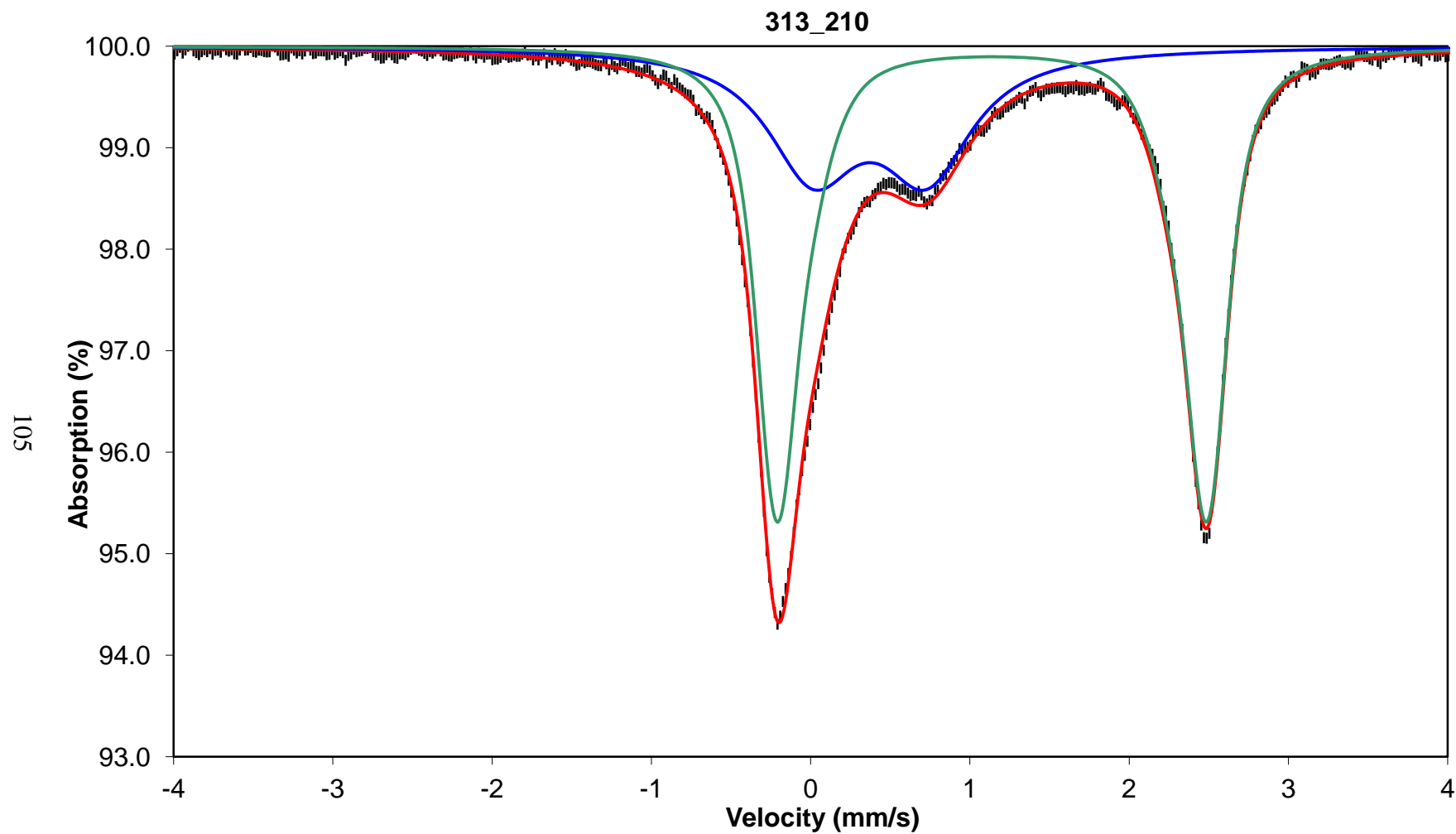
Figure 32. Mössbauer Spectroscopy 313_210 plot. The data (black dots) were fit using the Ghent program to obtain a best fit curve (red), Fe^{3+} (blue), and Fe^{2+} (green) curves.
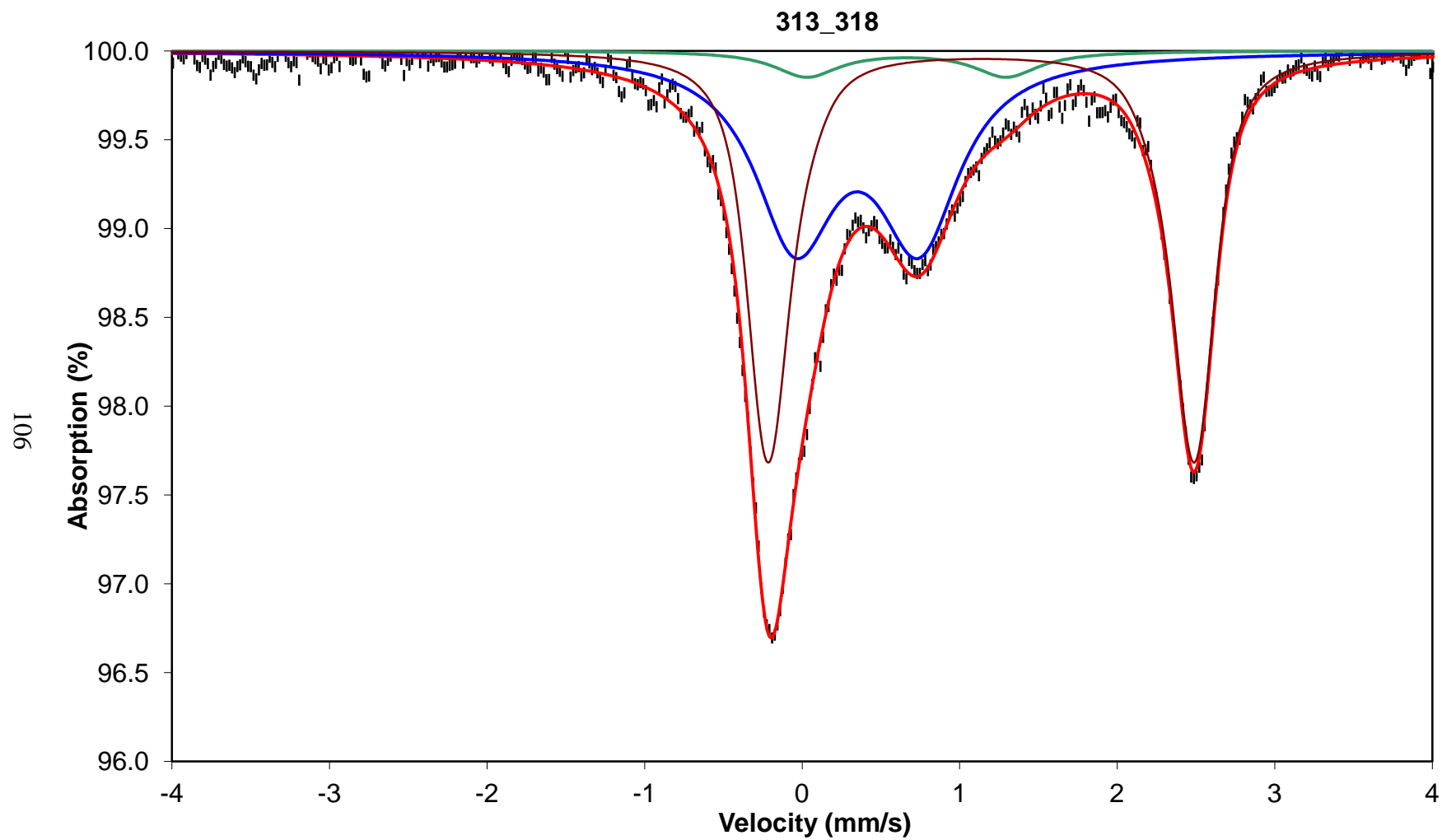
Figure 33. Mössbauer Spectroscopy 313_318 plot. The data (black dots) were fit using the Ghent program to obtain a best fit curve (red), Fe^{3+} (blue and green) and Fe^{2+} (brown) curves.
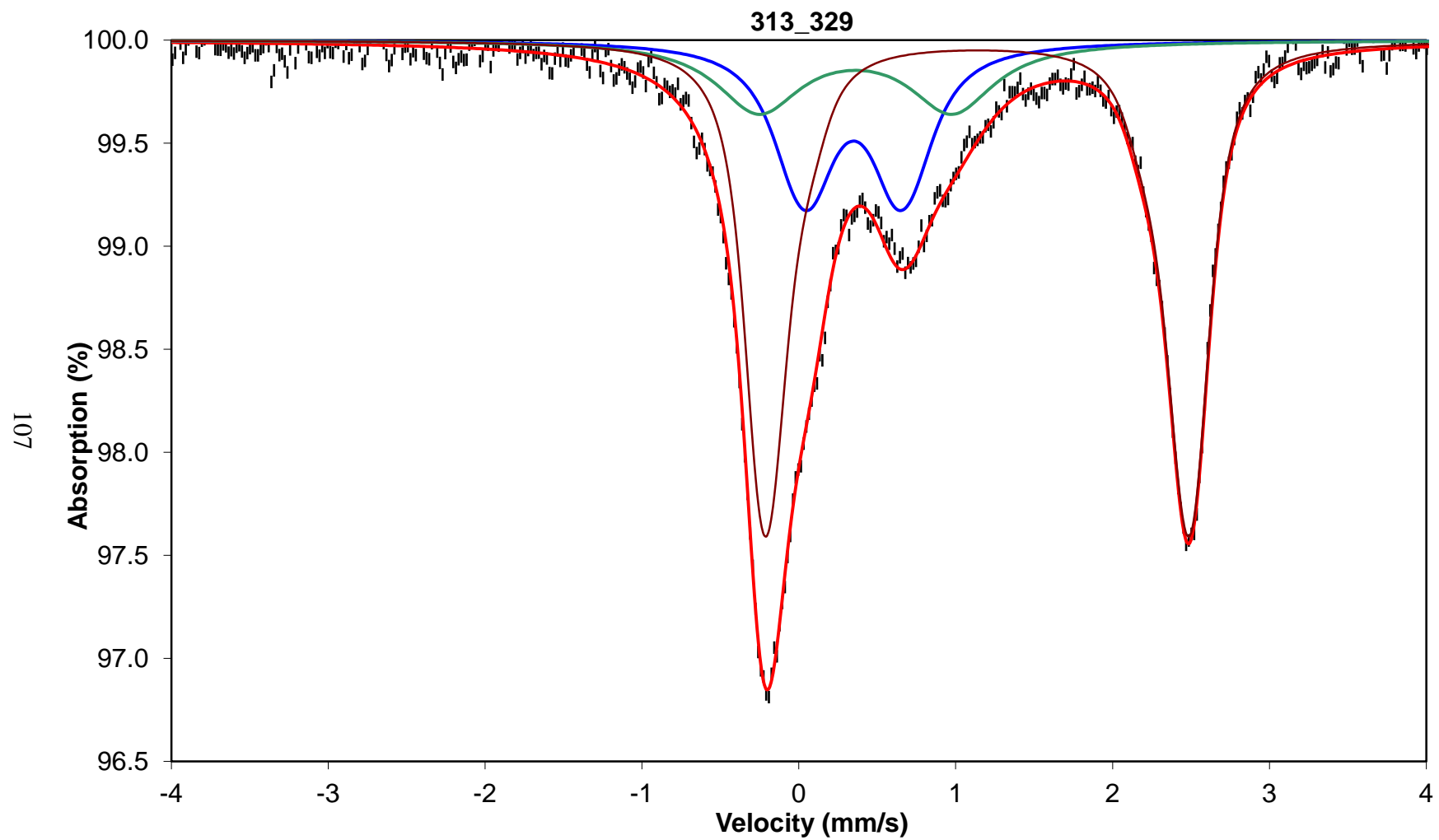
Figure 34. Mössbauer Spectroscopy 313_329 plot. The data (black dots) were fit using the Ghent program to obtain a best fit curve (red), Fe^{3+} (blue and green) and Fe^{2+} (brown) curves.
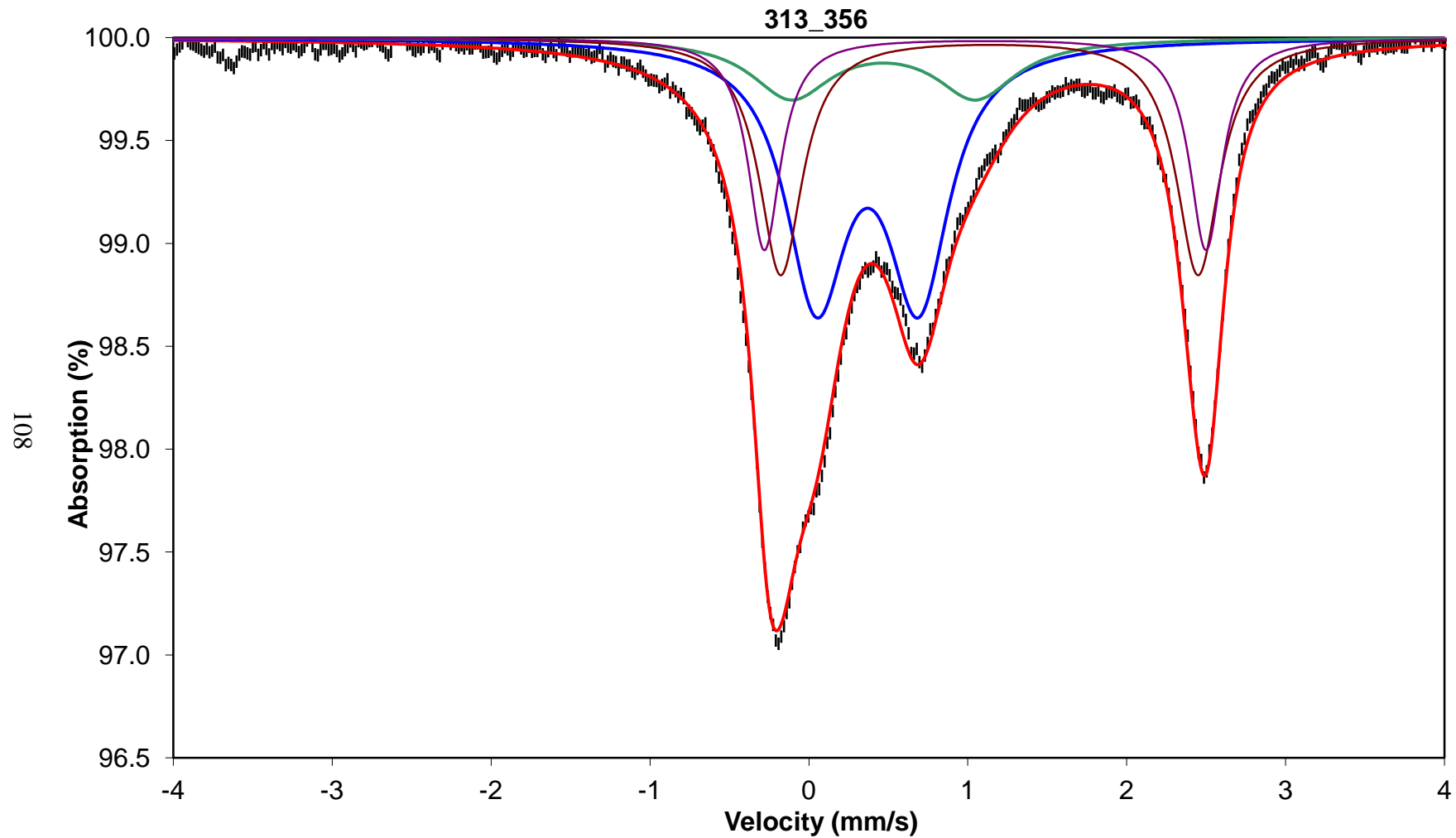
Figure 35. Mössbauer Spectroscopy 313_356 plot. The data (black dots) were fit using the Ghent program to obtain a best fit curve (red), Fe^{3+} (blue and green) and Fe^{2+} (brown and purple) curves.
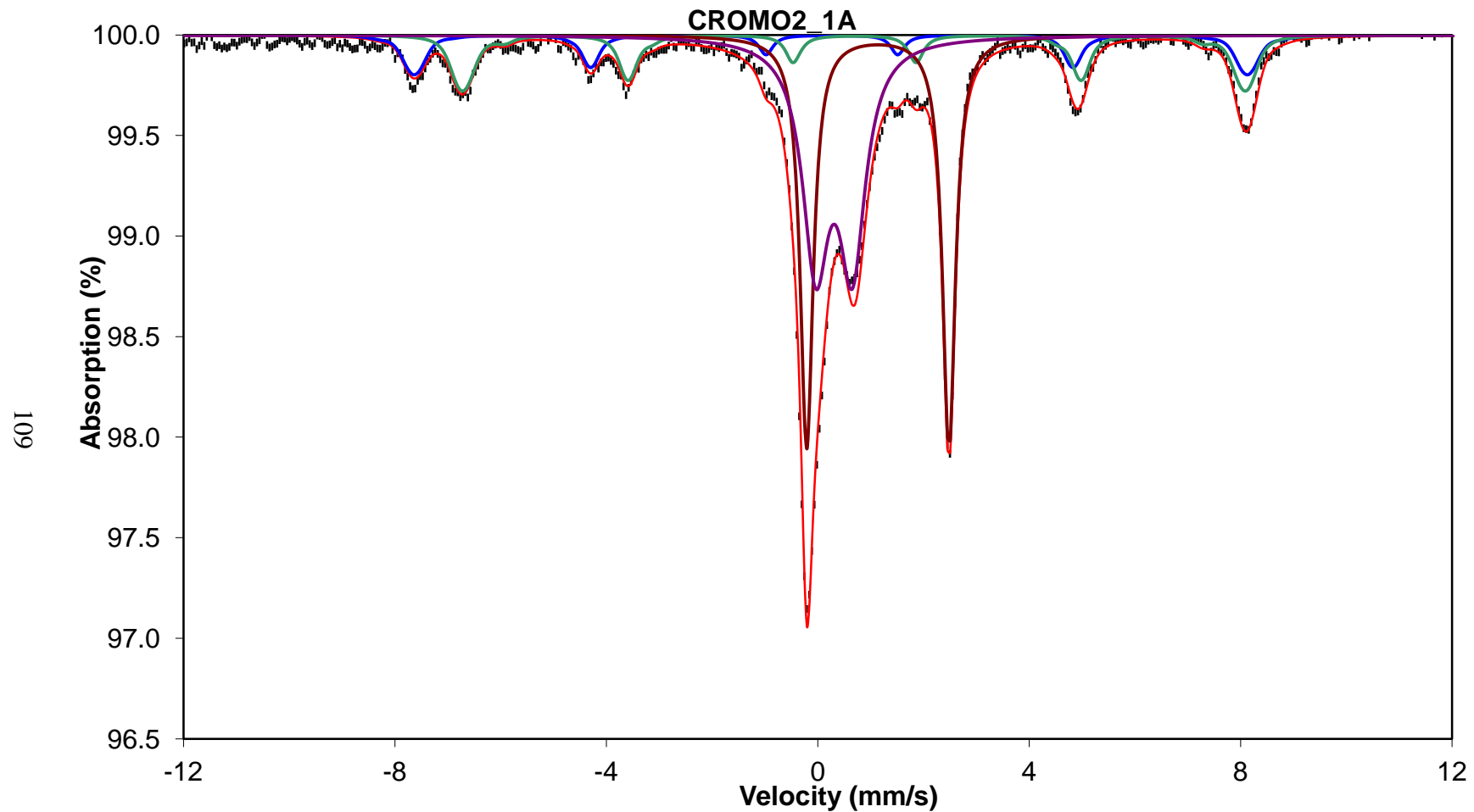
Figure 36. Mössbauer Spectroscopy CROMO2_1A plot. The data (black dots) were fit using the Ghent program to obtain a best fit curve (red) and Fe^{3+} (purple), Fe^{2+} (brown), and magnetite (blue and green) curves.
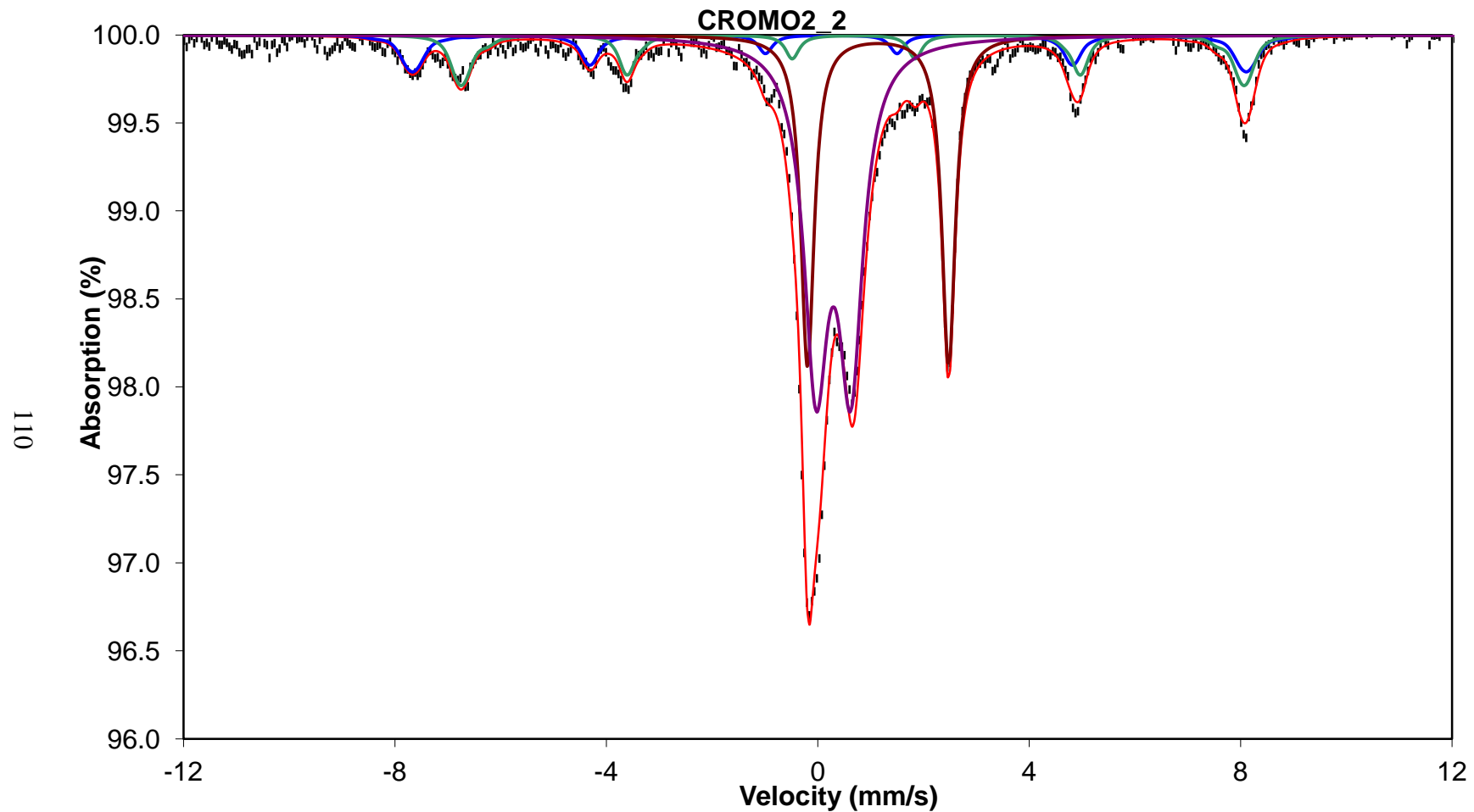
Figure 37. Mössbauer Spectroscopy CROMO2_2 plot. The data (black dots) were fit using the Ghent program to obtain a best fit curve (red) and Fe^{3+} (purple), Fe^{2+} (brown), and magnetite (blue and green) curves.
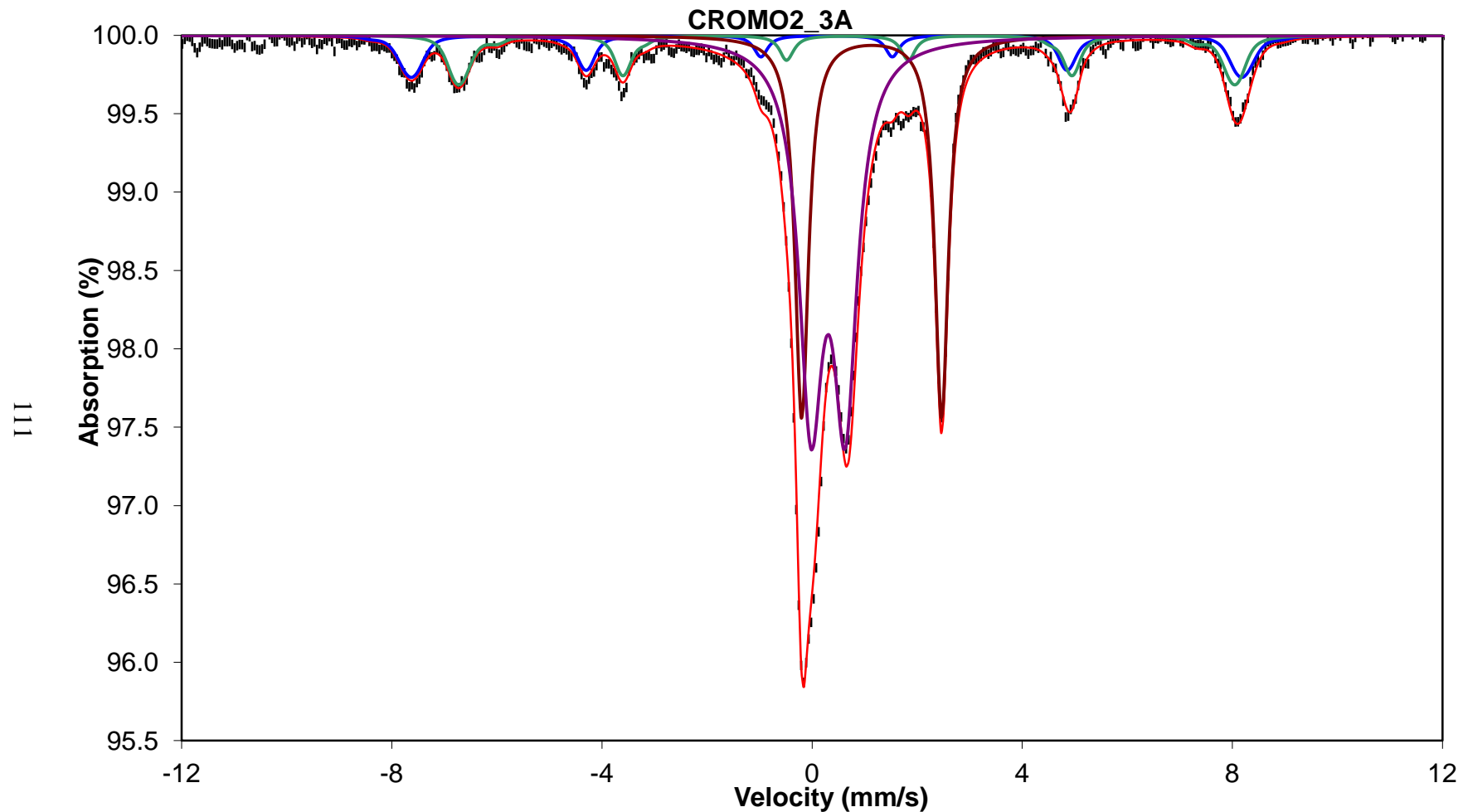
Figure 38. Mössbauer Spectroscopy CROMO2_3A plot. The data (black dots) were fit using the Ghent program to obtain a best fit curve (red) and Fe^{3+} (purple), Fe^{2+} (brown), and magnetite (blue and green) curves.
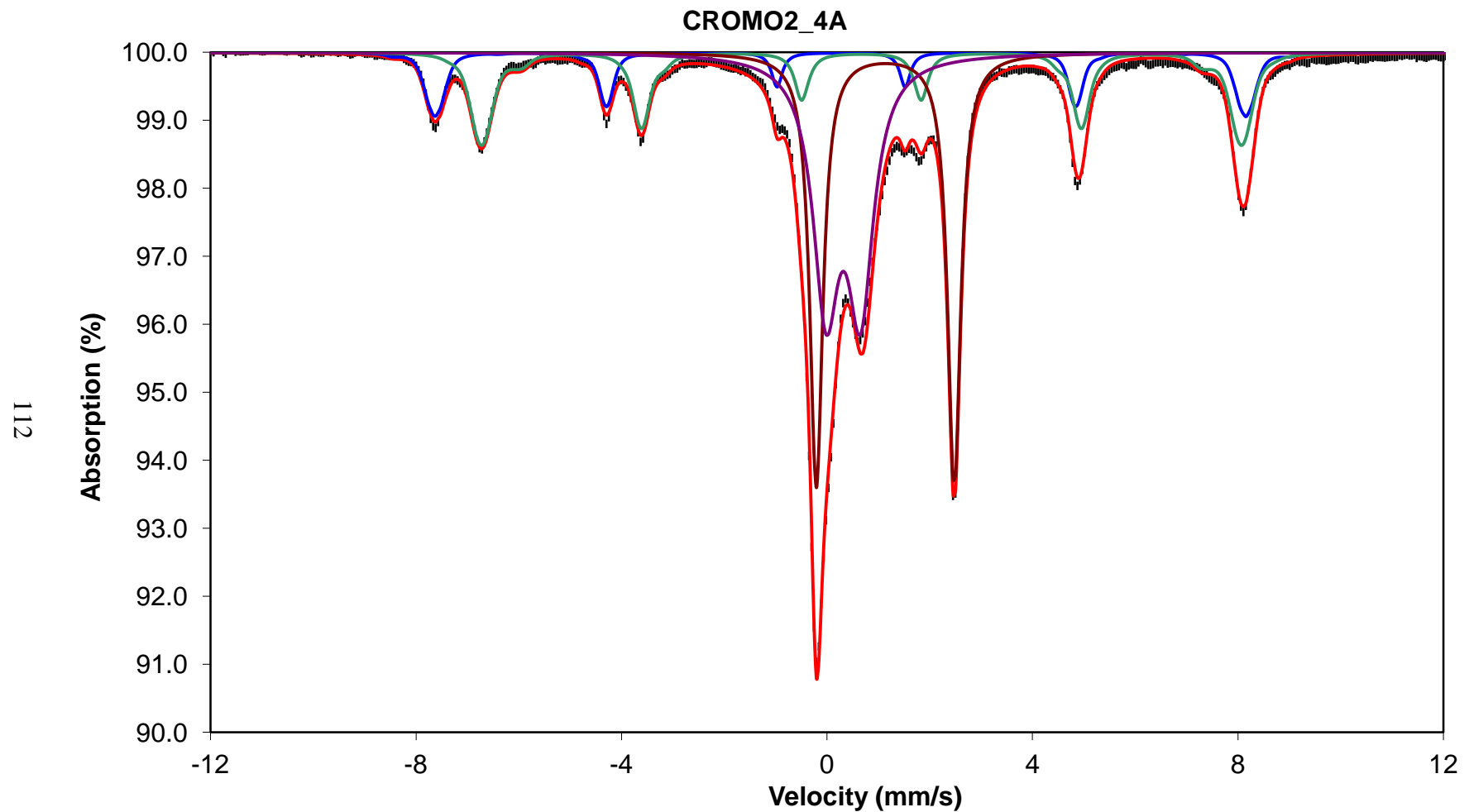
Figure 39. Mössbauer Spectroscopy CROMO2_4A plot. The data (black dots) were fit using the Ghent program to obtain a best fit curve (red) and Fe^{3+} (purple), Fe^{2+} (brown), and magnetite (blue & green) curves.
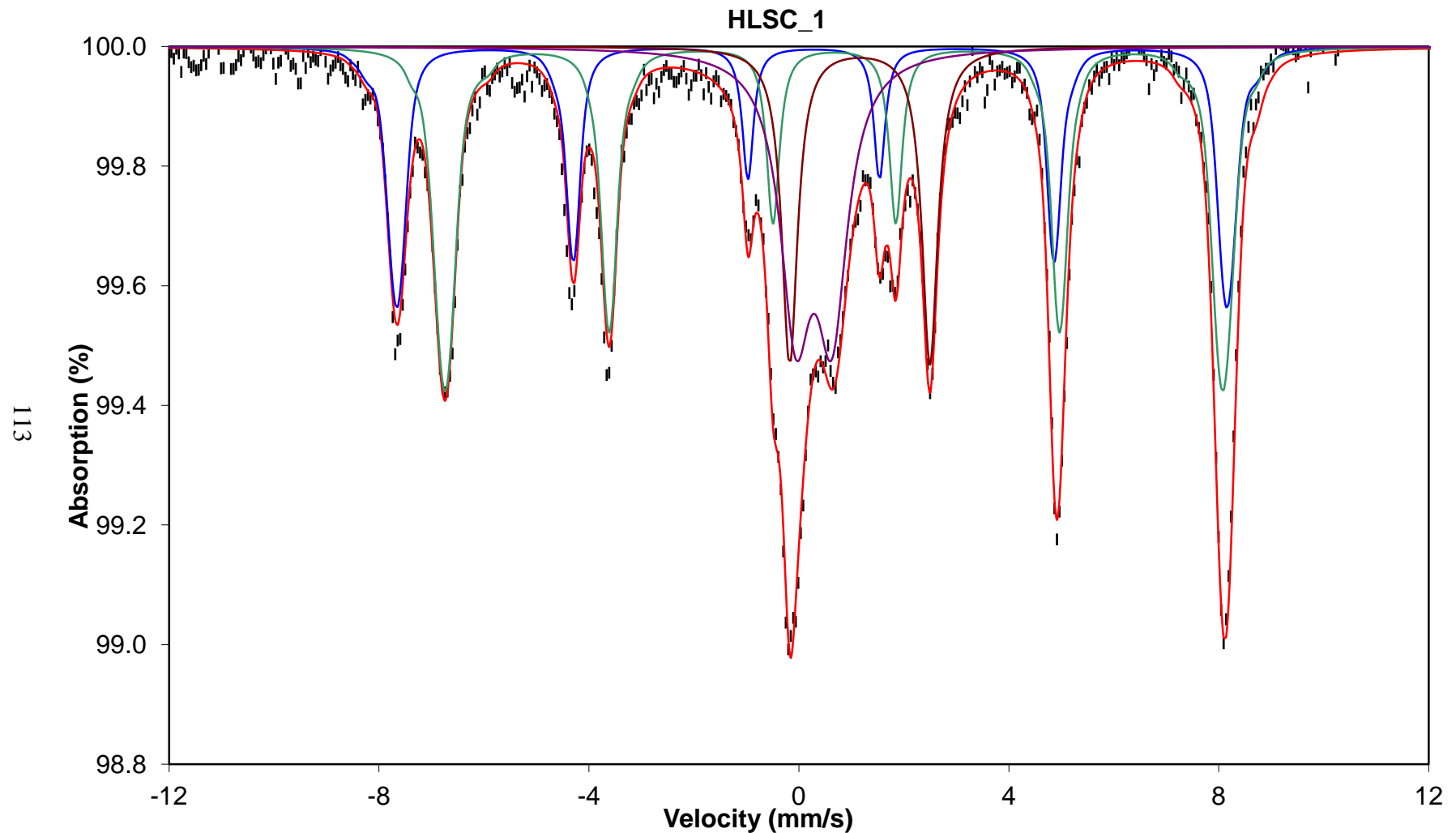
Figure 40. Mössbauer Spectroscopy HLSC_1 plot. The data (black dots) were fit using the Ghent program to obtain a best fit curve (red) and Fe^{3+} (purple), Fe^{2+} (brown), and magnetite (blue and green) curves.
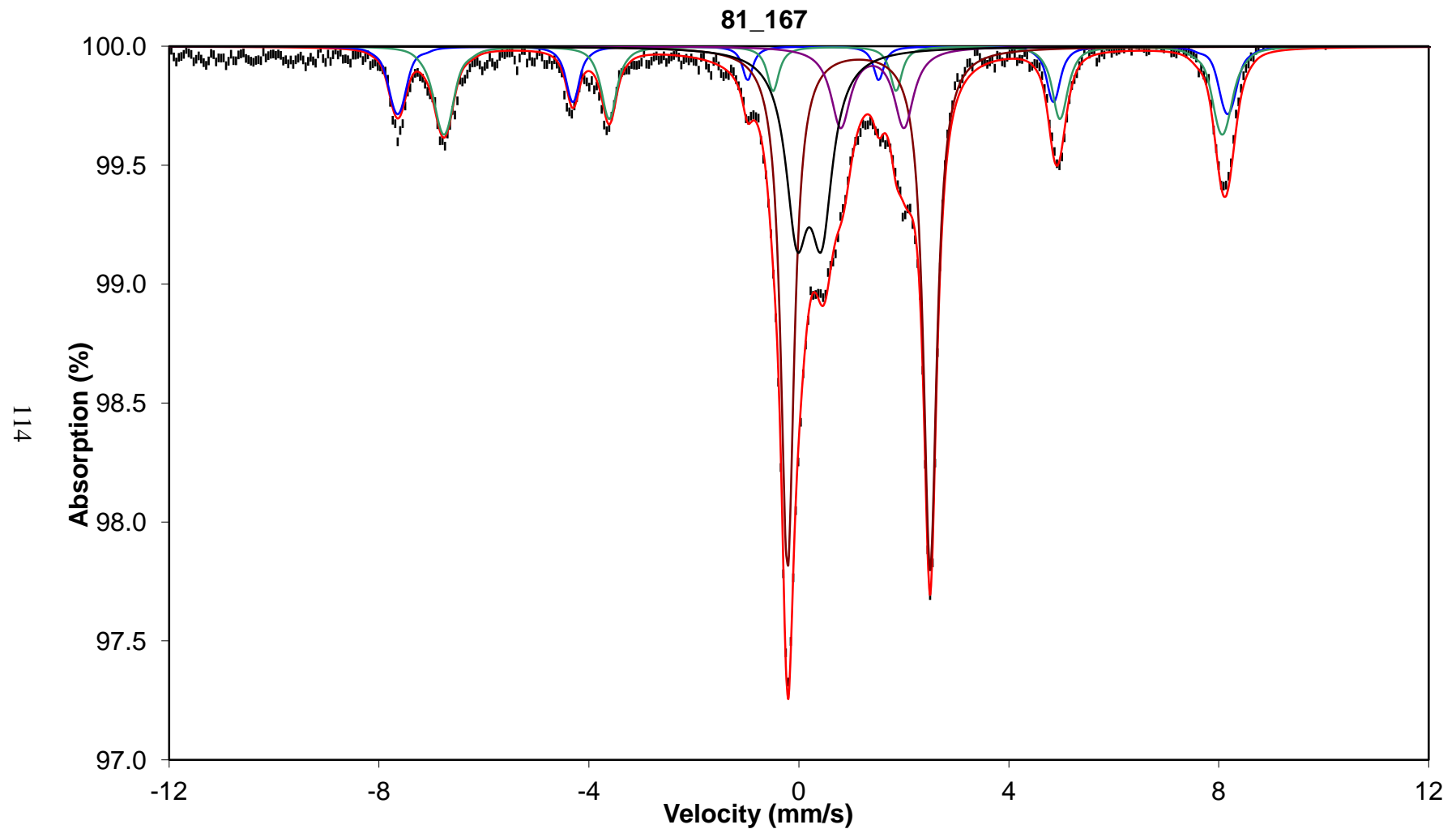
Figure 41. Mössbauer Spectroscopy 167_238 plot. The data (black dots) were fit using the Ghent program to obtain a best fit curve (red) and Fe^{3+} (black), Fe^{2+} (brown and purple), and magnetite (blue and green) curves.
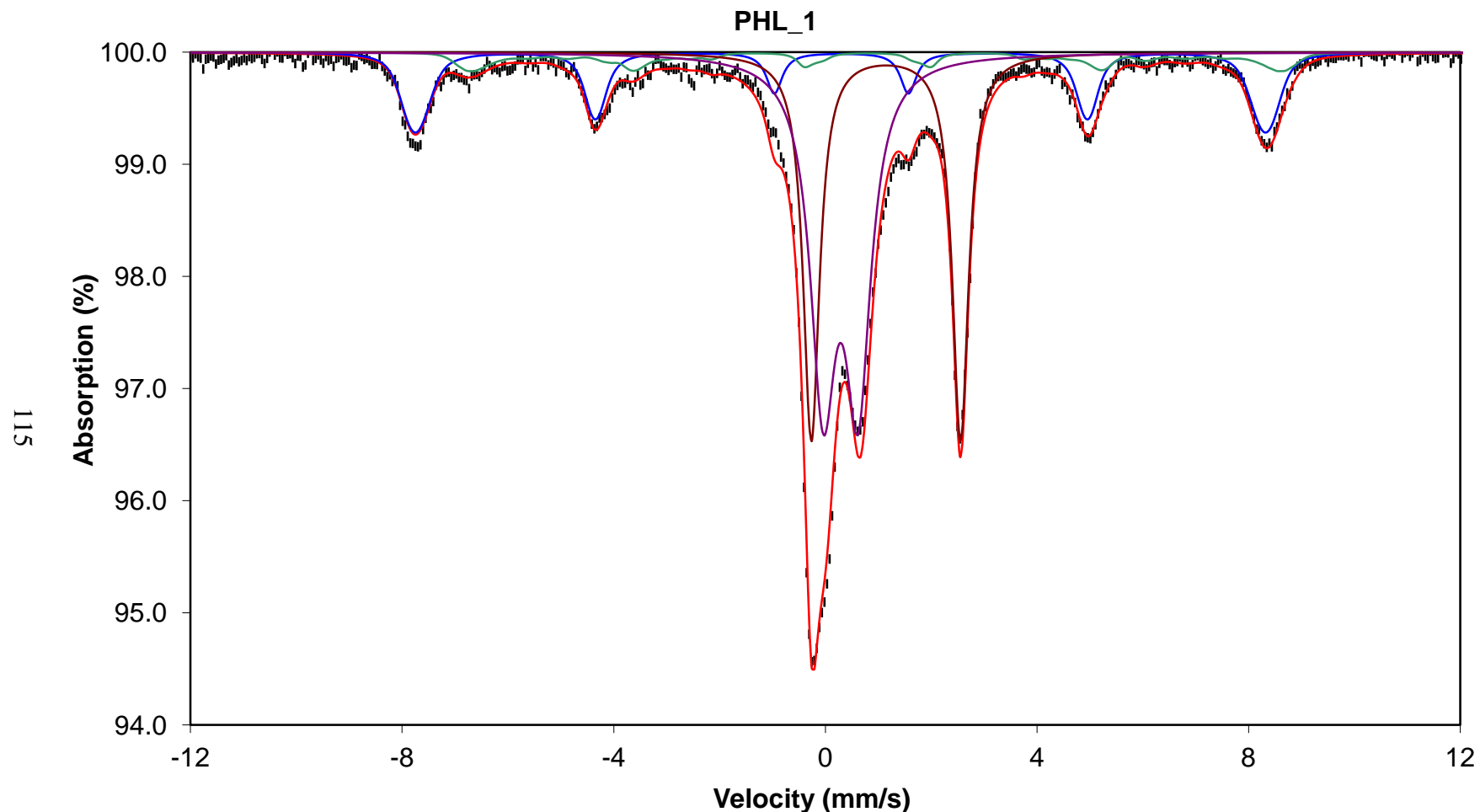
Figure 42. Mössbauer Spectroscopy PHL_1 plot. The data (black dots) were fit using the Ghent program to obtain a best fit curve (red) and Fe^{3+} (purple), Fe^{2+} (brown), and magnetite (blue and green) curves.
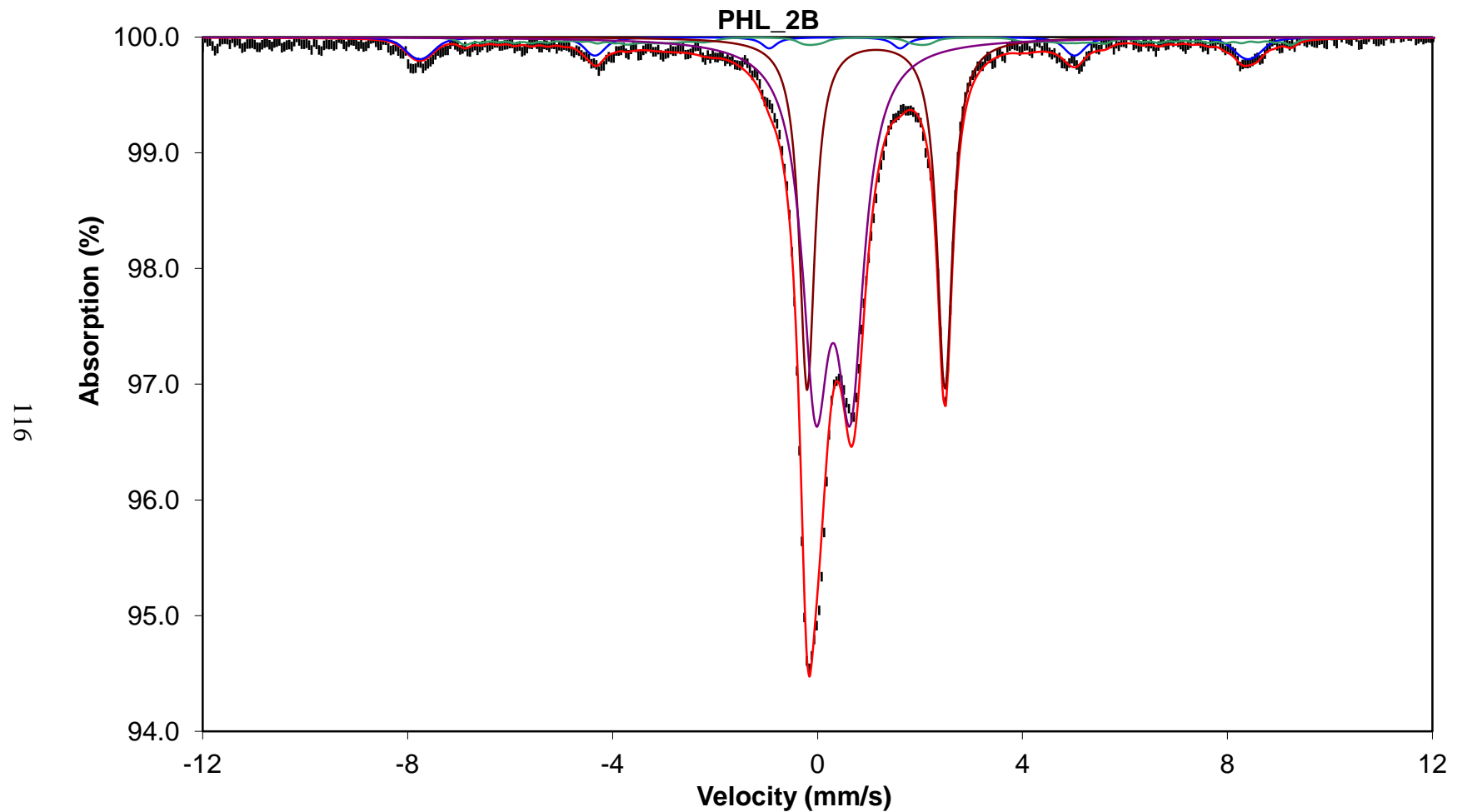
Figure 43. Mössbauer Spectroscopy PHL_2B plot. The data (black dots) were fit using the Ghent program to obtain a best fit curve (red) and Fe^{3+} (purple), Fe^{2+} (brown), and magnetite (blue and green) curves.
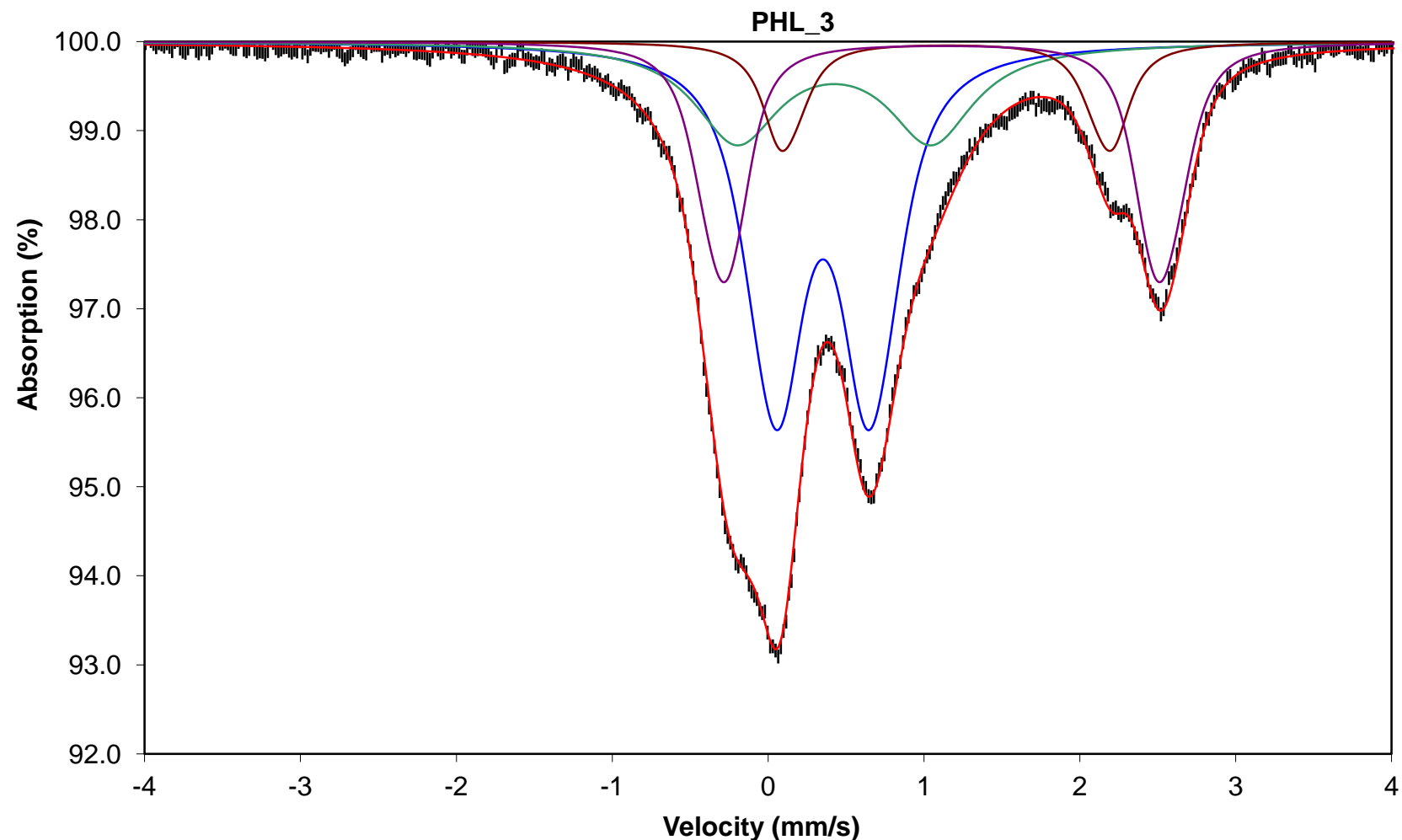
Figure 44. Mössbauer Spectroscopy PHL_3 plot. The data (black dots) were fit using the Ghent program to obtain a best fit (red), Fe^{3+} (blue and green), and Fe^{2+} (brown and purple) curves.
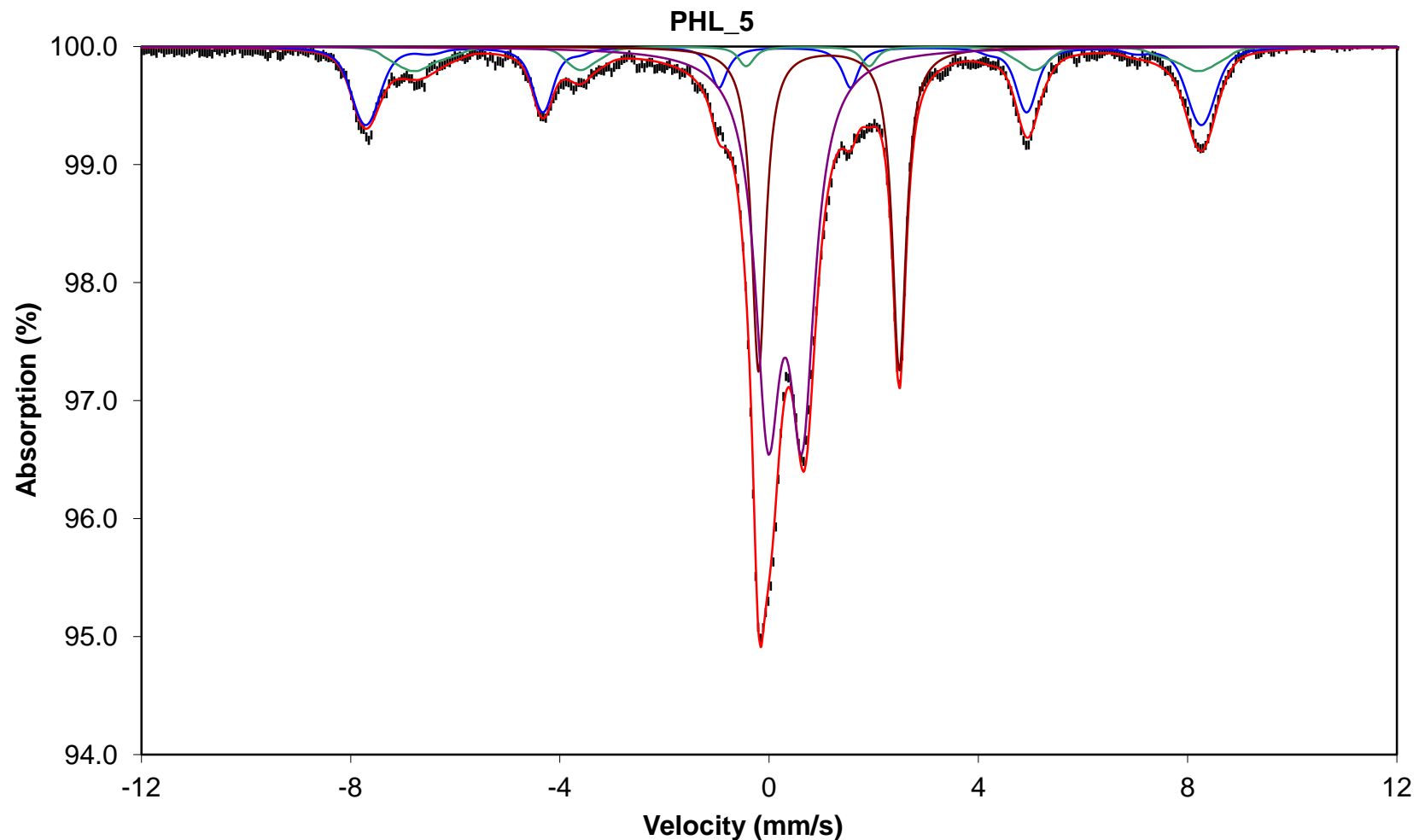
Figure 45. Mössbauer Spectroscopy PHL_5 plot. The data (black dots) were fit using the Ghent program to obtain a best fit curve (red) and Fe^{3+} (purple), Fe^{2+} (brown), and magnetite (blue and green) curves.

	HLSC_1	167_238	309_105_A	309_150	313_210	313_318	313_329	313_356	CROMO 2_1A	CROMO 2_2	CROMO 2_3A	CROMO 2_4A	PHL_1	PHL_2B	PHL_3	PHL_5
■ Magnetite	63	30	0	34	0	0	0	0	26	22	22	33	27	12	0	30
□ Ferrous (Fe(II))	23	30	70	50	65	51	58	46	38	50	49	35	31	34	35	24
▥ Ferric (Fe(III))	14	40	30	16	36	49	42	54	35	28	29	32	42	54	65	47
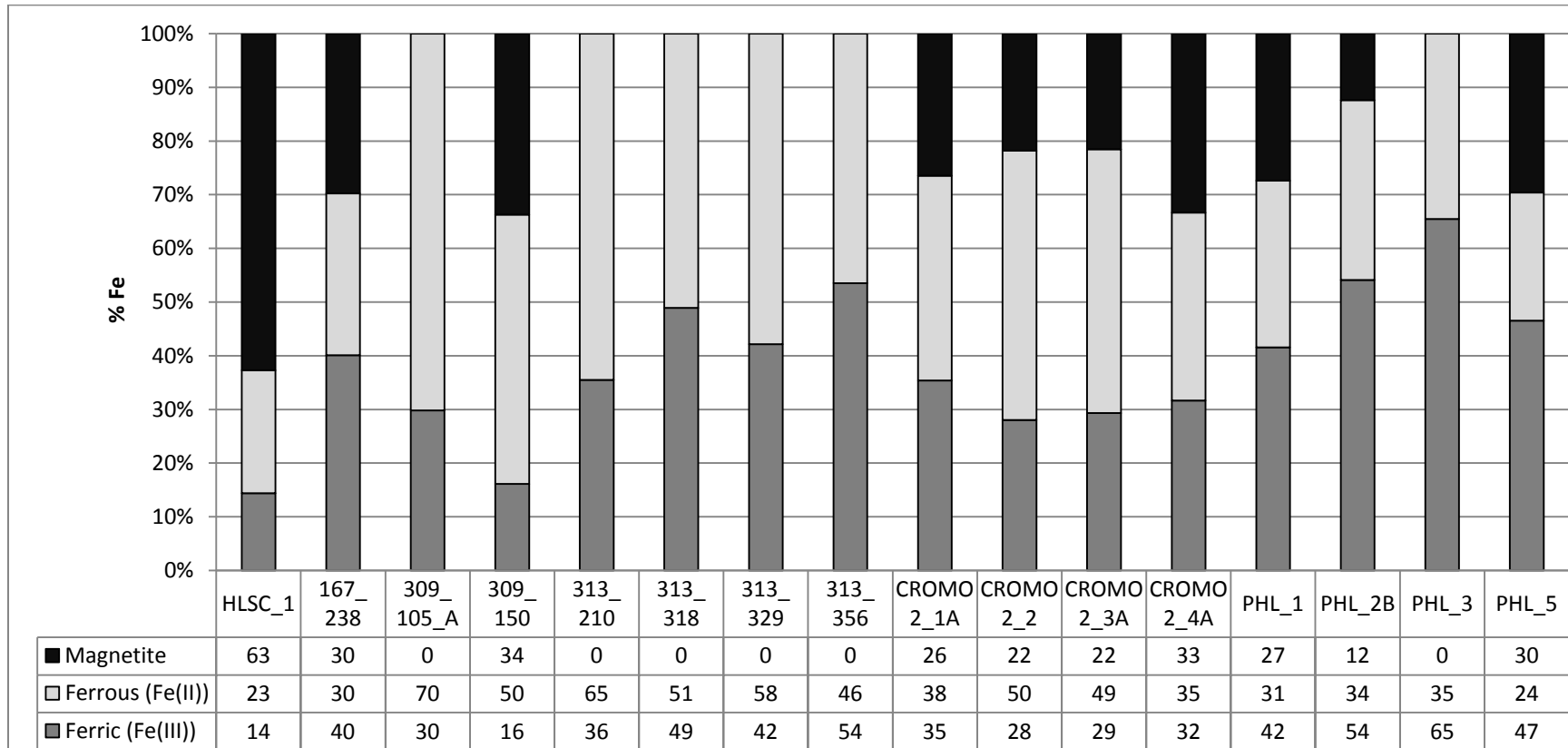
Figure 46. Percentages of Fe valence states for samples from CRO and ZO. The total area or the percentages of Fe valence states vary between ophiolites and between samples of the same ophiolite. %Fe^{2+} and %Fe^{3+} in mineral phases (serpentine, pyroxene, olivine, spinel) other than magnetite, and %magnetite.

	HLSC_1	167_238	309_105_A	309_150	313_210	313_318	313_329	313_356	CROMO 2_1A	CROMO 2_2	CROMO 2_3A	CROMO 2_4A	PHL_1	PHL_2B	PHL_3	PHL_5
▨ Total % Fe2+	44	40	70	61	65	51	58	46	47	57	56	46	40	38	35	34
■ Total % Fe3+	56	60	30	39	36	49	42	54	53	43	44	54	60	62	65	66
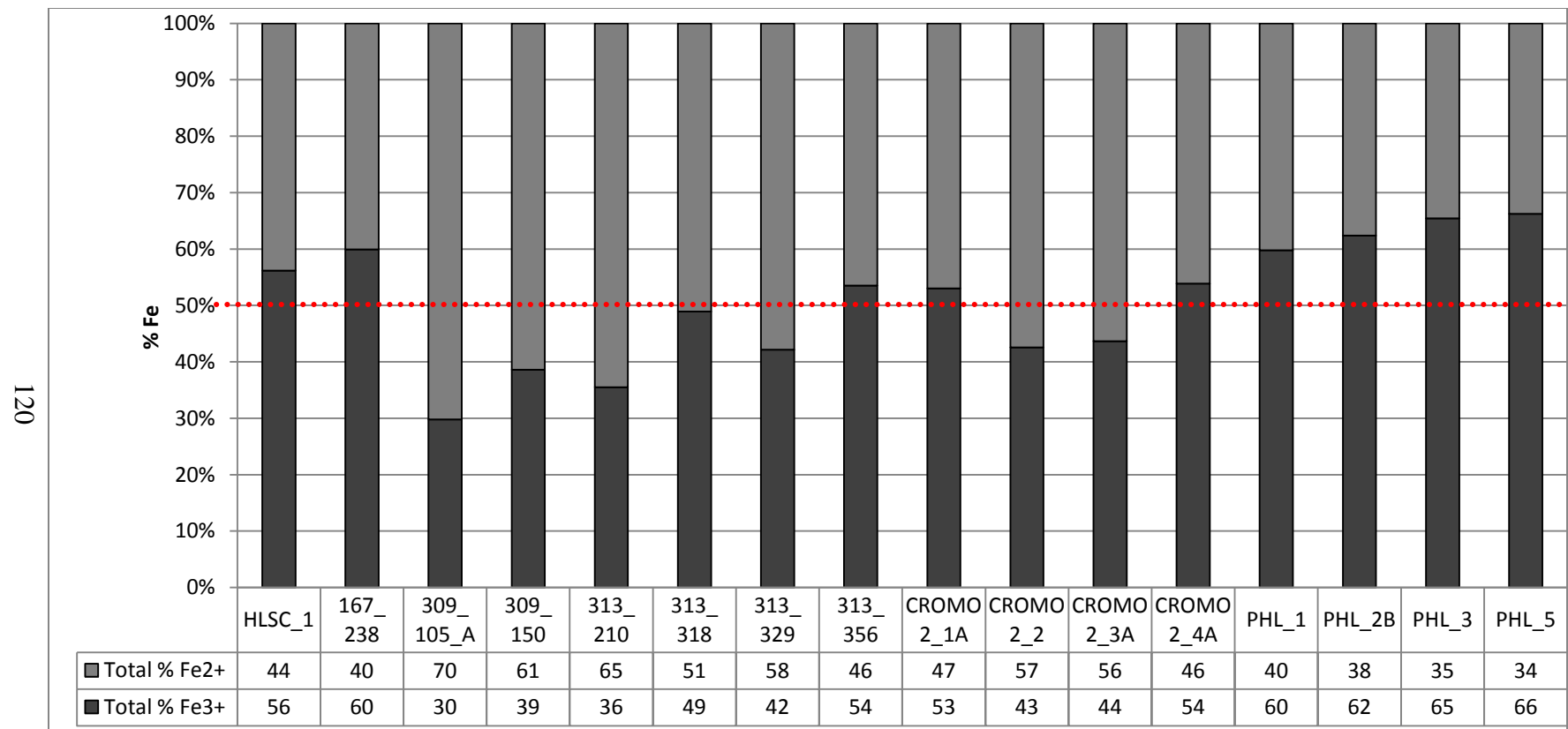
Figure 47. Total percent of Fe^{2+} and Fe^{3+} from MOSS and assuming magnetite is $Fe^{2+}Fe^{3+}_2O_4$. Total % Fe^{2+} in sample is calculated using (%Fe^{2+} + 1/3 magnetite) and total % Fe^{3+} in sample using (%Fe^{2+} + 2/3 magnetite).

	HLSC_1	167_238	309_105_A	309_150	313_210	313_318	313_329	313_356	CROMO 2_1A	CROMO 2_2	CROMO 2_3A	CROMO 2_4A	PHL_1	PHL_2B	PHL_3	PHL_5
☐ Ferrous (Fe(II))	61	43	70	76	65	51	58	46	52	64	63	53	43	38	35	34
■ Ferric (Fe(III))	39	57	30	24	36	49	42	54	48	36	37	47	57	62	65	66
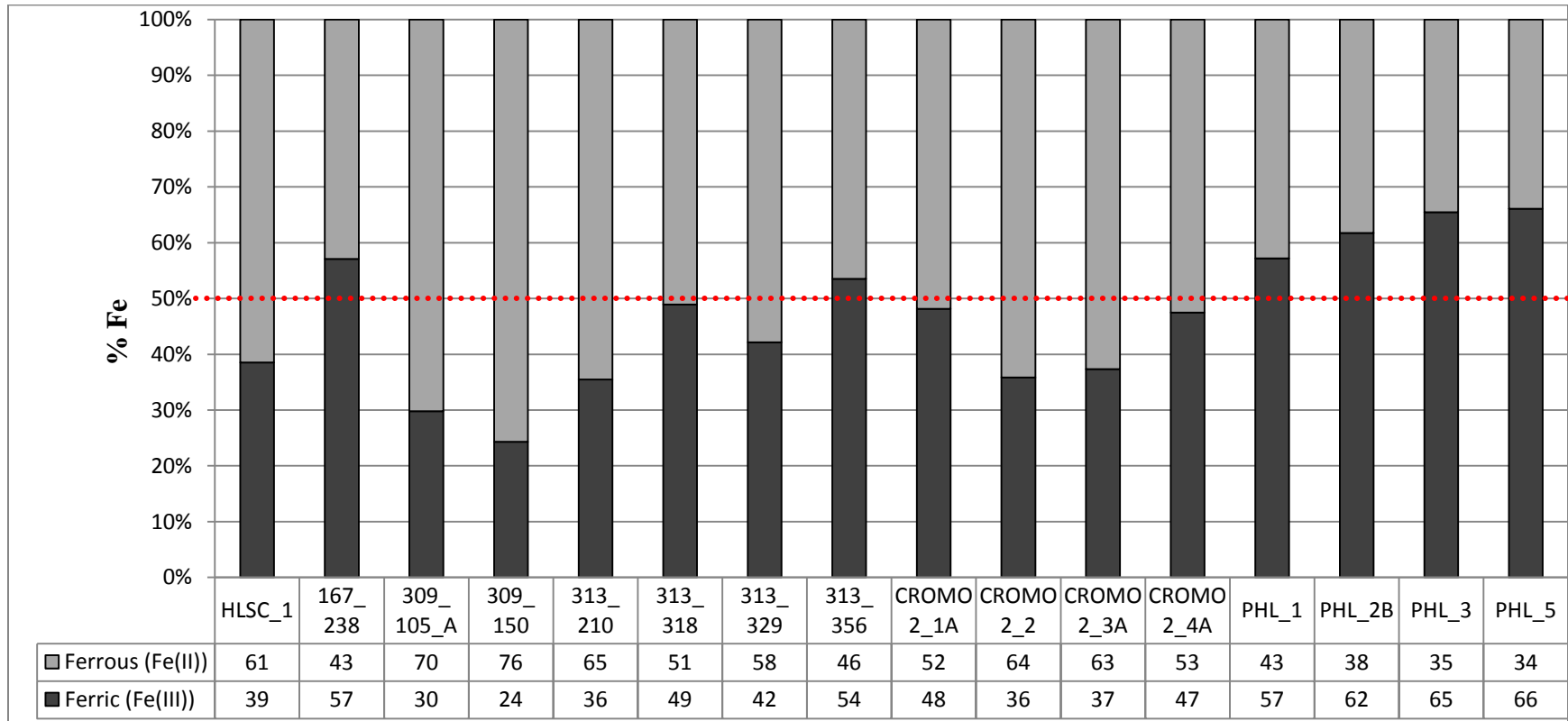
Figure 48. Total percent of Fe^{2+} and Fe^{3+} from MOSS in silicates (mostly serpentine but pyroxene, chlorite, etc…also may be represented) and factoring out magnetite.
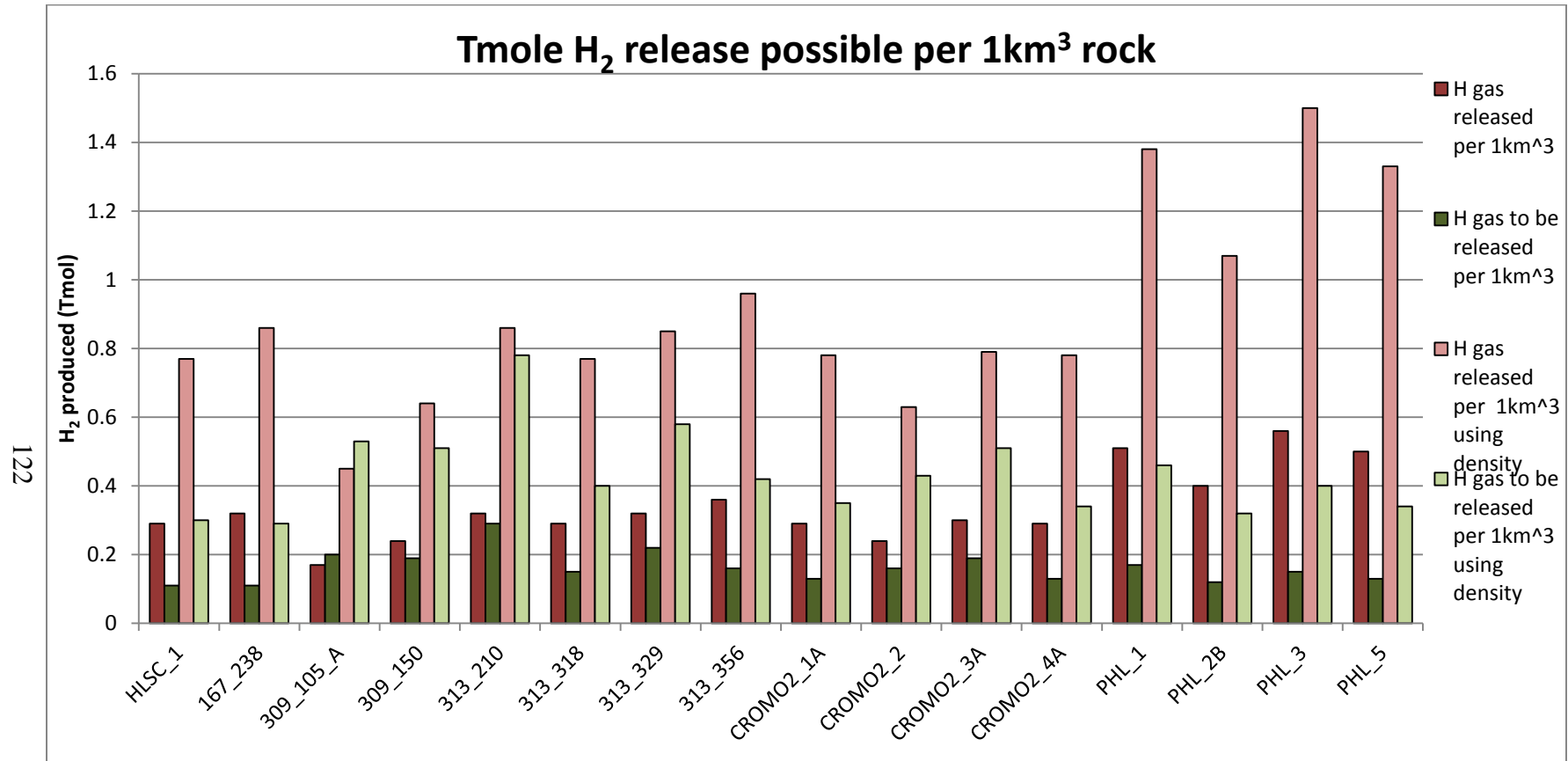
Figure 49. Possible hydrogen production normalized to a volume of one $1km^3$ of rock with the same compositions as each individual sample. This illustrates that even though the overall volume of the ZO is smaller, in general, it can produce more total hydrogen than the CRO based on the Fe concentration and the MOSS results. Red are calculated from the $\%Fe^{3+}$ assuming that H_2 was released as the Fe^{2+} was oxidized. Green are calculated from the $\%Fe^{2+}$ assuming that H_2 can be released as the Fe^{2+} is oxidized.
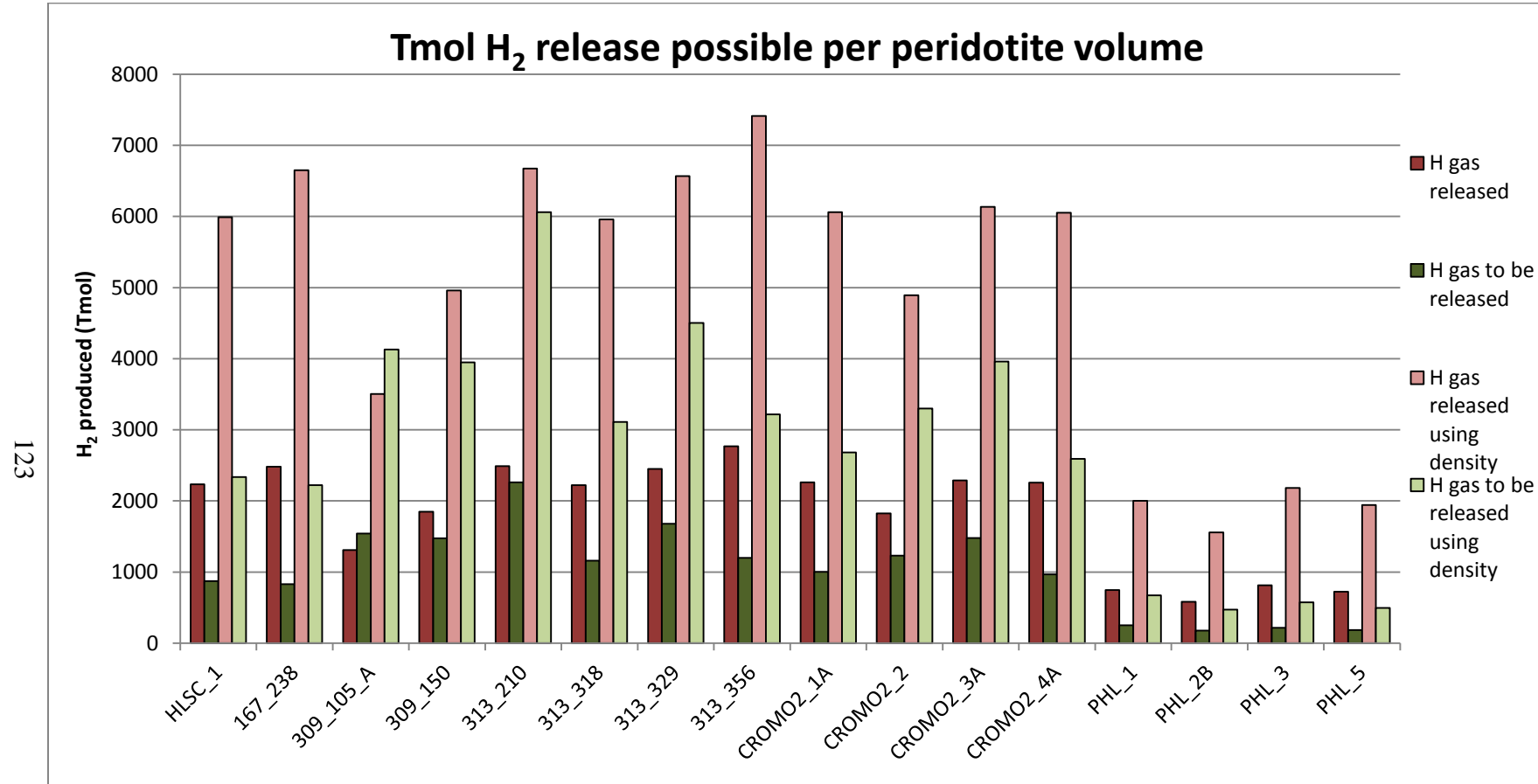
Figure 50. ZO and CRO calculated hydrogen generation in Tmoles (10^{12} = tera T) of H_{2g}. Red are calculated from the %Fe^{3+} assuming that H_2 was released as the Fe^{2+} was oxidized. Green are calculated from the %Fe^{2+} assuming that H_2 can be released as the Fe^{2+} is oxidized.
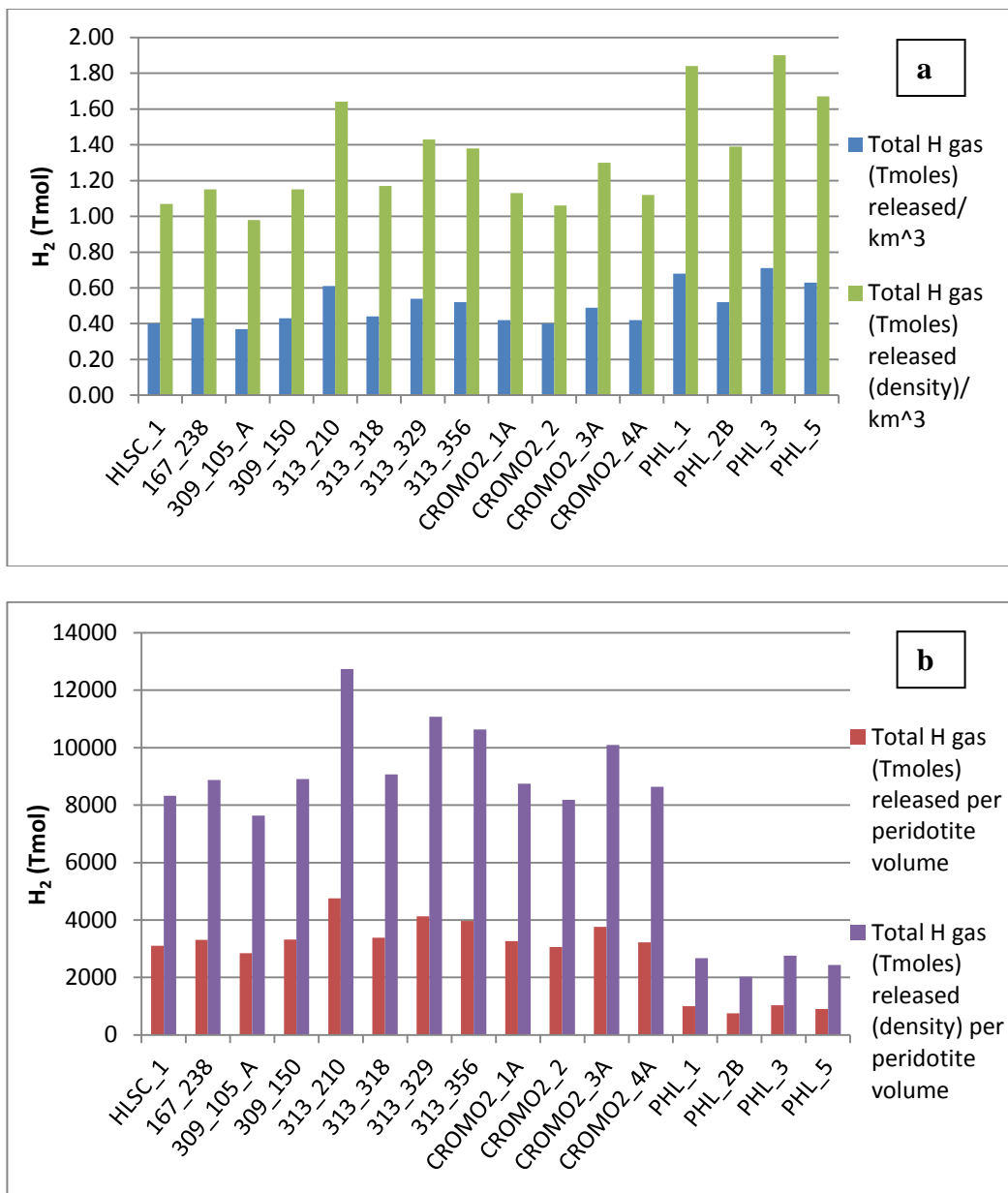
Figure 51. Total calculated hydrogen generation in Tmoles (10^{12} = tera T) of H_{2g} that could be released over the lifetime of the peridotite unit per km^3 (a) and for the whole peridotite unti (b). The total height of the bar (sum of both Fe^{3+} and Fe^{2+}) indicates the total amount of H_2 that could be released assuming that the whole volume of the peridotite unit of the ophiolite has the same composition as the individual sample.

APPENDICIES

Figure A1: Geologic map of the Coast Range Ophiolite and approximate location of sampling sites (stars). The peridotite unit, or ultramafic unit (um) is purple. Sample HLSC_1 is um float found in Kl (northern star). Image is taken from the California geologic map (http://www.quake.ca.gov/gmaps/GMC/stategeologicmap.html, September 2014).
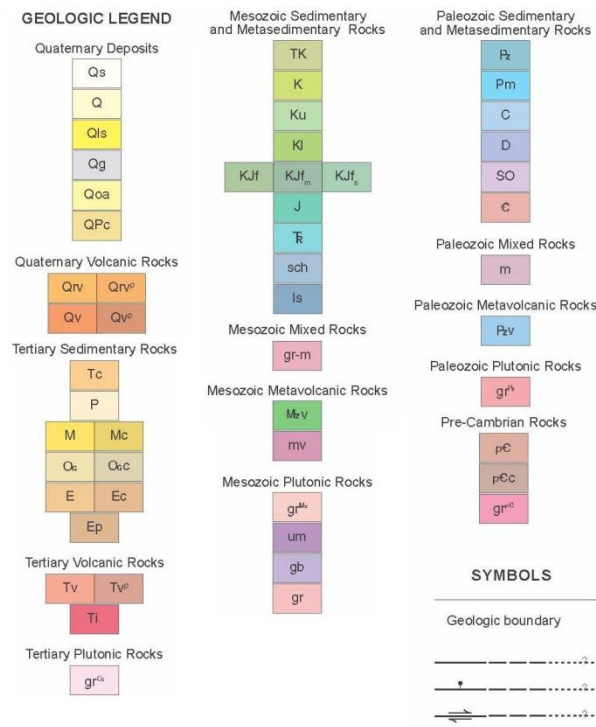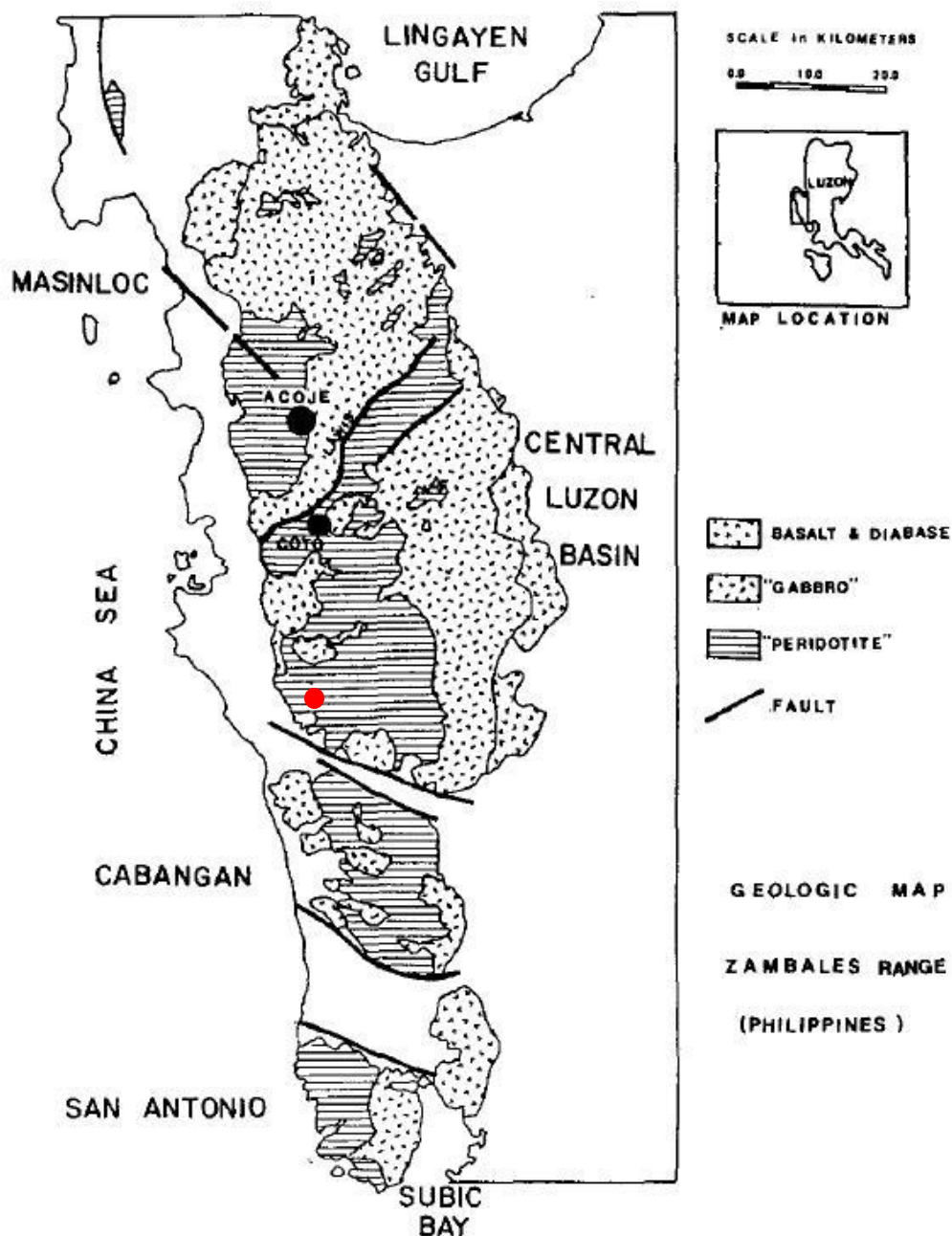
Figure A2: Regional geologic map of the Zambales Ophiolite taken from Abrajano and Pasteris [1989] showing the location of the Acoje massif. Approximate sampling location is indicated by a red dot. Black dots indicate the Acoje and Coto mines [Hawkins and Evan, 1983].

Table A1: Short literature review of microbiology of serpentinization sites, H_2, and additional references.

Location	Water source	Microbiology	Hydrogen in fluids	Source(s)
Lost City hydrothermal field on the Atlantis Massif near the Mid-Atlantic Ridge	White smokers; submarine seeps from fault-bounded peridotite	sulfur-cycling bacteria; methane-cycling archaea (Anaerobic methane-oxidizing *Archaea* (ANME-1); Methanosarcinales) and bacteria (methylobacter, methylophaga); H_2-utilizing and producing; aerobic carbon monoxide utilization and anaerobic carbon fixation	<14mmol/kg H_2; <1-2mmol/kg methane	Kelley *et al*., 2005; Kelley *et al*., 2007; Brazeton *et al*., 2006; Brazeton *et al*., 2012; Schrenk et al., 2004;
Tablelands ophiolite in Newfoundland	Ground water springs	H_2-utilizing and producing; aerobic carbon monoxide utilization and anaerobic carbon fixation	<~500μM H_2	Szponar *et al*., 2013; Brazeton *et al*., 2012

Additional references
Schrenk, Brazelton, and Lang [2013] have compiled types of analysis performed and characteristic Achaea found in both marine and terrestrial serpentinite habitats including Rainbow and Lost City hydrothermal fields, CRO, South Chamorro Seamount, Tablelands, and more.

Iron utilizing microorganisms: Chan *et al.* [2009], Iron oxyhydroxide mineralization on microbial extracellular polysaccharides*, Geochim. Cosmochim. Acta, 73*(13), 3807-3818.

Limiting factors on microbial life at depth: Hellevang *et al.* [2011], The potential for low-temperature abiotic hydrogen generation and a hydrogen-driven deep biosphere*, Astrobiology, 11*(7), 711-724.

Sleep *et al.* [2004], H_2-rich fluids from serpentinization: Geochemical and biotic implications*, Proc. Natl. Acad. Sci. U. S. A., 101*(35), 12818-12823.

McCollom and Seewald (2013), Serpentinites, hydrogen, and life*, Elements, 9*(2), 129-134.

Table A2: Mössbauer and wet chemistry %Fe^{3+}, and Fe concentrations from literature for fresh and serpentinized peridotites.

Site	Peridotite Type/ Geologic Setting/ Mineralogy	Fe conc. (ppm)	Fe^{3+} %Fe	Citation
Cassiar Serpentinite, North-central British Columbia	100% serpentinized harzburgite tectonite;	~13,400 - 25,000	22-88‡	O'Hanley and Dyar, 1993; O'Hanley and Dyar, 1998
United Mine Serpentinite, East-Central Ontario	100% serpentinized dunite cumulate from differentiated mafic-utlramafic sill		~88‡	O'Hanley and Dyar, 1993
Jeffery Serpentinite, Southeastern Quebec	Partially to completely serpentinized and recrystallized harzburgite tectonite; part of Ordovician ophiolite	~12,100 - 12,000	33-53‡	O'Hanley and Dyar, 1993; O'Hanley and Dyar, 1998
Woodsreef Serpentinite, Eastern New South Wales	Partially to completely serpentinized harzburgite tectonite	~17,200 – 29,000	40-72‡	O'Hanley and Dyar, 1993; O'Hanley and Dyar, 1998
ODP leg 125	40-100% serpentinized harzburgites and dunites; Marina Forarc; subduction zone forearc	~51,800 - 57,100	14-46‡	Klein *et al.*, 2013
ODP leg 153, MARK area	40-100% serpentinized harzburgites and dunites; mid-ocean ridge	~54,800 – 65,600	59-66‡	Klein *et al.*, 2013
ODP leg 153, MARK 7, bulk rock	50-100% serpentinized harzburgites	~54344	~69*	Andreani *et al.*, 2013B
MARK 7**	100% serpentinized harzburgites	~13059	~61†	Andreani *et al.*, 2013B
ODP leg 153, MARK 9, bulk rock	50-100% serpentinized harzburgites	~50917	~66*	Andreani *et al.*, 2013B
MARK 9**	100% serpentinized harzburgites	~11,300-15,400	54-100†	Andreani *et al.*, 2013B

Table A2: *Continued*

Site	Peridotite Type/ Geologic Setting/ Mineralogy	Fe conc. (ppm)	Fe^{3+} %Fe	Citation
ODP leg 153, MARK 11, bulk rock	50-100% serpentinized harzburgites	~58611	~34*	Andreani *et al.*, 2013B
MARK 11**	55-79 % serpentinized harzburgites	~31,900-42,700	58-63†	Andreani *et al.*, 2013B
ODP leg 153, MARK 24, bulk rock	50-100% serpentinized harzburgites	~59660	~42*	Andreani *et al.*, 2013B
MARK 24**	17-98% serpentinized harzburgites	~23,000-59,100	~4-77†	Andreani *et al.*, 2013B
ODP leg 173	40-100% serpentinized harzburgites and dunites; Iberia Margin; passive margin	~54,400 – 59,200	~58-63‡	Klein *et al.*, 2013
84-402	Spinel lherzolite from Porndon, Southeastern Australia	~60631	~2	Canil *et al.*, 1994
89-772	Dunite from Olmani Tanzania	~97164	~0	Canil *et al.*, 1994
89-680	Garnet harzburgite; Lashaine, Tanzania	~51303	~2	Canil *et al.*, 1994
89-719	Garnet harzburgite; Lashaine, Tanzania	~52857	~1	Canil *et al.*, 1994
89-773	Harzburgite; Olmani Tanzania	~46406	~1	Canil *et al.*, 1994
BD1201	Garnet lherzolite, coarse, Low T; Wesselton, Southern Africa	~52857	~3	Canil *et al.*, 1994
PHN5273	Garnet harzburgite, coarse, Low T; Premier, Southern Africa	~50525	~0	Canil *et al.*, 1994

Table A2: *Continued*

Site	Peridotite Type/ Geologic Setting/ Mineralogy	Fe conc. (ppm)	Fe^{3+} %Fe	Citation
FRB909	Garnet lherzolite, sheared, high T; Premier, Southern Africa	~62963	~2	Canil *et al.*, 1994
F865	Garnet harzburgite, coarse, Low T; Finsch, Southern Africa	~52857	~1	Canil *et al.*, 1994
F556	Garnet harzburgite, coarse, Low T; Finsch, Southern Africa	~71513	~2	Canil *et al.*, 1994
UV417/89	Garnet lherzolite, coarse, low T; Udachnaya, Siberia	~64517	~2	Canil *et al.*, 1994
Fr1	Spinel lherzolite; Landoz, Massif Central	~58765	~4	Canil *et al.*, 1994
Monte Fico North quarry	Recrystallized, granoblastic lizardite; Monte Fico, Island of Elba, Italy		~40	Fuch *et al.*, 1998
American-Antarctic Ridge	Spinels from abyssal spinel peridotites	~95800-114,000	~13-15	Bryndzia and Wood, 1990
South West Indian Ridge	Spinels from abyssal spinel peridotites	~85700-125,000	~5-15	Bryndzia and Wood, 1990
Mid-Atlantic Ridge	Spinels from abyssal spinel peridotites	~101,000-129,000	~11-22	Bryndzia and Wood, 1990
Mid Cayman Rift	Spinels from abyssal spinel peridotites	~94400-105,000	~9	Bryndzia and Wood, 1990
Central Indian Ridge	Spinels from abyssal spinel peridotites	~102,000-158,000	~11-25	Bryndzia and Wood, 1990

Table A2: *Continued*

Site	Peridotite Type/ Geologic Setting/ Mineralogy	Fe conc. (ppm)	Fe^{3+} %Fe	Citation
9 spinel separates	Spinel and garnet peridotite zenoliths in the Udachnaya kimerlite		~10-27	Goncharov *et al.*, 2012
28 garnet separates	Spinel and garnet peridotite zenoliths in the Udachnaya kimerlite		~2-19	Goncharov *et al.*, 2012
Mexico spinels	Spinel-peridotite xenoliths		~3-28	Peslier *et al.*, 2002
Simcoe, WA, USA spinels	Spinel-peridotite xenoliths		~27-39	Peslier *et al.*, 2002
Abyssal Serp, average 20 bulk samples	Dunite	~59870		Deschamps *et al.*, 2013
Abyssal Serp, average of 48 bulk samples	Harzburgite	~50428		Deschamps *et al.*, 2013
Mantle wedge, average of 88 bulk samples	Dunite	~52596		Deschamps *et al.*, 2013
Mantle wedge, average of 73 bulk samples	Harzburgite	~53505		Deschamps *et al.*, 2013
Subducted serp, average of 39 bulk samples	Dunite	~56163		Deschamps *et al.*, 2013
Subducted serp, average of 109 bulk samples	Harzburgite	~55463		Deschamps *et al.*, 2013

Mag= magnetite. ODP=Drilling Project. ‡Magnetite factored out as an impurity. *Obtained from titration of bulk samples.
**Measurements from veins, mesh rims and mesh cores. †μXANES measurements.

STANDARDS

Table A3: Normalized average Fe concentration converted to FeO wt%.

Sample name	Fe avg. normalized concentration (ppm)	Fe avg. normalized concentration (FeO wt%)
DTS-1	60710	7.81
DTS-2	41396	5.33
PCC-1	58759	7.56
XRF Empty sample holder	170	0.02

Table A4: Raw XRF elemental data for USGS standards—Mo, Zr, Sr, Rb, Th, Pb, Zn, Cu, Ni, Co, Fe, Mn, Cr, V, Ti, Sc, Ca, K.

SAMPLE	Type	Duration (s)	Units	Run	Mo	Mo Error	Zr	Zr Error
BCR-2	SOIL	201.41	ppm	1	163.11	7.43	210.17	11.02
BCR-2	SOIL	201.41	ppm	2	127.55	7.50	195.04	11.68
BCR-2	SOIL	201.77	ppm	3	175.62	8.02	233.21	12.05
BCR-2	SOIL	207.85	ppm	4	142.62	7.56	193.18	11.34
BCR-2	SOIL	204.05	ppm	5	141.53	7.74	208.14	11.89
BCR-2	SOIL	201.59	ppm	6	143.30	7.88	205.58	12.02
BHVO-2	SOIL	202.00	ppm	1	< LOD	7.11	215.17	11.57
BHVO-2	SOIL	201.95	ppm	2	< LOD	8.35	203.72	12.83
BHVO-2	SOIL	201.95	ppm	3	< LOD	8.19	200.48	12.78
BHVO-2	SOIL	201.89	ppm	4	< LOD	7.09	192.87	11.04
BHVO-2	SOIL	200.85	ppm	5	< LOD	7.22	197.42	11.36
BHVO-2	SOIL	201.26	ppm	6	< LOD	7.01	188.96	11.04
BIR-1	SOIL	201.33	ppm	1	< LOD	6.68	< LOD	8.56
BIR-1	SOIL	200.98	ppm	2	< LOD	7.12	12.49	6.41
BIR-1	SOIL	201.10	ppm	3	< LOD	6.92	< LOD	9.01
BIR-1	SOIL	201.10	ppm	4	< LOD	7.23	< LOD	9.40
BIR-1	SOIL	200.89	ppm	5	< LOD	7.23	< LOD	9.36
BIR-1	SOIL	201.13	ppm	6	< LOD	7.17	10.20	6.28
DTS-1	SOIL	200.88	ppm	1	< LOD	6.77	< LOD	6.56
DTS-1	SOIL	201.06	ppm	2	< LOD	6.18	< LOD	6.07
DTS-1	SOIL	201.19	ppm	3	< LOD	6.83	< LOD	6.27
DTS-1	SOIL	201.80	ppm	4	< LOD	6.47	< LOD	5.86
DTS-1	SOIL	201.06	ppm	5	< LOD	6.31	< LOD	6.11
DTS-1	SOIL	201.12	ppm	6	< LOD	6.26	< LOD	6.16
DTS-2	SOIL	201.90	ppm	1	< LOD	5.29	< LOD	5.12
DTS-2	SOIL	201.29	ppm	2	< LOD	5.69	< LOD	5.45
DTS-2	SOIL	201.18	ppm	3	< LOD	5.49	< LOD	5.16
DTS-2	SOIL	200.85	ppm	4	< LOD	5.89	< LOD	5.49
DTS-2	SOIL	210.19	ppm	5	< LOD	5.59	< LOD	5.18
DTS-2	SOIL	201.08	ppm	6	< LOD	5.92	< LOD	5.62
PCC-1	SOIL	201.24	ppm	1	< LOD	5.44	< LOD	5.20
PCC-1	SOIL	200.72	ppm	2	< LOD	7.73	< LOD	7.99
PCC-1	SOIL	201.87	ppm	3	< LOD	5.62	< LOD	5.15
PCC-1	SOIL	200.90	ppm	4	< LOD	6.96	< LOD	6.80
PCC-1	SOIL	201.37	ppm	5	< LOD	6.90	< LOD	6.74
PCC-1	SOIL	200.72	ppm	6	< LOD	7.01	< LOD	6.87

Table A4: *continued*

SAMPLE	Sr	Sr Error	Rb	Rb Error	Th	Th Error	Pb	Pb Error
BCR-2	352.95	11.09	45.89	5.02	< LOD	8.74	15.87	7.62
BCR-2	355.72	12.04	45.45	5.43	10.56	6.58	17.59	8.62
BCR-2	379.48	12.07	50.16	5.51	< LOD	8.72	17.87	8.36
BCR-2	346.74	11.60	43.14	5.26	10.15	6.43	24.58	8.95
BCR-2	348.12	11.91	35.33	5.05	12.49	6.75	21.56	9.06
BCR-2	349.85	12.12	43.06	5.39	< LOD	9.49	19.43	8.96
BHVO-2	433.20	12.51	7.85	3.06	< LOD	7.38	< LOD	10.63
BHVO-2	447.31	14.17	9.80	3.78	11.29	6.79	< LOD	12.28
BHVO-2	442.44	14.14	7.45	3.73	< LOD	9.45	< LOD	12.35
BHVO-2	408.74	12.06	7.31	3.21	< LOD	7.55	< LOD	9.94
BHVO-2	421.17	12.46	10.39	3.41	< LOD	8.05	< LOD	11.06
BHVO-2	403.35	12.07	5.83	3.08	< LOD	7.96	< LOD	9.70
BIR-1	108.25	6.66	< LOD	3.58	< LOD	7.93	< LOD	10.96
BIR-1	123.61	7.46	< LOD	3.88	< LOD	7.71	14.34	8.09
BIR-1	116.95	7.08	< LOD	3.63	< LOD	7.73	< LOD	11.12
BIR-1	128.61	7.58	< LOD	3.90	< LOD	7.42	19.14	8.41
BIR-1	127.05	7.51	< LOD	4.05	< LOD	7.56	< LOD	10.98
BIR-1	121.85	7.36	< LOD	3.66	< LOD	7.35	< LOD	11.59
DTS-1	< LOD	3.33	< LOD	3.19	< LOD	7.28	22.68	8.23
DTS-1	< LOD	3.01	< LOD	3.05	< LOD	6.91	14.85	7.01
DTS-1	< LOD	3.37	< LOD	3.41	< LOD	6.82	21.91	8.02
DTS-1	< LOD	3.22	< LOD	2.89	< LOD	5.88	12.91	6.96
DTS-1	< LOD	3.12	< LOD	2.92	< LOD	6.54	< LOD	9.71
DTS-1	< LOD	3.07	< LOD	2.97	< LOD	6.77	14.41	7.05
DTS-2	< LOD	2.53	< LOD	2.62	< LOD	5.81	< LOD	8.31
DTS-2	< LOD	2.82	< LOD	2.71	< LOD	6.27	< LOD	8.36
DTS-2	< LOD	2.51	< LOD	2.41	< LOD	5.19	< LOD	7.81
DTS-2	< LOD	2.89	< LOD	2.92	< LOD	5.89	< LOD	9.06
DTS-2	< LOD	2.78	< LOD	2.50	< LOD	6.03	8.85	5.84
DTS-2	< LOD	2.86	< LOD	2.91	< LOD	5.78	< LOD	8.90
PCC-1	< LOD	2.70	< LOD	2.56	< LOD	6.06	14.76	6.25
PCC-1	< LOD	4.16	< LOD	3.61	< LOD	8.45	< LOD	12.54
PCC-1	< LOD	2.72	< LOD	2.44	< LOD	5.31	15.95	6.25
PCC-1	< LOD	3.40	< LOD	3.31	< LOD	7.48	11.73	7.31
PCC-1	< LOD	3.46	< LOD	3.44	< LOD	7.64	11.29	7.36
PCC-1	< LOD	3.21	< LOD	3.62	< LOD	7.71	26.59	8.70

Table A4: *continued*

SAMPLE	Zn	Zn Error	Cu	Cu Error	Ni	Ni Error	Co	Co Error
BCR-2	82.96	21.04	< LOD	37.90	< LOD	79.20	< LOD	387.80
BCR-2	92.26	23.79	< LOD	44.96	< LOD	90.20	< LOD	444.58
BCR-2	93.07	22.81	< LOD	43.56	< LOD	86.00	< LOD	423.38
BCR-2	91.64	23.81	< LOD	46.31	< LOD	84.90	< LOD	443.12
BCR-2	103.66	24.52	< LOD	45.46	< LOD	90.35	< LOD	448.93
BCR-2	81.80	23.97	< LOD	45.05	< LOD	90.68	< LOD	458.09
BHVO-2	81.85	21.24	132.61	35.13	< LOD	85.02	< LOD	372.17
BHVO-2	66.59	24.08	125.11	41.97	139.78	74.87	< LOD	466.87
BHVO-2	104.21	26.40	142.90	42.71	< LOD	105.95	< LOD	464.04
BHVO-2	60.65	19.79	57.64	31.56	< LOD	88.23	< LOD	371.92
BHVO-2	64.21	20.43	111.00	34.56	< LOD	87.69	< LOD	381.10
BHVO-2	58.86	20.01	112.45	34.20	< LOD	88.96	< LOD	374.23
BIR-1	32.38	18.50	128.31	36.25	125.96	62.73	< LOD	369.37
BIR-1	< LOD	29.82	147.63	40.33	175.56	70.15	< LOD	410.78
BIR-1	38.68	19.53	121.71	37.36	167.08	65.73	< LOD	383.69
BIR-1	< LOD	29.23	117.33	38.63	< LOD	100.06	< LOD	410.21
BIR-1	49.35	21.36	121.62	38.85	164.54	68.58	< LOD	406.36
BIR-1	37.99	20.81	105.08	38.27	199.97	69.50	< LOD	404.38
DTS-1	< LOD	25.64	< LOD	54.95	4146.43	150.38	475.82	248.05
DTS-1	< LOD	22.06	< LOD	46.85	3651.22	132.19	< LOD	326.74
DTS-1	< LOD	26.50	< LOD	53.70	4282.54	153.40	< LOD	377.08
DTS-1	30.40	16.85	< LOD	51.49	3795.93	137.28	434.34	227.00
DTS-1	< LOD	23.48	< LOD	49.50	3668.76	135.22	359.13	226.72
DTS-1	< LOD	25.13	< LOD	49.79	3687.61	135.10	< LOD	336.68
DTS-2	< LOD	19.19	< LOD	42.75	4716.41	131.07	< LOD	242.14
DTS-2	< LOD	21.42	< LOD	48.84	5379.99	148.73	< LOD	276.93
DTS-2	< LOD	19.16	< LOD	44.67	4805.85	133.99	< LOD	247.15
DTS-2	< LOD	21.72	< LOD	51.09	5522.56	153.54	400.32	191.01
DTS-2	25.48	14.37	< LOD	47.83	5411.46	143.44	389.15	179.57
DTS-2	27.14	15.38	< LOD	50.52	5605.10	153.74	< LOD	284.56
PCC-1	< LOD	19.84	< LOD	41.47	3144.28	112.68	388.91	181.99
PCC-1	< LOD	33.01	< LOD	68.72	5481.92	194.52	< LOD	458.34
PCC-1	< LOD	19.63	< LOD	40.39	3025.99	109.50	< LOD	266.63
PCC-1	< LOD	27.57	< LOD	56.97	4565.26	162.60	< LOD	390.11
PCC-1	< LOD	26.89	< LOD	61.33	4619.18	162.94	< LOD	390.08
PCC-1	< LOD	27.71	< LOD	59.14	4551.79	163.12	< LOD	393.04

Table A4: *continued*

SAMPLE	Fe	Fe Error	Mn	Mn Error	Cr	Cr Error	V	V Error
BCR-2	118422.48	902.64	1810.10	173.09	< LOD	44.35	385.33	84.37
BCR-2	134716.19	1040.08	2087.95	199.76	< LOD	40.39	372.72	76.74
BCR-2	128138.24	986.22	2299.80	200.45	< LOD	42.31	373.39	81.17
BCR-2	138761.06	1029.92	2411.87	205.95	< LOD	41.20	305.31	78.75
BCR-2	138442.64	1054.00	2503.39	214.18	< LOD	40.92	343.15	78.53
BCR-2	139390.48	1073.77	2441.34	215.53	< LOD	41.91	382.65	78.47
BHVO-2	105403.20	870.43	1590.76	168.56	195.31	30.48	324.85	75.21
BHVO-2	132517.16	1087.61	2150.53	215.56	227.56	31.61	231.66	77.38
BHVO-2	131647.09	1087.53	2266.48	219.06	204.84	30.44	277.31	74.30
BHVO-2	105036.20	861.68	1787.37	174.30	220.24	31.74	226.50	76.97
BHVO-2	106298.99	882.36	1628.76	171.90	213.18	31.62	279.84	77.30
BHVO-2	104927.68	867.36	1825.57	176.00	220.57	31.52	352.46	77.30
BIR-1	98982.34	858.50	1919.08	182.26	240.77	29.03	244.71	50.12
BIR-1	110751.69	958.69	2087.59	201.06	255.49	29.19	225.61	50.03
BIR-1	103446.48	900.34	1897.47	187.17	263.62	29.04	192.86	48.82
BIR-1	109882.01	951.75	2029.93	197.53	206.54	28.32	260.58	50.64
BIR-1	110774.65	952.85	1937.77	194.13	265.55	29.53	214.23	49.57
BIR-1	110449.42	952.44	1959.26	195.61	211.18	28.53	253.55	51.06
DTS-1	102595.43	857.46	1731.42	205.56	3528.99	71.97	< LOD	44.92
DTS-1	91365.79	758.47	1683.11	184.24	3584.77	72.66	< LOD	44.66
DTS-1	107422.77	885.72	1908.17	214.26	3695.75	73.41	< LOD	45.15
DTS-1	94530.18	784.71	1577.97	186.17	3557.05	72.22	< LOD	45.30
DTS-1	94878.32	786.38	1735.92	190.35	3445.07	71.32	< LOD	46.29
DTS-1	94693.48	785.56	1711.26	189.53	3461.89	72.12	< LOD	45.08
DTS-2	61917.10	559.98	1118.93	197.26	14467.74	138.63	< LOD	45.93
DTS-2	71787.61	641.33	1073.31	220.55	14141.71	136.65	< LOD	47.42
DTS-2	63397.38	574.63	1262.48	204.84	14683.96	139.97	< LOD	50.03
DTS-2	72855.77	657.59	1502.78	233.74	13919.52	135.79	< LOD	47.13
DTS-2	72427.46	618.50	1423.95	216.76	13848.33	133.45	< LOD	46.14
DTS-2	73922.34	659.74	1242.54	227.31	13853.78	135.77	< LOD	46.97
PCC-1	74439.40	627.28	1347.29	145.93	2538.99	62.65	51.34	30.53
PCC-1	126578.55	1084.25	2381.20	252.56	2557.21	61.27	64.58	30.15
PCC-1	73596.48	618.22	1332.83	143.42	2449.48	61.38	< LOD	43.29
PCC-1	108575.68	915.84	1777.29	206.35	2448.98	59.57	< LOD	42.22
PCC-1	108789.84	913.47	1930.45	210.22	2497.66	60.56	< LOD	45.01
PCC-1	108119.17	916.32	1867.04	209.94	2452.03	60.07	< LOD	44.92

Table A4: *continued*

SAMPLE	Ti	Ti Error	Sc	Sc Error	Ca	Ca Error	K	K Error
BCR-2	11454.68	246.05	79.51	35.53	37052.39	570.29	12599.45	497.13
BCR-2	10481.78	224.12	79.29	34.28	37466.61	551.76	12507.76	477.42
BCR-2	11586.90	238.82	69.71	34.86	37771.21	563.19	12923.05	492.12
BCR-2	10513.73	230.70	< LOD	50.42	37284.17	555.15	12632.83	483.29
BCR-2	10420.38	228.46	< LOD	50.74	37214.88	552.07	13510.72	494.64
BCR-2	10511.71	227.88	< LOD	50.47	37436.92	557.63	12967.36	489.85
BHVO-2	11557.15	226.36	84.89	42.32	63066.06	691.18	3664.64	309.37
BHVO-2	11970.98	236.56	77.35	42.96	62741.05	702.75	3769.00	318.08
BHVO-2	11574.00	226.30	88.18	42.43	62904.45	692.43	3674.35	310.63
BHVO-2	11992.14	236.50	69.50	43.28	63116.95	709.81	3649.93	317.35
BHVO-2	11935.86	234.86	< LOD	64.22	63156.02	706.53	3434.22	310.36
BHVO-2	11892.21	231.98	93.98	43.03	63540.17	701.10	3741.23	315.08
BIR-1	3811.98	137.51	122.61	44.10	74997.05	719.07	326.24	208.31
BIR-1	3966.46	138.96	104.85	43.84	74882.21	717.79	< LOD	306.93
BIR-1	3810.69	136.31	70.54	43.29	75768.41	715.25	< LOD	304.81
BIR-1	3912.17	138.10	< LOD	65.48	76268.52	724.19	< LOD	307.04
BIR-1	3759.29	137.47	115.70	44.54	76237.20	727.94	413.64	213.32
BIR-1	3757.72	138.71	79.01	44.12	76339.86	727.51	< LOD	307.53
DTS-1	< LOD	101.21	< LOD	14.48	297.37	111.94	267.11	142.80
DTS-1	< LOD	102.71	< LOD	14.39	487.19	117.99	< LOD	204.12
DTS-1	< LOD	97.98	< LOD	14.29	435.33	115.78	< LOD	210.23
DTS-1	< LOD	97.50	< LOD	13.66	344.30	113.23	< LOD	206.72
DTS-1	< LOD	101.80	< LOD	13.27	333.95	112.92	< LOD	206.81
DTS-1	< LOD	97.68	< LOD	13.92	348.65	114.32	< LOD	204.26
DTS-2	< LOD	102.33	< LOD	14.94	261.46	112.62	288.59	145.97
DTS-2	< LOD	105.37	< LOD	13.80	356.81	115.38	287.72	145.60
DTS-2	< LOD	112.71	< LOD	13.92	232.34	112.22	228.91	143.60
DTS-2	< LOD	105.10	< LOD	13.71	256.19	111.74	< LOD	208.96
DTS-2	< LOD	102.71	< LOD	13.20	342.70	112.79	< LOD	206.57
DTS-2	< LOD	102.37	< LOD	13.14	279.83	112.75	239.43	143.54
PCC-1	< LOD	96.98	< LOD	18.18	2990.79	177.43	< LOD	211.66
PCC-1	< LOD	94.68	< LOD	18.26	2973.70	172.99	< LOD	207.11
PCC-1	< LOD	96.09	19.29	12.58	2676.08	169.63	< LOD	195.55
PCC-1	93.65	60.84	< LOD	17.45	2648.24	164.48	207.24	137.44
PCC-1	< LOD	97.38	< LOD	17.56	2693.53	166.45	< LOD	195.50
PCC-1	< LOD	96.57	< LOD	17.04	2771.80	168.21	< LOD	207.31

The first 4 runs were shaken between each run and used to gauge accuracy. The last 3 runs (4-6) were not shaken between each run and used to gauge precision.
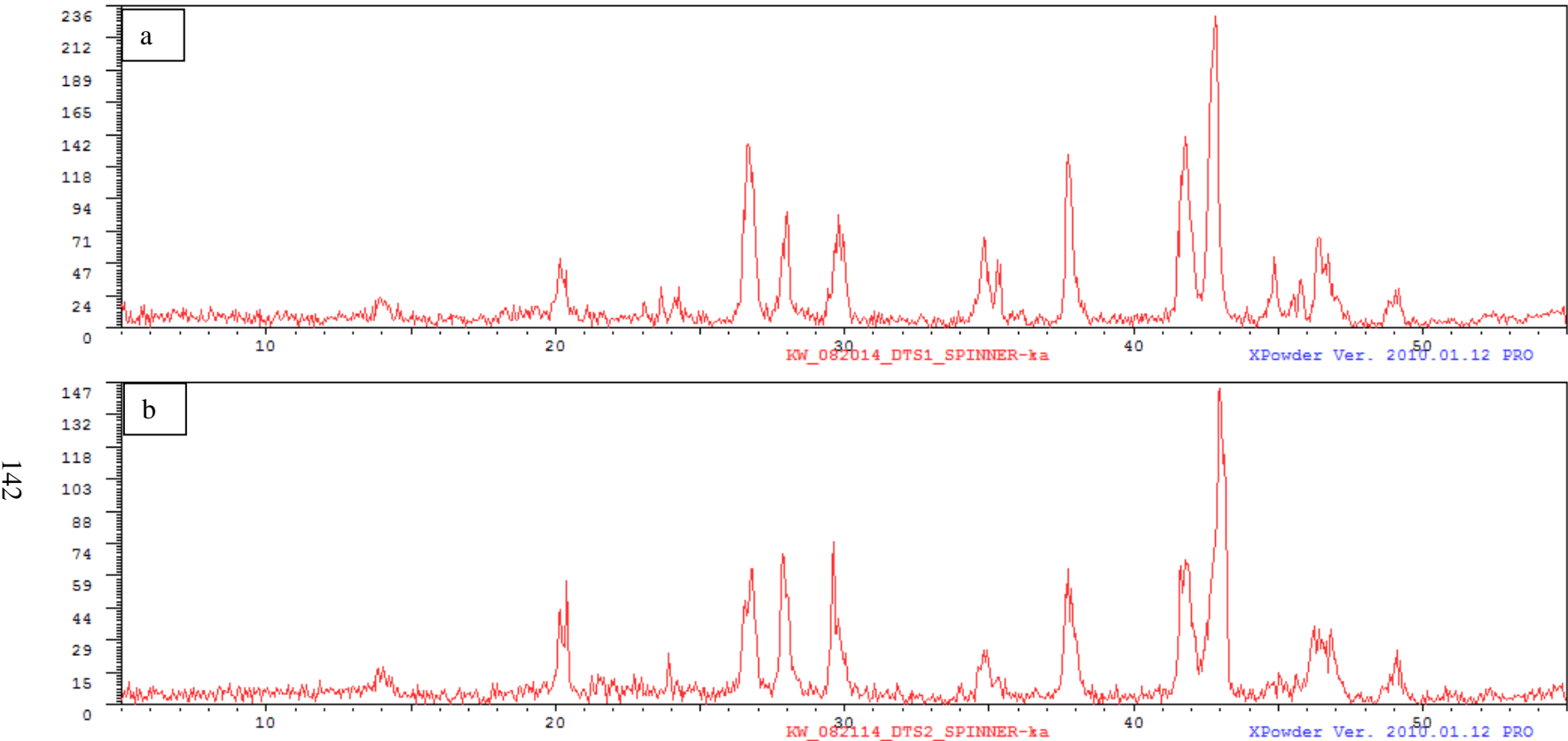
Figure A3: XRD diffractograms for USGS rock standards DTS-1 (a) and DTS-2 (b).
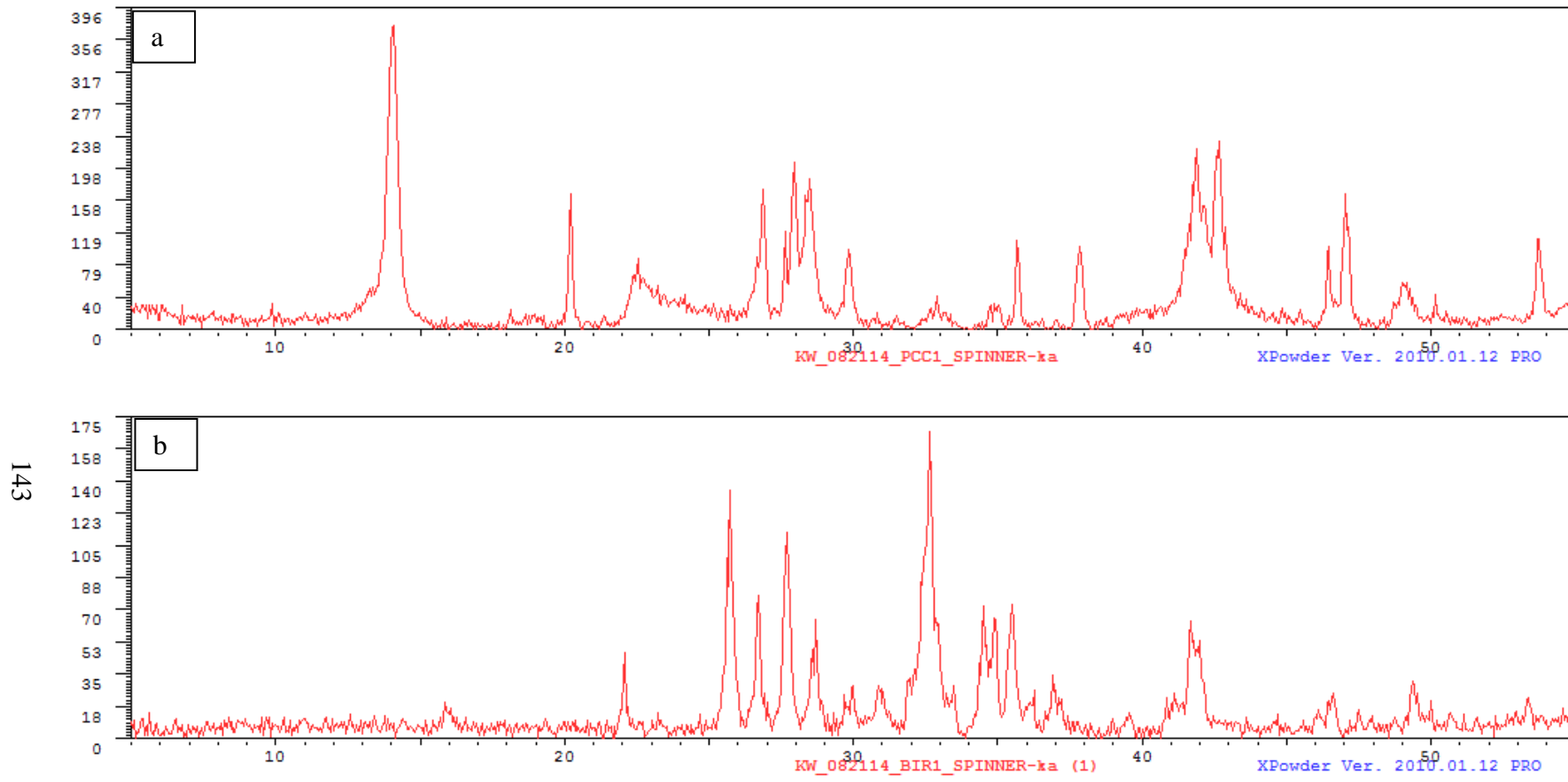
Figure A4: XRD diffractograms for USGS rock standards PCC-1 (a) and BIR-1 (b).
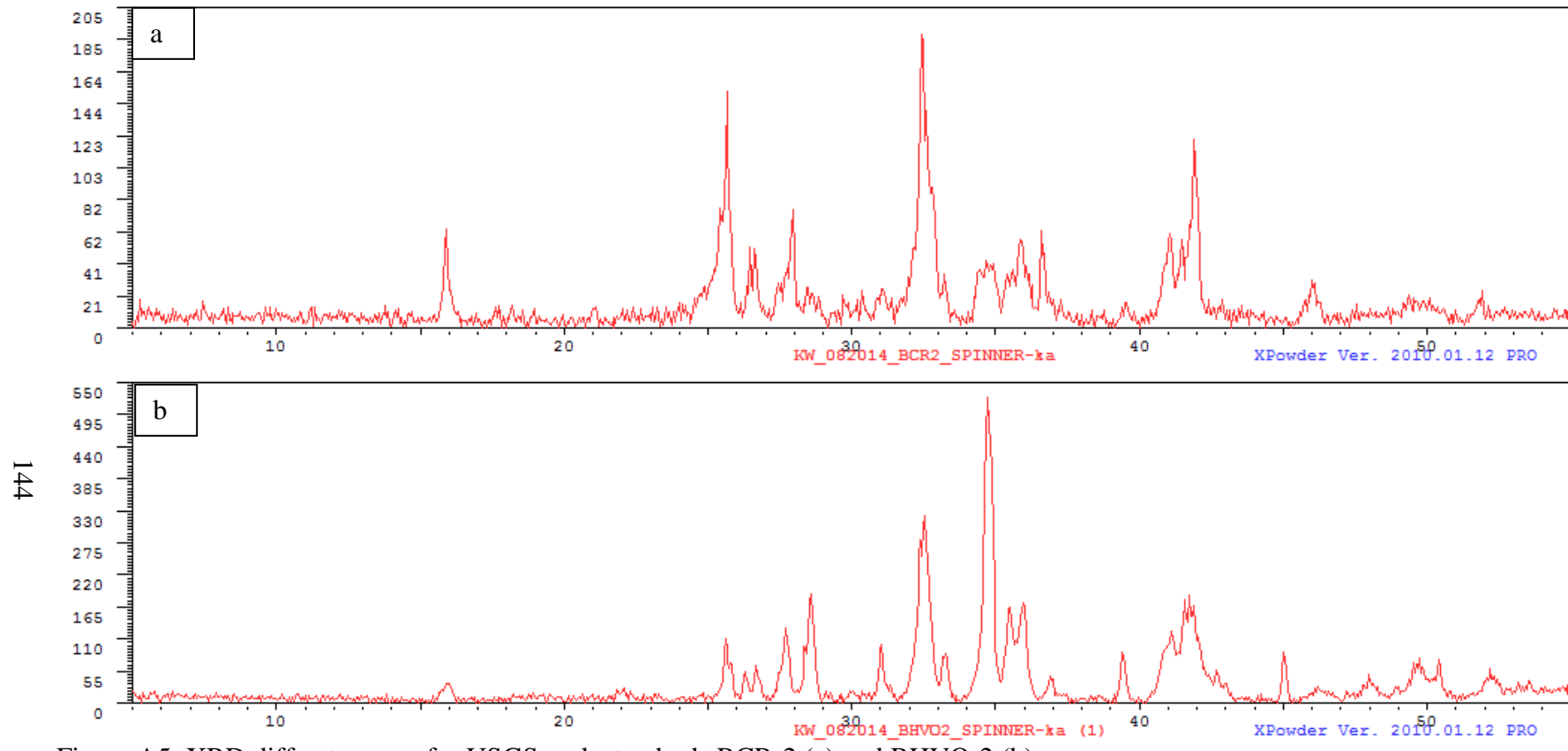
Figure A5: XRD diffractograms for USGS rock standards BCR-2 (a) and BHVO-2 (b).

SAMPLES

Table A5: Full sample names and shortened name.

SAMPLE	Sample short name
HLSC_1_A	HLSC_1
HLSC_4	HLSC_4
McL_81-167_238 to EOH_B22_B	167_238
McL_M81-309_84_B8_A1	309_84
McL_M81-309_105_B11_B1	309_105_A
McL_M81-309_105_B11_B2	309_105_B
McL_M81-309_150_B15_A	309_150
McL_M81-313_210_B22_A3	313_210
McL_M81-313_318_B34_B	313_318
McL_M81-313_329	313_329
McL_M81-313_356-356.6_B38_B	313_356
CSW1_27/28_SHOE?_A*	CROMO1_1_A
CSW1_27/28_SHOE?_B*	CROMO1_1_B
CSW1_28a_CLAY_A*	CROMO1_2_AA
CSW1_28a_CLAY_B*	CROMO1_2_AB
CSW1_28a_hard	CROMO1_2_AC
CSW1_28c_A*	CROMO1_2_CA
CSW1_28c_B*	CROMO1_2_CB
MLC_QV1_140_M-BMIX_A*	CROMO2_1A
MLC_QV1_140_M-BMIX_B*	CROMO2_1B
MLC_QV1_140_Mdkgrn	CROMO2_2
MLC_QV1_140_SERPMUD_A*	CROMO2_3A
MLC_QV1_140_SERPMUD_B*	CROMO2_3B
MLC_QV2_140_SHOE_A*	CROMO2_4A
MLC_QV2_140_SHOE_B*	CROMO2_4B
PHL_PB_1_BULK	PHL_1
PHL_PB_2_GRN_BULK	PHL_2A
PHL_PB_2_MIX_BULK	PHL_2B
PHL_PB_2_RED_BULK	PHL_2C
PHL_PB_3_BULK	PHL_3
PHL_PB_4_BULK	PHL_4
PHL_PB_5_BULK	PHL_5
Empty sample holder	ESH
Body of thesis/ main samples	Appendix/ additional samples

* 'A' samples are the harder residue left after vibrating the samples in water; 'B' samples are the clay minerals suspended in the water during vibration. Both A and B samples were oven-dried at 60°C.
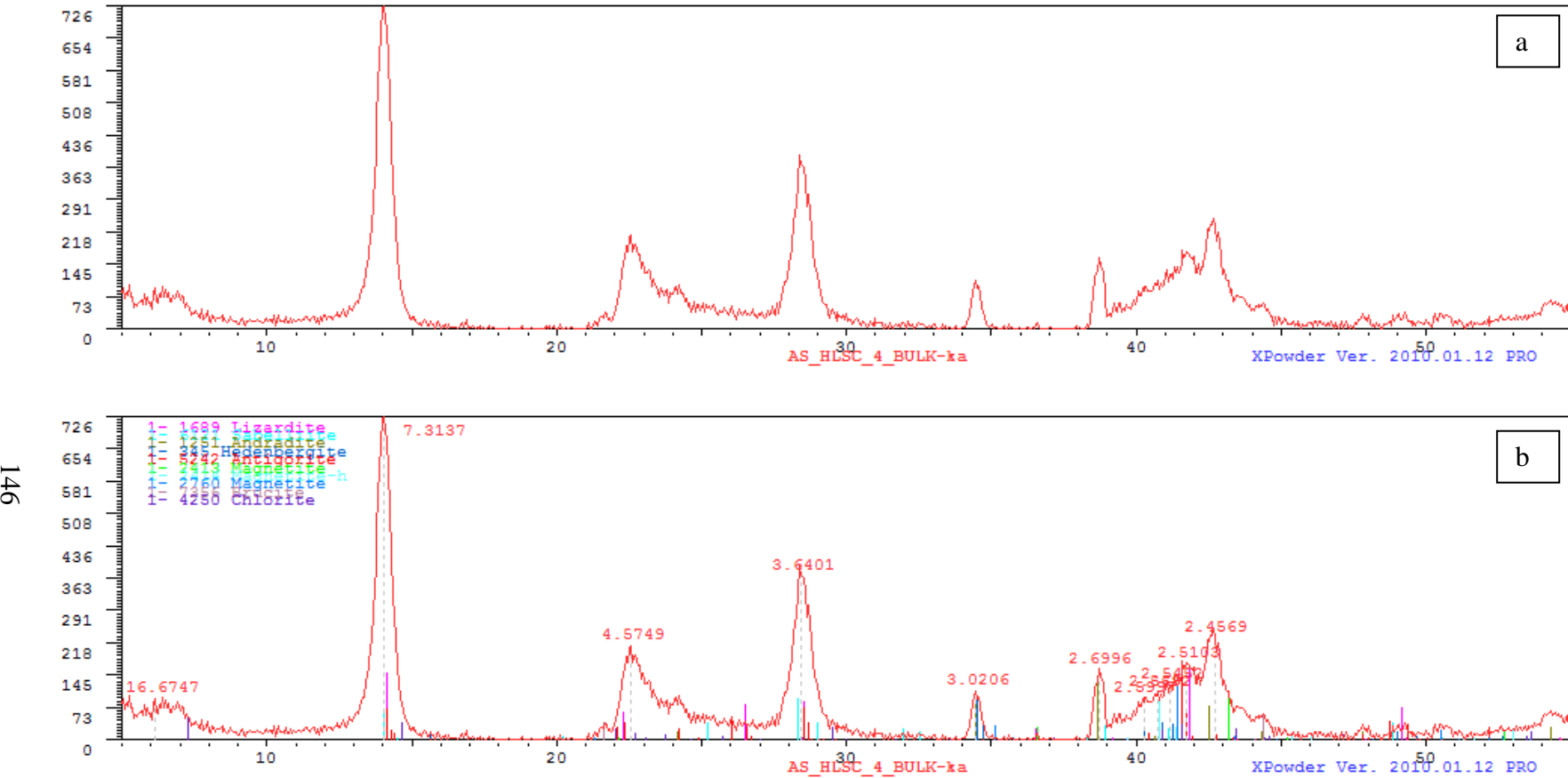
Figure A6: XRD diffractograms for sample HLSC_4 (a) with background subtracted and (b) peak d-spacing numbers and mineral diffraction patterns identified (serpentine, garnet, magnetite/spinel, chlorite, and possibly brucite) using XPowder.
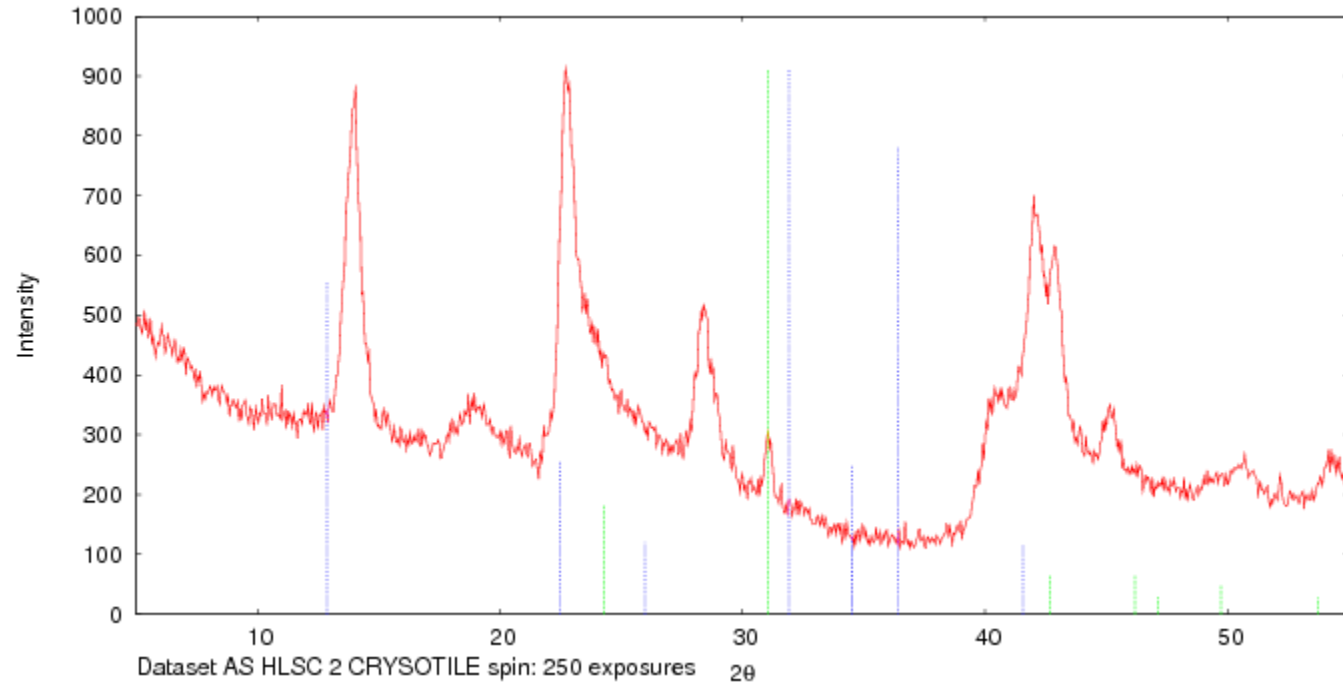
Figure A7: XRD diffractograms for sample HLSC_2 chrysotile raw file without background subtraction. Peak locations probably indicate serpentine, spinel group minerals, and possibly other minerals.
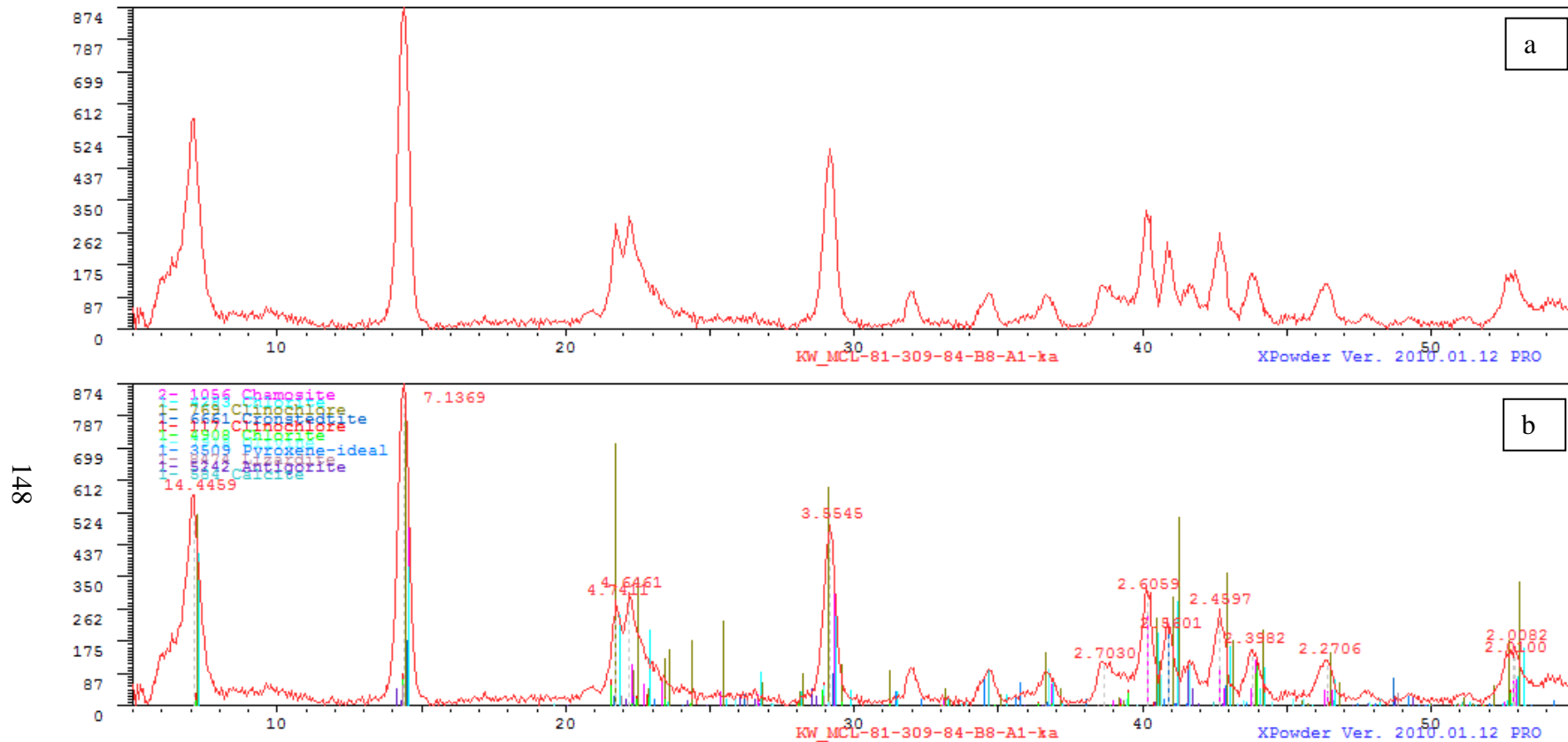
Figure A8: XRD diffractograms for sample 309_84 (a) with background subtracted and (b) peak d-spacing numbers and mineral diffraction patterns identified ((serpentine, pyroxene, chlorite, and calcite) using XPowder.
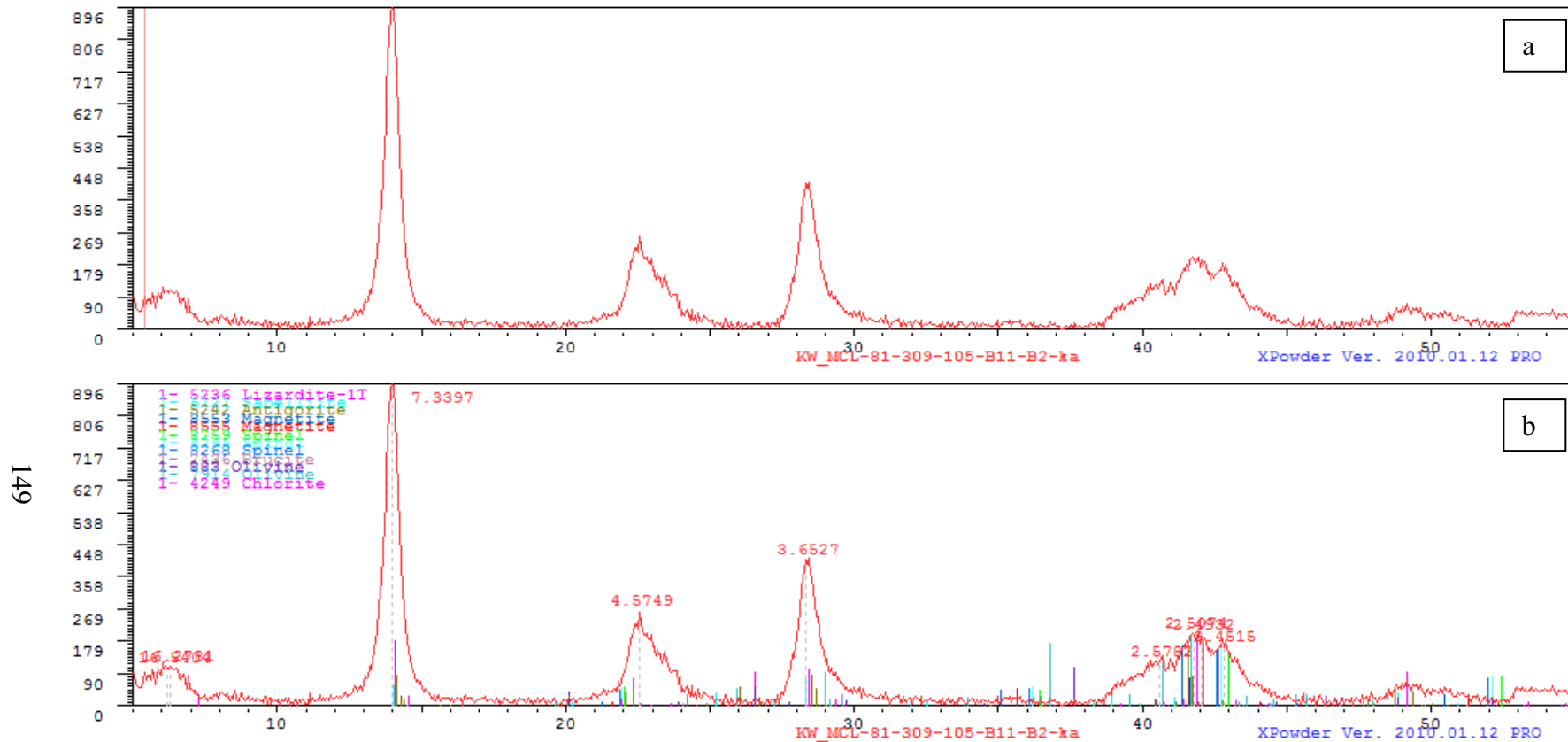
Figure A9: XRD diffractograms for sample 309_105_B (a) with background subtracted and (b) peak d-spacing numbers and mineral diffraction patterns identified (serpentine, magnetite/spinel, chlorite, and possibly olivine) using XPowder.

CROMO1_1_B
CROMO1_1_A
CROMO1_2_CB
CROMO1_2_AC
CROMO1_2_AB
CROMO1_2_AA
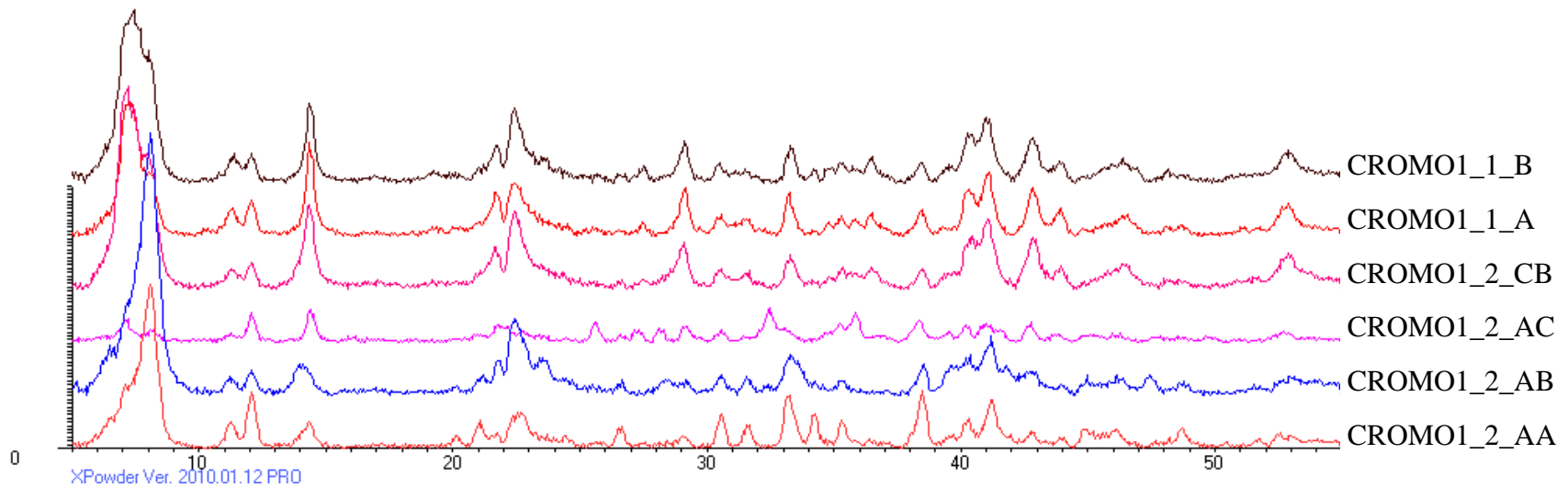
Figure A10: Stacked XRD diffractograms for samples CROMO1_1_B, CROMO1_1_A, CROMO1_2_CB, CROMO1_2_AC, CROMO1_2_AB, and CROMO1_2_AA
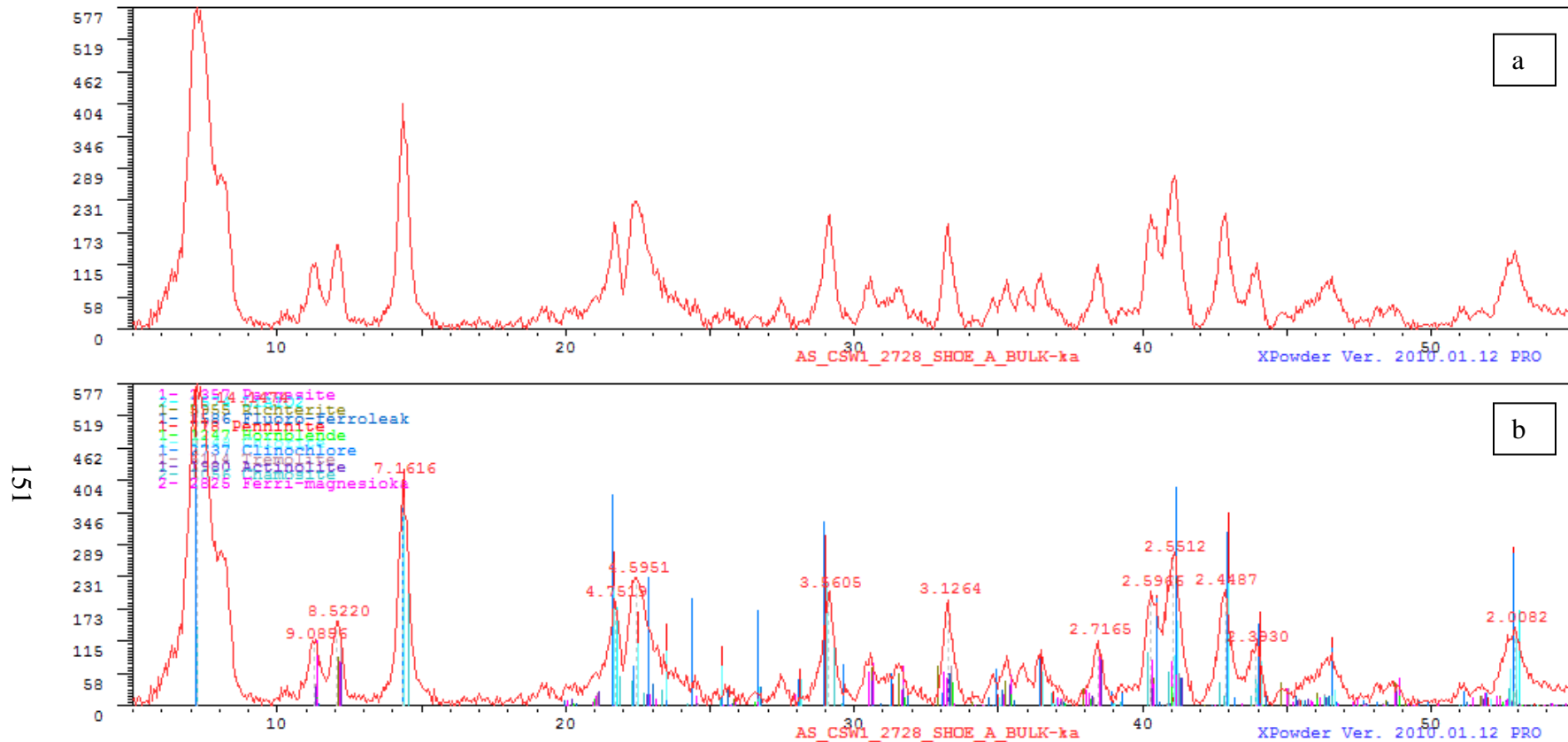
Figure A11: XRD diffractograms for samples CROMO1_1_A (a) with background subtracted and (b) peak d-spacing numbers and mineral diffraction patterns identified (chlorite and amphiboles) using XPowder.
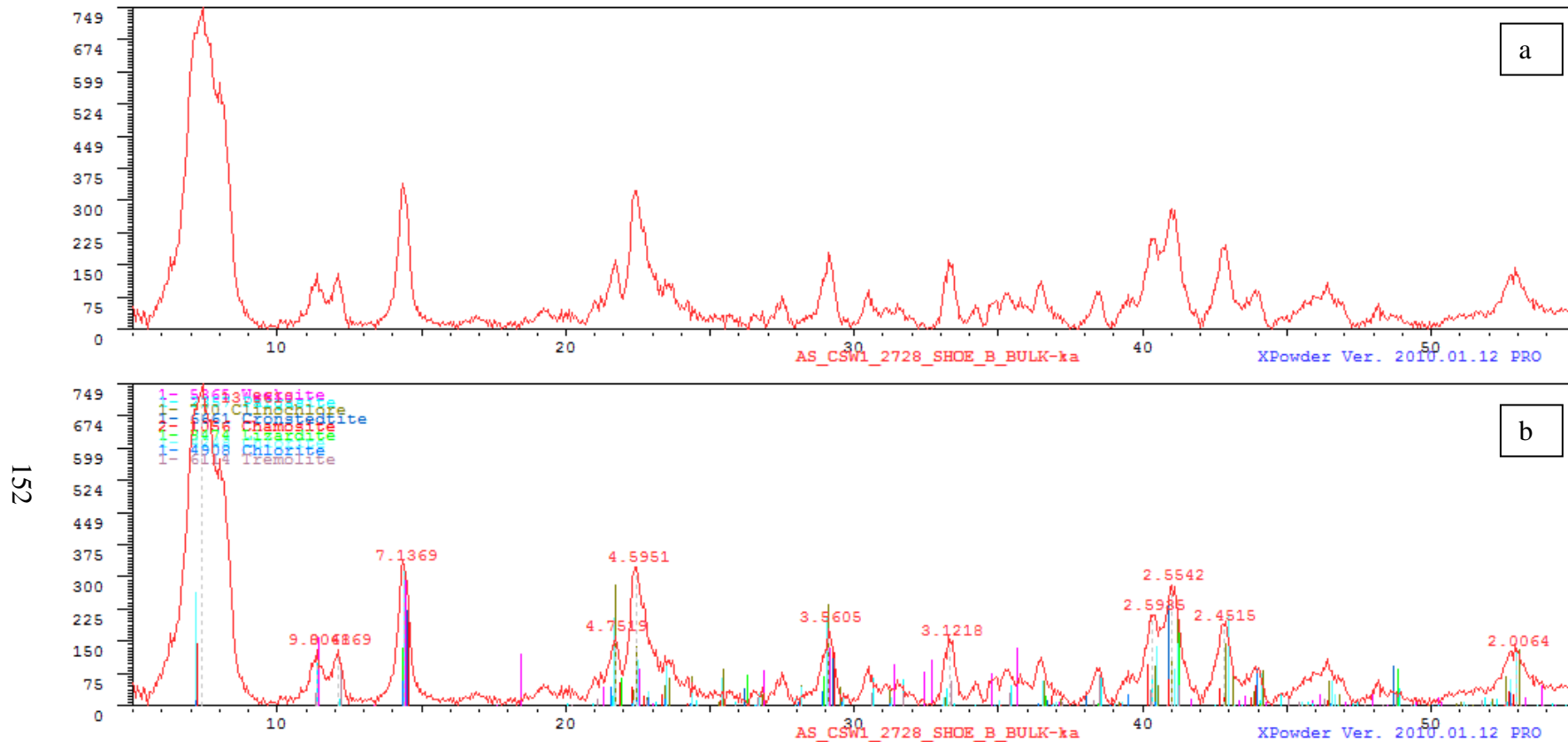
Figure A12: XRD diffractograms for sample CROMO1_1_B (a) with background subtracted and (b) peak d-spacing numbers and mineral diffraction patterns identified (chlorite and amphiboles) using XPowder.
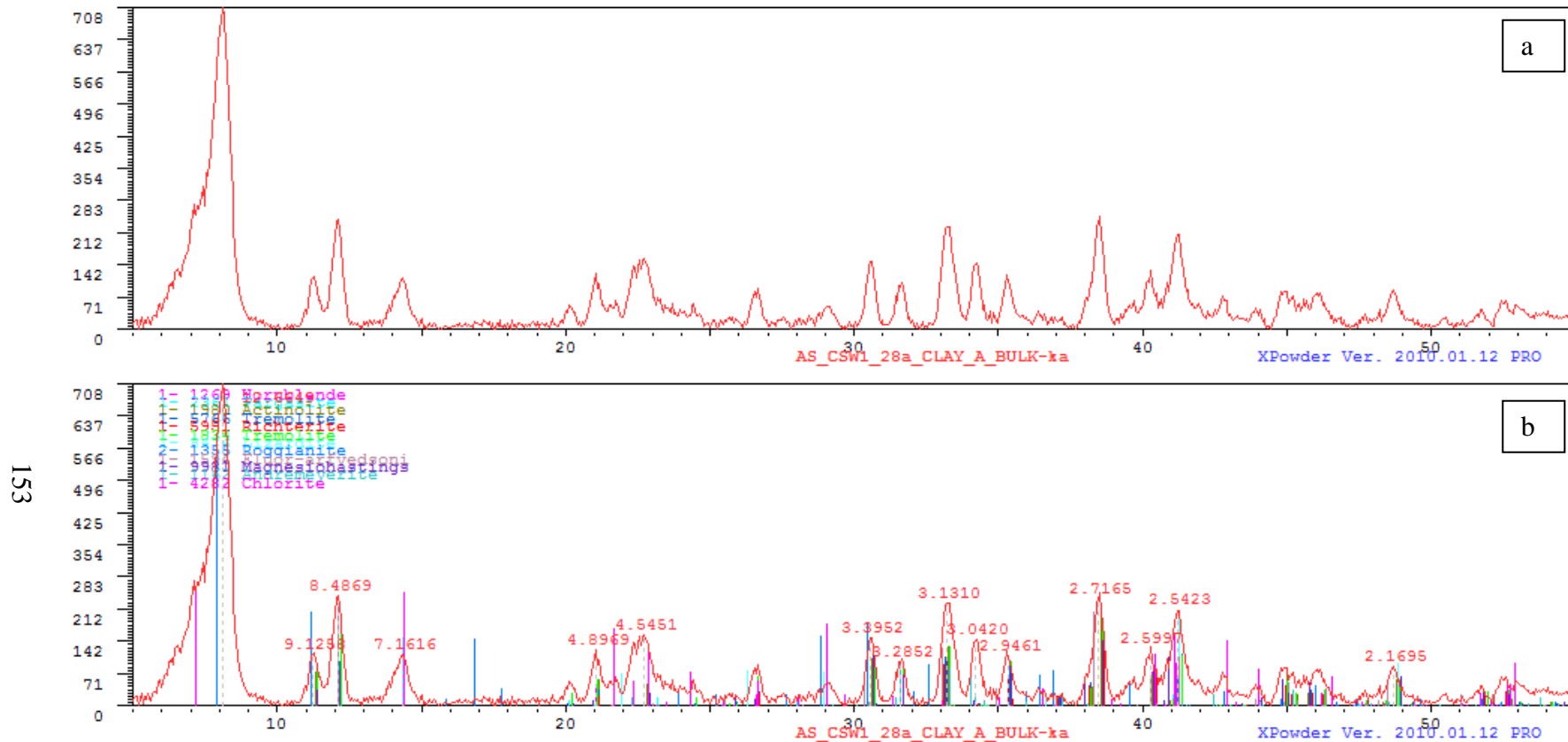
Figure A13: XRD diffractograms for sample CROMO1_2_AA (a) with background subtracted and (b) peak d-spacing numbers and mineral diffraction patterns identified (chlorite and amphiboles) using XPowder.
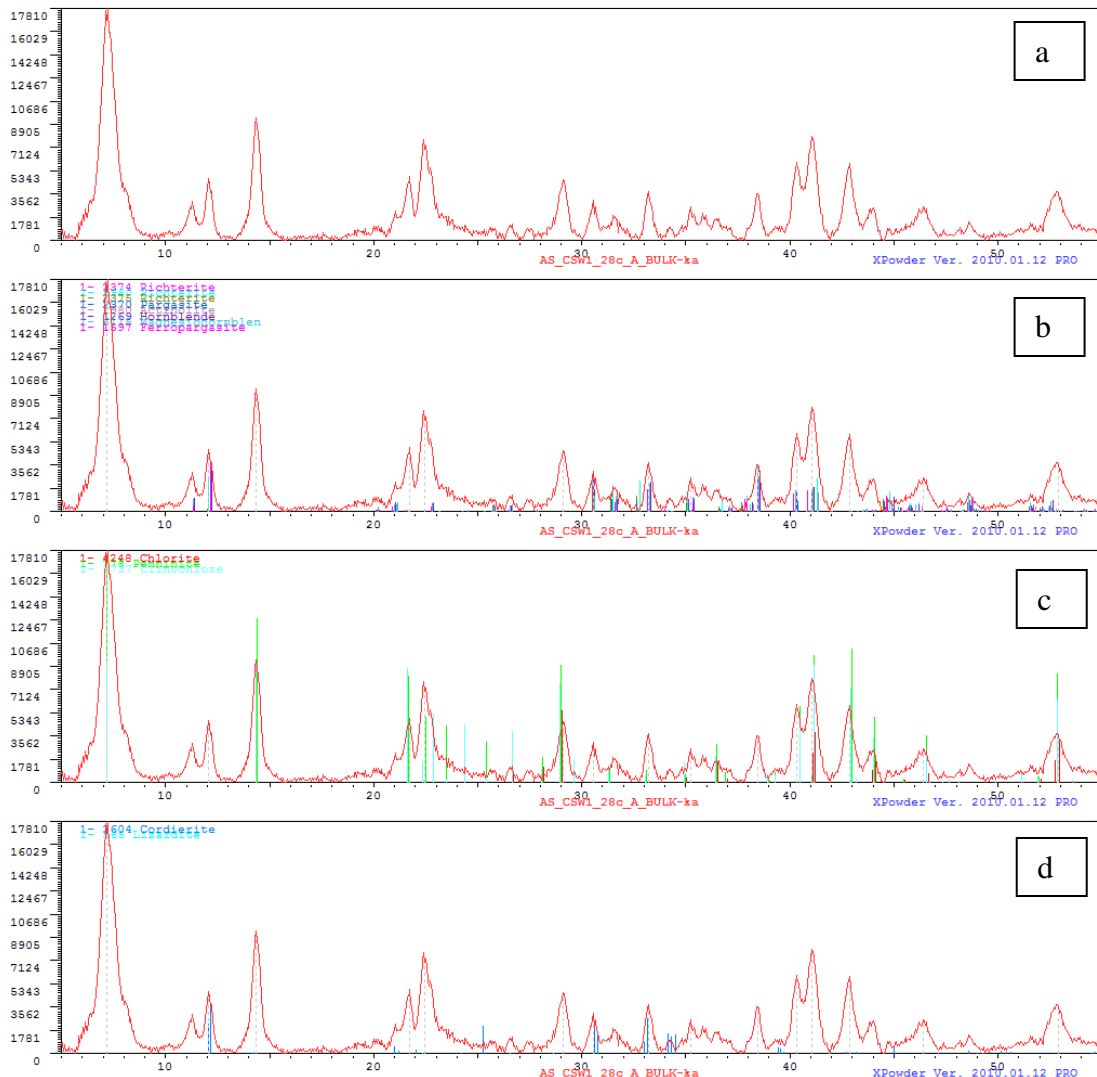
Figure A14: XRD diffractograms for sample CROMO1_2_CA (a) with background subtracted and peak mineral diffraction patterns identified (b-amphiboles, c-chlorite, d-serpentine and maybe cordierite) using XPowder.

154
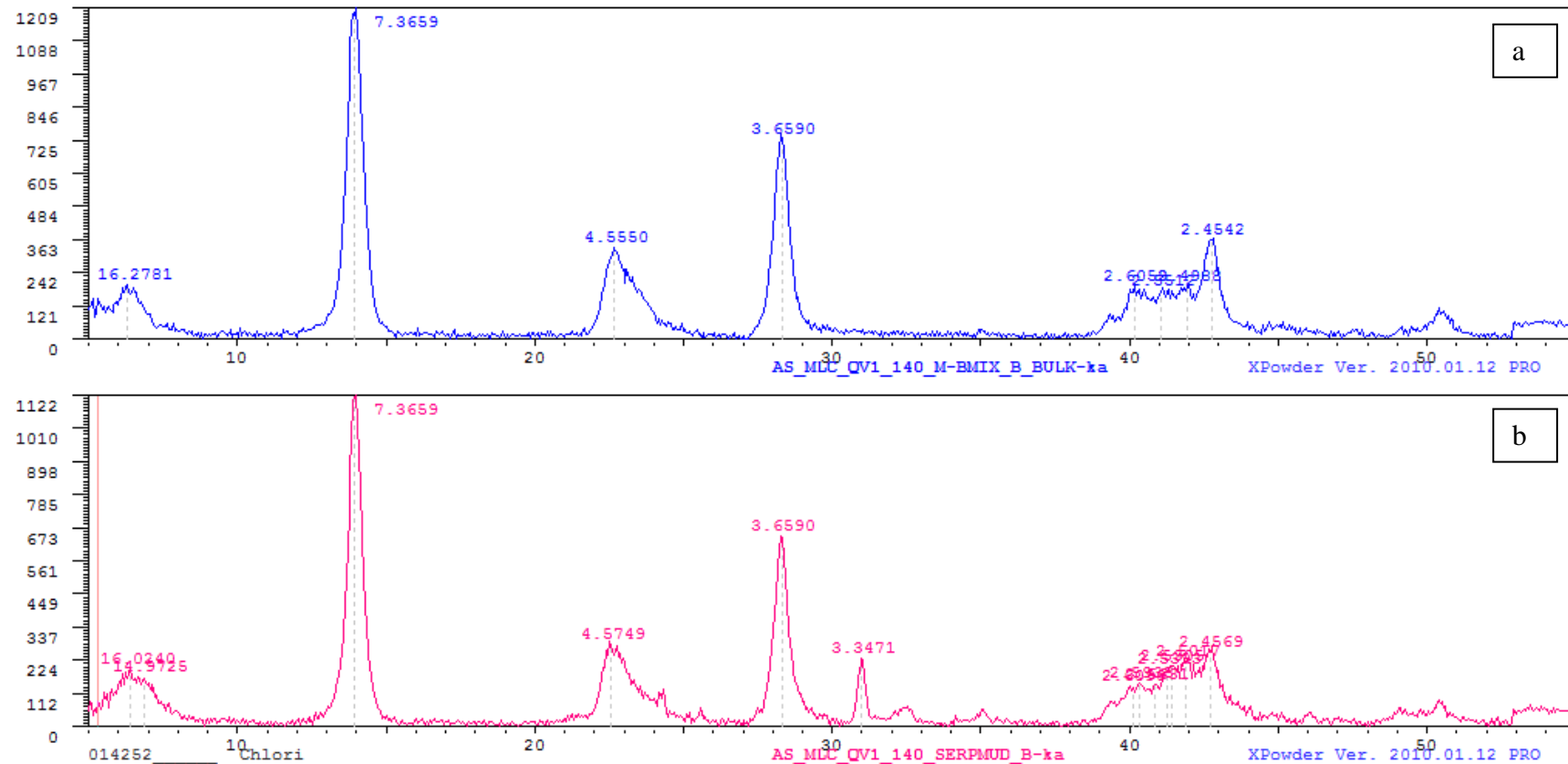
Figure A15: XRD diffractograms with peak d-spacing numbers for samples (a) CROMO2_1B and (b) CROMO2_3B.
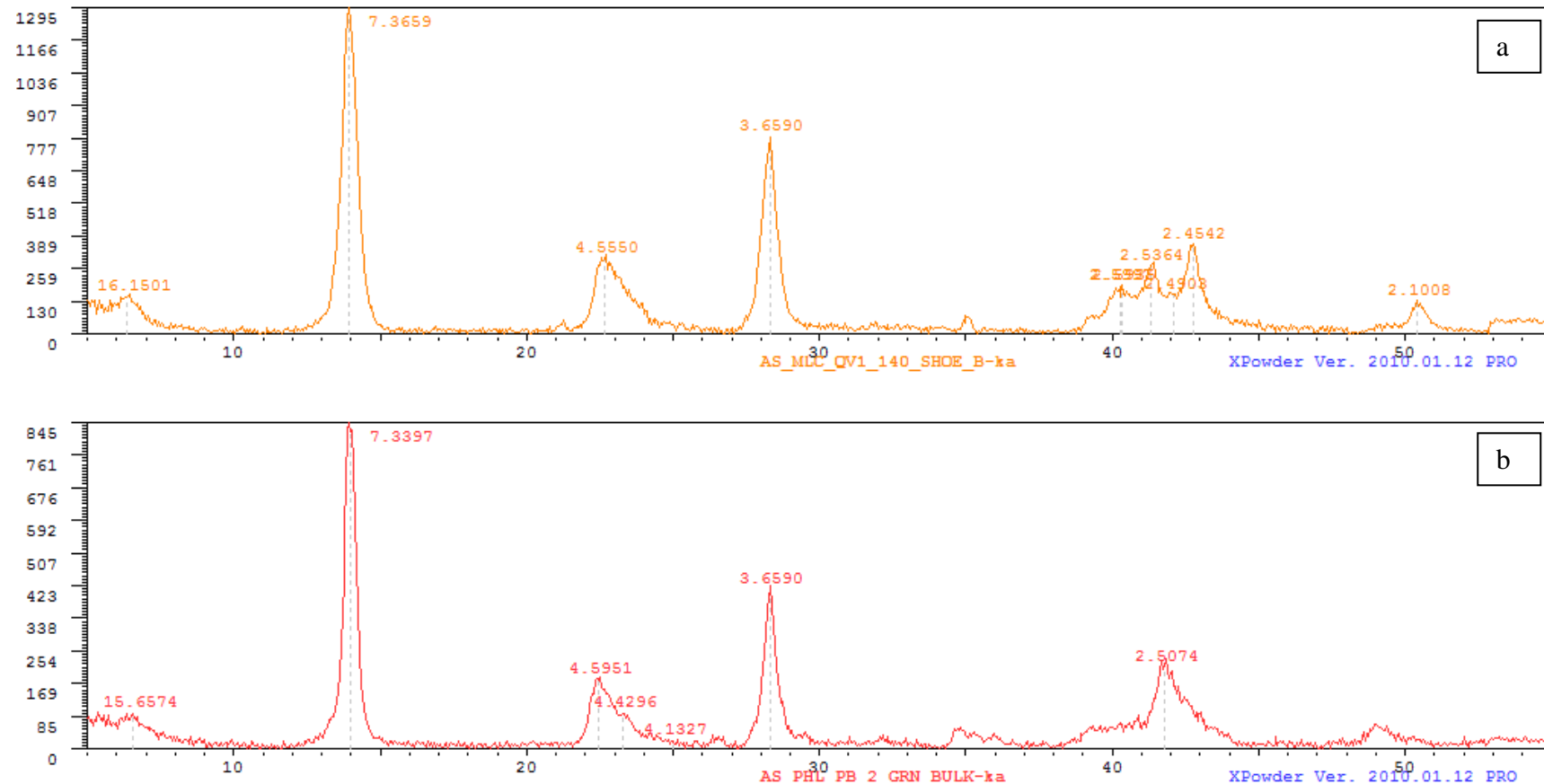
Figure A16: XRD diffractograms with peak d-spacing numbers for samples (a) CROMO2_4B and (b) PHL_2A.
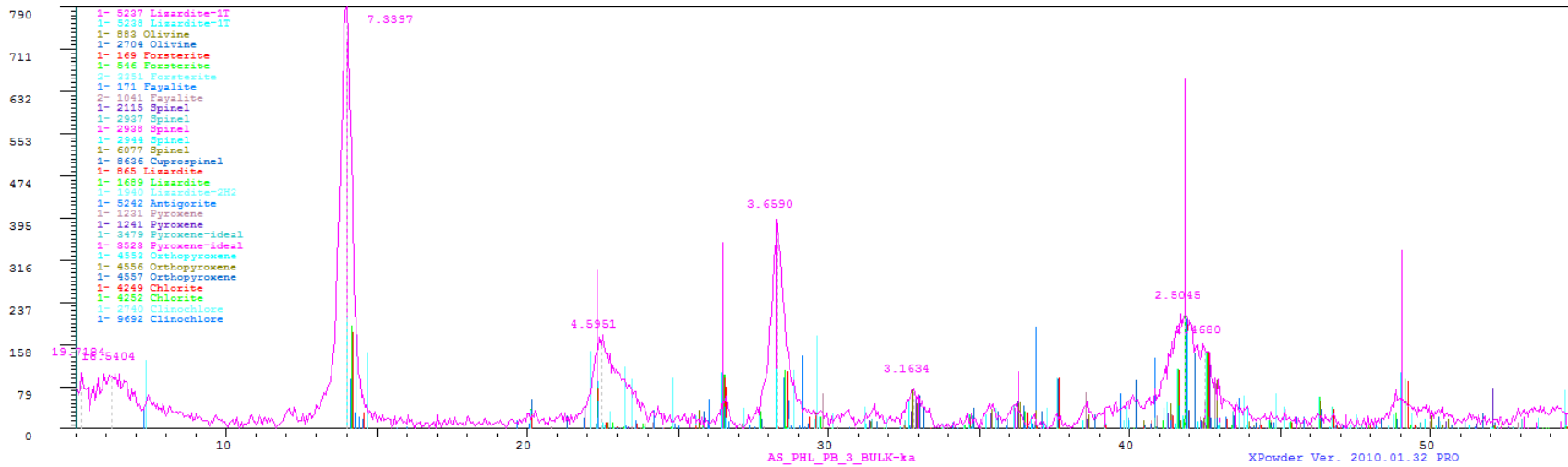
Figure A17: XRD diffractogram for sample PHL_3 with background subtracted, peak d-spacing numbers, and mineral diffraction patterns identified (serpentine, olivine, spinel, pyroxene, and chlorite) using XPowder
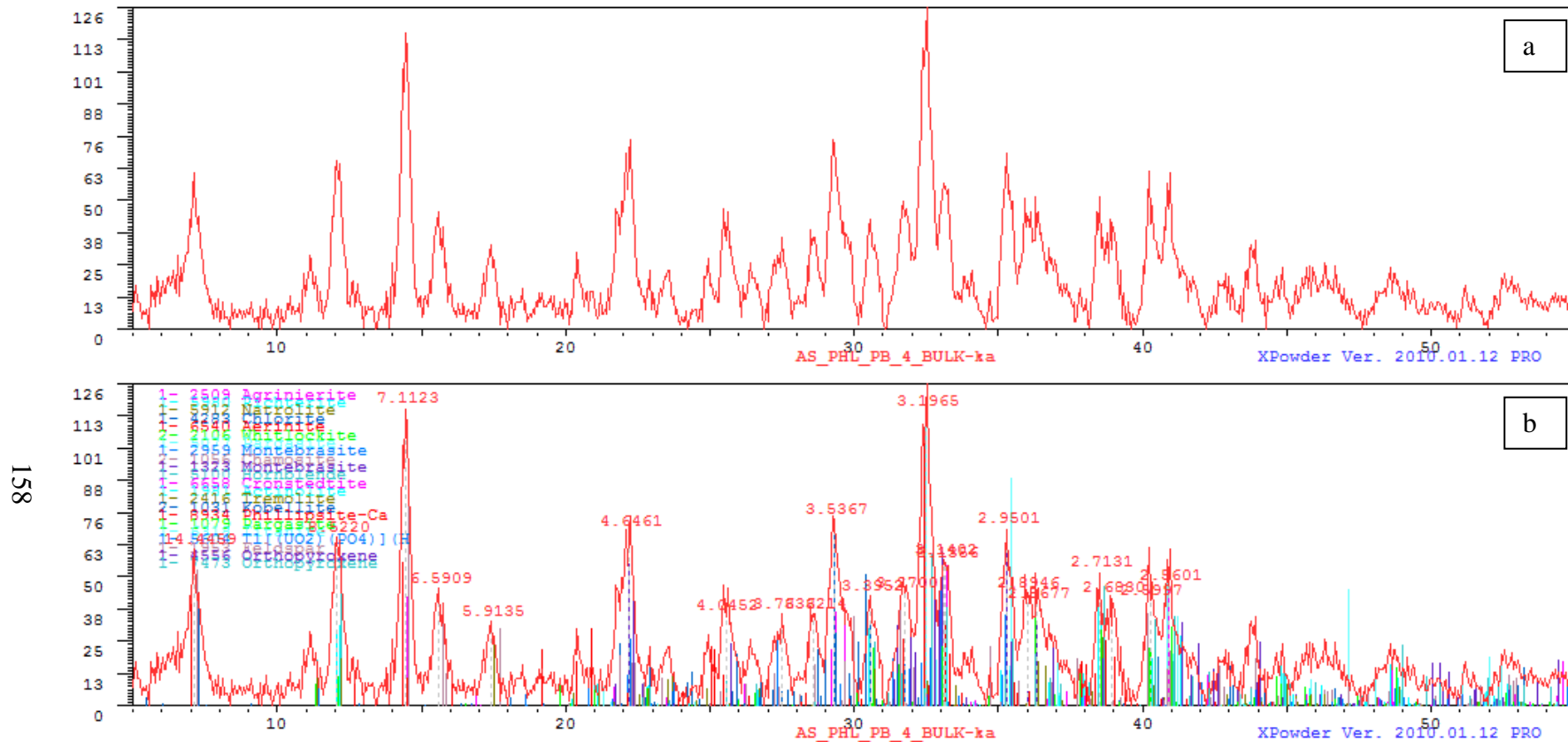
Figure A18: XRD diffractograms with peak d-spacing numbers for sample PHL_4 (a) with background subtracted and (b) peak d-spacing numbers and mineral diffraction patterns identified (amphibole, pyroxene) using XPowder.

Table A6: Additional samples' Fe concentrations averaged and normalized to DTS-1.

Sample	Run	Fe (ppm)	Fe Error (ppm)	Avg. (ppm)	Std Dev	Avg Error of 3 runs	Norm. factor (DTS-1)	Norm. Avg (ppm)
309_84	1	225056.98	1270.07	221539	5948	1251	0.613	135803
	2	224888.53	1267.51					
	3	214671.36	1215.55					
309_105_B	1	48973.15	462.79	59039	8827	552	0.613	36191
	2	62686.34	582.55					
	3	65457.8	611.89					
CROMO1_1_A	1	80662.95	702.97	72875	11914	637	0.613	44672
	2	59160.3	521.08					
	3	78801.42	688.07					
CROMO1_1_B	1	116188.96	1092.01	116675	3584	1089	0.613	71522
	2	120477.61	1105.82					
	3	113358.7	1070.41					
CROMO1_2_AA	1	53738.29	507.00	54678	1137	513	0.613	33518
	2	54353.24	507.37					
	3	55942.11	524.35					
CROMO1_2_AB	1	97748.95	801.78	98824	2342	807	0.613	60579
	2	97212.96	793.13					
	3	101510.9	825.13					
CROMO1_2_AC	1	91002.48	702.93	87714	3743	680	0.613	53768
	2	88496.77	686.92					
	3	83641.25	650.70					
CROMO1_2_CA	1	88302.38	752.58	89281	3076	767	0.613	54729
	2	86812.97	749.12					
	3	92726.28	798.86					
CROMO1_2_CB	1	110297.95	1019.36	115318	9048	1079	0.613	70690
	2	109892.79	1039.11					
	3	125762.21	1178.53					
CROMO2_1B	1	69066.38	724.97	72767	3347	753	0.613	44606
	2	75582.87	780.68					
	3	73652.82	753.47					
CROMO2_3B	1	134003.28	1149.10	136339	9007	1187	0.613	83576
	2	128730.48	1109.87					
	3	146283.61	1301.87					
CROMO2_4B	1	119009.69	1025.93	132135	13883	1157	0.613	80999
	2	130727.7	1141.79					
	3	146668.91	1302.27					
PHL_2A	1	59311.35	529.75	54264	4731	485	0.613	33264
	2	49929.81	448.40					
	3	53550.11	476.96					
PHL_2C	1	78372.31	619.80	66184	17951	529	0.613	40571
	2	74610.47	592.38					
	3	45569.93	374.98					

Table A6: *continued*

Sample	Run	Fe (ppm)	Fe Error (ppm)	Avg. (ppm)	Std Dev	Avg Error of 3 runs	Norm. factor (DTS-1)	Norm. Avg (ppm)
PHL_4	1	50564.68	507.16	50585	385	510	0.613	31009
	2	50980.34	517.53					
	3	50210.2	504.86					
HLSC_4	1	72466.3	614.58	71320	10220	597	0.613	43719
	2	60575.23	521.90					
	3	80918.5	654.09					
ESH	1	408.6	128.14	278	115	100	0.613	170
	2	196.51	84.89					
	3	227.71	87.57					

Empty sample holder (ESH)

Table A7: Normalized average Fe concentration in ppm and FeO wt%.

Sample name	Fe avg. normalized concentration (ppm)	Fe avg. normalized concentration (FeO wt%)
HLSC_1	28741	3.7
167_238	29910	3.8
309_105_A	31705	4.1
309_105_B	36191	4.7
309_150	34651	4.5
309_84	135803	17.5
313_210	50673	6.5
313_318	32835	4.2
313_329	41989	5.4
313_356	37335	4.8
CROMO1_1_A	44672	5.7
CROMO1_1_B	71522	9.2
CROMO1_2_AA	33518	4.3
CROMO1_2_AB	60579	7.8
CROMO1_2_AC	53768	6.9
CROMO1_2_CA	54729	7.0
CROMO1_2_CB	70690	9.1
CROMO2_1A	30803	4.0
CROMO2_1B	44606	5.7
CROMO2_2	30966	4.0
CROMO2_3A	37889	4.9
CROMO2_3B	83576	10.8
CROMO2_4A	30290	3.9
CROMO2_4B	80999	10.4
PHL_1	47976	6.2
PHL_2A	33264	4.3
PHL_2B	35777	4.6
PHL_2C	40571	5.2
PHL_3	47745	6.1
PHL_4	31009	4.0
HLSC_4	43719	5.6
PHL_5	41969	5.4

Table A8: Samples raw elemental XRF data. Elements analyzed for include As, Ca, Co, Cr, Cu, Fe, Hg, K, Mn, Mo, Ni, Pb, Rb, S, Sb, Sc, Se, Sr, Th, Ti, V, Zn, and Zr. Additional elements below the limits of detection (<LOD): U, W, Ba, Cs, Te, Sn, Cd, Ag and Pd.

SAMPLE	Sample short name	Type	Duration (s)	Units	Mo	Mo Error	Zr	Zr Error	Sr	Sr Error	Rb	Rb Error
McL_81-167_238 to EOH_B22_B	167_238	SOIL	208.70	ppm	< LOD	4.48	< LOD	5.46	153.78	5.51	< LOD	2.27
McL_81-167_238 to EOH_B22_B	167_238	SOIL	243.97	ppm	< LOD	4.74	< LOD	5.88	171.78	5.99	< LOD	2.51
McL_81-167_238 to EOH_B22_B	167_238	SOIL	244.33	ppm	< LOD	4.42	< LOD	5.45	154.06	5.43	< LOD	2.18
HLSC_1_A	HLSC_1	SOIL	221.31	ppm	< LOD	4.83	< LOD	6.03	177.18	6.21	< LOD	2.42
HLSC_1_A	HLSC_1	SOIL	207.46	ppm	< LOD	4.83	< LOD	6.17	180.12	6.31	< LOD	2.45
HLSC_1_A	HLSC_1	SOIL	213.75	ppm	< LOD	4.99	< LOD	6.25	183.16	6.36	< LOD	2.51
HLSC_4	HLSC_4	SOIL	205.99	ppm	< LOD	5.53	< LOD	5.70	< LOD	2.84	< LOD	2.73
HLSC_4	HLSC_4	SOIL	205.52	ppm	< LOD	4.95	< LOD	5.01	< LOD	2.49	< LOD	2.33
HLSC_4	HLSC_4	SOIL	228.54	ppm	< LOD	5.60	< LOD	5.75	< LOD	2.85	< LOD	2.56
McL_M81-313_210_B22_A3	313_210	SOIL	219.25	ppm	< LOD	5.93	< LOD	6.63	69.24	4.80	< LOD	2.97
McL_M81-313_210_B22_A3	313_210	SOIL	204.64	ppm	< LOD	5.07	< LOD	6.01	66.03	4.27	< LOD	2.34
McL_M81-313_210_B22_A3	313_210	SOIL	205.33	ppm	< LOD	5.78	< LOD	6.64	61.47	4.50	< LOD	2.95
McL_M81-313_329	313_329	SOIL	203.86	ppm	< LOD	6.30	< LOD	6.57	39.55	3.96	< LOD	2.87
McL_M81-313_329	313_329	SOIL	202.94	ppm	< LOD	6.33	< LOD	6.39	41.89	4.09	< LOD	2.82
McL_M81-313_329	313_329	SOIL	203.45	ppm	< LOD	5.85	< LOD	6.11	37.01	3.70	< LOD	2.73
McL_M81-313_356-356.6_B38_B	313_356	SOIL	210.15	ppm	< LOD	6.22	< LOD	6.42	44.53	4.22	< LOD	3.06
McL_M81-313_356-356.6_B38_B	313_356	SOIL	204.20	ppm	< LOD	5.50	< LOD	5.84	44.22	3.82	< LOD	2.61
McL_M81-313_356-356.6_B38_B	313_356	SOIL	202.49	ppm	< LOD	5.03	< LOD	5.30	37.84	3.36	< LOD	2.50
McL_M81-313_318_B34_B	313_318	SOIL	202.64	ppm	< LOD	5.12	< LOD	5.24	36.70	3.35	< LOD	2.53
McL_M81-313_318_B34_B	313_318	SOIL	202.81	ppm	< LOD	5.41	< LOD	5.73	41.44	3.68	< LOD	2.59
McL_M81-313_318_B34_B	313_318	SOIL	202.57	ppm	< LOD	5.25	< LOD	5.45	34.98	3.31	< LOD	2.49
McL_M81-309_105_B11_B2	309_105_B	SOIL	202.69	ppm	< LOD	4.92	< LOD	5.03	3.88	1.92	< LOD	2.25
McL_M81-309_105_B11_B2	309_105_B	SOIL	203.18	ppm	< LOD	5.67	< LOD	6.08	< LOD	3.21	< LOD	2.73
McL_M81-309_105_B11_B2	309_105_B	SOIL	203.16	ppm	< LOD	5.83	< LOD	6.14	6.97	2.42	< LOD	2.78
McL_M81-309_105_B11_B1	309_105_A	SOIL	217.46	ppm	< LOD	4.69	< LOD	4.61	10.21	2.12	< LOD	2.15
McL_M81-309_105_B11_B1	309_105_A	SOIL	202.94	ppm	< LOD	4.92	< LOD	5.07	8.57	2.15	< LOD	2.17
McL_M81-309_105_B11_B1	309_105_A	SOIL	202.41	ppm	< LOD	4.73	< LOD	4.74	7.12	2.03	< LOD	2.20

Table A8: *continued*

SAMPLE	Sample short name	Type	Duration (s)	Units	Mo	Mo Error	Zr	Zr Error	Sr	Sr Error	Rb	Rb Error
McL_M81-309_150_B15_A	**309_150**	SOIL	202.48	ppm	< LOD	5.05	< LOD	5.09	16.11	2.54	< LOD	2.22
McL_M81-309_150_B15_A	**309_150**	SOIL	202.19	ppm	< LOD	5.46	< LOD	5.33	16.93	2.72	< LOD	2.58
McL_M81-309_150_B15_A	**309_150**	SOIL	202.17	ppm	< LOD	4.99	< LOD	4.75	11.45	2.29	< LOD	2.27
McL_M81-309_84_B8_A1	**309_84**	SOIL	202.26	ppm	< LOD	6.61	96.96	7.79	44.44	4.53	8.96	3.04
McL_M81-309_84_B8_A1	**309_84**	SOIL	203.76	ppm	< LOD	6.62	96.01	7.79	47.81	4.66	8.80	2.96
McL_M81-309_84_B8_A1	**309_84**	SOIL	203.67	ppm	< LOD	6.50	99.03	7.68	43.76	4.42	7.42	2.97
Empty sample holder	**ESH**	SOIL	202.11	ppm	< LOD	13.82	< LOD	12.64	< LOD	7.54	< LOD	6.98
Empty sample holder	**ESH**	SOIL	205.11	ppm	< LOD	11.04	< LOD	10.59	< LOD	6.20	< LOD	5.82
Empty sample holder	**ESH**	SOIL	203.07	ppm	< LOD	10.91	< LOD	10.78	< LOD	6.02	< LOD	6.11
CSW1_28a_hard	**CROMO1_2_AC**	SOIL	202.68	ppm	< LOD	5.39	< LOD	7.03	130.29	6.16	< LOD	3.24
CSW1_28a_hard	**CROMO1_2_AC**	SOIL	202.35	ppm	< LOD	5.33	< LOD	7.07	129.26	6.08	< LOD	3.28
CSW1_28a_hard	**CROMO1_2_AC**	SOIL	202.70	ppm	< LOD	5.20	12.92	4.89	124.57	5.82	3.67	2.14
CSW1_28a_CLAY_A	**CROMO1_2_AA**	SOIL	201.69	ppm	< LOD	5.03	< LOD	6.66	128.83	5.74	< LOD	2.51
CSW1_28a_CLAY_A	**CROMO1_2_AA**	SOIL	203.03	ppm	< LOD	5.07	< LOD	6.52	119.70	5.52	< LOD	2.33
CSW1_28a_CLAY_A	**CROMO1_2_AA**	SOIL	203.22	ppm	< LOD	5.13	< LOD	6.88	124.85	5.74	< LOD	2.70
CSW1_28a_CLAY_B	**CROMO1_2_AB**	SOIL	202.09	ppm	< LOD	6.41	< LOD	9.00	225.43	8.75	< LOD	3.39
CSW1_28a_CLAY_B	**CROMO1_2_AB**	SOIL	202.72	ppm	< LOD	6.44	< LOD	8.84	229.80	8.76	< LOD	3.35
CSW1_28a_CLAY_B	**CROMO1_2_AB**	SOIL	202.40	ppm	< LOD	6.45	< LOD	9.03	232.53	8.97	< LOD	3.31
CSW1_27/28_SHOE?_A	**CROMO1_1_A**	SOIL	202.70	ppm	< LOD	6.14	20.76	6.08	200.68	7.99	6.49	2.60
CSW1_27/28_SHOE?_A	**CROMO1_1_A**	SOIL	202.50	ppm	< LOD	4.91	18.15	4.93	160.55	6.22	4.30	2.04
CSW1_27/28_SHOE?_A	**CROMO1_1_A**	SOIL	202.26	ppm	< LOD	6.02	17.44	5.91	201.57	7.93	5.51	2.62
CSW1_27/28_SHOE?_B	**CROMO1_1_B**	SOIL	202.83	ppm	< LOD	8.61	< LOD	11.39	207.32	10.54	< LOD	5.23
CSW1_27/28_SHOE?_B	**CROMO1_1_B**	SOIL	208.08	ppm	< LOD	8.64	< LOD	11.45	194.11	10.17	< LOD	5.14
CSW1_27/28_SHOE?_B	**CROMO1_1_B**	SOIL	203.42	ppm	< LOD	8.60	< LOD	11.44	207.37	10.45	7.05	3.56

Table A8: *continued*

SAMPLE	Sample short name	Type	Duration (s)	Units	Mo	Mo Error	Zr	Zr Error	Sr	Sr Error	Rb	Rb Error
CSW1_28c_A	**CROMO1_2_CA**	SOIL	202.04	ppm	< LOD	6.26	< LOD	8.73	185.00	7.87	< LOD	3.43
CSW1_28c_A	**CROMO1_2_CA**	SOIL	201.72	ppm	< LOD	6.44	10.66	5.91	184.69	7.89	< LOD	3.57
CSW1_28c_A	**CROMO1_2_CA**	SOIL	201.77	ppm	< LOD	6.54	20.21	6.32	178.74	8.02	< LOD	3.62
CSW1_28c_B	**CROMO1_2_CB**	SOIL	203.87	ppm	< LOD	8.13	< LOD	10.80	228.04	10.54	< LOD	4.43
CSW1_28c_B	**CROMO1_2_CB**	SOIL	201.59	ppm	< LOD	8.27	< LOD	11.01	227.66	10.77	< LOD	4.76
CSW1_28c_B	**CROMO1_2_CB**	SOIL	202.28	ppm	9.24	6.05	< LOD	11.95	239.25	11.69	< LOD	4.79
MLC_QV2_140_SHOE_A	**CROMO2_4A**	SOIL	202.47	ppm	< LOD	5.16	< LOD	4.97	8.23	2.19	< LOD	2.48
MLC_QV2_140_SHOE_A	**CROMO2_4A**	SOIL	202.78	ppm	< LOD	4.82	< LOD	4.51	7.30	2.04	< LOD	2.04
MLC_QV2_140_SHOE_A	**CROMO2_4A**	SOIL	202.60	ppm	< LOD	4.86	< LOD	4.58	8.28	2.08	< LOD	2.11
MLC_QV2_140_SHOE_B	**CROMO2_4B**	SOIL	202.34	ppm	9.02	5.31	< LOD	7.71	21.30	3.95	< LOD	3.93
MLC_QV2_140_SHOE_B	**CROMO2_4B**	SOIL	202.49	ppm	< LOD	8.38	< LOD	8.36	17.64	4.03	< LOD	4.26
MLC_QV2_140_SHOE_B	**CROMO2_4B**	SOIL	202.72	ppm	< LOD	8.99	< LOD	9.50	21.67	4.64	< LOD	4.39
MLC_QV1_140_Mdkgrn	**CROMO2_2**	SOIL	202.68	ppm	< LOD	4.72	< LOD	4.78	18.73	2.54	< LOD	2.20
MLC_QV1_140_Mdkgrn	**CROMO2_2**	SOIL	204.20	ppm	< LOD	5.19	< LOD	5.02	20.31	2.73	< LOD	2.28
MLC_QV1_140_Mdkgrn	**CROMO2_2**	SOIL	203.48	ppm	< LOD	5.05	< LOD	4.79	12.10	2.37	< LOD	2.46
MLC_QV1_140_SERPMUD_A	**CROMO2_3A**	SOIL	202.06	ppm	< LOD	5.88	19.86	4.87	40.29	3.83	6.05	2.35
MLC_QV1_140_SERPMUD_A	**CROMO2_3A**	SOIL	202.22	ppm	< LOD	4.60	7.65	3.63	30.80	2.90	4.65	1.86
MLC_QV1_140_SERPMUD_A	**CROMO2_3A**	SOIL	202.19	ppm	< LOD	4.99	10.77	3.93	30.97	3.04	6.05	2.04
MLC_QV1_140_SERPMUD_B	**CROMO2_3B**	SOIL	204.18	ppm	< LOD	8.35	27.97	7.08	47.86	5.54	6.95	3.51
MLC_QV1_140_SERPMUD_B	**CROMO2_3B**	SOIL	202.41	ppm	< LOD	8.08	15.77	6.51	45.84	5.33	8.32	3.54
MLC_QV1_140_SERPMUD_B	**CROMO2_3B**	SOIL	201.88	ppm	< LOD	8.97	21.87	7.46	43.81	5.80	6.57	3.93
MLC_QV1_140_M-BMIX_A	**CROMO2_1A**	SOIL	202.41	ppm	< LOD	5.44	< LOD	5.31	11.05	2.43	< LOD	2.52
MLC_QV1_140_M-BMIX_A	**CROMO2_1A**	SOIL	203.12	ppm	< LOD	5.21	< LOD	5.15	8.28	2.22	< LOD	2.57
MLC_QV1_140_M-BMIX_A	**CROMO2_1A**	SOIL	201.84	ppm	< LOD	5.40	< LOD	5.50	9.66	2.38	< LOD	2.53
MLC_QV1_140_M-BMIX_B	**CROMO2_1B**	SOIL	202.15	ppm	< LOD	6.95	< LOD	6.84	5.30	2.73	< LOD	3.46
MLC_QV1_140_M-BMIX_B	**CROMO2_1B**	SOIL	202.67	ppm	< LOD	7.31	< LOD	7.12	5.33	2.78	< LOD	3.22
MLC_QV1_140_M-BMIX_B	**CROMO2_1B**	SOIL	201.74	ppm	< LOD	7.04	< LOD	7.22	6.63	2.80	< LOD	3.38

Table A8: *continued*

SAMPLE	Sample short name	Type	Duration (s)	Units	Mo	Mo Error	Zr	Zr Error	Sr	Sr Error	Rb	Rb Error
PHL_PB_1_BULK	**PHL_1**	SOIL	202.49	ppm	< LOD	5.07	< LOD	4.66	< LOD	2.65	< LOD	2.37
PHL_PB_1_BULK	**PHL_1**	SOIL	202.71	ppm	< LOD	4.94	< LOD	4.83	< LOD	2.59	< LOD	2.26
PHL_PB_1_BULK	**PHL_1**	SOIL	214.89	ppm	< LOD	4.57	< LOD	4.45	< LOD	2.29	< LOD	2.17
PHL_PB_2_MIX_BULK	**PHL_2B**	SOIL	202.57	ppm	< LOD	4.95	< LOD	4.86	< LOD	2.60	< LOD	2.25
PHL_PB_2_MIX_BULK	**PHL_2B**	SOIL	201.42	ppm	< LOD	5.00	< LOD	4.90	< LOD	2.62	< LOD	2.12
PHL_PB_2_MIX_BULK	**PHL_2B**	SOIL	202.66	ppm	< LOD	5.09	< LOD	4.87	< LOD	2.75	< LOD	2.28
PHL_PB_2_RED_BULK	**PHL_2C**	SOIL	201.71	ppm	< LOD	5.17	< LOD	4.99	< LOD	2.64	< LOD	2.49
PHL_PB_2_RED_BULK	**PHL_2C**	SOIL	201.43	ppm	< LOD	5.08	< LOD	4.87	< LOD	2.39	< LOD	2.37
PHL_PB_2_RED_BULK	**PHL_2C**	SOIL	201.75	ppm	< LOD	3.80	< LOD	3.35	< LOD	1.78	< LOD	1.83
PHL_PB_2_GRN_BULK	**PHL_2A**	SOIL	201.49	ppm	< LOD	5.01	< LOD	4.76	< LOD	2.68	< LOD	2.27
PHL_PB_2_GRN_BULK	**PHL_2A**	SOIL	201.62	ppm	< LOD	4.56	< LOD	4.48	< LOD	2.53	< LOD	2.10
PHL_PB_2_GRN_BULK	**PHL_2A**	SOIL	202.47	ppm	< LOD	4.77	< LOD	4.56	< LOD	2.36	< LOD	2.28
PHL_PB_3_BULK	**PHL_3**	SOIL	201.52	ppm	< LOD	5.49	< LOD	5.29	< LOD	2.87	< LOD	2.42
PHL_PB_3_BULK	**PHL_3**	SOIL	201.98	ppm	< LOD	5.22	< LOD	5.07	< LOD	2.71	< LOD	2.66
PHL_PB_3_BULK	**PHL_3**	SOIL	201.87	ppm	< LOD	5.74	< LOD	5.51	< LOD	2.92	< LOD	2.61
PHL_PB_4_BULK	**PHL_4**	SOIL	202.54	ppm	< LOD	5.25	< LOD	10.32	632.79	12.63	< LOD	3.27
PHL_PB_4_BULK	**PHL_4**	SOIL	201.35	ppm	< LOD	5.29	< LOD	10.52	623.33	12.74	< LOD	3.13
PHL_PB_4_BULK	**PHL_4**	SOIL	201.76	ppm	< LOD	5.16	< LOD	10.40	607.21	12.37	< LOD	3.08
PHL_PB_5_BULK	**PHL_5**	SOIL	201.78	ppm	< LOD	4.73	< LOD	4.48	< LOD	2.09	< LOD	2.23
PHL_PB_5_BULK	**PHL_5**	SOIL	201.83	ppm	< LOD	4.65	< LOD	4.40	< LOD	2.25	< LOD	2.10
PHL_PB_5_BULK	**PHL_5**	SOIL	203.28	ppm	< LOD	4.79	< LOD	4.42	< LOD	2.38	< LOD	2.22

Table A8: *continued*

Sample	Th	Th Error	Pb	Pb Error	Se	Se Error	As	As Error	Hg	Hg Error	Zn	Zn Error	Cu	Cu Error
167_238	< LOD	4.60	< LOD	6.13	< LOD	4.12	< LOD	5.13	< LOD	10.83	< LOD	13.38	< LOD	33.70
167_238	< LOD	5.22	< LOD	6.25	< LOD	4.07	< LOD	5.10	< LOD	11.83	< LOD	13.35	< LOD	35.84
167_238	< LOD	4.09	< LOD	6.46	< LOD	4.06	< LOD	5.15	< LOD	10.48	< LOD	13.12	< LOD	34.05
HLSC_1	< LOD	5.47	< LOD	6.94	< LOD	4.45	< LOD	5.66	< LOD	11.93	< LOD	15.67	< LOD	34.02
HLSC_1	< LOD	4.68	< LOD	7.08	< LOD	4.63	< LOD	5.89	< LOD	11.73	< LOD	16.19	< LOD	34.67
HLSC_1	< LOD	4.88	< LOD	7.42	< LOD	4.94	< LOD	5.75	< LOD	12.22	17.77	11.45	< LOD	36.75
HLSC_4	< LOD	5.48	< LOD	6.88	< LOD	5.08	< LOD	5.67	< LOD	13.05	< LOD	17.91	< LOD	41.58
HLSC_4	< LOD	5.31	< LOD	6.81	< LOD	4.32	< LOD	5.56	< LOD	11.01	< LOD	15.17	< LOD	34.45
HLSC_4	< LOD	5.88	< LOD	8.45	< LOD	5.37	< LOD	5.97	< LOD	13.90	< LOD	20.04	< LOD	43.36
313_210	< LOD	5.63	< LOD	8.26	< LOD	5.49	< LOD	6.28	< LOD	14.63	< LOD	22.86	< LOD	47.97
313_210	< LOD	5.33	< LOD	7.81	< LOD	4.42	< LOD	5.65	< LOD	11.87	< LOD	18.04	< LOD	35.98
313_210	< LOD	6.75	< LOD	7.83	< LOD	5.64	< LOD	6.11	< LOD	13.85	< LOD	20.67	< LOD	43.44
313_329	< LOD	6.67	< LOD	8.62	< LOD	5.90	< LOD	6.54	< LOD	14.41	< LOD	20.25	< LOD	44.27
313_329	< LOD	5.42	< LOD	8.66	< LOD	5.84	< LOD	6.74	< LOD	14.63	< LOD	21.11	< LOD	44.17
313_329	< LOD	5.99	< LOD	7.27	< LOD	5.25	< LOD	5.66	< LOD	12.44	< LOD	19.21	< LOD	40.92
313_356	< LOD	6.02	< LOD	8.25	< LOD	6.06	< LOD	6.37	< LOD	16.66	< LOD	21.98	< LOD	51.66
313_356	< LOD	5.69	< LOD	8.11	< LOD	5.11	< LOD	5.79	< LOD	13.75	< LOD	18.46	< LOD	41.69
313_356	< LOD	5.05	< LOD	7.43	< LOD	4.49	< LOD	5.61	< LOD	11.69	< LOD	15.89	< LOD	35.67
313_318	< LOD	5.25	< LOD	6.91	< LOD	4.67	< LOD	5.18	< LOD	11.82	40.35	12.77	< LOD	37.26
313_318	< LOD	5.50	< LOD	7.58	< LOD	5.08	< LOD	6.17	< LOD	13.13	27.51	13.41	53.19	29.90
313_318	< LOD	4.75	< LOD	6.50	< LOD	4.72	< LOD	5.26	< LOD	12.33	26.04	12.31	< LOD	38.27
309_105_B	< LOD	4.46	< LOD	7.00	< LOD	4.69	21.23	5.04	< LOD	13.73	43.41	13.01	< LOD	41.37
309_105_B	< LOD	5.77	< LOD	7.55	< LOD	5.59	32.88	6.20	20.99	11.13	37.56	14.89	< LOD	50.01
309_105_B	< LOD	6.44	< LOD	7.74	< LOD	6.10	32.66	6.37	< LOD	18.05	26.41	15.39	< LOD	53.55
309_105_A	< LOD	4.62	< LOD	6.48	< LOD	4.27	22.32	4.78	< LOD	12.63	25.49	11.51	< LOD	37.13
309_105_A	< LOD	5.03	< LOD	6.96	< LOD	4.63	24.44	5.17	< LOD	12.96	27.35	12.09	< LOD	40.14
309_105_A	< LOD	4.39	< LOD	7.04	< LOD	4.33	17.30	4.78	< LOD	12.56	41.62	12.33	< LOD	36.23

Table A8: *continued*

Sample	Th	Th Error	Pb	Pb Error	Se	Se Error	As	As Error	Hg	Hg Error	Zn	Zn Error	Cu	Cu Error
309_150	< LOD	4.97	< LOD	6.56	< LOD	4.44	< LOD	5.43	< LOD	11.82	23.41	11.93	< LOD	36.22
309_150	< LOD	5.20	< LOD	8.11	< LOD	4.71	< LOD	5.94	< LOD	12.87	33.20	13.53	< LOD	39.14
309_150	< LOD	4.77	< LOD	6.77	< LOD	4.37	< LOD	5.30	< LOD	11.13	36.89	12.45	< LOD	34.56
309_84	< LOD	6.80	< LOD	9.78	< LOD	6.28	41.29	8.26	< LOD	14.47	112.58	26.10	175.11	36.96
309_84	< LOD	7.70	< LOD	9.81	< LOD	6.25	49.36	8.69	< LOD	14.88	141.25	27.23	186.84	37.51
309_84	< LOD	7.11	< LOD	9.24	< LOD	5.97	45.60	8.20	< LOD	13.96	139.79	26.28	180.32	36.05
ESH	< LOD	16.74	< LOD	25.86	< LOD	19.53	< LOD	19.03	< LOD	45.36	< LOD	54.90	< LOD	125.35
ESH	22.44	10.71	23.06	14.10	< LOD	13.71	< LOD	15.17	< LOD	29.85	49.10	26.99	< LOD	96.80
ESH	< LOD	14.17	< LOD	20.15	16.26	9.63	< LOD	15.60	< LOD	30.09	< LOD	35.01	< LOD	94.00
CROMO1_2_AC	< LOD	5.75	< LOD	7.50	< LOD	4.93	< LOD	5.61	< LOD	10.65	< LOD	20.88	57.12	24.85
CROMO1_2_AC	< LOD	5.25	< LOD	6.91	< LOD	4.68	< LOD	5.63	< LOD	10.17	21.48	13.87	85.50	25.70
CROMO1_2_AC	< LOD	5.48	< LOD	7.43	< LOD	4.33	< LOD	5.85	< LOD	9.95	< LOD	19.78	62.67	23.59
CROMO1_2_AA	< LOD	5.17	< LOD	8.08	< LOD	4.57	< LOD	5.99	< LOD	10.84	20.26	11.69	< LOD	33.40
CROMO1_2_AA	< LOD	4.84	< LOD	7.25	< LOD	4.39	< LOD	6.17	< LOD	11.44	< LOD	16.73	< LOD	32.98
CROMO1_2_AA	< LOD	5.75	< LOD	8.29	< LOD	4.40	< LOD	6.35	< LOD	11.31	29.66	12.78	< LOD	36.00
CROMO1_2_AB	< LOD	6.48	< LOD	9.12	< LOD	6.21	< LOD	7.31	< LOD	15.31	< LOD	23.53	< LOD	51.00
CROMO1_2_AB	< LOD	6.64	< LOD	9.62	< LOD	5.93	< LOD	7.15	< LOD	16.07	< LOD	23.20	< LOD	47.40
CROMO1_2_AB	< LOD	6.82	< LOD	9.70	< LOD	6.13	< LOD	7.72	< LOD	16.40	< LOD	23.66	< LOD	47.97
CROMO1_1_A	< LOD	6.91	< LOD	8.61	< LOD	5.10	< LOD	6.54	< LOD	12.33	< LOD	19.09	< LOD	34.39
CROMO1_1_A	< LOD	4.85	< LOD	6.86	< LOD	4.30	< LOD	5.59	< LOD	8.68	< LOD	13.76	< LOD	26.86
CROMO1_1_A	< LOD	5.79	14.29	6.75	< LOD	5.14	< LOD	7.16	< LOD	11.73	< LOD	18.01	< LOD	33.37
CROMO1_1_B	< LOD	9.00	< LOD	12.65	< LOD	8.84	< LOD	10.05	< LOD	20.09	< LOD	30.76	< LOD	58.88
CROMO1_1_B	< LOD	9.49	< LOD	13.03	< LOD	9.15	< LOD	9.71	< LOD	21.34	< LOD	33.20	< LOD	60.12
CROMO1_1_B	< LOD	9.67	< LOD	11.01	< LOD	8.36	< LOD	9.65	< LOD	20.85	< LOD	31.31	< LOD	61.08

Table A8: *continued*

Sample	Th	Th Error	Pb	Pb Error	Se	Se Error	As	As Error	Hg	Hg Error	Zn	Zn Error	Cu	Cu Error
CROMO1_2_CA	< LOD	7.43	< LOD	8.93	< LOD	5.83	< LOD	7.09	< LOD	12.51	< LOD	21.15	< LOD	34.07
CROMO1_2_CA	< LOD	7.37	< LOD	9.64	< LOD	6.22	< LOD	7.28	< LOD	12.49	< LOD	21.84	< LOD	36.77
CROMO1_2_CA	< LOD	6.66	< LOD	9.44	< LOD	6.21	< LOD	7.28	< LOD	12.95	< LOD	22.08	< LOD	36.84
CROMO1_2_CB	< LOD	9.59	< LOD	11.99	< LOD	7.90	< LOD	9.45	< LOD	18.34	< LOD	29.32	< LOD	53.68
CROMO1_2_CB	< LOD	8.13	< LOD	12.16	< LOD	8.99	< LOD	10.03	< LOD	20.27	< LOD	30.46	< LOD	57.97
CROMO1_2_CB	< LOD	9.22	< LOD	11.28	< LOD	9.93	< LOD	10.00	< LOD	21.24	< LOD	31.12	< LOD	64.45
CROMO2_4A	< LOD	5.21	< LOD	6.87	< LOD	4.58	< LOD	5.35	< LOD	13.26	< LOD	15.74	< LOD	40.59
CROMO2_4A	< LOD	4.79	< LOD	7.30	< LOD	4.34	< LOD	5.17	< LOD	11.90	< LOD	14.07	< LOD	36.27
CROMO2_4A	< LOD	4.61	< LOD	6.76	< LOD	4.24	< LOD	5.15	< LOD	11.65	< LOD	13.82	< LOD	37.20
CROMO2_4B	< LOD	8.06	< LOD	11.40	< LOD	8.37	< LOD	8.53	< LOD	22.69	< LOD	30.35	< LOD	70.75
CROMO2_4B	< LOD	9.12	< LOD	12.48	< LOD	9.15	< LOD	10.03	< LOD	26.03	< LOD	34.49	< LOD	76.67
CROMO2_4B	< LOD	9.03	< LOD	12.99	12.98	7.61	< LOD	10.24	< LOD	29.90	< LOD	38.43	< LOD	89.08
CROMO2_2	< LOD	4.34	< LOD	6.97	< LOD	4.38	< LOD	4.96	< LOD	12.64	< LOD	13.56	< LOD	38.84
CROMO2_2	< LOD	4.46	< LOD	6.61	< LOD	4.64	< LOD	5.34	< LOD	13.98	< LOD	16.18	< LOD	44.38
CROMO2_2	< LOD	5.15	< LOD	7.34	< LOD	4.71	< LOD	5.29	< LOD	13.40	< LOD	15.40	< LOD	42.83
CROMO2_3A	< LOD	5.84	< LOD	8.23	< LOD	5.63	< LOD	6.68	< LOD	13.91	23.70	14.32	< LOD	44.62
CROMO2_3A	< LOD	4.53	< LOD	6.84	< LOD	4.19	< LOD	5.61	< LOD	10.18	23.71	10.69	< LOD	30.05
CROMO2_3A	< LOD	5.61	< LOD	7.15	< LOD	4.37	< LOD	5.63	< LOD	11.22	< LOD	16.70	< LOD	34.94
CROMO2_3B	< LOD	8.91	< LOD	12.52	< LOD	8.57	< LOD	9.95	29.55	15.92	88.83	26.88	< LOD	75.50
CROMO2_3B	< LOD	9.05	< LOD	12.63	< LOD	8.74	< LOD	10.44	< LOD	23.96	81.33	26.59	< LOD	72.00
CROMO2_3B	< LOD	8.78	< LOD	14.88	< LOD	10.82	< LOD	11.45	< LOD	28.24	51.21	28.79	< LOD	86.45
CROMO2_1A	< LOD	5.30	< LOD	6.75	< LOD	5.04	< LOD	5.40	< LOD	13.48	< LOD	17.39	< LOD	41.69
CROMO2_1A	< LOD	5.02	< LOD	7.92	< LOD	4.36	< LOD	5.56	< LOD	12.65	< LOD	15.25	< LOD	39.72
CROMO2_1A	< LOD	5.51	< LOD	7.58	< LOD	5.16	< LOD	5.72	< LOD	13.56	< LOD	16.17	< LOD	42.08
CROMO2_1B	< LOD	6.52	< LOD	9.90	< LOD	7.46	< LOD	7.99	< LOD	19.49	< LOD	24.36	< LOD	59.70
CROMO2_1B	< LOD	6.59	< LOD	10.46	< LOD	7.46	< LOD	8.45	< LOD	21.63	< LOD	24.79	< LOD	65.10
CROMO2_1B	< LOD	6.85	< LOD	10.75	< LOD	7.48	< LOD	7.88	< LOD	20.31	< LOD	24.85	< LOD	61.38

168

Table A8: *continued*

Sample	Th	Th Error	Pb	Pb Error	Se	Se Error	As	As Error	Hg	Hg Error	Zn	Zn Error	Cu	Cu Error
PHL_1	< LOD	5.11	< LOD	6.99	< LOD	4.36	< LOD	5.13	< LOD	11.70	< LOD	18.14	< LOD	36.29
PHL_1	< LOD	5.05	< LOD	7.04	< LOD	4.24	< LOD	5.45	< LOD	11.34	< LOD	17.29	< LOD	35.99
PHL_1	< LOD	4.43	< LOD	6.50	< LOD	4.03	< LOD	4.74	< LOD	10.48	< LOD	16.78	< LOD	32.40
PHL_2B	< LOD	4.85	< LOD	6.45	< LOD	4.39	< LOD	4.98	< LOD	11.28	< LOD	16.63	57.51	25.97
PHL_2B	< LOD	4.89	< LOD	6.60	< LOD	4.19	< LOD	4.77	< LOD	11.51	< LOD	16.23	53.96	25.43
PHL_2B	< LOD	4.98	< LOD	7.08	< LOD	4.54	< LOD	5.39	< LOD	11.10	< LOD	16.39	62.91	26.38
PHL_2C	< LOD	5.08	< LOD	7.18	< LOD	5.00	< LOD	5.64	< LOD	12.51	< LOD	17.65	< LOD	36.40
PHL_2C	< LOD	5.13	< LOD	7.33	< LOD	4.63	< LOD	5.59	< LOD	11.86	< LOD	17.19	< LOD	37.50
PHL_2C	< LOD	4.15	< LOD	5.15	< LOD	3.34	< LOD	3.98	< LOD	8.07	< LOD	11.79	< LOD	23.99
PHL_2A	< LOD	4.59	< LOD	6.88	< LOD	4.58	< LOD	5.09	< LOD	11.75	< LOD	16.76	86.12	28.72
PHL_2A	< LOD	4.66	< LOD	6.05	< LOD	4.14	< LOD	4.82	< LOD	10.54	< LOD	14.73	51.04	23.88
PHL_2A	< LOD	4.78	< LOD	6.63	< LOD	4.12	< LOD	4.90	< LOD	11.24	< LOD	15.52	72.82	25.95
PHL_3	< LOD	5.39	< LOD	7.02	< LOD	5.06	< LOD	5.73	< LOD	12.94	< LOD	18.55	< LOD	41.02
PHL_3	< LOD	5.09	< LOD	6.93	< LOD	4.47	< LOD	5.52	< LOD	12.53	< LOD	16.84	< LOD	38.14
PHL_3	< LOD	6.08	< LOD	7.68	< LOD	5.30	< LOD	5.82	< LOD	13.69	< LOD	19.47	< LOD	43.66
PHL_4	< LOD	5.46	< LOD	7.18	< LOD	4.55	< LOD	5.87	< LOD	10.20	< LOD	18.18	348.63	34.59
PHL_4	< LOD	5.94	< LOD	7.34	< LOD	4.82	< LOD	6.25	< LOD	10.37	25.36	13.18	358.54	35.52
PHL_4	< LOD	6.13	< LOD	8.04	< LOD	4.70	< LOD	6.02	< LOD	10.34	< LOD	18.10	374.58	35.35
PHL_5	< LOD	5.03	< LOD	6.40	< LOD	4.26	< LOD	4.77	< LOD	10.81	< LOD	15.22	< LOD	32.71
PHL_5	< LOD	4.28	< LOD	5.86	< LOD	4.12	< LOD	4.46	< LOD	10.53	< LOD	14.15	< LOD	33.58
PHL_5	< LOD	5.15	< LOD	7.08	< LOD	4.06	< LOD	5.24	< LOD	11.00	< LOD	16.05	< LOD	33.31

169

Table A8: *continued*

Sample	Ni	Ni Error	Co	Co Error	Fe	Fe Error	Mn	Mn Error	Cr	Cr Error	V	V Error
167_238	3334.03	95.64	186.19	122.01	47495.71	422.28	1331.67	109.26	1080.69	41.72	43.87	27.12
167_238	3805.79	105.31	324.75	132.66	51785.91	454.97	1495.75	118.36	1069.95	33.35	< LOD	32.60
167_238	3538.81	96.89	311.18	120.94	47098.51	414.06	1227.17	103.52	984.76	32.46	< LOD	31.24
HLSC_1	2852.23	94.72	237.31	128.24	46779.33	441.75	1268.17	118.04	2005.01	44.56	51.52	23.50
HLSC_1	2670.33	92.73	258.89	127.66	45341.33	438.63	1297.06	119.07	1967.19	47.14	< LOD	38.50
HLSC_1	2903.19	96.42	219.96	131.52	48535.79	454.10	1390.14	122.17	1941.42	46.39	42.05	25.41
HLSC_4	2787.01	106.26	296.41	177.49	72466.30	614.58	1447.33	141.13	1617.09	49.79	47.82	29.36
HLSC_4	2292.47	89.87	< LOD	225.64	60575.23	521.90	1165.44	118.78	1576.32	48.63	49.89	28.71
HLSC_4	3158.89	113.58	294.50	188.54	80918.50	654.09	1450.29	145.01	1564.19	43.92	62.29	26.45
313_210	3214.69	119.01	< LOD	311.55	93366.91	729.15	1409.90	150.80	1392.28	45.96	67.16	29.37
313_210	2442.97	95.16	< LOD	247.86	69685.15	574.34	1032.01	118.53	1395.20	49.29	< LOD	48.92
313_210	2923.15	112.70	321.92	198.19	84939.34	687.18	1331.50	143.34	1421.55	49.10	80.17	32.64
313_329	1992.64	100.63	< LOD	285.99	73110.38	666.21	1345.43	145.65	990.13	39.00	40.45	26.96
313_329	1956.37	101.33	< LOD	290.85	73426.34	676.01	1268.54	143.73	927.04	37.42	42.75	25.93
313_329	1882.79	94.19	353.63	177.28	66603.80	610.67	1227.87	133.17	910.61	37.79	41.11	26.42
313_356	3896.19	135.41	< LOD	293.79	75455.58	687.13	1391.53	155.00	1458.91	43.79	< LOD	38.62
313_356	3052.59	109.86	270.22	159.48	58312.07	550.53	1105.34	126.26	1384.70	43.75	59.23	25.78
313_356	2682.63	96.24	< LOD	204.37	48949.02	472.13	952.46	109.34	1372.99	42.69	< LOD	38.48
313_318	2848.42	99.59	< LOD	210.60	51081.21	485.88	1268.37	131.57	3634.48	67.26	77.48	30.52
313_318	3242.36	111.34	< LOD	234.72	57859.56	543.31	1410.06	147.05	3556.75	65.74	69.91	28.96
313_318	3051.70	103.67	302.97	143.45	51752.05	492.80	1314.07	135.06	3559.70	66.66	86.03	30.40
309_105_B	4726.52	121.47	335.73	135.38	48973.15	462.79	876.07	102.55	1111.61	41.22	< LOD	39.77
309_105_B	5789.82	149.30	310.35	168.99	62686.34	582.55	1237.33	131.67	1016.32	39.87	46.79	26.33
309_105_B	6155.90	158.37	467.39	179.05	65457.80	611.89	1227.78	135.97	1065.65	40.20	< LOD	36.93
309_105_A	4129.92	108.24	299.99	132.63	52935.22	455.82	1106.13	119.60	4391.95	73.44	59.54	29.22
309_105_A	4085.77	113.18	307.97	138.78	52355.28	476.57	1117.27	124.14	4230.49	74.62	49.13	30.23
309_105_A	4073.97	110.30	198.45	131.62	49873.58	455.36	1100.50	120.57	4354.20	76.24	63.79	30.54

Table A8: *continued*

Sample	Ni	Ni Error	Co	Co Error	Fe	Fe Error	Mn	Mn Error	Cr	Cr Error	V	V Error
309_150	2703.41	96.50	< LOD	215.22	54727.32	498.42	994.61	121.21	2939.46	60.11	83.34	30.93
309_150	2889.50	105.20	337.20	160.80	61134.53	553.21	964.81	128.69	2889.03	60.26	75.84	29.79
309_150	2541.58	92.84	< LOD	211.23	53718.55	488.20	987.27	117.59	2825.78	58.97	82.96	29.90
309_84	148.18	65.73	< LOD	536.78	225056.98	1270.07	4678.70	270.79	295.94	49.87	582.32	103.13
309_84	150.69	67.15	< LOD	538.82	224888.53	1267.51	4457.99	264.96	284.90	47.50	589.07	97.41
309_84	126.08	63.40	< LOD	515.48	214671.36	1215.55	4414.56	257.70	218.22	45.50	448.94	96.39
ESH	< LOD	187.95	< LOD	77.79	408.60	128.14	< LOD	153.28	13.21	8.28	< LOD	14.25
ESH	< LOD	136.16	< LOD	54.54	196.51	84.89	< LOD	125.28	< LOD	12.30	< LOD	13.55
ESH	< LOD	146.53	< LOD	66.70	227.71	87.57	< LOD	120.65	< LOD	12.60	< LOD	13.88
CROMO1_2_AC	< LOD	64.51	< LOD	300.04	91002.48	702.93	1699.55	145.11	< LOD	42.05	359.02	56.38
CROMO1_2_AC	< LOD	64.39	< LOD	295.44	88496.77	686.92	1562.83	139.14	< LOD	42.89	306.36	54.22
CROMO1_2_AC	< LOD	57.62	< LOD	277.02	83641.25	650.70	1520.65	133.73	< LOD	41.17	305.27	55.67
CROMO1_2_AA	1780.69	83.36	< LOD	218.26	53738.29	507.00	963.57	116.12	1531.57	48.18	114.72	35.33
CROMO1_2_AA	1729.61	82.26	< LOD	219.66	54353.24	507.37	951.29	114.94	1616.50	49.58	93.99	36.11
CROMO1_2_AA	1815.98	85.74	262.51	151.92	55942.11	524.35	973.41	123.40	1970.29	53.10	131.05	35.37
CROMO1_2_AB	3046.67	125.68	< LOD	345.26	97748.95	801.78	1376.59	165.22	2109.70	58.47	96.94	37.87
CROMO1_2_AB	3026.97	124.39	< LOD	342.24	97212.96	793.13	1292.00	161.72	2092.50	58.24	90.16	36.59
CROMO1_2_AB	3047.88	127.17	< LOD	354.77	101510.90	825.13	1493.67	173.73	2124.97	59.00	97.44	36.28
CROMO1_1_A	< LOD	68.19	< LOD	300.31	80662.95	702.97	1761.48	154.26	< LOD	33.88	166.88	41.36
CROMO1_1_A	< LOD	53.33	< LOD	220.84	59160.30	521.08	1236.31	113.37	< LOD	34.81	191.92	41.58
CROMO1_1_A	< LOD	65.74	< LOD	293.60	78801.42	688.07	1766.78	152.69	< LOD	34.32	156.65	40.88
CROMO1_1_B	< LOD	116.02	< LOD	454.88	116188.96	1092.01	2763.97	246.26	< LOD	32.47	129.57	35.82
CROMO1_1_B	< LOD	113.68	< LOD	461.79	120477.61	1105.82	2881.82	249.92	66.23	22.34	121.86	35.63
CROMO1_1_B	164.88	80.49	< LOD	452.58	113358.70	1070.41	2720.24	243.21	43.36	22.08	160.69	36.42

Table A8: *continued*

Sample	Ni	Ni Error	Co	Co Error	Fe	Fe Error	Mn	Mn Error	Cr	Cr Error	V	V Error
CROMO1_2_CA	< LOD	74.47	< LOD	323.36	88302.38	752.58	1922.24	165.20	< LOD	34.59	172.09	41.65
CROMO1_2_CA	< LOD	73.16	< LOD	322.22	86812.97	749.12	2089.01	169.94	< LOD	35.99	184.11	41.48
CROMO1_2_CA	< LOD	77.52	< LOD	341.55	92726.28	798.86	2047.86	175.91	< LOD	35.22	212.81	41.66
CROMO1_2_CB	392.55	81.99	< LOD	420.07	110297.95	1019.36	2532.72	229.70	161.84	25.03	130.18	35.67
CROMO1_2_CB	289.43	81.63	< LOD	434.50	109892.79	1039.11	2586.39	235.22	174.84	24.89	128.43	34.47
CROMO1_2_CB	331.24	90.38	< LOD	487.48	125762.21	1178.53	2860.96	263.62	168.69	25.04	143.31	35.70
CROMO2_4A	4451.60	121.52	452.80	142.47	50800.18	483.10	648.93	95.99	561.95	30.47	< LOD	33.69
CROMO2_4A	4107.47	111.42	210.64	131.63	49182.21	454.53	541.97	86.73	549.55	31.19	< LOD	35.20
CROMO2_4A	4016.99	110.27	264.43	130.95	48254.96	449.99	522.42	87.07	770.91	33.87	< LOD	35.20
CROMO2_4B	6630.28	206.33	< LOD	433.30	119009.69	1025.93	1134.67	173.47	257.44	26.02	< LOD	37.39
CROMO2_4B	7505.56	233.52	< LOD	489.13	130727.70	1141.79	1181.14	190.39	321.03	26.49	< LOD	34.47
CROMO2_4B	8186.73	262.21	< LOD	547.51	146668.91	1302.27	1390.38	219.02	306.31	25.96	< LOD	35.48
CROMO2_2	4824.22	119.55	308.86	129.44	46999.31	442.87	769.95	96.70	752.70	35.28	47.93	25.34
CROMO2_2	5554.99	134.65	386.05	145.49	53525.53	496.68	752.67	104.64	761.68	35.69	< LOD	38.29
CROMO2_2	5317.52	130.39	232.53	139.21	51019.72	480.18	713.58	102.07	792.77	35.73	< LOD	38.13
CROMO2_3A	3781.32	126.12	373.79	189.22	75864.01	652.94	1397.20	154.75	2192.13	55.32	< LOD	50.02
CROMO2_3A	2431.36	85.51	246.60	131.35	52121.28	453.27	1090.27	112.19	2285.62	57.41	67.18	34.68
CROMO2_3A	2671.35	93.61	< LOD	215.40	57443.68	498.23	1055.18	118.69	1972.33	53.67	71.61	33.81
CROMO2_3B	5515.54	201.58	< LOD	482.18	134003.28	1149.10	2001.84	232.71	980.44	39.73	74.19	32.69
CROMO2_3B	5405.32	197.64	< LOD	475.09	128730.48	1109.87	1819.99	220.39	933.86	39.10	< LOD	47.05
CROMO2_3B	5918.07	226.97	< LOD	544.64	146283.61	1301.87	2074.58	259.90	962.38	38.48	59.77	31.84
CROMO2_1A	4047.89	121.96	338.93	148.86	51628.15	509.48	708.01	100.84	327.33	26.01	< LOD	32.91
CROMO2_1A	3690.55	112.90	354.39	140.02	48556.89	477.83	777.45	98.93	269.99	25.22	< LOD	33.56
CROMO2_1A	3904.00	121.09	530.16	150.54	50564.79	507.40	639.82	98.01	306.99	25.83	< LOD	34.29
CROMO2_1B	5034.05	167.60	< LOD	310.29	69066.38	724.97	857.96	136.11	208.50	22.75	< LOD	32.03
CROMO2_1B	5744.64	184.06	< LOD	337.80	75582.87	780.68	1220.76	157.63	206.43	22.87	< LOD	32.48
CROMO2_1B	5310.24	173.17	< LOD	324.03	73652.82	753.47	993.46	144.15	185.59	22.54	< LOD	31.99

Table A8: *continued*

Sample	Ni	Ni Error	Co	Co Error	Fe	Fe Error	Mn	Mn Error	Cr	Cr Error	V	V Error
PHL_1	2809.97	100.50	382.58	177.62	80763.18	613.56	1329.35	130.23	1313.04	51.12	< LOD	47.89
PHL_1	2718.53	97.71	368.13	172.82	78394.73	597.02	1241.70	127.23	1530.65	54.58	< LOD	50.27
PHL_1	2646.27	89.51	299.13	157.29	75637.00	545.04	1357.92	122.21	1939.61	58.26	< LOD	48.51
PHL_2B	2165.92	88.67	284.31	150.29	58750.50	518.51	1037.73	117.61	1890.39	53.50	76.64	31.92
PHL_2B	2069.52	86.61	340.77	148.29	57221.90	509.30	984.15	114.64	1835.24	52.78	65.26	31.23
PHL_2B	2229.52	90.06	227.43	150.91	59120.38	522.72	1043.06	118.36	1884.94	52.96	63.59	30.35
PHL_2C	2831.10	103.33	288.56	178.69	78372.31	619.80	1244.51	133.04	1479.67	51.92	< LOD	44.27
PHL_2C	2745.78	99.63	280.58	170.85	74610.47	592.38	1198.55	127.61	1390.46	51.50	< LOD	46.37
PHL_2C	1650.42	63.35	181.48	108.39	45569.93	374.98	751.84	81.31	1238.46	49.20	< LOD	46.73
PHL_2A	2896.22	101.63	< LOD	227.61	59311.35	529.75	911.61	118.74	2231.59	57.08	68.84	31.34
PHL_2A	2504.46	87.45	199.40	129.62	49929.81	448.40	776.82	101.74	2292.26	57.92	51.90	30.00
PHL_2A	2686.15	92.93	218.94	137.89	53550.11	476.96	870.66	108.86	2240.21	57.71	< LOD	46.48
PHL_3	3090.42	111.86	531.18	186.09	77207.58	637.25	1294.85	141.89	2247.84	60.00	66.98	32.92
PHL_3	2859.16	103.49	287.34	172.43	73148.43	597.45	1315.76	135.68	2190.65	59.25	< LOD	48.07
PHL_3	3317.70	118.01	< LOD	291.03	83304.90	679.64	1364.77	151.06	2329.26	61.07	< LOD	47.72
PHL_4	270.34	48.94	< LOD	216.10	50564.68	507.16	959.80	108.47	< LOD	33.59	343.84	59.18
PHL_4	275.62	50.24	< LOD	221.40	50980.34	517.53	919.52	108.46	< LOD	33.30	346.40	58.34
PHL_4	290.88	50.32	< LOD	218.71	50210.20	504.86	889.23	105.60	< LOD	33.35	318.87	57.88
PHL_5	2752.68	94.60	373.12	156.82	68477.06	539.98	1161.57	117.71	1685.87	55.47	< LOD	47.12
PHL_5	2627.79	91.12	301.64	151.42	66160.68	523.18	1079.51	111.73	1411.48	51.90	< LOD	47.53
PHL_5	3031.60	98.77	240.46	158.50	70756.62	550.29	1195.72	120.63	1723.83	55.70	< LOD	51.22

Table A8: *continued*

Sample	Ti	Ti Error	Sc	Sc Error	Ca	Ca Error	K	K Error	S	S Error	Sb	Sb Error
167_238	< LOD	85.99	< LOD	27.55	13070.62	297.21	212.63	137.52	< LOD	739.55	< LOD	12.16
167_238	< LOD	70.67	< LOD	22.30	12805.88	237.21	296.90	113.94	< LOD	598.73	< LOD	12.04
167_238	< LOD	67.88	< LOD	22.36	12666.83	236.63	< LOD	162.89	< LOD	591.75	< LOD	12.23
HLSC_1	136.15	51.93	33.65	20.30	22904.92	328.43	< LOD	181.11	< LOD	665.47	< LOD	12.00
HLSC_1	93.15	57.52	< LOD	31.85	22381.04	345.71	< LOD	191.34	< LOD	666.33	< LOD	12.11
HLSC_1	99.69	56.77	< LOD	31.64	22360.15	342.46	< LOD	188.63	< LOD	617.68	< LOD	12.21
HLSC_4	98.84	65.00	< LOD	33.66	18098.57	357.12	< LOD	222.14	< LOD	731.40	< LOD	13.35
HLSC_4	113.85	63.45	36.85	21.67	16943.48	341.81	< LOD	219.18	< LOD	790.22	< LOD	13.36
HLSC_4	145.63	58.11	< LOD	29.51	17343.23	313.73	238.51	134.92	< LOD	712.76	< LOD	13.12
313_210	222.35	64.88	31.12	18.01	10792.62	276.00	302.37	144.29	< LOD	835.33	< LOD	13.55
313_210	354.05	75.67	< LOD	30.53	13694.44	327.67	275.48	155.21	< LOD	850.42	< LOD	12.82
313_210	262.82	72.14	< LOD	29.04	11376.88	298.27	< LOD	210.89	< LOD	909.39	< LOD	12.43
313_329	< LOD	87.69	< LOD	14.97	1973.56	135.00	256.16	125.05	< LOD	658.25	< LOD	12.24
313_329	< LOD	83.32	< LOD	13.83	1973.72	132.82	354.66	127.74	< LOD	626.39	< LOD	12.51
313_329	< LOD	84.26	< LOD	13.88	1933.40	133.31	< LOD	180.43	< LOD	611.46	< LOD	11.86
313_356	< LOD	84.30	< LOD	14.73	2538.72	142.47	289.38	124.44	< LOD	665.21	< LOD	12.17
313_356	112.34	53.75	< LOD	15.26	2446.29	142.92	317.67	126.78	< LOD	687.09	< LOD	11.85
313_356	< LOD	85.48	< LOD	15.07	2448.41	139.68	290.87	122.45	< LOD	676.22	< LOD	11.63
313_318	144.76	65.63	< LOD	26.38	12075.60	283.91	< LOD	201.40	< LOD	747.90	< LOD	11.82
313_318	147.77	62.33	< LOD	26.64	12582.32	285.72	284.11	138.62	< LOD	769.40	< LOD	11.64
313_318	181.28	65.02	< LOD	27.54	13523.69	299.09	208.29	137.83	< LOD	709.60	< LOD	11.71
309_105_B	89.80	58.20	< LOD	11.30	238.99	90.27	275.52	124.28	847.59	491.64	< LOD	11.81
309_105_B	111.20	55.78	< LOD	11.21	382.41	94.48	< LOD	172.91	1174.84	521.26	< LOD	12.10
309_105_B	< LOD	83.13	< LOD	11.68	270.48	90.44	< LOD	178.24	1458.22	542.67	< LOD	11.84
309_105_A	223.07	63.47	< LOD	12.41	480.62	103.59	< LOD	181.53	1177.78	547.57	< LOD	12.16
309_105_A	159.67	65.90	< LOD	12.80	447.40	105.83	< LOD	189.02	837.16	533.21	< LOD	11.94
309_105_A	149.47	65.04	< LOD	13.16	553.11	110.16	< LOD	194.40	< LOD	760.00	< LOD	12.40

Table A8: *continued*.

Sample	Ti	Ti Error	Sc	Sc Error	Ca	Ca Error	K	K Error	S	S Error	Sb	Sb Error
309_150	470.44	69.70	< LOD	12.03	414.00	95.87	270.83	124.29	< LOD	697.44	< LOD	12.12
309_150	548.06	67.86	< LOD	11.70	376.19	95.72	218.03	123.11	< LOD	685.38	< LOD	12.07
309_150	489.67	67.20	< LOD	12.02	473.42	97.53	265.77	124.03	754.28	484.39	< LOD	12.17
309_84	9243.00	283.21	78.17	39.94	25707.33	612.95	760.39	279.72	< LOD	1627.94	< LOD	18.48
309_84	8624.25	264.79	61.60	37.97	25474.83	588.84	980.24	279.19	< LOD	1439.50	< LOD	18.89
309_84	8484.45	267.09	63.46	37.70	25324.74	582.82	861.54	271.50	< LOD	1616.48	21.29	13.44
ESH	< LOD	28.90	< LOD	3.92	635.81	40.89	< LOD	101.36	< LOD	229.90	< LOD	19.62
ESH	< LOD	27.60	< LOD	4.02	584.23	39.32	< LOD	101.82	< LOD	253.06	< LOD	18.98
ESH	< LOD	28.51	< LOD	4.01	591.12	39.65	124.66	68.97	< LOD	238.16	< LOD	17.99
CROMO1_2_AC	2566.92	138.48	94.47	43.25	57789.48	702.56	2247.04	283.50	< LOD	1143.99	< LOD	16.79
CROMO1_2_AC	2635.52	136.47	83.68	42.71	57737.67	696.31	2559.25	290.23	< LOD	1133.94	< LOD	16.92
CROMO1_2_AC	2521.87	139.00	< LOD	63.79	58853.18	699.14	2124.58	276.77	< LOD	1202.31	< LOD	16.07
CROMO1_2_AA	1096.15	88.83	< LOD	58.41	62509.09	643.36	321.61	192.05	< LOD	1006.23	< LOD	14.50
CROMO1_2_AA	986.21	91.25	70.38	39.53	62990.42	650.18	< LOD	280.41	< LOD	1034.89	< LOD	14.46
CROMO1_2_AA	1020.89	87.22	60.66	38.92	62655.52	642.18	< LOD	282.72	< LOD	1014.69	< LOD	14.33
CROMO1_2_AB	617.37	88.65	< LOD	32.22	14209.68	337.12	< LOD	232.43	< LOD	866.85	< LOD	12.91
CROMO1_2_AB	639.46	85.91	< LOD	31.97	14338.89	338.54	293.01	160.36	< LOD	820.15	< LOD	13.00
CROMO1_2_AB	681.88	85.09	< LOD	32.66	14527.41	343.08	387.73	166.11	< LOD	944.59	< LOD	12.78
CROMO1_1_A	1884.52	105.47	52.65	29.10	33313.57	471.35	2725.73	244.10	< LOD	848.24	< LOD	13.27
CROMO1_1_A	2015.25	105.52	47.98	29.41	33565.10	477.80	2620.74	243.57	< LOD	853.74	< LOD	14.01
CROMO1_1_A	1949.93	105.78	82.44	30.03	33962.97	479.34	2269.19	233.85	< LOD	862.71	< LOD	13.58
CROMO1_1_B	1239.37	89.55	73.71	27.53	31582.04	440.25	1864.44	209.93	< LOD	848.38	< LOD	14.43
CROMO1_1_B	1116.47	88.70	79.32	27.67	31524.12	441.14	2097.57	217.26	< LOD	849.55	< LOD	15.20
CROMO1_1_B	1267.81	89.28	58.48	27.48	31749.75	443.24	1930.24	212.81	< LOD	861.80	< LOD	14.58

Table A8: *continued*

Sample	Ti	Ti Error	Sc	Sc Error	Ca	Ca Error	K	K Error	S	S Error	Sb	Sb Error
CROMO1_2_CA	1688.89	104.26	60.27	27.92	28821.60	446.19	922.04	189.01	< LOD	892.00	< LOD	13.11
CROMO1_2_CA	1853.60	104.16	< LOD	40.79	29381.91	446.11	949.56	188.99	< LOD	968.44	< LOD	13.51
CROMO1_2_CA	1718.14	101.89	< LOD	40.61	29012.79	443.96	1149.43	195.67	< LOD	876.79	< LOD	13.22
CROMO1_2_CB	967.63	86.02	37.07	23.60	22760.47	379.15	738.17	168.65	< LOD	805.33	< LOD	13.96
CROMO1_2_CB	1024.33	83.43	< LOD	34.38	22850.04	374.11	555.88	159.40	< LOD	727.45	< LOD	14.42
CROMO1_2_CB	1089.99	86.38	39.63	23.45	22517.97	375.86	845.84	171.83	< LOD	772.05	< LOD	14.60
CROMO2_4A	< LOD	71.71	< LOD	9.71	< LOD	110.99	< LOD	154.87	< LOD	616.98	< LOD	11.52
CROMO2_4A	< LOD	73.73	< LOD	9.71	186.67	79.56	< LOD	160.08	< LOD	640.06	< LOD	12.02
CROMO2_4A	< LOD	75.93	< LOD	9.15	125.31	76.27	< LOD	160.45	< LOD	614.34	< LOD	12.00
CROMO2_4B	< LOD	81.08	< LOD	10.99	385.29	90.82	< LOD	171.74	< LOD	681.27	< LOD	13.19
CROMO2_4B	< LOD	74.72	< LOD	10.38	376.71	88.48	< LOD	168.64	681.21	445.42	< LOD	14.08
CROMO2_4B	< LOD	77.17	< LOD	10.35	322.13	85.96	< LOD	165.17	906.34	463.66	< LOD	15.32
CROMO2_2	102.79	53.02	< LOD	10.28	201.17	85.21	184.56	115.91	864.37	476.41	< LOD	11.90
CROMO2_2	< LOD	81.66	< LOD	11.05	271.74	88.47	< LOD	172.43	946.84	489.24	< LOD	11.73
CROMO2_2	< LOD	81.83	< LOD	10.63	343.82	89.68	192.47	117.68	952.46	484.46	< LOD	11.18
CROMO2_3A	653.79	80.35	< LOD	16.24	2253.23	151.97	1756.12	192.76	< LOD	752.95	< LOD	12.23
CROMO2_3A	742.60	82.97	< LOD	16.92	2745.11	165.08	1788.79	197.39	< LOD	751.12	< LOD	12.53
CROMO2_3A	736.91	80.53	< LOD	16.94	2725.02	163.74	1955.59	201.69	< LOD	808.44	< LOD	12.33
CROMO2_3B	685.47	77.78	< LOD	13.64	1704.22	137.49	1748.40	191.16	< LOD	734.80	< LOD	14.57
CROMO2_3B	737.62	78.39	< LOD	14.22	1410.96	130.70	1711.15	189.62	< LOD	666.29	< LOD	14.25
CROMO2_3B	691.00	77.18	< LOD	14.01	1570.50	130.97	1634.79	184.01	< LOD	658.15	< LOD	15.12
CROMO2_1A	< LOD	71.30	< LOD	10.23	327.28	79.07	< LOD	159.27	1054.57	449.48	< LOD	11.24
CROMO2_1A	< LOD	72.96	< LOD	9.68	259.57	77.68	< LOD	159.13	< LOD	569.54	< LOD	11.38
CROMO2_1A	< LOD	72.71	< LOD	9.79	346.40	79.95	< LOD	157.58	< LOD	575.05	< LOD	11.67
CROMO2_1B	< LOD	68.84	< LOD	8.58	< LOD	102.93	< LOD	158.49	< LOD	590.82	< LOD	12.69
CROMO2_1B	< LOD	69.86	< LOD	8.50	124.29	70.59	221.26	109.31	796.53	416.76	< LOD	13.02
CROMO2_1B	< LOD	69.46	< LOD	8.77	109.98	70.27	190.43	107.92	< LOD	542.77	< LOD	12.85

Table A8: *continued*

Sample	Ti	Ti Error	Sc	Sc Error	Ca	Ca Error	K	K Error	S	S Error	Sb	Sb Error
PHL_1	< LOD	106.88	< LOD	13.55	< LOD	154.23	290.94	150.55	< LOD	858.98	< LOD	12.85
PHL_1	< LOD	110.58	< LOD	14.63	< LOD	158.15	310.18	152.86	< LOD	826.60	< LOD	12.58
PHL_1	132.73	71.13	< LOD	13.61	< LOD	144.17	< LOD	207.09	< LOD	798.40	< LOD	12.67
PHL_2B	270.15	70.92	37.49	19.34	11906.07	296.57	< LOD	214.40	< LOD	662.92	< LOD	12.36
PHL_2B	313.15	70.16	< LOD	27.15	10903.87	284.72	215.57	142.96	< LOD	806.94	< LOD	12.49
PHL_2B	250.91	67.29	< LOD	27.52	11476.23	289.15	< LOD	209.00	< LOD	791.43	< LOD	12.25
PHL_2C	105.18	64.19	< LOD	13.87	< LOD	161.36	< LOD	209.75	< LOD	780.89	< LOD	12.65
PHL_2C	< LOD	99.99	< LOD	14.42	< LOD	166.59	269.26	147.49	< LOD	781.86	< LOD	12.56
PHL_2C	< LOD	104.22	< LOD	14.03	< LOD	168.51	278.64	146.45	< LOD	828.34	< LOD	12.29
PHL_2A	311.34	70.22	< LOD	28.36	12224.85	299.55	< LOD	208.01	< LOD	826.52	< LOD	12.30
PHL_2A	336.36	68.47	< LOD	30.08	13823.78	318.20	224.89	147.33	< LOD	681.76	< LOD	12.90
PHL_2A	265.46	70.77	< LOD	29.48	13245.48	313.65	< LOD	213.90	< LOD	782.31	< LOD	13.11
PHL_3	139.63	71.20	< LOD	21.28	4857.25	213.29	< LOD	213.06	< LOD	789.13	< LOD	12.71
PHL_3	120.34	71.87	< LOD	21.10	4859.33	212.99	< LOD	213.38	< LOD	707.96	< LOD	12.83
PHL_3	140.82	71.33	< LOD	20.45	4920.45	215.53	< LOD	216.99	< LOD	799.55	< LOD	12.66
PHL_4	7456.69	170.75	105.87	44.99	87853.82	740.54	< LOD	308.32	< LOD	998.59	< LOD	16.23
PHL_4	7462.30	168.70	128.41	44.80	87578.43	733.80	< LOD	303.14	< LOD	1061.48	< LOD	16.20
PHL_4	7394.78	167.93	106.52	44.31	87460.70	729.08	< LOD	302.50	< LOD	1063.51	< LOD	15.89
PHL_5	< LOD	102.88	< LOD	13.17	< LOD	151.99	< LOD	212.40	< LOD	785.08	< LOD	13.02
PHL_5	< LOD	102.51	< LOD	14.18	< LOD	154.46	< LOD	211.62	< LOD	793.93	< LOD	12.88
PHL_5	< LOD	114.87	< LOD	13.24	< LOD	149.84	< LOD	207.49	< LOD	766.64	< LOD	12.88
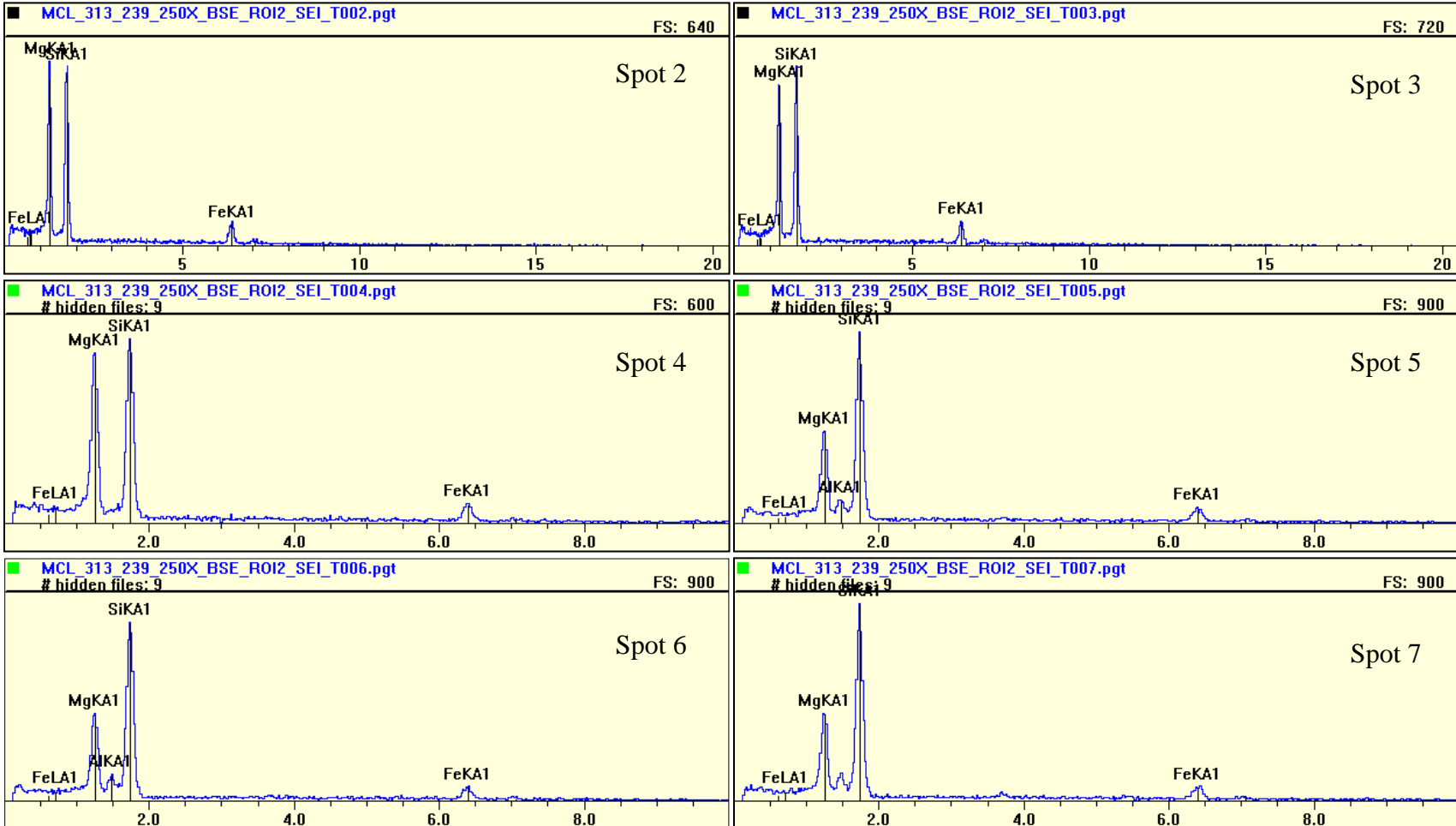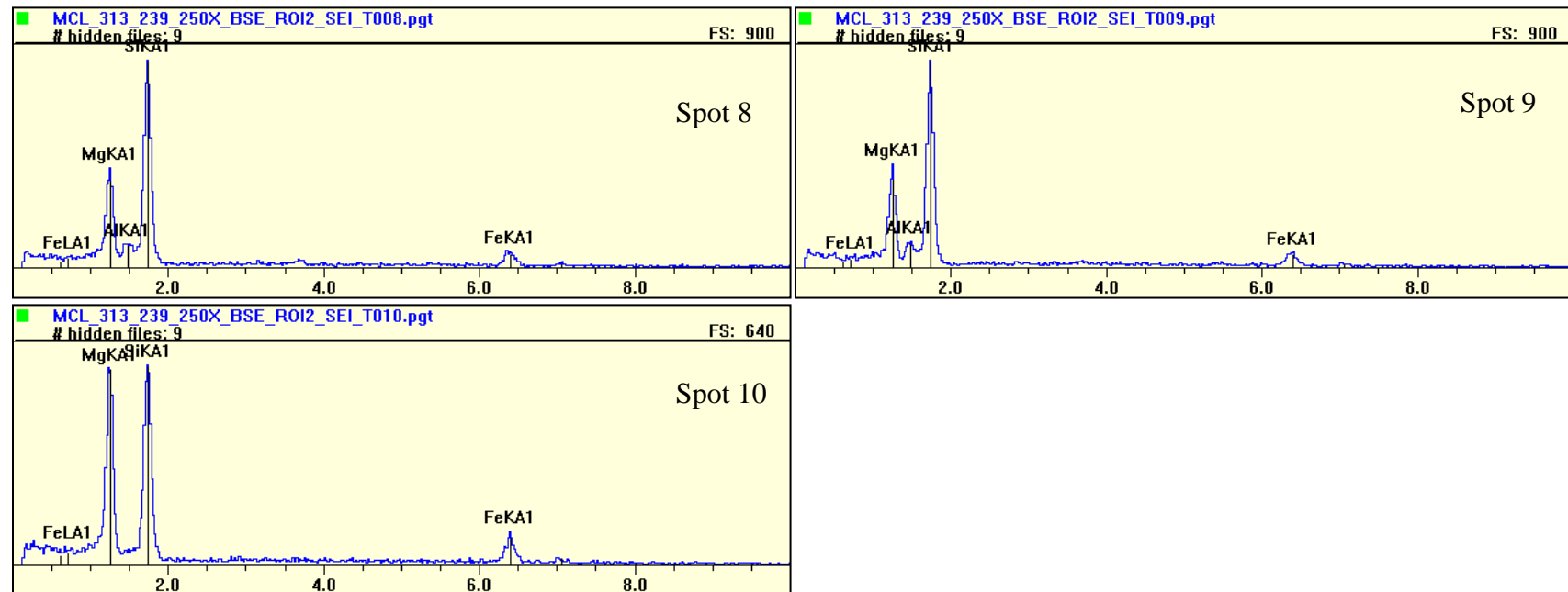
Figure A19: SEM-EDS spectra images for sample 313_329 for the inside of olivine grains (1). See also Table 7 and Figure 25.
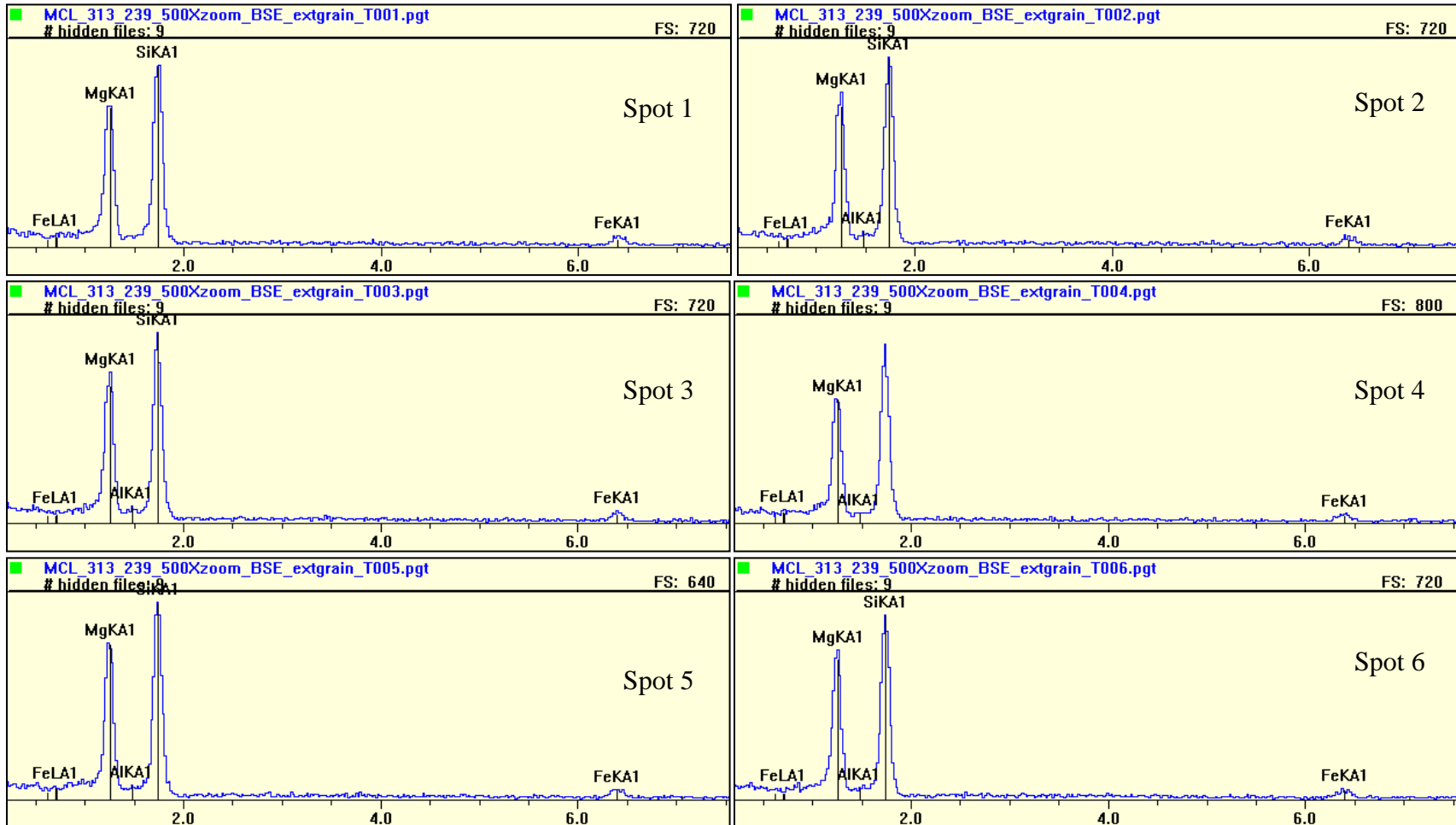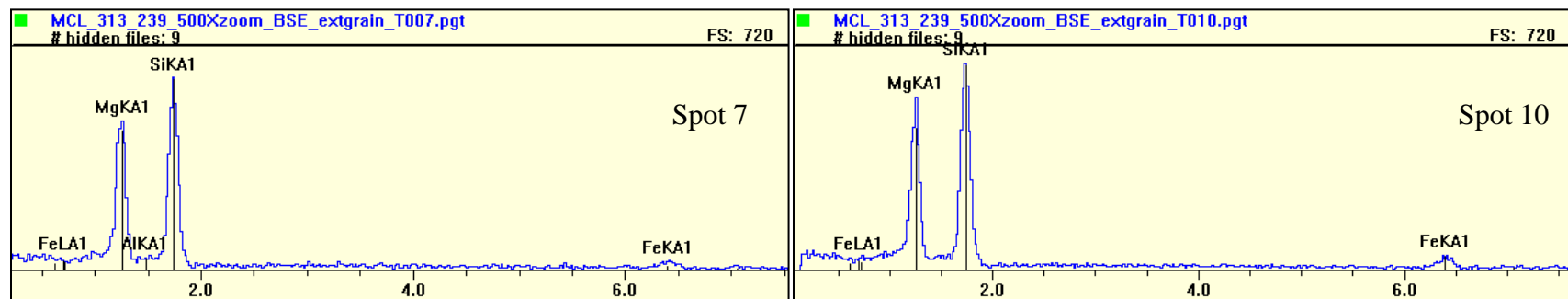
Figure A20: SEM-EDS spectra images for sample 313_329 along edges of olivine grains. See also Table 8 and Figure 26.
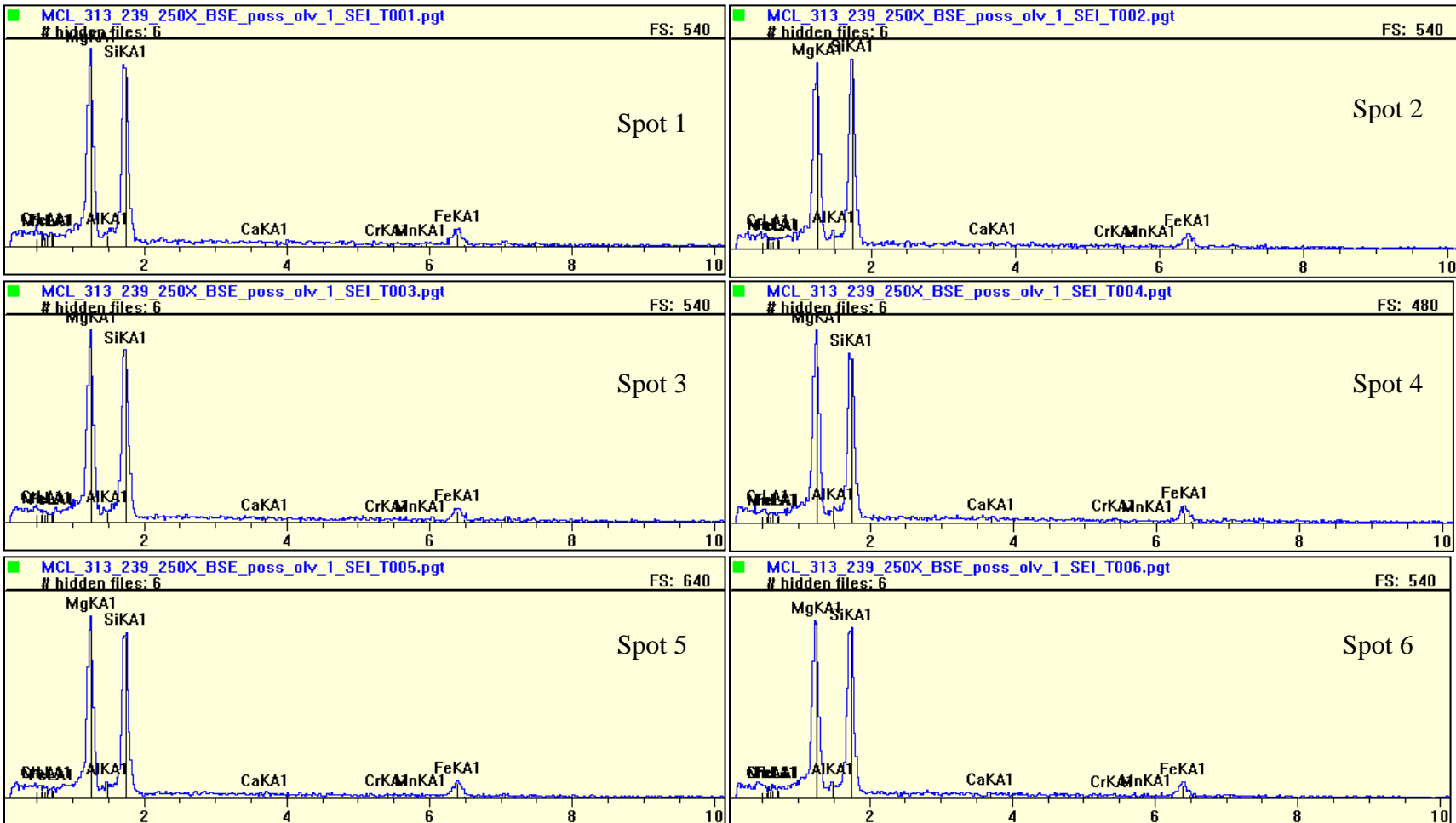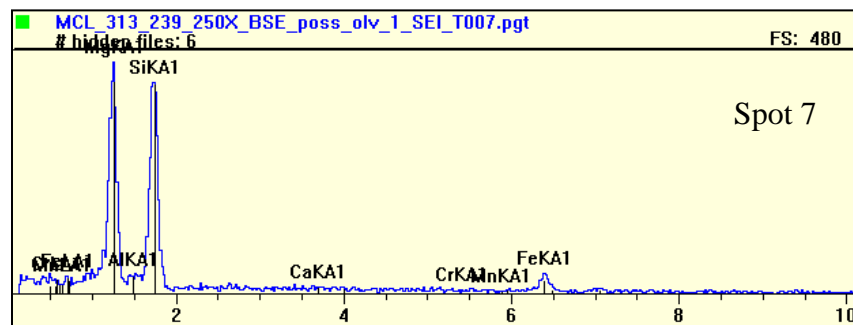
Figure A21: SEM-EDS spectra for sample 313_329 for the inside of olivine grains. See also Table 9 and Figure 27.
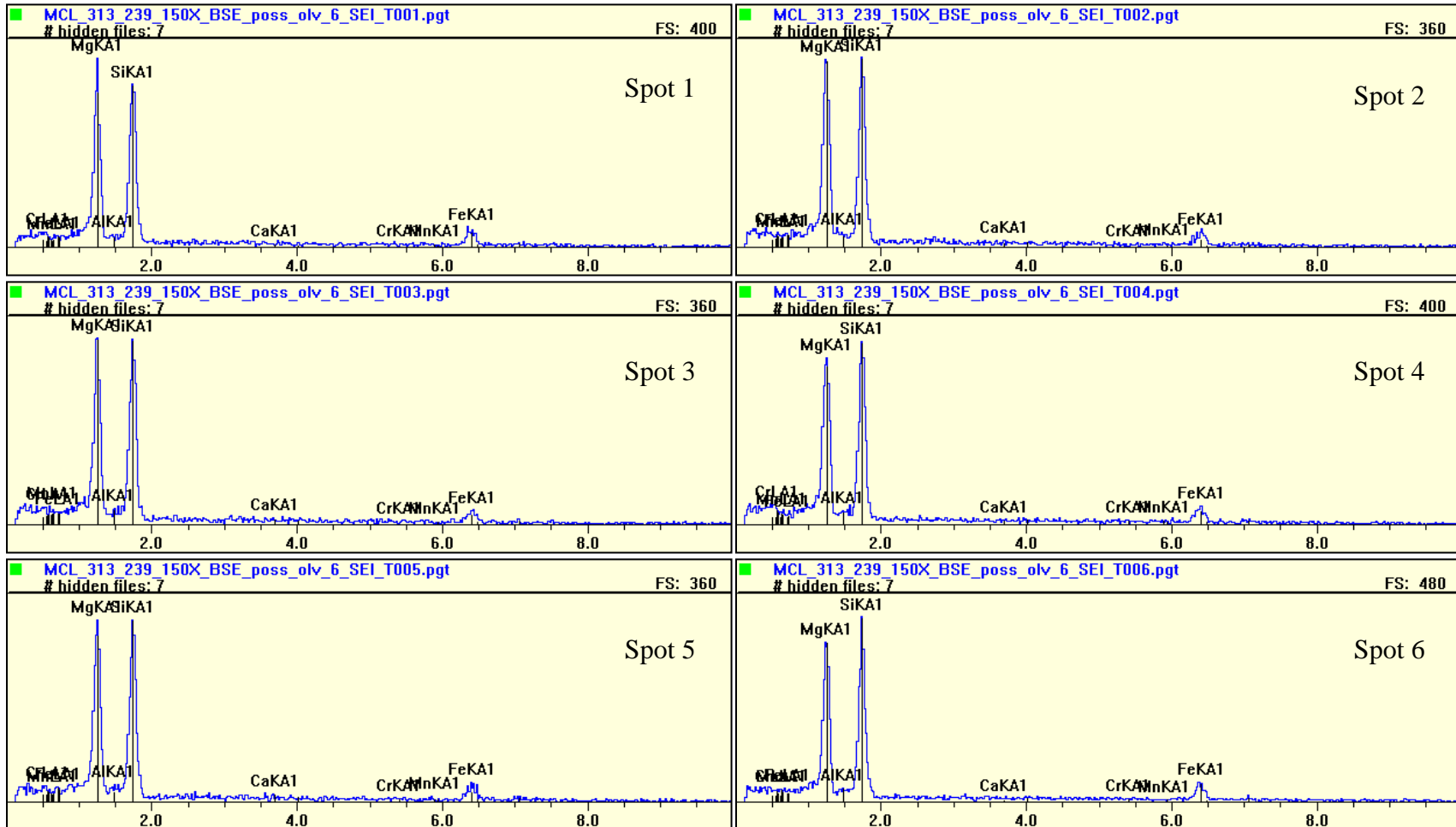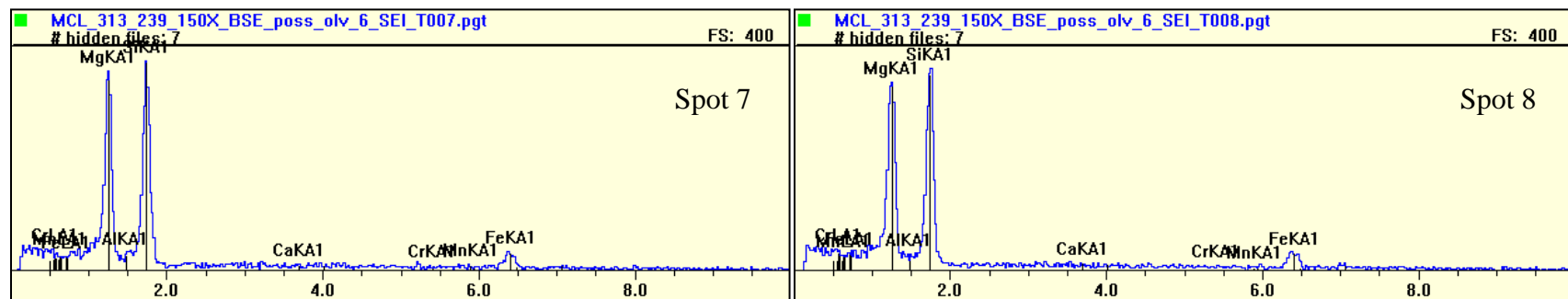
Figure A22: SEM-EDS spectra for sample 313_329 for the inside of pyroxene grains. See also Table 10 and Figure 28.
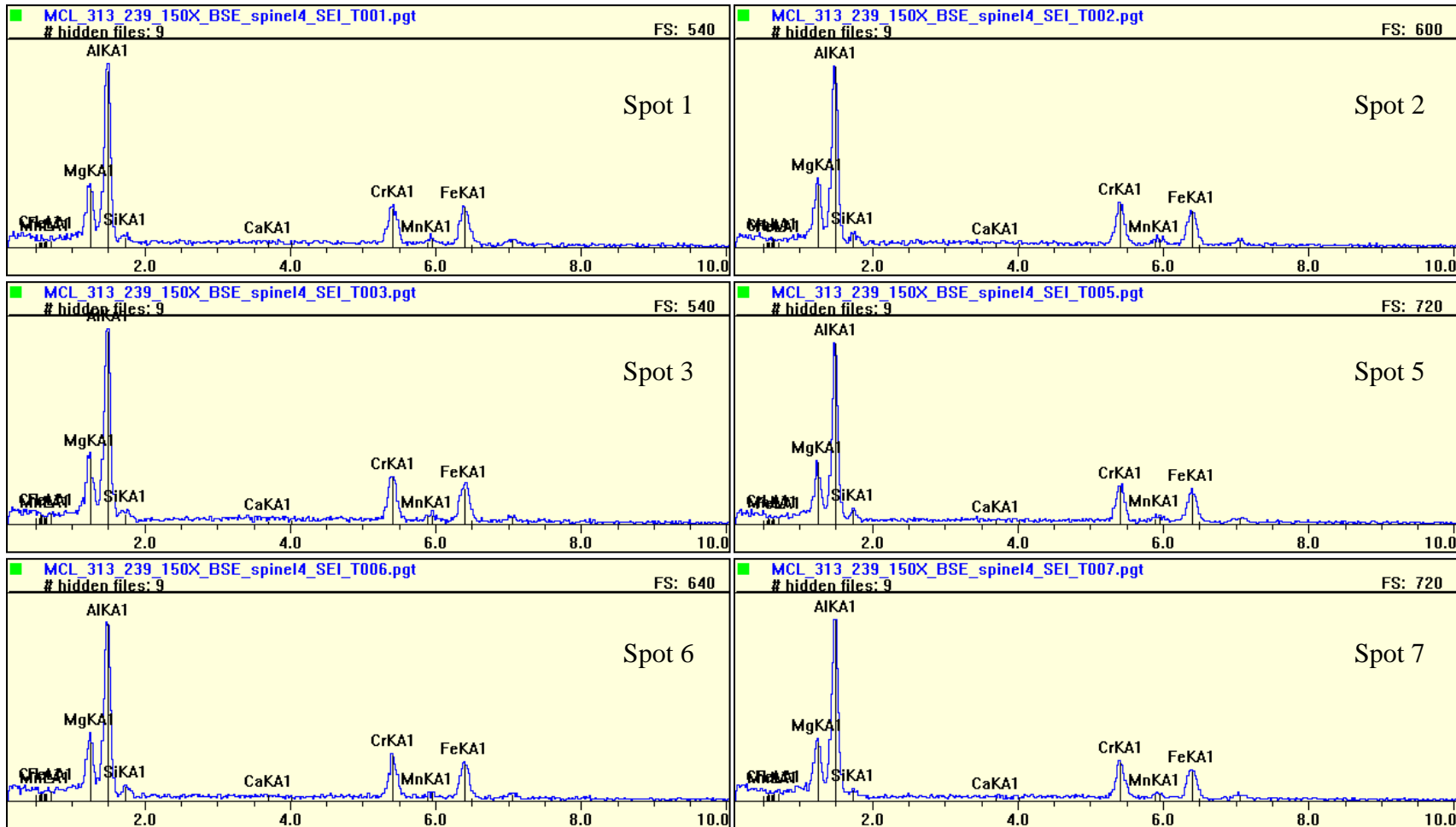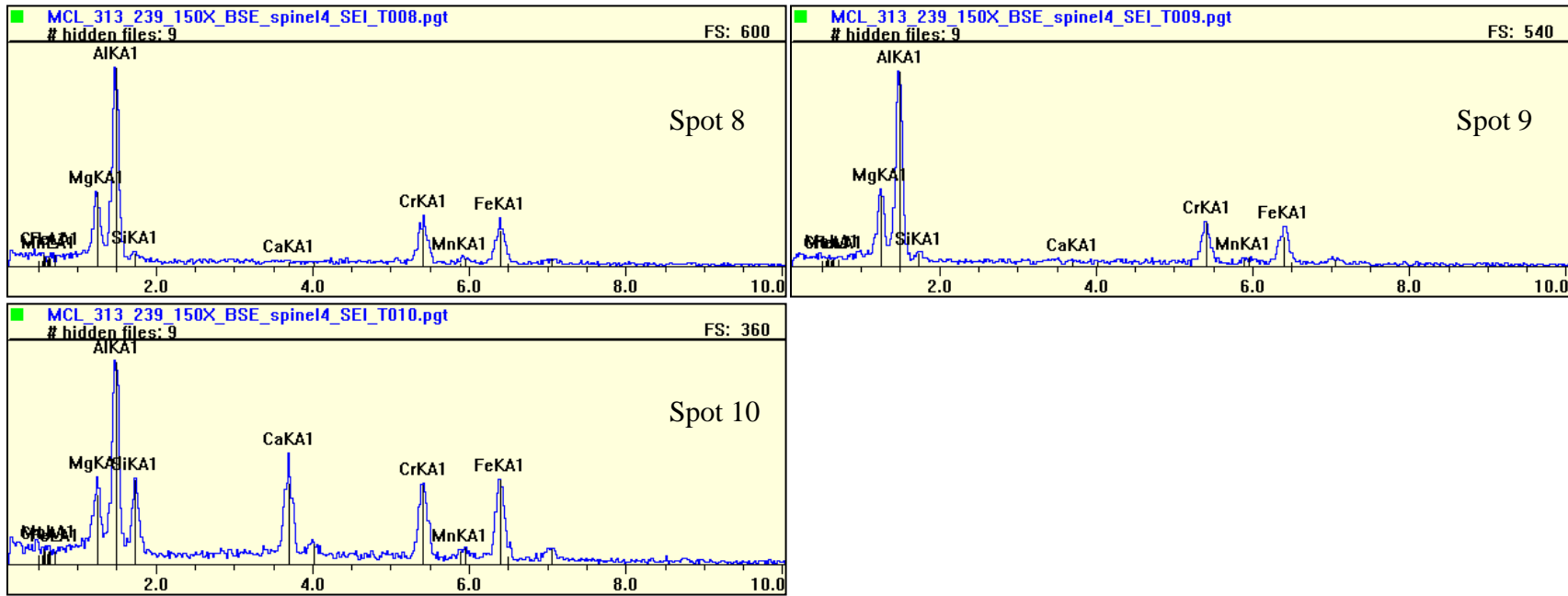
Figure A23: SEM-EDS spectra for sample 313_329 inside of a spinel grain. See also Table 11 and Figure 29.

Table A9: Mössbauer parameters for other samples collected from prospecting cores, CROMO well cores, and Philippines hand samples.

Sample		309_84	309_105_B	CROMO1_1_A‡	CROMO1_1_B‡
Sextet 1 Magnetite	IS				
	QS				
	W				
	A				
	B_{hf}				
Sextet 2 Magnetite	IS				
	QS				
	W				
	A				
	B_{hf}				
Ferric 1 Silicate	IS	0.30	0.30*	0.30*	0.37
	QS	0.66	0.41	0.41	1.17
	W	0.53	0.50	0.50	0.50
	A	17	8	8	12
Ferric 2 Silicate	IS		0.77	0.77	0.02
	QS		1.20	1.20	0.58
	W		0.40*	0.40*	0.52
	A		8	8	6
Ferrous 1 Silicate	IS	1.14	1.13	1.13	1.13
	QS	2.66	2.67	2.67	2.69
	W	0.23*	0.25	0.25	0.23*
	A	83	79	79	82
Ferrous 2 Silicate	IS		0.71	0.71	
	QS		2.77	2.77	
	W		0.30*	0.30*	
	A		5	5	
X^2		3081.07	575.85	534.21	520.74
$|X^2|$		5.6865	1.1206	1.0436	1.0125
Sum areas		100	100	100	100
Magnetite		0	0	0	0
Fe(III)		17	32	16	18
Fe(II)		83	68	84	82
%Fe^{3+} in silicates		17	32	16	18

Table A9: *continued*

Sample		CROMO1_2_AA	CROMO1_2_AB	CROMO1_2_AC‡
Sextet 1 Magnetite	**IS**			
	QS			
	W			
	A			
	Bhf			
Sextet 2 Magnetite	**IS**			
	QS			
	W			
	A			
	Bhf			
Ferric 1 Silicate	**IS**	0.33	0.39	0.45
	QS	0.67	1.19	0.41
	W	0.49	0.49	0.50
	A	13	37	15
Ferric 2 Silicate	**IS**	0.42		
	QS	1.23		
	W	0.52		
	A	16		
Ferrous 1 Silicate	**IS**	1.16	1.13	1.14
	QS	1.88	2.71	2.71
	W	0.25	0.23*	0.20
	A	12	63	78
Ferrous 2 Silicate	**IS**	1.13		0.36
	QS	2.77		2.04
	W	0.23*		0.30
	A	60		7
X^2		597.75	684.34	760.45
$|X^2|$		1.1645	1.3276	1.4754
Sum areas		100	100	100
Magnetite		0	0	0
Fe(III)		29	37	15
Fe(II)		71	63	85
%Fe $^{3+}$ in silicates		29	37	15

Table A9: *continued*

Sample		CROMO1_2_CA‡	CROMO1_2_CB‡	CROMO2_1B‡	CROMO2_3B‡
Sextet 1 Magnetite	IS			0.28	0.26
	QS			0.00	-0.04
	W			0.30	0.30
	A			10	13
	B_{hf}			493.1	488.6
Sextet 2 Magnetite	IS			0.69	0.68
	QS			-0.01	-0.02
	W			0.32	0.25
	A			11	17
	B_{hf}			461.5	461.2
Ferric 1 Silicate	IS	0.43	0.31	0.36	0.35
	QS	0.82	1.03	0.71	0.68
	W	0.50	0.91	0.64	0.56
	A	8	25	42	27
Ferric 2 Silicate	IS	0.99			
	QS	0.80			
	W	0.34			
	A	4			
Ferrous 1 Silicate	IS	1.13	1.13	1.15	1.14
	QS	2.69	2.69	2.70	2.67
	W	0.20	0.12	0.31	0.30
	A	88	75	37	44
Ferrous 2 Silicate	IS				
	QS				
	W				
	A				
X^2		1012.73	481.61	959.7	1582.26
$|X^2|$		1.9766	0.9379	1.8725	3.086
Sum areas		100	100	100	100
Magnetite		0	0	21	29
Fe(III)		12	25	42	27
Fe(II)		88	75	37	44
%Fe $^{3+}$ in silicates		12	25	53	38

Table A9: *continued*

Sample		CROMO2_4B‡	PHL_2A‡	PHL_2C‡	PHL_4
Sextet 1 Magnetite	IS	0.27	0.30	0.29	
	QS	-0.02	-0.06	0.02	
	W	0.23	0.35	0.35	
	A	19	4	14	
	B_{hf}	488.8	499.5	500.2	
Sextet 2 Magnetite	IS	0.67	1.16	1.01	
	QS	0.00	0.45	0.31	
	W	0.30	0.30	0.35	
	A	33	4	5	
	B_{hf}	458.7	413.3	331.4	
Ferric 1 Silicate	IS	0.34	0.35	0.35	0.54
	QS	0.70	0.67	0.67	0.55
	W	0.60	0.62	0.57	0.25*
	A	23	58	56	5
Ferric 2 Silicate	IS				1.03
	QS				0.76
	W				0.33
	A				8
Ferrous 1 Silicate	IS	1.13	1.14	1.14	0.54
	QS	2.68	2.67	2.79	1.68
	W	0.29	0.37	0.38	0.3*
	A	25	34	25	9
Ferrous 2 Silicate	IS				0.64
	QS				2.67
	W				0.3*
	A				6
Ferrous 3 Silicate	IS				1.15
	QS				2.66
	W				0.25*
	A				72
X^2		965.96	1975.26	1483.44	1321.81
$|X^2|$		1.8841	3.7966	2.8448	2.5599
Sum areas		100	100	100	100
Magnetite		52	8	19	0
Fe(III)		23	58	56	14
Fe(II)		25	34	25	86
%Fe $^{3+}$ in silicates		48	63	69	14

Isomer shift (IS) is in mm/s; Quadrupole splitting (QS) is in mm/s; Peak width (W) is in mm/s; magnetic hyperfine field (B_{hf}) is in tesla; % Area (A) under the curve; CHI-squared (X^2), and normalized CHI-squared ($|X^2|$). Silicates are serpentine, pyroxene, and/or chlorite.
*Indicates restricted (fixed) parameter.
‡MOSS curves fit by M.Nelms in Dyar Lab and rest were fit by A.Stander.
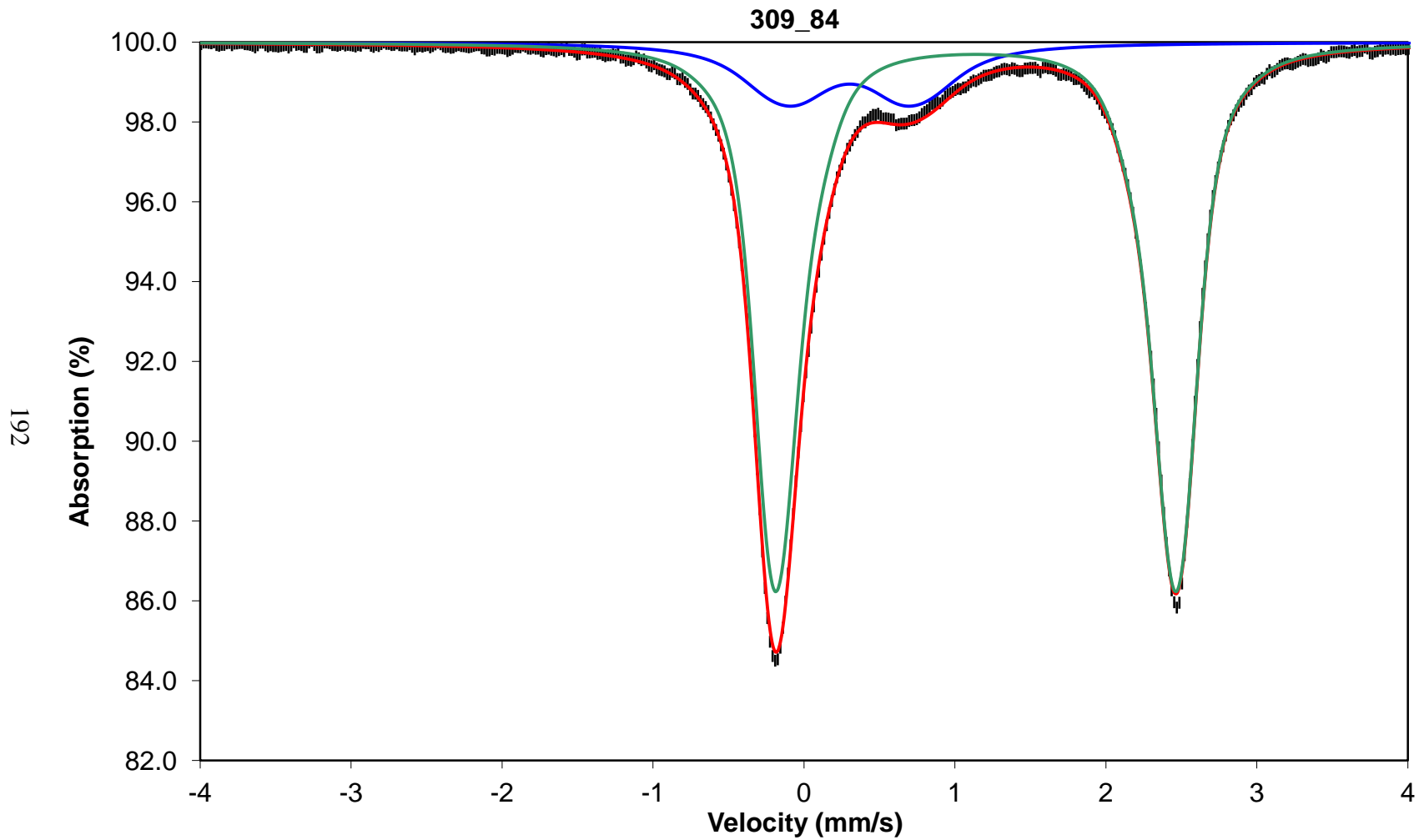
Figure A24. Mössbauer Spectroscopy 309_84 plot. The data (black dots) were fit using the Ghent program to obtain a best fit curve (red), Fe^{3+} (blue) and Fe^{2+} (green) curves.
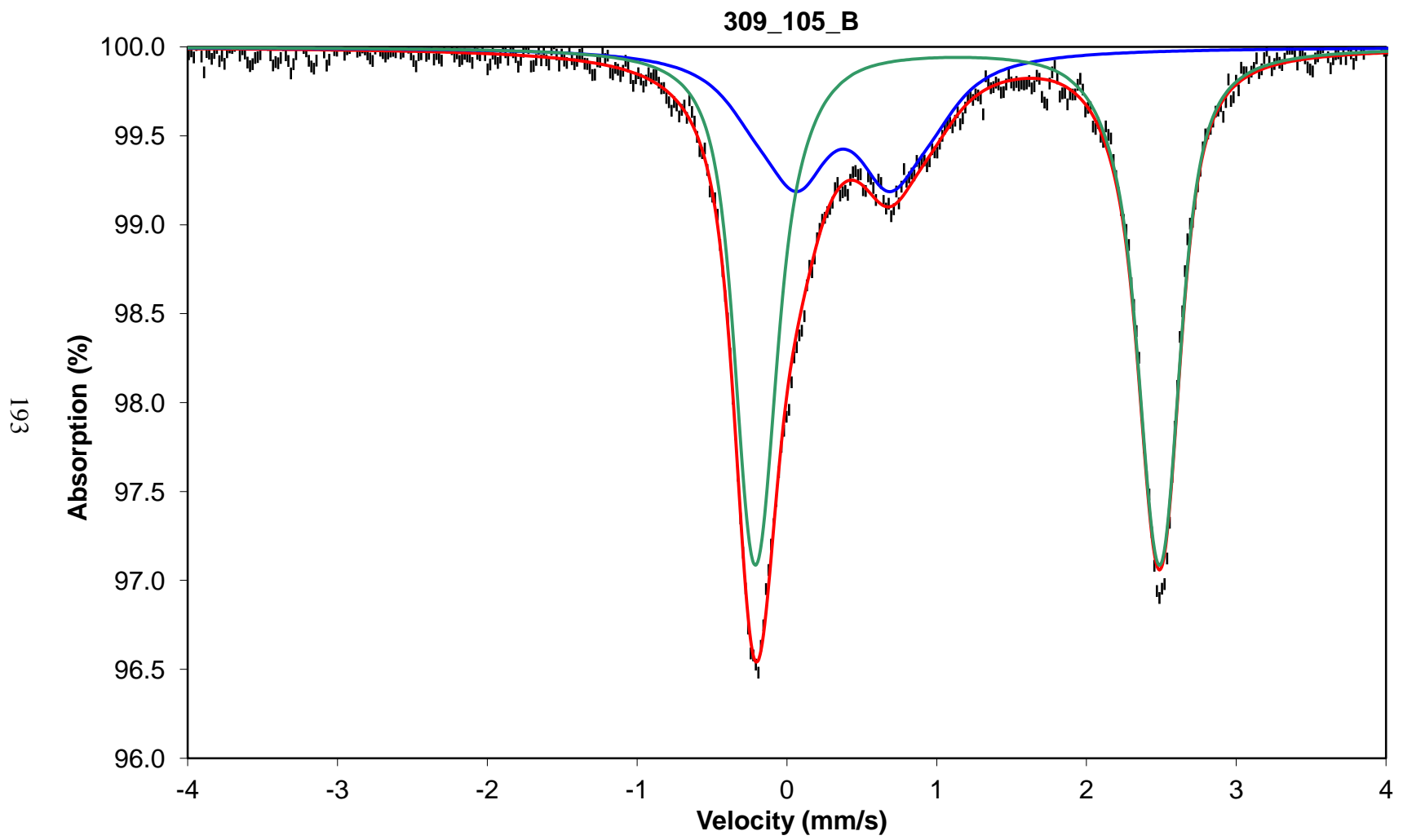
Figure A25. Mössbauer Spectroscopy 309_105_B plot. The data (black dots) were fit using the Ghent program to obtain a best fit curve (red), Fe^{3+} (blue) and Fe^{2+} (green) curves.
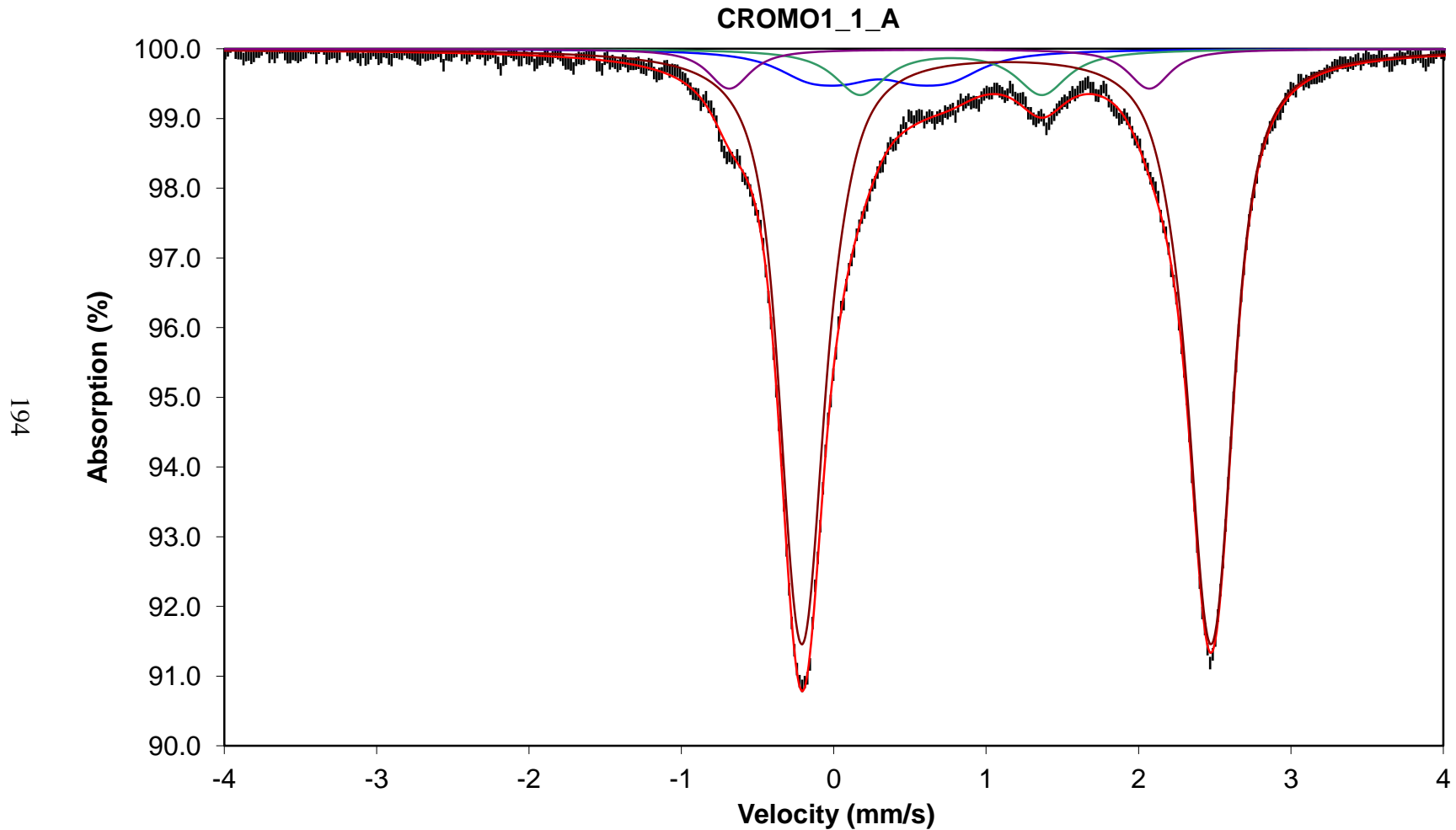
Figure A26. Mössbauer Spectroscopy CROMO1_1_A plot. The data (black dots) were fit using the Ghent program to obtain a best fit curve (red), Fe^{3+} (blue and green) and Fe^{2+} (brown and purple) curves.
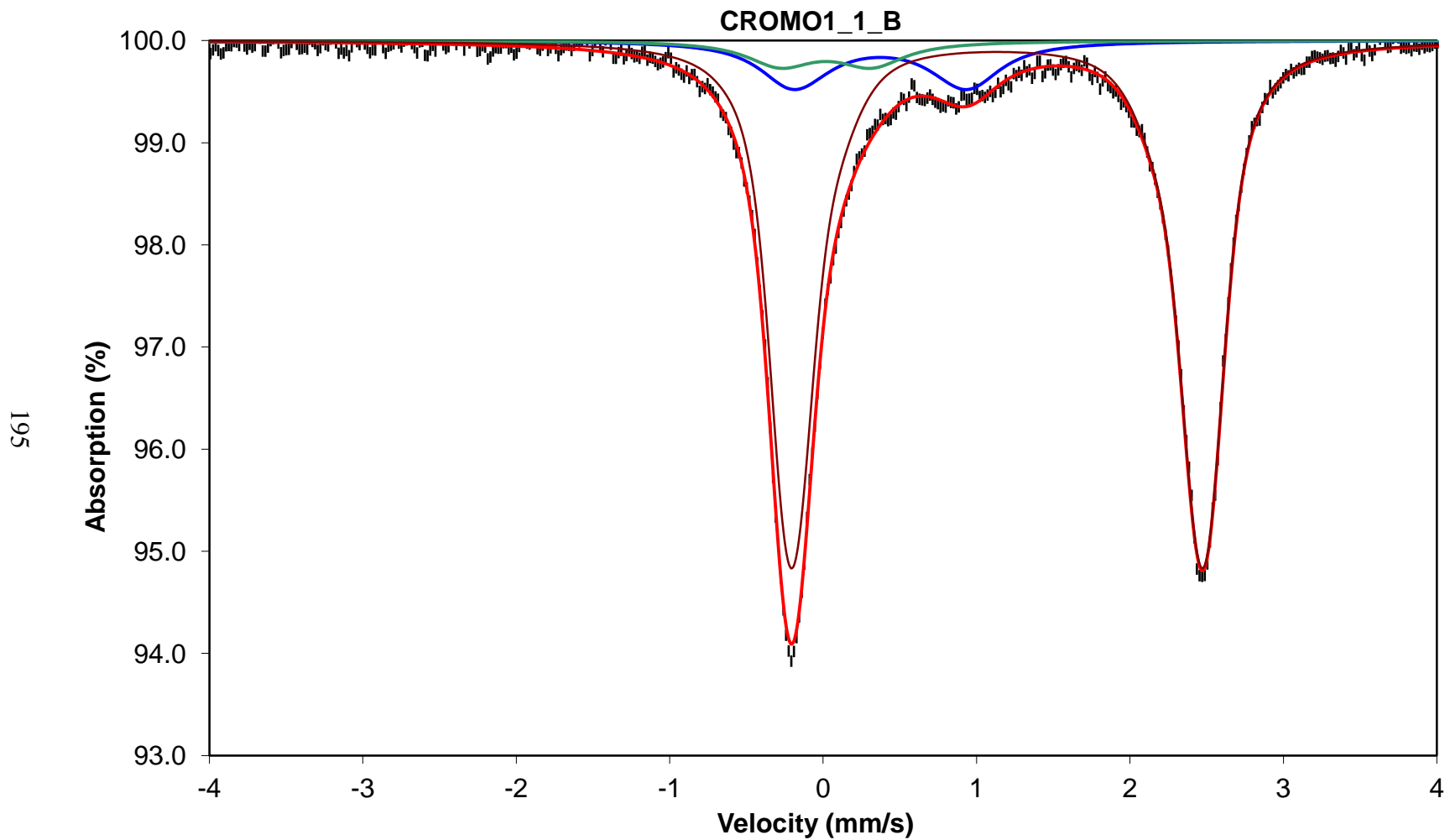
Figure A27. Mössbauer Spectroscopy CROMO1_1_B plot. The data (black dots) were fit using the Ghent program to obtain a best fit curve (red), Fe^{3+} (blue and green) and Fe^{2+} (brown) curves.
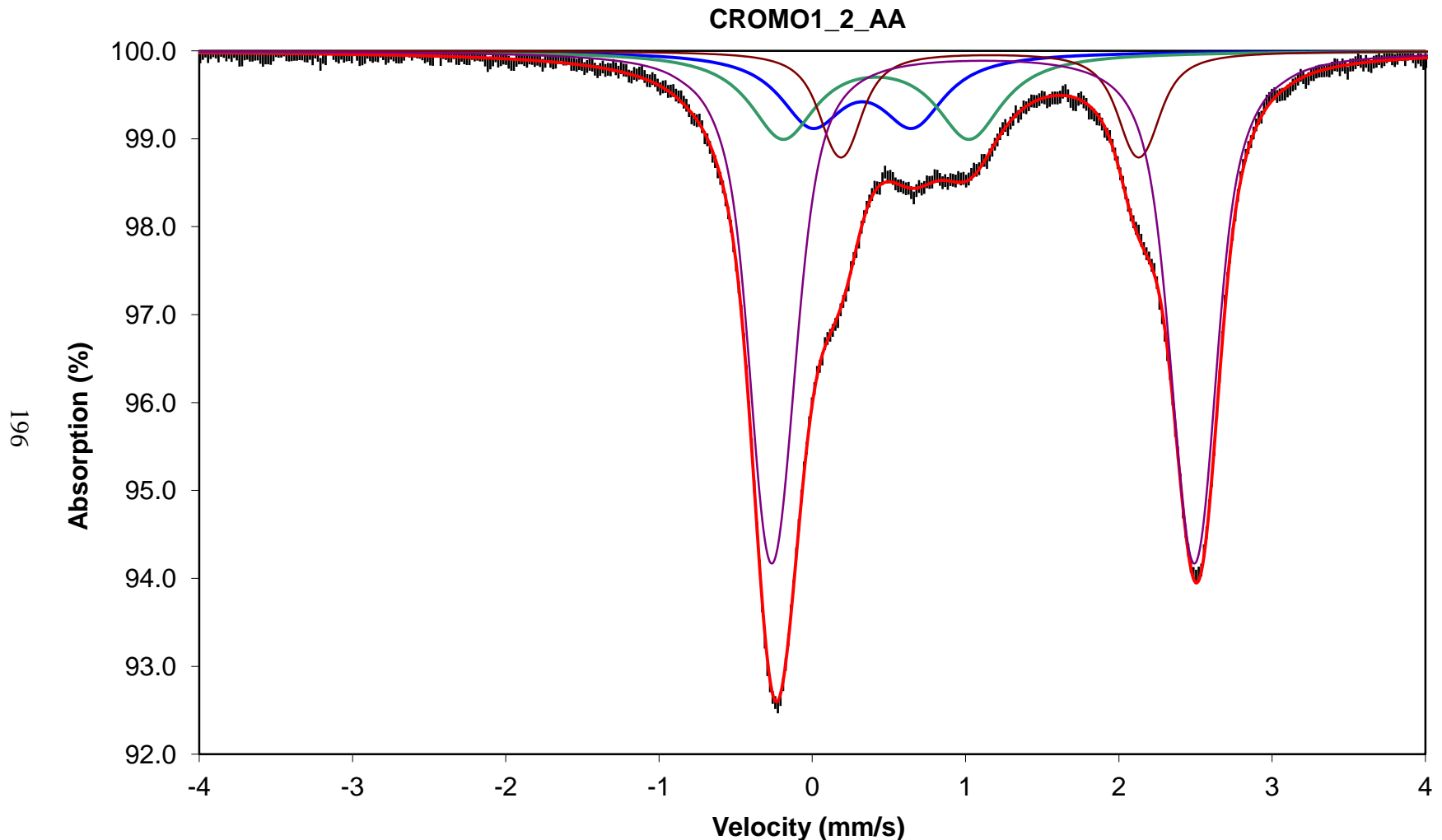
Figure A28. Mössbauer Spectroscopy CROMO1_2_AA plot. The data (black dots) were fit using the Ghent program to obtain a best fit curve (red), Fe^{3+} (blue and green) and Fe^{2+} (brown and purple) curves.
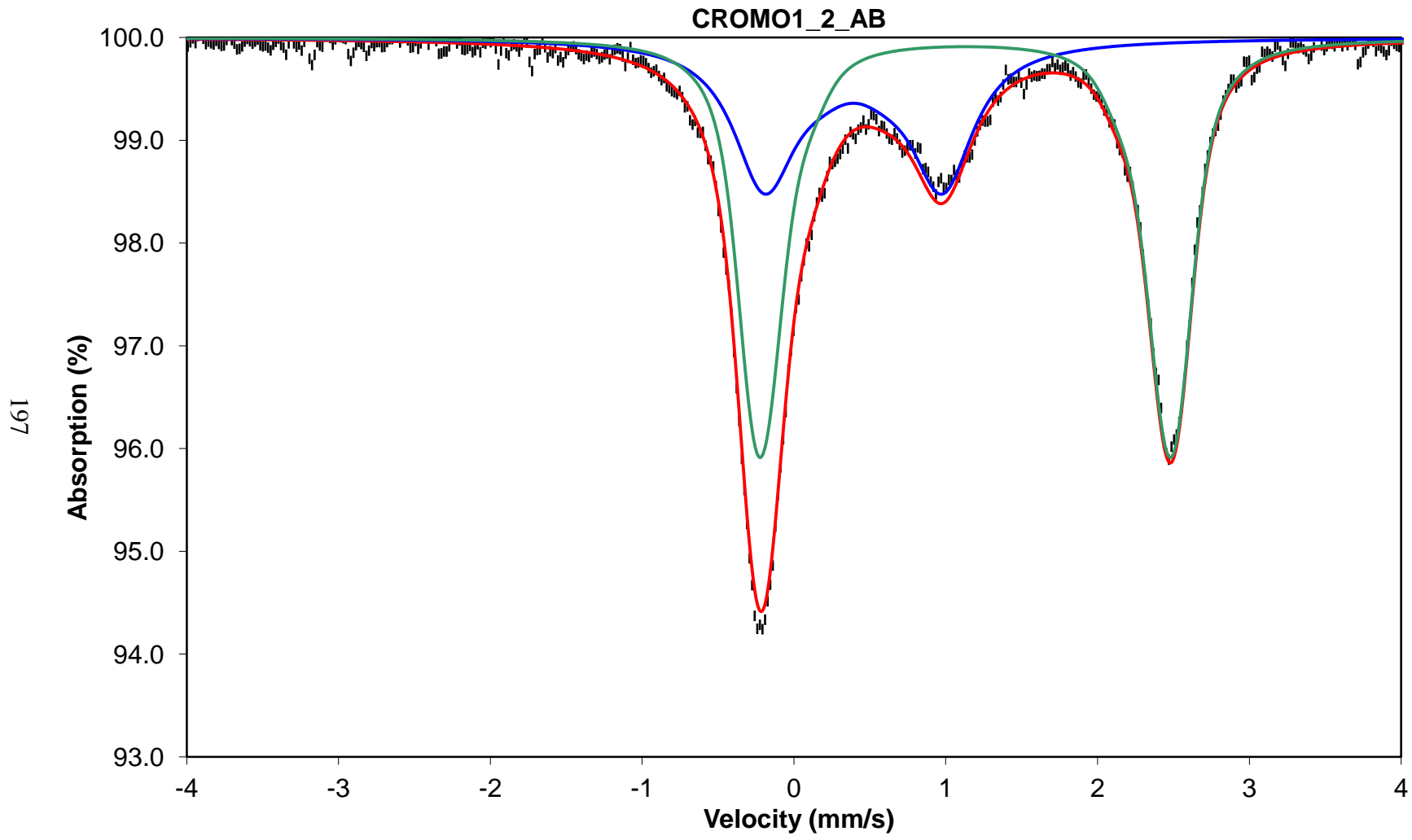
Figure A29. Mössbauer Spectroscopy CROMO1_2_AB plot. The data (black dots) were fit using the Ghent program to obtain a best fit curve (red), Fe^{3+} (blue) and Fe^{2+} (green) curves.
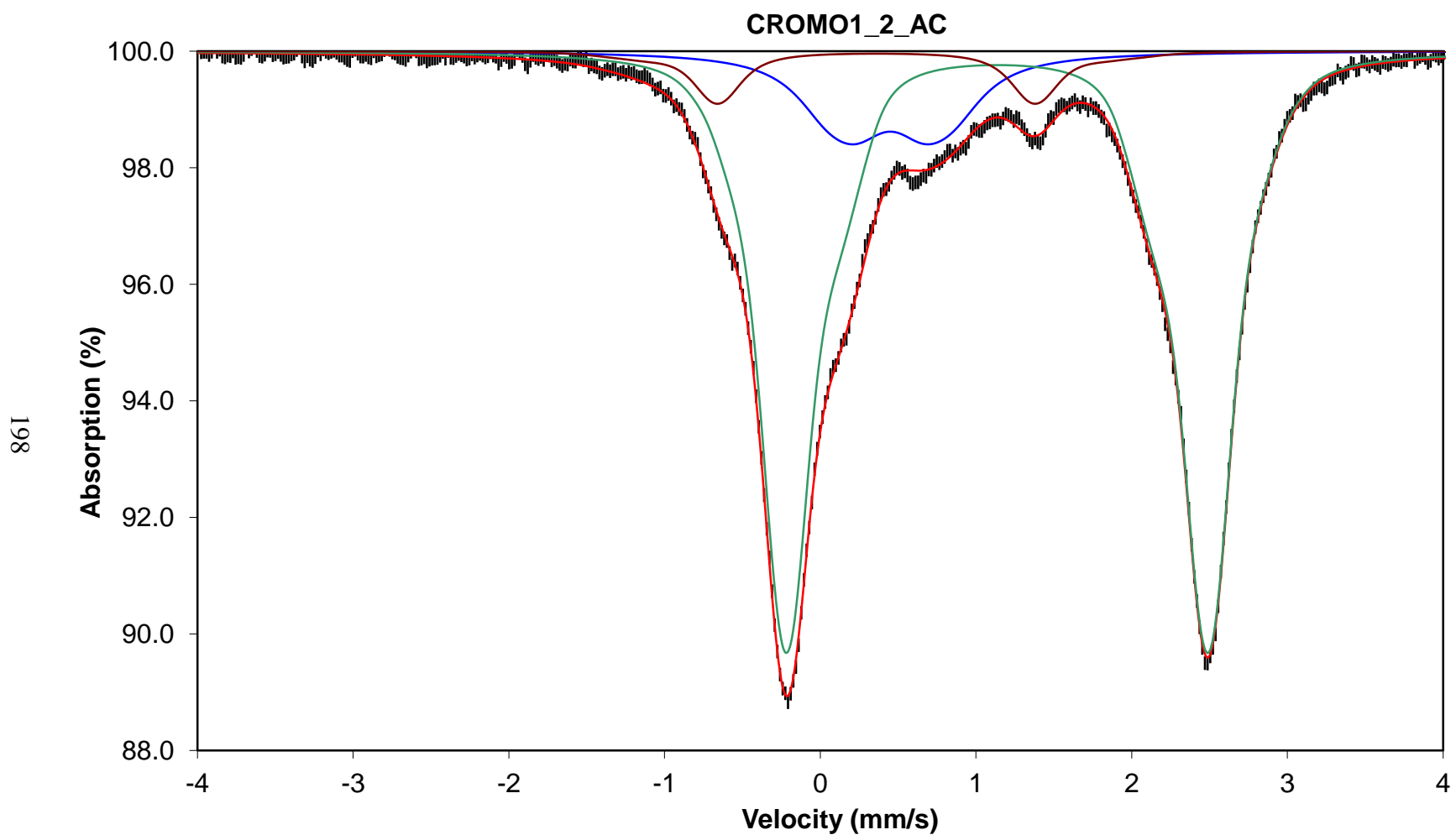
Figure A30. Mössbauer Spectroscopy CROMO1_2_AC plot. The data (black dots) were fit using the Ghent program to obtain a best fit curve (red), Fe^{3+} (blue) and Fe^{2+} (green and brown) curves.
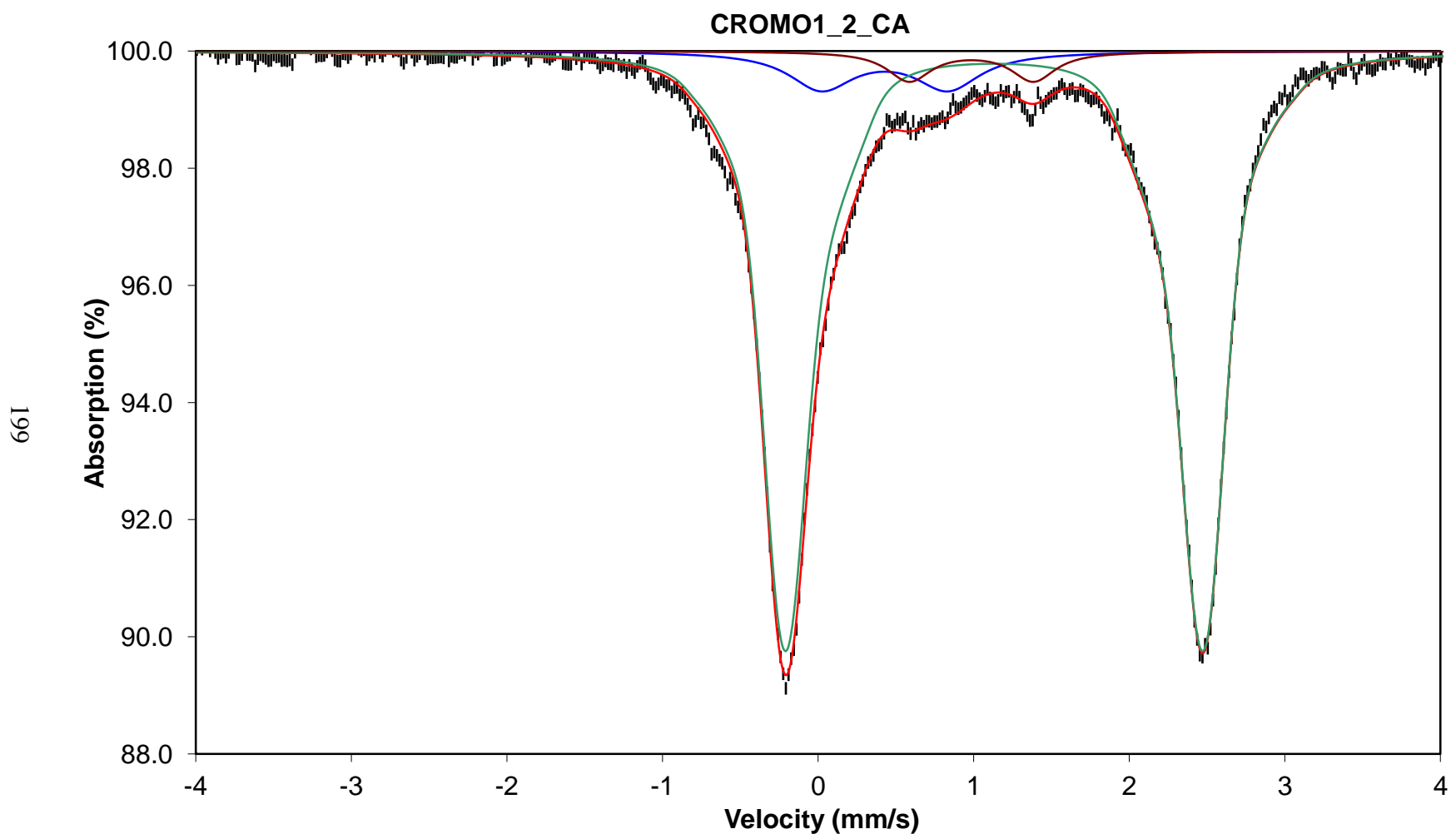
Figure A31. Mössbauer Spectroscopy CROMO1_2_CA plot. The data (black dots) were fit using the Ghent program to obtain a best fit curve (red), Fe^{3+} (blue and brown) and Fe^{2+} (green) curves.
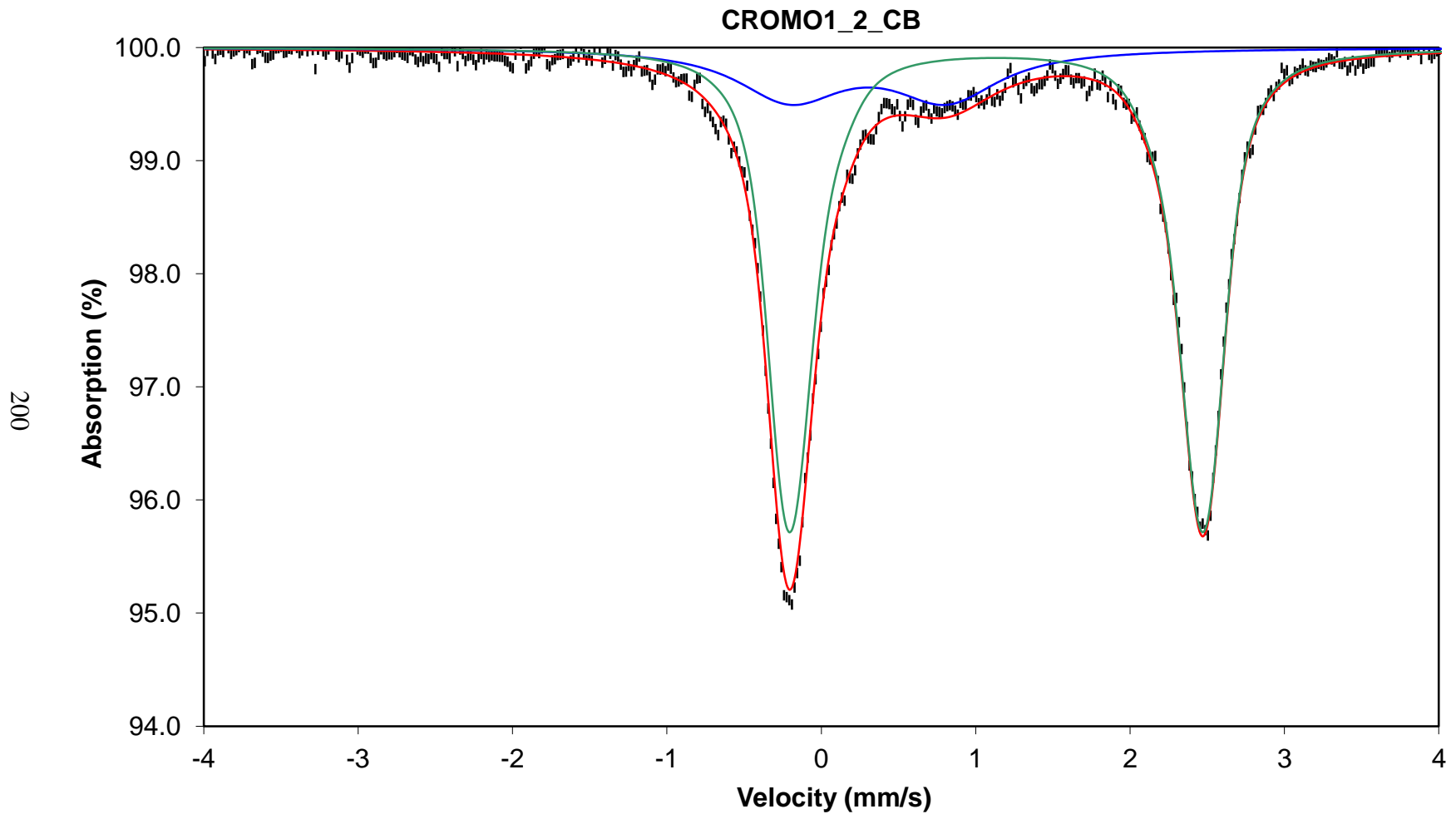
Figure A32. Mössbauer Spectroscopy CROMO1_2_CB plot. The data (black dots) were fit using the Ghent program to obtain a best fit curve (red), Fe^{3+} (blue) and Fe^{2+} (green) curves.
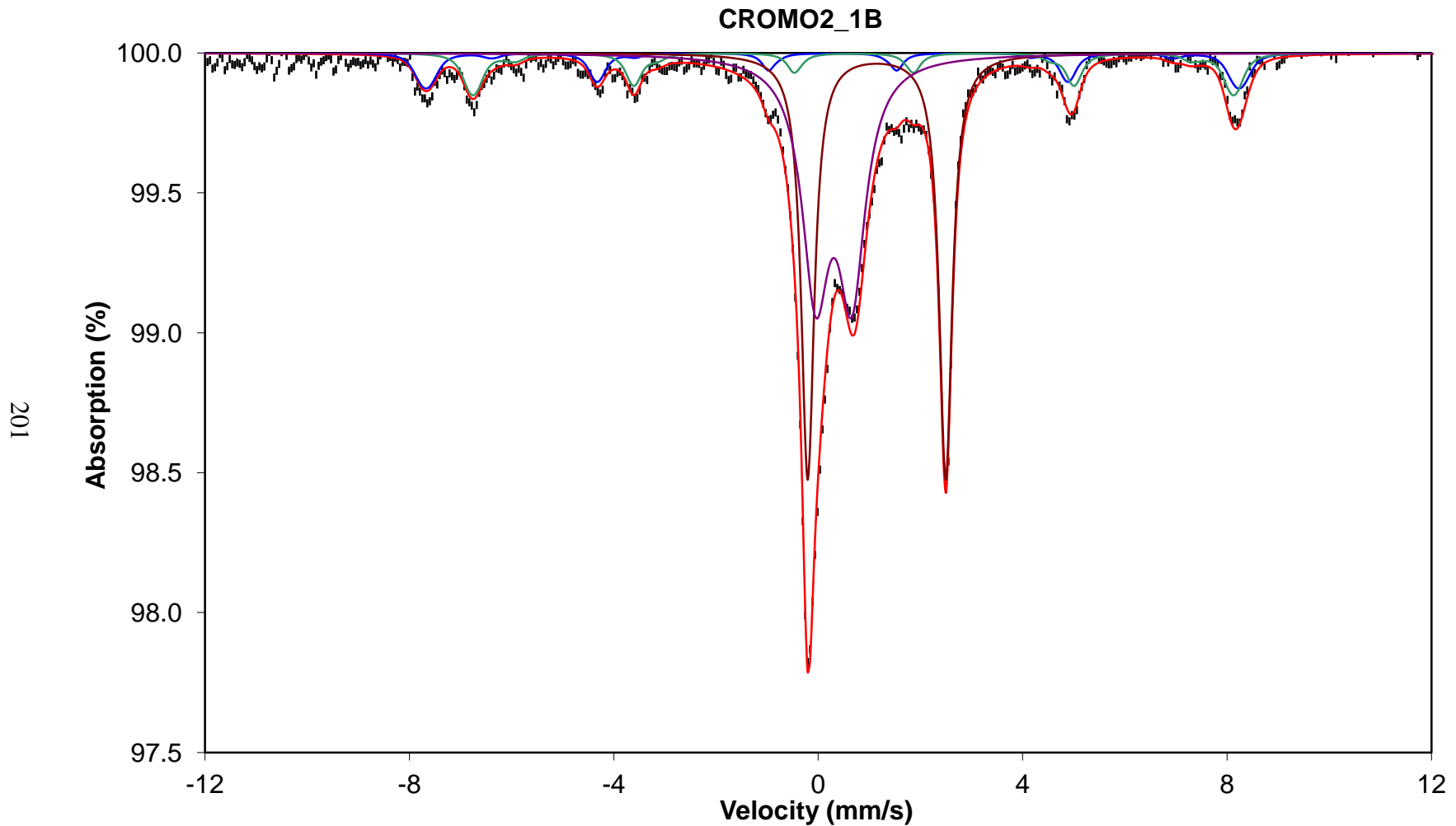
Figure A33. Mössbauer Spectroscopy CROMO2_1B plot. The data (black dots) were fit using the Ghent program to obtain a best fit curve (red), magnetite (blue and green), Fe^{3+} (purple) and Fe^{2+} (brown) curves.
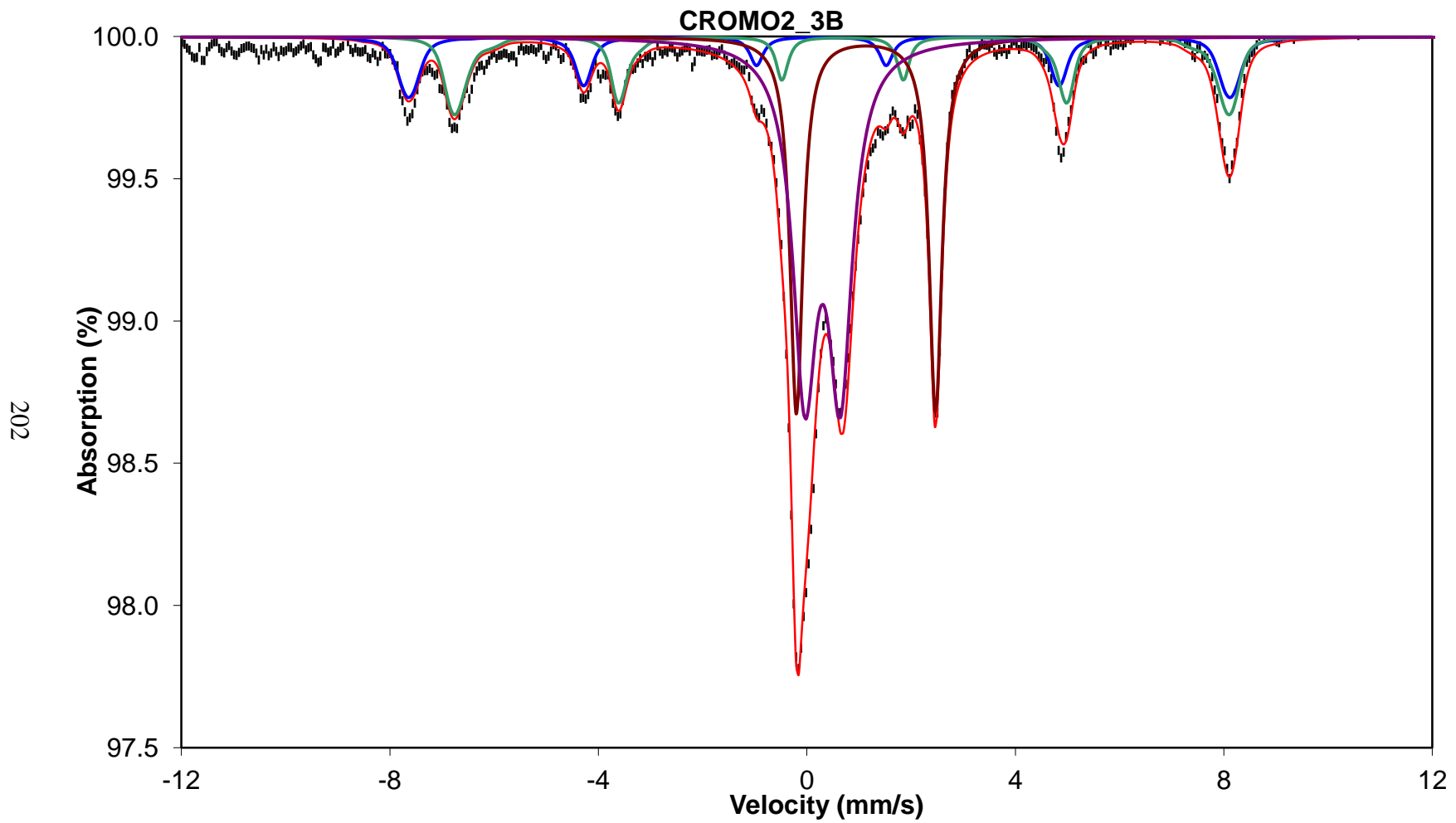
Figure A34. Mössbauer Spectroscopy CROMO2_3B plot. The data (black dots) were fit using the Ghent program to obtain a best fit curve (red), magnetite (blue and green), Fe^{3+} (purple) and Fe^{2+} (brown) curves.
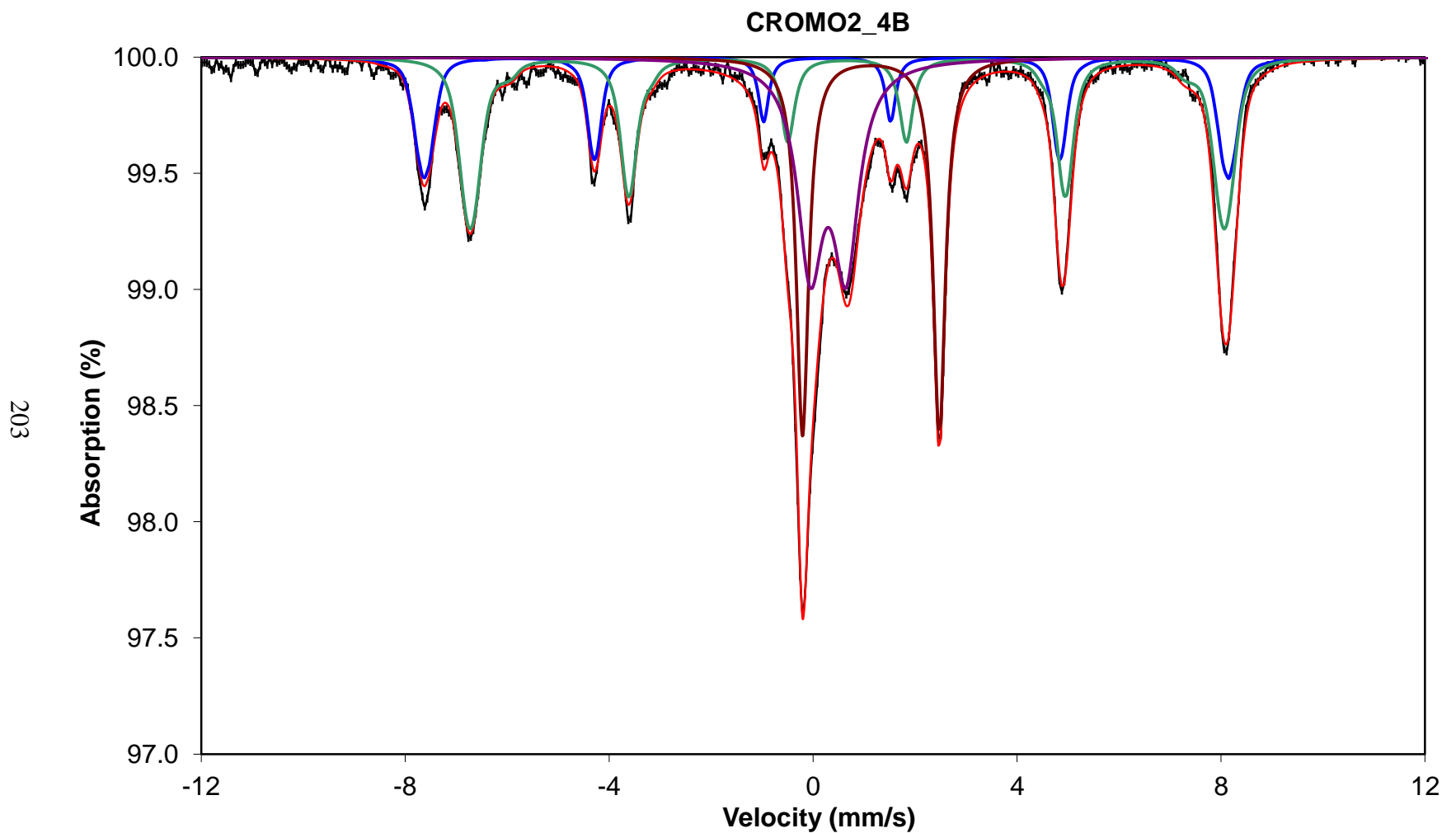
Figure A35. Mössbauer Spectroscopy CROMO2_4B plot. The data (black dots) were fit using the Ghent program to obtain a best fit curve (red), magnetite (blue and green), Fe^{3+} (purple) and Fe^{2+} (brown) curves.
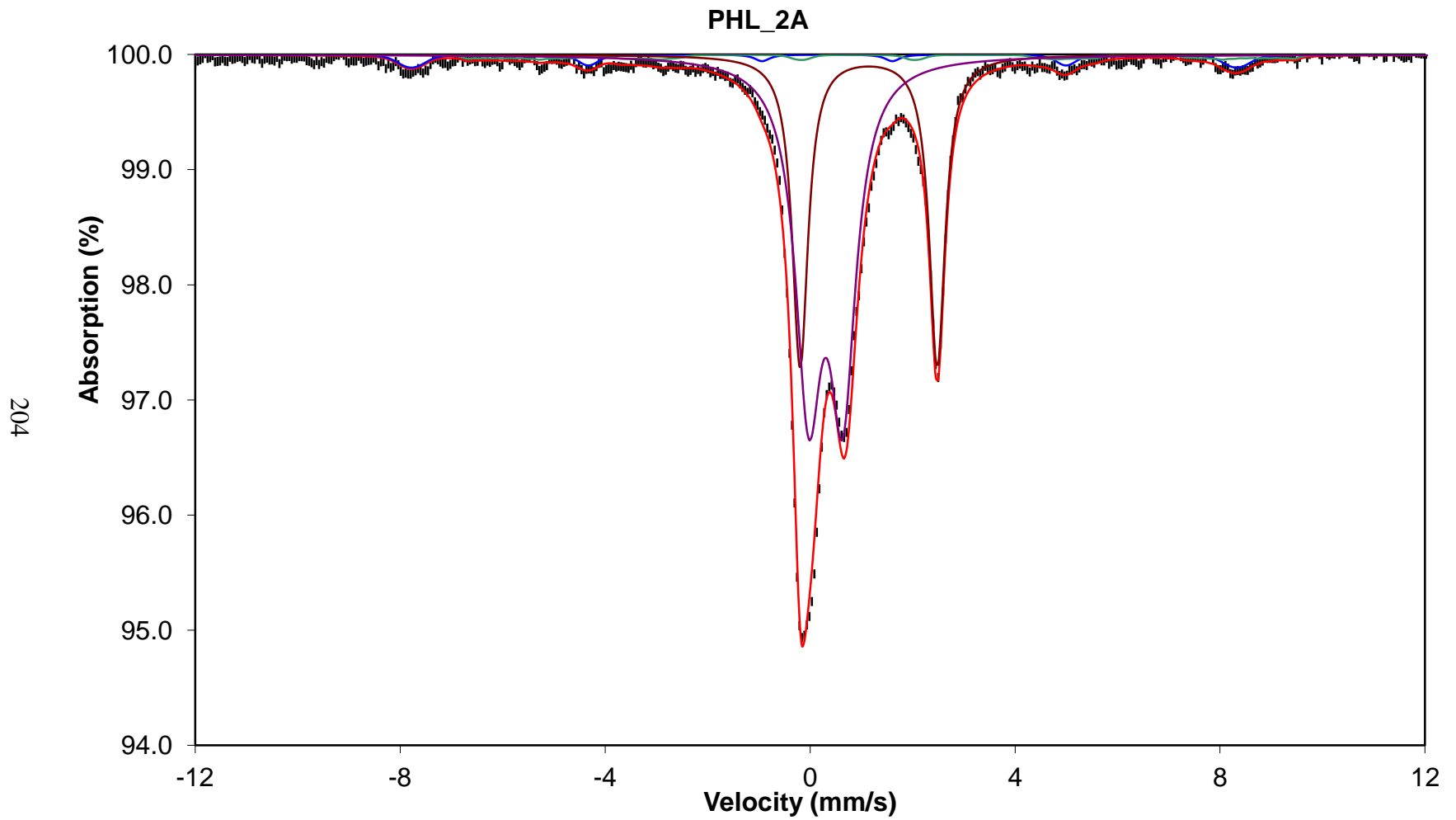
Figure A36. Mössbauer Spectroscopy PHL_2A plot. The data (black dots) were fit using the Ghent program to obtain a best fit curve (red), magnetite (blue and green), Fe^{3+} (purple) and Fe^{2+} (brown) curves.
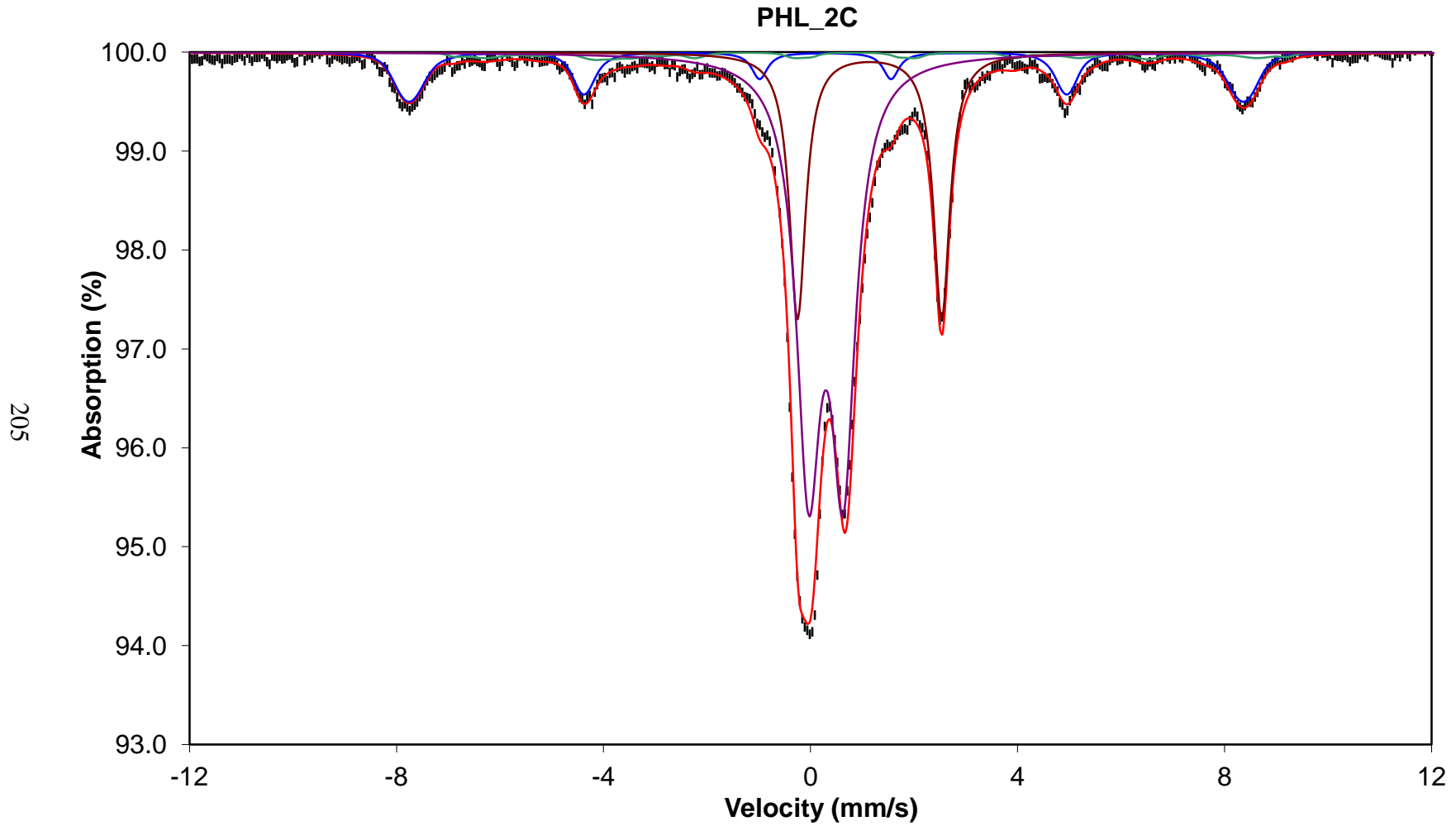
Figure A37. Mössbauer Spectroscopy PHL_2C plot. The data (black dots) were fit using the Ghent program to obtain a best fit curve (red), magnetite (blue and green), Fe^{3+} (purple) and Fe^{2+} (brown) curves.
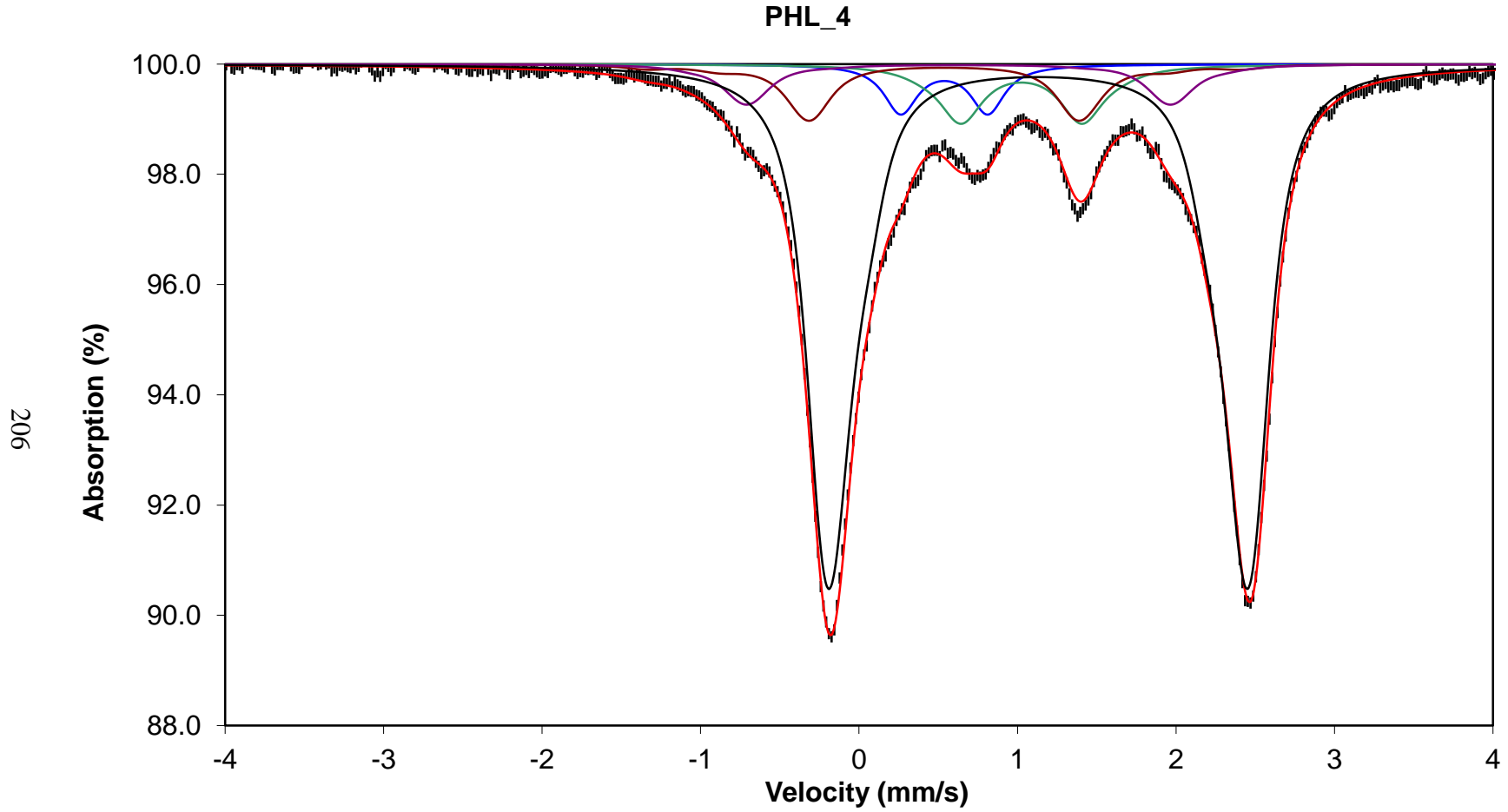
Figure A38. Mössbauer Spectroscopy PHL_4 plot. The data (black dots) were fit using the Ghent program to obtain a best fit curve (red), Fe^{3+} (blue and green) and Fe^{2+} (purple, brown, black) curves. PHL_4 still requires additional fitting because the parameters are not within the general range of values for Fe^{2+} and Fe^{3+}.
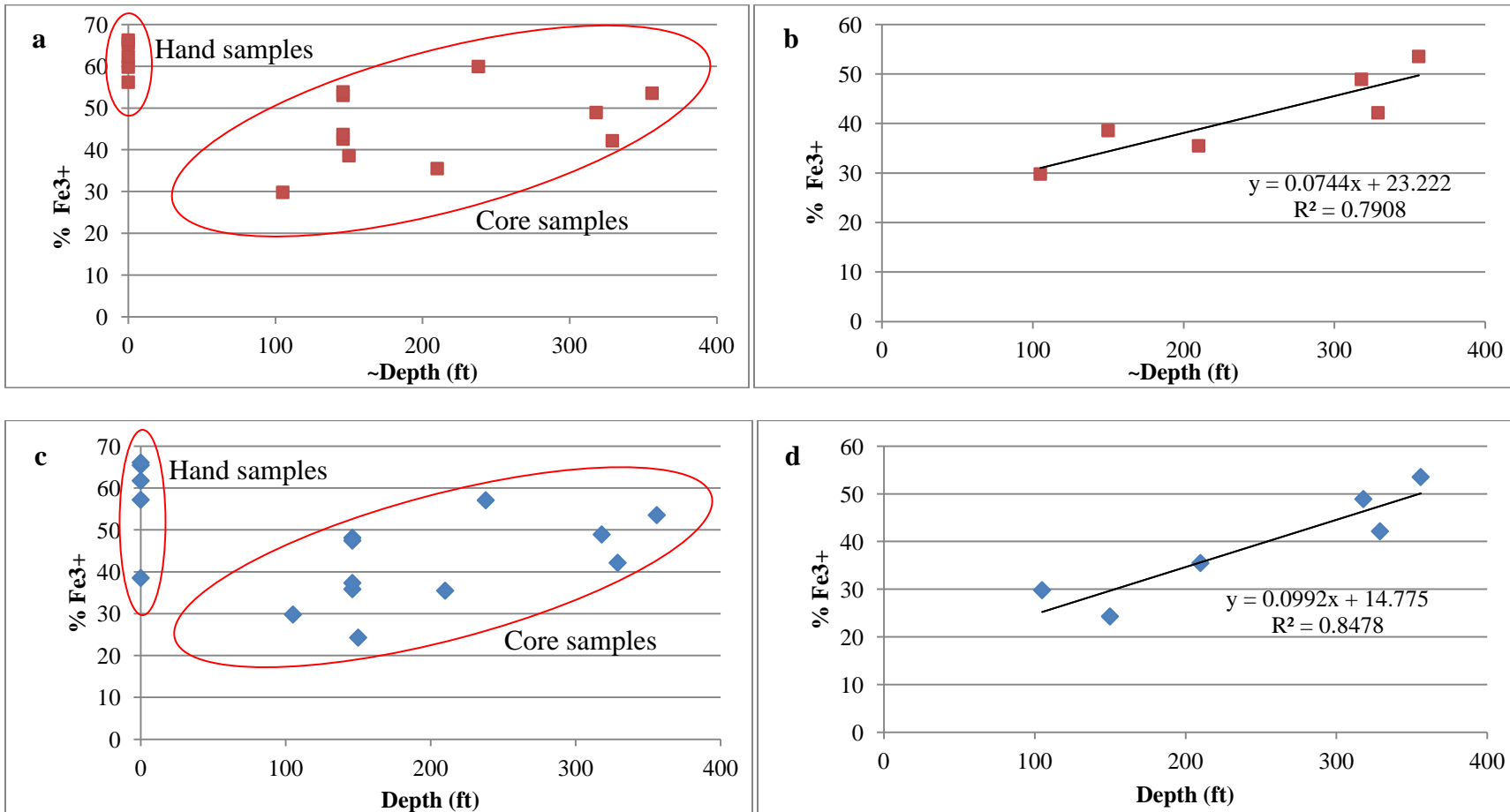
Figure A39. Sample depth vs. %Fe^{3+}. (a) All samples with magnetite split up and included in %Fe^{3+} and (b) only cores 309 and 313; (c) Silicates only (no magnetite) %Fe^{3+} for all samples and (d) only cores 309 and 313

Table A10: H_2 generation using average density (2.68g cm^{-3}) and mg/kg conversion.

Sample	MOSS			Fe conc. (ppm)*	mol H_2/kg rock to be released	mol H_2/kg rock released	Volume Peridotite (km^3)*	H_{gas} released per 1km^3 (Tmol)	H_{gas} to be released per 1km^3 (Tmol)	H_{gas} released (mol)	H_{gas} to be released (mol)	H_{gas} released (Tmol)	H_{gas} to be released (Tmol)
	% Mag	% Fe^{3+}	% Fe^{2+}										
309_84	0	17	83	135803	1.01	0.40	7730	1.08	2.72	8.34182E+15	2.10157E+16	8342	21016
309_105_B	0	32	68	36191	0.22	0.21	7730	0.55	0.59	4.27296E+15	4.57567E+15	4273	4576
CROMO1_1_A	0	16	84	44672	0.34	0.13	7730	0.34	0.90	2.64195E+15	6.96427E+15	2642	6964
CROMO1_1_B	0	18	82	71522	0.53	0.23	7730	0.62	1.41	4.75782E+15	1.08864E+16	4758	10886
CROMO1_2_AA	0	29	71	33518	0.21	0.17	7730	0.46	0.57	3.57319E+15	4.42981E+15	3573	4430
CROMO1_2_AB	0	37	63	60579	0.34	0.40	7730	1.07	0.92	8.3096E+15	7.08046E+15	8310	7080
CROMO1_2_AC	0	15	85	53768	0.41	0.15	7730	0.39	1.10	3.01156E+15	8.46598E+15	3012	8466
CROMO1_2_CA	0	12	88	54729	0.43	0.12	7730	0.32	1.15	2.46652E+15	8.91703E+15	2467	8917
CROMO1_2_CB	0	25	75	70690	0.48	0.31	7730	0.84	1.28	6.50281E+15	9.85909E+15	6503	9859
CROMO2_1B	21	42	37	44606	0.18	0.44	7730	1.19	0.47	9.20347E+15	3.67085E+15	9203	3671
CROMO2_3B	29	27	44	83576	0.40	0.69	7730	1.85	1.08	1.43079E+16	8.34644E+15	14308	8346
CROMO2_4B	52	23	25	80999	0.31	0.83	7730	2.23	0.83	1.72738E+16	6.38554E+15	17274	6386
PHL_2A	8	58	34	33264	0.11	0.38	1455	1.02	0.29	1.48001E+15	4.2133E+14	1480	421
PHL_2C	19	56	25	40571	0.11	0.50	1455	1.34	0.30	1.94876E+15	4.42009E+14	1949	442
PHL_4	0	14	86	31009	0.24	0.08	1455	0.20	0.64	2.93101E+14	9.35928E+14	293	936

Mag = % Fe in magnetite; mol is mole; *normalized average Fe concentration in ppm; % Fe^{3+} was used in H_{2gas} released calculations; % Fe^{2+} was used in H_{2gas} to be released calculations.

Table A11: H_2 generation using mg/L conversion units.

Sample	mol H_2/L rock to be released	mol H_2/L rock released	H_{gas} released (mol)	H_{gas} to be released (mol)	H gas released per $1km^3$ (Tmol)	H gas to be released per $1km^3$ (Tmol)	H_{gas} released (Tmol)	H_{gas} to be released (Tmol)
309_84	1.01	0.40	3.1126E+15	7.8417E+15	0.40	1.01	3113	7842
309_105_B	0.22	0.21	1.5944E+15	1.7073E+15	0.21	0.22	1594	1707
CROMO1_1_A	0.34	0.13	1.6082E+15	4.2392E+15	0.13	0.34	1608	4239
CROMO1_1_B	0.53	0.23	2.8961E+15	6.6266E+15	0.23	0.53	2896	6627
CROMO1_2_AA	0.21	0.17	2.175E+15	2.6964E+15	0.17	0.21	2175	2696
CROMO1_2_AB	0.34	0.40	5.0581E+15	4.3099E+15	0.40	0.34	5058	4310
CROMO1_2_AC	0.41	0.15	1.8332E+15	5.1533E+15	0.15	0.41	1833	5153
CROMO1_2_CA	0.43	0.12	1.5014E+15	5.4278E+15	0.12	0.43	1501	5428
CROMO1_2_CB	0.48	0.31	3.9583E+15	6.0012E+15	0.31	0.48	3958	6001
CROMO2_1B	0.18	0.44	3.4341E+15	1.3697E+15	0.44	0.18	3434	1370
CROMO2_3B	0.40	0.69	5.3388E+15	3.1143E+15	0.69	0.40	5339	3114
CROMO2_4B	0.31	0.83	6.4455E+15	2.3827E+15	0.83	0.31	6445	2383
PHL_2A	0.11	0.38	5.5224E+14	1.5721E+14	0.38	0.11	552	157
PHL_2C	0.11	0.50	7.2715E+14	1.6493E+14	0.50	0.11	727	165
PHL_4	0.24	0.08	1.7841E+14	5.697E+14	0.08	0.24	178	570

% Fe3+ (Table A10) was used in H_{2gas} released calculations; % Fe2+ was used in H_{2gas} to be released calculations.

Table A12: IC-PMS concentration data for standards and CRO sample 313-329. Standards analyzed include BCR, BHVO, BIR, GOR, StHls, T1, ML3B, KL2, and San Carlos olivine. Data was collected in 4 different areas of the thin section and the mineral grains are labeled accordingly (sp1 for spinel grain in area 1, opx1 orthopyroxene grain in area 1, ol 1 for olivine grain in area 1, cpx2 for clinopyroxene in area 2, etc…). Ol3-2 is probably actually cpx or opx based on the chemical data below and opx3 maybe cpx (exsolution lamelle) due to the high CaO concentrations measured. The raw data was input into the "LazyBoy" version 3.73 macro spreadsheet developed by Joel Sparks (jwsparks@bu.edu; ©2011; version date 2/1/2013). Figures A40-42 illustrate the mineral grains sampled. Concentrations are in ppm unless indicated as wt%. Electron microprobe data of major cations in spinel(s) (Mg, Al, Cr, Fe) are needed to better assess the IC-PMS data, especially in regards to further analysis of the partitioning of the trace elements, such as V which has multiple valence states and may be another way to understand the redox status of rocks [Mallmann and O'Neill, 2009].

Table A12: IC-PMS concentration data for standards and CRO sample 313-329.

Atomic number		26	27	43	45	47	51	52	55	57	59	60	65	66	85	88	89	208
Sample/ Beam information	M026 Conc.	MgO%	Al2O3%	CaO%	Sc	TiO2%	V	Cr	MnO%	FeO*%	Co	Ni	Cu	Zn	Rb	Sr	Y	Pb
BCR 70% 10hz 80um 1	3.56	3.56	13.41	6.94	31.15	2.28	401.44	20.92	0.19	11.20	34.71	12.28	17.37	149.50	45.71	332.33	34.64	10.91
BHVO 70% 10Hz 80 um	7.13	7.13	13.62	11.57	31.24	2.75	296.68	306.94	0.17	11.32	42.80	112.01	122.93	115.40	8.98	399.53	26.27	1.80
BIR 70% 10hz 80um	9.4	9.40	15.46	13.17	41.71	0.91	283.90	385.87	0.17	9.87	46.36	149.34	109.48	62.90	0.20	106.95	16.41	3.16
GOR132 70% 10hz 80um	22.4	22.40	10.33	7.91	33.32	0.27	207.82	2,522.57	0.17	10.95	95.18	1,188.10	211.28	66.17	2.12	14.00	13.68	20.25
StHls 70% 10hz 80um	1.97	1.97	17.99	5.15	12.89	0.71	76.35	20.83	0.07	4.25	12.44	20.90	36.42	54.76	28.51	471.49	12.91	10.30
T1 70% 10hz 80um	3.75	3.75	16.67	6.69	24.79	0.73	178.70	23.07	0.13	6.39	18.15	9.58	18.80	67.80	85.11	270.63	23.86	10.42
ML3B 70% 10hz 80um	6.59	6.59	14.24	10.95	30.90	2.18	271.98	175.26	0.17	11.13	41.67	100.06	115.55	112.03	5.98	329.28	26.76	1.39
KL2 70% 10hz 80um	7.34	7.34	13.52	11.36	30.75	2.61	296.47	303.48	0.17	11.05	41.18	104.84	90.28	111.92	8.63	370.67	26.50	2.10
San Carlos Olivine	49.42	49.42	0.02	0.07	6.80	0.00	3.15	188.18	0.14	7.84	124.40	2,281.98	1.69	50.71	0.01	0.00	0.01	0.01
SP1 5 hz 80um 70%	23.14	23.14	64.11	0.19	0.27	0.11	552.49	78,659.60	0.12	12.77	346.14	2,630.19	1.67	1,843.97	0.18	0.00	-0.01	0.03
OPX1 5hz 95um 70%	34.42	34.42	4.42	0.72	25.16	0.13	149.51	3,840.76	0.18	7.66	63.65	711.77	0.97	42.11	0.17	0.58	1.30	0.02
OL1 10hz 40um 70%	48.74	48.74	0.01	0.04	3.62	0.00	0.49	15.69	0.15	10.09	130.78	2,786.68	0.51	23.01	0.08	0.18	-0.02	0.02
cpx2-1 10hz 30um 70%	16.7	16.70	6.69	25.82	90.14	0.48	262.90	5,568.98	0.09	2.45	17.69	275.76	0.48	5.94	-0.22	10.49	32.48	0.00
opx3-1 10hz 80um 70%	34.74	34.74	4.95	0.63	27.63	0.12	125.96	2,874.02	0.16	6.92	53.27	591.79	0.25	32.22	0.13	0.15	1.23	0.02
opx3-2 10hz 60um 70%	34.82	34.82	5.26	0.82	27.71	0.13	123.21	3,059.35	0.16	6.73	55.77	657.34	0.56	35.32	0.04	0.25	1.36	0.00
ol3-1 10hz 80um 70%	49.09	49.09	0.00	0.01	3.22	0.00	0.34	8.30	0.15	9.34	124.92	2,510.58	0.48	25.88	0.01	0.01	0.00	0.01
ol3-2 10hz 60um 70%	16.59	16.59	6.19	25.15	90.50	0.45	271.20	4,426.63	0.09	2.73	19.70	278.52	0.21	8.61	0.04	10.95	27.09	0.00
sp4 10hz 80um 70%	21.18	21.18	67.42	0.08	0.18	0.06	464.45	69,469.90	0.10	11.40	315.43	2,420.44	0.51	1,518.13	0.19	0.06	-0.01	0.03
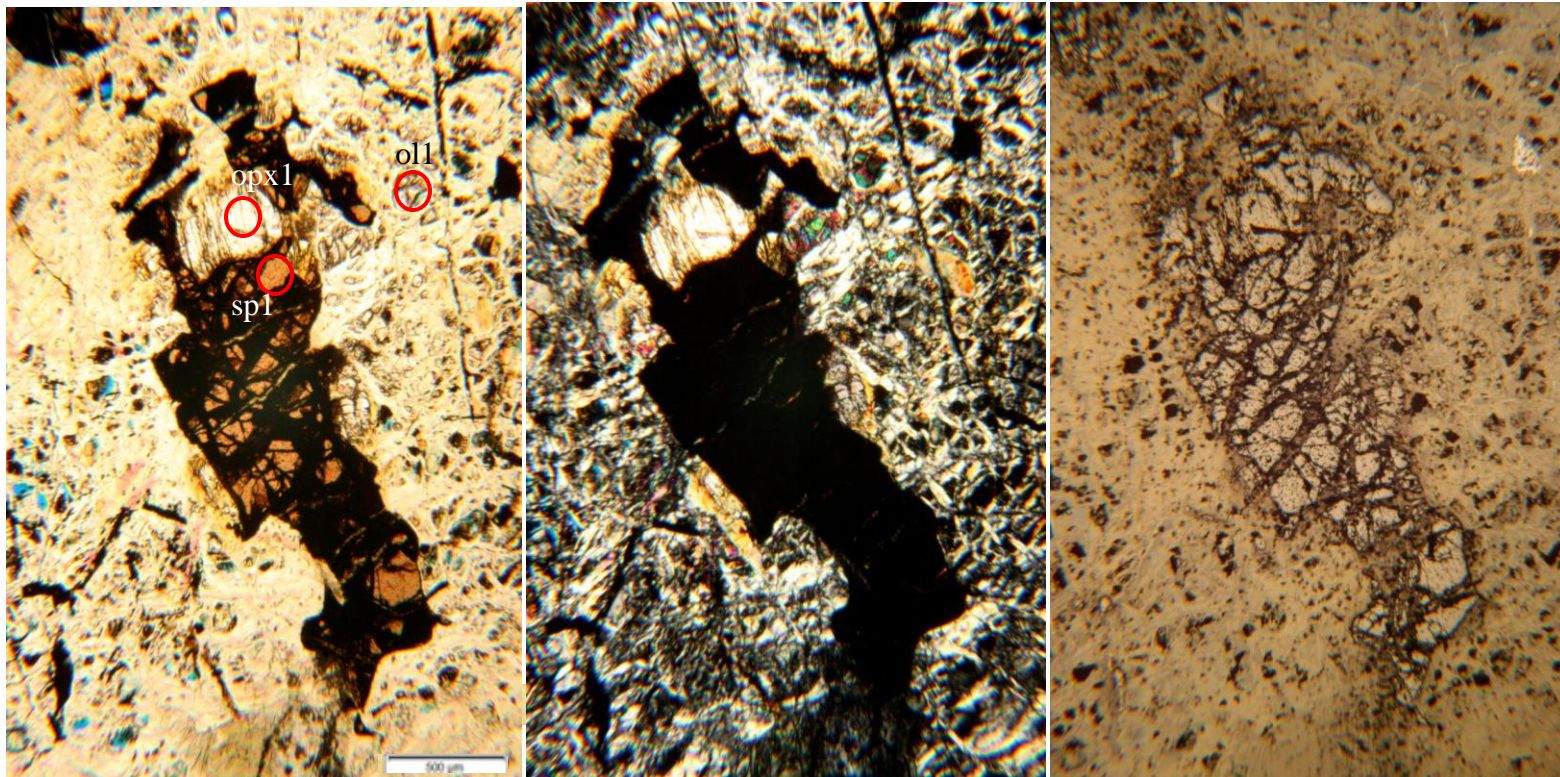
Figure A40: Thin section images of sample 313-329 ICPMS area 1 before laser ablation. Areas of analysis are indicated by red circle; spinel 1 (sp1), orthopyroxene 1(opx1), and olivine 1 (ol1). From right to left, images are in plane polarized light (scale bar is ~500µm), cross-polarized light, and reflected light. See Figure 12 for thin section images after laser ablation and general field of view.
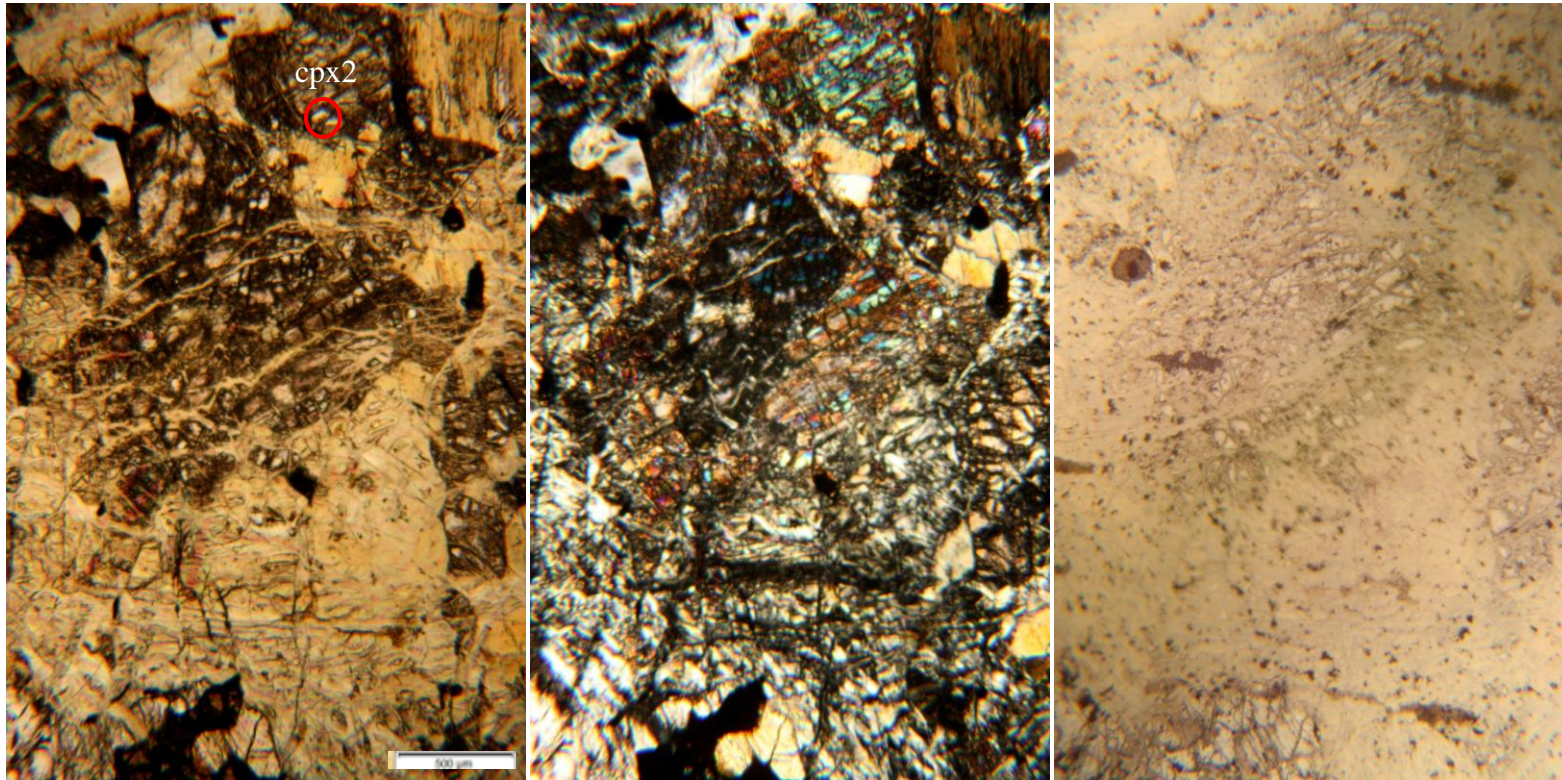
Figure A41: Thin section images of sample 313-329 ICPMS area 2 before laser ablation. Area of analysis is indicated by red circle; clinopyroxene (cpx2). From right to left, images are in plane polarized light (scale bar is ~500µm), cross-polarized light, and reflected light.
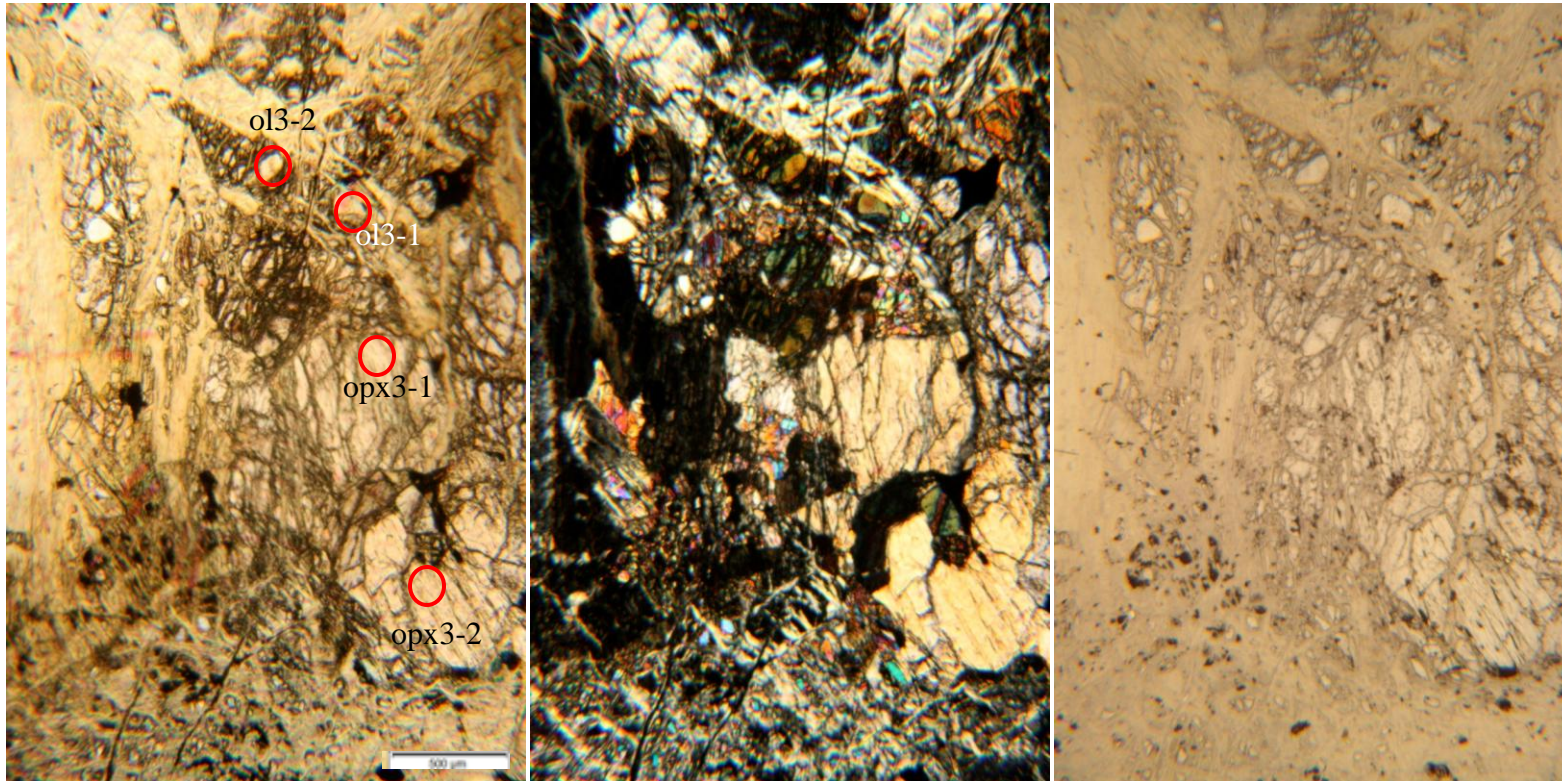
Figure A42: Thin section images of sample 313-329 ICPMS area 3 before laser ablation. Areas of analysis are indicated by red circle; orthopyroxene 3 (opx3), and olivine 3 (ol3). Ol3-2 is probably cpx not ol based on chemical analysis and the opx may be cpx based on the high Ca concentration, or an exsolution lamelle. From right to left, images are in plane polarized light (scale bar is ~500μm), cross-polarized light, and reflected light.

BIBLIOGRAPHY

Abrajano, T. A. and J. D. Pasteris (1989), Zambales ophiolite, Philippines II. Sulfide petrology of the critical zone of the Acoje Massif, *Tectonophysics, 103*, 64-77.

Abrajano, T. A., J. D. Pasteris, and G. Bacuta (1989), Zambales ophiolite, Philippines I. Geology and petrology of the critical zone of the Acoje massif, *Tectonophysics, 168*(1), 65-100.

Abrajano, T., N. Sturchio, B. Kennedy, G. Lyon, K. Muehlenbachs, and J. Bohlke (1990), Geochemistry of reduced gas related to serpentinization of the Zambales ophiolite, Philippines, *Appl. Geochem., 5*(5), 625-630.

Aja, S. U. and M. Darby Dyar (2002), The stability of Fe–Mg chlorites in hydrothermal solutions—I. Results of experimental investigations, *Appl. Geochem., 17*(9), 1219-1239, doi: http://dx.doi.org/10.1016/S0883-2927(01)00131-7.

Alexander, E. B. (2014), Arid to humid serpentine soils, mineralogy, and vegetation across the Klamath Mountains, USA, *Catena, 116*(0), 114-122, doi: http://dx.doi.org/10.1016/j.catena.2013.12.003.

Alinz, M., P. Floyd, and M. Goncuoglu (1996), Supra-subduction zone ophiolites of Central Anatolia: geochemical evidence from the Sarikaraman ophiolite, Aksaray, Turkey, *Mineralogical Magazine, 60*(402), 697-710.

Alt, J., R. Frost, and A. McCaig (2009), Drilling in Serpentine Sea, *INVEST, Bremen.Sept*, 23-25.

Alt, J. C., C. J. Garrido, W. Shanks Iii, A. Turchyn, J. A. Padrón-Navarta, V. López Sánchez-Vizcaíno, M. T. Gómez Pugnaire, and C. Marchesi (2012), Recycling of water, carbon, and sulfur during subduction of serpentinites: A stable isotope study of Cerro del Almirez, Spain, *Earth Planet. Sci. Lett., 327*, 50-60.

Alt, J. C., W. Shanks III, L. Crispini, L. Gaggero, E. M. Schwarzenbach, G. L. Frueh-Green, and S. M. Bernasconi (2012), Uptake of carbon and sulfur during seafloor serpentinization and the effects of subduction metamorphism in Ligurian peridotites, *Chem. Geol., 322*, 268-277.

Amend, J. P. and E. L. Shock (2006), Energetics of overall metabolic reactions of thermophilic and hyperthermophilic Archaea and Bacteria, *FEMS Microbiol. Rev., 25*(2), 175-243.

Anderson, R. E., W. J. Brazelton, and J. A. Baross (2013), The Deep Viriosphere: Assessing the Viral Impact on Microbial Community Dynamics in the Deep Subsurface*, Rev. Mineral. Geochem., 75*, 649-675, doi: 10.2138/rmg.2013.75.20.

Andreani, M., M. Godard, and C. Mével (2009), LA-(HR-) ICPMS study of serpentinites from ODP Site 920 (23 N MAR): insights on transfers and trace element distribution during serpentinization, EGU General Assembly Conference Abstracts.

Andreani, M., I. Daniel, and M. Pollet-Villard (2013), Aluminum speeds up the hydrothermal alteration of olivine*, Am. Mineral., 98*(10), 1738-1744.

Andreani, M., O. Grauby, A. Baronnet, and M. Muñoz (2008), Occurrence, composition and growth of polyhedral serpentine*, European Journal of Mineralogy, 20*(2), 159-171.

Andreani, M., M. Muñoz, C. Marcaillou, and A. Delacour (2013B), µXANES study of iron redox state in serpentine during oceanic serpentinization*, Lithos, 178*(0), 70-83, doi: http://dx.doi.org/10.1016/j.lithos.2013.04.008.

Angiboust, S., P. Agard, J. De Hoog, J. Omrani, and A. Plunder (2013), Insights on deep, accretionary subduction processes from the Sistan ophiolitic "mélange"(Eastern Iran)*, Lithos, 156*, 139-158.

Arai, S., S. Ishimaru, and T. Mizukami (2012), Methane and propane micro-inclusions in olivine in titanoclinohumite-bearing dunites from the Sanbagawa high-P metamorphic belt, Japan: Hydrocarbon activity in a subduction zone and Ti mobility*, Earth Planet. Sci. Lett., 353*, 1-11.

Assima, G. P., F. Larachi, J. Molson, and G. Beaudoin (2013), Accurate and direct quantification of native brucite in serpentine ores—New methodology and implications for CO2 sequestration by mining residues*, Thermochimica Acta, 566*(0), 281-291, doi: http://dx.doi.org/10.1016/j.tca.2013.06.006.

Atreya, S. K., P. R. Mahaffy, and A. Wong (2007), Methane and related trace species on Mars: Origin, loss, implications for life, and habitability*, Planet. Space Sci., 55*(3), 358-369.

Bach, W., H. Paulick, C. J. Garrido, B. Ildefonse, W. P. Meurer, and S. E. Humphris (2006), Unraveling the sequence of serpentinization reactions: petrography, mineral chemistry, and petrophysics of serpentinites from MAR 15 N (ODP Leg 209, Site 1274)*, Geophys. Res. Lett., 33*(13).

Balucan, R. D. and B. Z. Dlugogorski (2012), Thermal activation of antigorite for mineralization of CO2*, Environ. Sci. Technol., 47*(1), 182-190.

Barnes, I., J. O'neil, and J. Trescases (1978), Present day serpentinization in New Caledonia, Oman and Yugoslavia, *Geochim. Cosmochim. Acta, 42*(1), 144-145.

Beard, J. S., B. R. Frost, P. Fryer, A. McCaig, R. Searle, B. Ildefonse, P. Zinin, and S. K. Sharma (2009), Onset and progression of serpentinization and magnetite formation in olivine-rich troctolite from IODP Hole U1309D, *J. Petrol., 50*(3), 387-403.

Beinlich, A., O. Plümper, J. Hövelmann, H. Austrheim, and B. Jamtveit (2012), Massive serpentinite carbonation at Linnajavri, N–Norway, *Terra Nova*.

Belley, F., E. C. Ferré, F. Martín-Hernández, M. J. Jackson, M. D. Dyar, and E. J. Catlos (2009), The magnetic properties of natural and synthetic (Fex, Mg1 − x)2 SiO4 olivines, *Earth Planet. Sci. Lett., 284*(3–4), 516-526, doi: http://dx.doi.org/10.1016/j.epsl.2009.05.016.

Bishop, J., E. Murad, and M. Dyar (2002), The influence of octahedral and tetrahedral cation substitution on the structure of smectites and serpentines as observed through infrared spectroscopy, *Clay Miner., 37*(4), 617-628.

Bishop, J., M. Lane, M. Dyar, and A. Brown (2008), Reflectance and emission spectroscopy study of four groups of phyllosilicates: Smectites, kaolinite-serpentines, chlorites and micas, *Clay Miner., 43*(1), 35-54.

Bishop, J. L. et al. (2013), Coordinated analyses of Antarctic sediments as Mars analog materials using reflectance spectroscopy and current flight-like instruments for CheMin, SAM and MOMA, *Icarus, 224*(2), 309-325, doi: http://dx.doi.org/10.1016/j.icarus.2012.05.014.

Bishop, J. L., D. Loizeau, N. K. McKeown, L. Saper, M. D. Dyar, D. J. Des Marais, M. Parente, and S. L. Murchie (2013), What the ancient phyllosilicates at Mawrth Vallis can tell us about possible habitability on early Mars, *Planet. Space Sci., 86*(0), 130-149, doi: http://dx.doi.org/10.1016/j.pss.2013.05.006.

Blake, D., D. Vaniman, C. Achilles, R. Anderson, D. Bish, T. Bristow, C. Chen, S. Chipera, J. Crisp, and D. Des Marais (2012), Characterization and calibration of the CheMin mineralogical instrument on Mars Science Laboratory, *Space science reviews, 170*(1-4), 341-399.

Bloomer, S. and J. Hawkins (1983), Gabbroic and ultramafic rocks from the Mariana Trench: an island arc ophiolite, *The Tectonic and Geologic Evolution of Southeast Asian Seas and Islands: Part 2*, 294-317.

Bloomer, S. H., B. Taylor, C. J. MacLeod, R. J. Stern, P. Fryer, J. W. Hawkins, and L. Johnson (1995), Early arc volcanism and the ophiolite problem: a perspective from drilling in the western Pacific, *Active margins and marginal basins of the western Pacific*, 1-30.

Boillot, G., M. Recq, E. Winterer, A. Meyer, J. Applegate, M. Baltuck, J. Bergen, M. Comas, T. Davies, and K. Dunham (1987), Tectonic denudation of the upper mantle along passive margins: a model based on drilling results (ODP leg 103, western Galicia margin, Spain)*, Tectonophysics, 132*(4), 335-342.

Bonev, N. and G. Stampfli (2009), Gabbro, plagiogranite and associated dykes in the supra-subduction zone Evros Ophiolites, NE Greece*, Geol. Mag., 146*(01), 72-91.

Bortolotti, V., M. Marroni, L. Pandolfi, G. Principi, and E. Saccani (2002), Interaction between mid-ocean ridge and subduction magmatism in Albanian ophiolites*, J. Geol., 110*(5), 561-576.

Boschi, C., A. Dini, G. L. Früh-Green, and D. S. Kelley (2008), Isotopic and element exchange during serpentinization and metasomatism at the Atlantis Massif (MAR 30 N): insights from B and Sr isotope data*, Geochim. Cosmochim. Acta, 72*(7), 1801-1823.

Boschi, C., G. L. Früh-Green, A. Delacour, J. A. Karson, and D. S. Kelley (2006), Mass transfer and fluid flow during detachment faulting and development of an oceanic core complex, Atlantis Massif (MAR 30 N)*, Geochem. Geophys. Geosyst., 7*(1).

Brazelton, W. J., K. A. Ludwig, M. L. Sogin, E. N. Andreishcheva, D. S. Kelley, C. C. Shen, R. L. Edwards, and J. A. Baross (2010), Archaea and bacteria with surprising microdiversity show shifts in dominance over 1,000-year time scales in hydrothermal chimneys*, Proc. Natl. Acad. Sci. U. S. A., 107*(4), 1612-1617, doi: 10.1073/pnas.0905369107 [doi].

Brazelton, W. J., P. L. Morrill, N. Szponar, and M. O. Schrenk (2013), Bacterial communities associated with subsurface geochemical processes in continental serpentinite springs*, Appl. Environ. Microbiol., 79*(13), 3906-3916, doi: 10.1128/AEM.00330-13; 10.1128/AEM.00330-13.

Brazelton, W. J., B. Nelson, and M. O. Schrenk (2012), Metagenomic evidence for H_2 oxidation and H_2 production by serpentinite-hosted subsurface microbial communities*, Frontiers inMicrobiology, 2*, 268, doi: 10.3389/fmicb.2011.00268; 10.3389/fmicb.2011.00268.

Brazelton, W. J., M. O. Schrenk, D. S. Kelley, and J. A. Baross (2006), Methane- and sulfur-metabolizing microbial communities dominate the Lost City hydrothermal field ecosystem*, Appl. Environ. Microbiol., 72*(9), 6257-6270, doi: 72/9/6257 [pii].

Briais, A., P. Patriat, and P. Tapponnier (1993), Updated interpretation of magnetic anomalies and seafloor spreading stages in the South China Sea: Implications for the Tertiary tectonics of Southeast Asia*, Journal of Geophysical Research: Solid Earth (1978–2012), 98*(B4), 6299-6328.

Brown, A. J., S. J. Hook, A. M. Baldridge, J. K. Crowley, N. T. Bridges, B. J. Thomson, G. M. Marion, de Souza Filho, Carlos R, and J. L. Bishop (2010), Hydrothermal formation of Clay-Carbonate alteration assemblages in the Nili Fossae region of Mars, *Earth Planet. Sci. Lett., 297*(1), 174-182.

Bryndzia, L. T. and B. J. Wood (1990), Oxygen thermobarometry of abyssal spinel peridotites: the redox state and C–O–H volatile composition of the Earth's sub-oceanic upper mantle, *Am. J. Sci., 290*(10), 1093-1116.

Bucher, K. and R. Grapes (2011), Metamorphism of ultramafic rocks, in *Petrogenesis of Metamorphic Rocks*Anonymous , pp. 191-224, Springer.

Canil, D., H. S. C. O'Neill, D. Pearson, R. Rudnick, W. McDonough, and D. Carswell (1994), Ferric iron in peridotites and mantle oxidation states, *Earth Planet. Sci. Lett., 123*(1), 205-220.

Cardace, D., T. Hoehler, T. McCollom, M. Schrenk, D. Carnevale, and M. Kubo (2013), Establishment of the Coast Range ophiolite microbial observatory (CROMO): drilling objectives and preliminary outcomes., *Scientific Drilling*(16).

Cardace, D. and D. Meyer-Dombard (2011), Bioenergetics of Continental Serpentinites, AGU Fall Meeting Abstracts.

Cardace, D. and T. M. Hoehler (2009), Serpentinizing fluids craft microbial habitat, *Northeast. Nat., 16*(5), 272-284.

Carnevale, D. C. (2013), Carbon sequestration potential of the Coast Range Ophiolite in California, Masters of Science thesis, 15 pp., The University of Rhode Island.

Case, D. H., A. Ijiri , Y. Morono , V. J. Orphan, and F. Inagaki (2013), Microbiological and Geochemical Characterization of the Deep Subsurface Environment: Kumano Mud Volcano, Nankai Trough, Japan, *Abstract B13C-0483 presented at 2013 Fall Meeting, AGU, San Francisco, Calif. , 9-13 Dec.*

Chan, C. S., S. C. Fakra, D. C. Edwards, D. Emerson, and J. F. Banfield (2009), Iron oxyhydroxide mineralization on microbial extracellular polysaccharides, *Geochim. Cosmochim. Acta, 73*(13), 3807-3818.

Charlou, J. L., J. P. Donval, C. Konn, H. Ondréas, Y. Fouquet, P. Jean-Baptiste, and E. Fourré (2010), High production and fluxes of H2 and CH4 and evidence of abiotic hydrocarbon synthesis by serpentinization in ultramafic-hosted hydrothermal systems on the Mid-Atlantic Ridge, *Geophysical Monograph Series, 188*, 265-296, doi: 10.1029/2008GM000752.

Charlou, J., J. Donval, Y. Fouquet, P. Jean-Baptiste, and N. Holm (2002), Geochemistry of high H_2 and CH_4 vent fluids issuing from ultramafic rocks at the Rainbow hydrothermal field (36° 14′ N, MAR), *Chem. Geol., 191*(4), 345-359.

Chavagnac, V., C. Monnin, G. Ceuleneer, C. Boulart, and G. Hoareau (2013), Characterization of hyperalkaline fluids produced by low-temperature serpentinization of mantle peridotites in the Oman and Ligurian ophiolites, *Geochem. Geophys. Geosyst., 14*(7), 2496-2522.

Choi, S. H., S. B. Mukasa, and J. W. Shervais (2008), Initiation of Franciscan subduction along a large-offset fracture zone: Evidence from mantle peridotites, Stonyford, California, *Geology, 36*(8), 595-598.

Choi, S. H., J. W. Shervais, and S. B. Mukasa (2008), Supra-subduction and abyssal mantle peridotites of the Coast Range ophiolite, California, *Contributions to Mineralogy and Petrology, 156*(5), 551-576.

Choi, K., H. Kim, and S. Moon (2011), Numerical studies on the geometrical characterization of serpentine flow-field for efficient PEMFC, *Int J Hydrogen Energy, 36*(2), 1613-1627, doi: http://dx.doi.org/10.1016/j.ijhydene.2010.10.073.

Christensen, N. I. (1978), Ophiolites, seismic velocities and oceanic crustal structure, *Tectonophysics, 47*(1), 131-157.

Cipolli, F., B. Gambardella, L. Marini, G. Ottonello, and M. Vetuschi Zuccolini (2004), Geochemistry of high-pH waters from serpentinites of the Gruppo di Voltri (Genova, Italy) and reaction path modeling of CO_2 sequestration in serpentinite aquifers, *Appl. Geochem., 19*(5), 787-802.

Coes, L. (1955), High pressure minerals, *J Am Ceram Soc, 38*(298), 1094-1098.

Coleman, R. G. (1981), *Tectonic setting for ophiolite obduction in Oman, Journal of Geophysical Research, 86*, 2497-2508.

Coleman, R. G. (1977), What is an ophiolite?, *Ophiolites*, pp. 1-7, Springer.

Coleman, R. G. (2000), Prospecting for ophiolites along the California continental margin, *Special Papers-Geological Society Of America*, 351-364.

Colwell, F. S. and S. D'Hondt (2013), Nature and extent of the deep biosphere, *Rev Mineral Geochem, 75*, 547-574.

Cuadros, J., J. R. Michalski, V. Dekov, J. Bishop, S. Fiore, and M. D. Dyar (2013), Crystal-chemistry of interstratified Mg/Fe-clay minerals from seafloor hydrothermal sites, *Chem. Geol., 360–361*(0), 142-158, doi: http://dx.doi.org/10.1016/j.chemgeo.2013.10.016.

D'antonio, M. and M. Kristensen (2004), Serpentine and brucite of ultramafic clasts from the South Chamorro Seamount (Ocean Drilling Program Leg 195, Site 1200): inferences for the serpentinization of the Mariana forearc mantle, *Mineralogical Magazine, 68*(6), 887-904.

Daae, F. L., I. Okland, H. Dahle, S. L. Jorgensen, I. H. Thorseth, and R. B. Pedersen (2013), Microbial life associated with low-temperature alteration of ultramafic rocks in the Leka ophiolite complex, *Geobiology, 11*(4), 318-339.

Dando, P., J. Hughes, Y. Leahy, S. Niven, L. Taylor, and C. Smith (1995), Gas venting rates from submarine hydrothermal areas around the island of Milos, Hellenic Volcanic Arc, *Cont. Shelf Res., 15*(8), 913-929.

Dyar, M. D. and D. P. Birnie III (1984), Quench media effects on iron partitioning and ordering in a lunar glass, *J. Non Cryst. Solids, 67*(1–3), 397-412, doi: http://dx.doi.org/10.1016/0022-3093(84)90165-0.

Daval, D., R. Hellmann, I. Martinez, S. Gangloff, and F. Guyot (2013), Lizardite serpentine dissolution kinetics as a function of pH and temperature, including effects of elevated pCO2, *Chem. Geol., 351*(0), 245-256, doi: http://dx.doi.org/10.1016/j.chemgeo.2013.05.020.

De Guire, M. R., M. Darby Dyar, R. C. O'Handley, and G. Kalonji (1986), Magnetic ordering in splat-quenched spinel ferrite-silica compositions, *J Magn Magn Mater, 54–57, Part 3*(0), 1337-1338, doi: http://dx.doi.org/10.1016/0304-8853(86)90845-0.

De Guire, M. R., R. C. O'Handley, G. Kalonji, and M. Darby Dyar (1986), Spinel ferrite-silica glass obtained by splat quenching, *J. Non Cryst. Solids, 81*(3), 351-364, doi: http://dx.doi.org/10.1016/0022-3093(86)90502-8.

Defant, M. J., D. Jacques, R. C. Maury, J. de Boer, and J. Joron (1989), Geochemistry and tectonic setting of the Luzon arc, Philippines, *Geological Society of America Bulletin, 101*(5), 663-672.

Deines, P., S. L. Goldstein, E. H. Oelkers, R. L. Rudnick, and L. M. Walter (2003), Standards for publication of isotope ratio and chemical data in Chemical Geology, *Chem. Geol., 202*(1), 1-4.

Dennis, A. J. and J. W. Shervais (1991), Arc rifting of the Carolina terrane in northwestern South Carolina, *Geology, 19*(3), 226-229.

Deschamps, F., M. Godard, S. Guillot, and K. Hattori (2013), Geochemistry of subduction zone serpentinites: A review, *Lithos, 178*, 96-127.

Deschamps, F., S. Guillot, M. Godard, M. Andreani, and K. Hattori (2011), Serpentinites act as sponges for fluid-mobile elements in abyssal and subduction zone environments, *Terra Nova, 23*(3), 171-178.

Dewey, J. (2003), Ophiolites and lost oceans: Rifts, ridges, arcs, and/or scrapings?, *Special Papers-Geological Society Of America*, 153-158.

Dickinson, W. R., C. A. Hopson, J. B. Saleeby, R. Schweickert, R. Ingersoll, E. Pessagno Jr, J. Mattinson, B. Luyendyk, W. Beebe, and D. Hull (1996), Alternate origins of the Coast Range ophiolite (California): Introduction and implications, *GSA today, 6*(2), 1-10.

Dilek, Y. (2000), *Ophiolites and Oceanic Crust: New Insights from Field Studies and the Ocean Drilling Program*, vol. 349, Geological Society of America.

Dilek, Y. (2003), Ophiolite concept and its evolution, *Special Papers-Geological Society Of America*, 1-16.

Dilek, Y. and M. F. Flower (2003), Arc-trench rollback and forearc accretion: 2. A model template for ophiolites in Albania, Cyprus, and Oman, *Special Publication-Geological Society Of London, 218*, 43-68.

Dilek, Y. and H. Furnes (2009), Structure and geochemistry of Tethyan ophiolites and their petrogenesis in subduction rollback systems, *Lithos, 113*(1), 1-20.

Dilek, Y. and A. Polat (2008), Suprasubduction zone ophiolites and Archean tectonics, *Geology, 36*(5), 431-432.

Dimalanta, C. B. and G. P. Yumul (2006), Magmatic and amagmatic contributions to crustal growth in the Philippine island arc system: Comparison of the Cretaceous and post-Cretaceous periods, *Geosciences Journal, 10*(3), 321-329.

Dlugogorski, B. Z. and R. D. Balucan (2014), Dehydroxylation of serpentine minerals: Implications for mineral carbonation, *Renewable and Sustainable Energy Reviews, 31*, 353-367.

Dlugogorski, B. Z. and R. D. Balucan (2014), Dehydroxylation of serpentine minerals: Implications for mineral carbonation, *Renewable and Sustainable Energy Reviews, 31*(0), 353-367, doi: http://dx.doi.org/10.1016/j.rser.2013.11.002.

Donald and Sylvia McLaughlin Natural Reserve, University of California, UC Davis, The Regents of the University of California (2007), Geology, *2013*, http://nrs.ucdavis.edu/McL/index.html; http://nrs.ucdavis.edu/McL/maps/geology.html,.

Dyar, M. D., D. G. Agresti, M. W. Schaefer, C. A. Grant, and E. C. Sklute (2006), Mössbauer spectroscopy of Earth and planetary materials, *Annu. Rev. Earth Planet. Sci., 34*, 83-125.

Dyar, M., M. Schaefer, E. Sklute, and J. Bishop (2008), Mössbauer spectroscopy of phyllosilicates: Effects of fitting models on recoil-free fractions and redox ratios, *Clay Miner., 43*(1), 3-33.

Dyar, M. D., M. L. Carmosino, J. M. Tucker, E. A. Brown, S. M. Clegg, R. C. Wiens, J. E. Barefield, J. S. Delaney, G. M. Ashley, and S. G. Driese (2012), Remote laser-induced breakdown spectroscopy analysis of East African Rift sedimentary samples under Mars conditions, *Chem. Geol., 294–295*(0), 135-151, doi: http://dx.doi.org/10.1016/j.chemgeo.2011.11.019.

Dyar, M. D. et al. (2011), Spectroscopy of Yamato 984028, *Polar Science, 4*(4), 530-549, doi: http://dx.doi.org/10.1016/j.polar.2010.06.001.

Dyar, M. D., C. V. Guidorttri, M. J. Holdaway, and M. CoLucci (1993), Nonstoichiometric hydrogen contents in common rock-forming hydroxyl silicates, *Geochim. Cosmochim. Acta, 57*(12), 2913-2918, doi: http://dx.doi.org/10.1016/0016-7037(93)90399-H.

Dyar, M. D., A. V. McGuire, and M. D. Harrell (1992), Crystal chemistry of iron in two styles of metasomatism in the upper mantle, *Geochim. Cosmochim. Acta, 56*(6), 2579-2586, doi: http://dx.doi.org/10.1016/0016-7037(92)90212-2.

Dyar, M. D. and M. W. Schaefer (2004), Mössbauer spectroscopy on the surface of Mars: constraints and expectations, *Earth Planet. Sci. Lett., 218*(3–4), 243-259, doi: http://dx.doi.org/10.1016/S0012-821X(03)00689-7.

Dyar, M. D., J. M. Tucker, S. Humphries, S. M. Clegg, R. C. Wiens, and M. D. Lane (2011), Strategies for Mars remote Laser-Induced Breakdown Spectroscopy analysis of sulfur in geological samples, *Spectrochimica Acta Part B: Atomic Spectroscopy, 66*(1), 39-56, doi: http://dx.doi.org/10.1016/j.sab.2010.11.016.

Earley III, D., M. D. Dyar, E. S. Ilton, and A. A. Granthem (1995), The influence of structural fluorine on biotite oxidation in copper-bearing, aqueous solutions at low temperatures and pressures, *Geochim. Cosmochim. Acta, 59*(12), 2423-2433, doi: http://dx.doi.org/10.1016/0016-7037(95)00136-0.

Edwards, C., M. Menzies, and M. Thirlwall (1991), Evidence from Muriah, Indonesia, for the interplay of supra-subduction zone and intraplate processes in the genesis of potassic alkaline magmas, *J. Petrol., 32*(3), 555-592.

Edwards, K. J., W. Bach, and T. M. McCollom (2005), Geomicrobiology in oceanography: microbe–mineral interactions at and below the seafloor, *Trends Microbiol., 13*(9), 449-456.

Ehlmann, B. L., J. F. Mustard, R. N. Clark, G. A. Swayze, and S. L. Murchie (2011), Evidence for low-grade metamorphism, hydrothermal alteration, and diagenesis on Mars from phyllosilicate mineral assemblages, *Clays Clay Miner., 59*(4), 359-377.

Ehlmann, B. L., J. F. Mustard, S. L. Murchie, J. Bibring, A. Meunier, A. A. Fraeman, and Y. Langevin (2011), Subsurface water and clay mineral formation during the early history of Mars, *Nature, 479*(7371), 53-60.

Ehlmann, B., J. Mustard, and S. Murchie (2010), Geologic setting of serpentine deposits on Mars, *Geophys. Res. Lett., 37*(6).

Ehlmann, B. L. et al. (2008), Orbital identification of carbonate-bearing rocks on Mars, *Science, 322*(5909), 1828-1832, doi: 10.1126/science.1164759; 10.1126/science.1164759.

Encarnación, J. P., S. B. Mukasa, and E. C. Obille (1993), Zircon U-Pb geochronology of the Zambales and Angat Ophiolites, Luzon, Philippines: Evidence for an Eocene arc-back arc pair, *Journal of Geophysical Research: Solid Earth (1978–2012), 98*(B11), 19991-20004.

EPA (2007), Method 6200: Field portable x-ray fluorescence spectrometry for the determination of elemental concentrations in soil and sediment.

Escartin, J., G. Hirth, and B. Evans (1997), Effects of serpentinization on the lithospheric strength and the style of normal faulting at slow-spreading ridges, *Earth Planet. Sci. Lett., 151*(3), 181-189.

Escartin, J., G. Hirth, and B. Evans (1997), Nondilatant brittle deformation of serpentinites: Implications for Mohr-Coulomb theory and the strength of faults, *Journal of Geophysical Research: Solid Earth (1978–2012), 102*(B2), 2897-2913.

Etiope, G., A. Feyzullayev, and C. L. Baciu (2009), Terrestrial methane seeps and mud volcanoes: A global perspective of gas origin, *Mar. Pet. Geol., 26*(3), 333-344, doi: http://dx.doi.org/10.1016/j.marpetgeo.2008.03.001.

Evans, B. W. (1977), Metamorphism of alpine peridotite and serpentinite, *Annu. Rev. Earth Planet. Sci., 5*, 397.

Evans, B. W. (2004), The serpentinite multisystem revisited: chrysotile is metastable, *Int. Geol. Rev., 46*(6), 479-506.

Evans, B. W. (2008), Control of the products of serpentinization by the Fe2 Mg− 1 exchange potential of olivine and orthopyroxene, *J. Petrol., 49*(10), 1873-1887.

Evans, B. W. (2010), Lizardite versus antigorite serpentinite: Magnetite, hydrogen, and life (?), *Geology, 38*(10), 879-882.

Evans, B. W., M. D. Dyar, and S. M. Kuehner (2012), Implications of ferrous and ferric iron in antigorite, *Am. Mineral., 97*(1), 184-196.

Evans, B. W., K. Hattori, and A. Baronnet (2013), Serpentinite: What, Why, Where?, *Elements, 9*(2), 99-106.

Evans, B. W., S. M. Kuehner, and A. Chopelas (2009), Magnetite-free, yellow lizardite serpentinization of olivine websterite, Canyon Mountain complex, NE Oregon, *Am. Mineral., 94*(11-12), 1731-1734.

Evans, K., R. Powell, and B. Frost (2013), Using equilibrium thermodynamics in the study of metasomatic alteration, illustrated by an application to serpentinites, *Lithos, 168*, 67-84.

Evans, C. and J. W. Hawkins Jr. (1989), Compositional heterogeneities in upper mantle peridotites from the Zambales Range Ophiolite, Luzon, Philippines, *Tectonophysics, 168*(1–3), 23-41, doi: http://dx.doi.org/10.1016/0040-1951(89)90367-3.

Faust, G. T. and J. J. Fahey (1962), The Serpentine-Group Minerals, *USGS Professional Paper, 384-A*, 1-92.

Fedo, C. M. and M. J. Whitehouse (2002), Metasomatic origin of quartz-pyroxene rock, Akilia, Greenland, and implications for Earth's earliest life, *Science, 296*(5572), 1448-1452, doi: 10.1126/science.1070336.

Feng, B., Y. Lu, Q. Feng, P. Ding, and N. Luo (2013), Mechanisms of surface charge development of serpentine mineral, *Transactions of Nonferrous Metals Society of China, 23*(4), 1123-1128, doi: http://dx.doi.org/10.1016/S1003-6326(13)62574-1.

Fernández-Remolar, D. C. et al. (2012), Carbonate precipitation under bulk acidic conditions as a potential biosignature for searching life on Mars, *Earth Planet. Sci. Lett., 351–352*(0), 13-26, doi: http://dx.doi.org/10.1016/j.epsl.2012.07.015.

Ferré, E. C., S. A. Friedman, F. Martín-Hernández, J. M. Feinberg, J. A. Conder, and D. A. Ionov (2013), The magnetism of mantle xenoliths and potential implications for sub-Moho magnetic sources, *Geophys. Res. Lett., 40*(1), 105-110.

Flanagan, F. J. (1976), Descriptions and Analyses of Eight New USGS Rock Standards: Twenty-eight papers present analytical data on new and previously

described whole-rock standards*, United States Geologic Survey Professional Paper, 840*, 171.

Frost, B. R., K. A. Evans, S. M. Swapp, J. S. Beard, and F. E. Mothersole (2013), The process of serpentinization in dunite from New Caledonia*, Lithos, 178*, 24-39.

Frueh-Green, G., C. Boschi, D. Kelley, J. Connolly, and M. Schrenk (2002), The role of serpentinization in metasomatism, carbonate precipitation and microbial activity: Stable isotope constraints from the Lost City Vent Field (MAR 30 N), AGU Fall Meeting Abstracts.

Fryer, P. (2012), Serpentinite mud volcanism: observations, processes, and implications*, Annual review of marine science, 4*, 345-373.

Fryer, P., M. Mottl, L. Johnson, J. Haggerty, S. Phipps, and H. Maekawa (1995), Serpentine bodies in the forearcs of western Pacific convergent margins: Origin and associated fluids*, Geophysical Monograph Series, 88*, 259-279.

Fuchs, Y., J. Linares, and M. Mellini (1998), Mössbauer and infrared spectrometry of lizardite-1T from Monte Fico, Elba*, Physics and Chemistry of Minerals, 26*(2), 111-115.

Fudali, R. F., M. D. Dyar, D. L. Griscom, and H. D. Schreiber (1987), The oxidation state of iron in tektite glass*, Geochim. Cosmochim. Acta, 51*(10), 2749-2756, doi: http://dx.doi.org/10.1016/0016-7037(87)90154-2.

Fujioka, K., T. Yamanaka, T. Gamo, F. Inagaki, T. Miwa, and H. Sato (2002), An Introduction to the Serpentinite Biosphere in the Mariana Forearc: Capsule of the Deep Subsurface Biosphere from the Chamorro Seamount.

Fuller, M., R. Haston, J. Lin, B. Richter, E. Schmidtke, and J. Almasco (1991), Tertiary paleomagnetism of regions around the South China Sea*, Journal of Southeast Asian Earth Sciences, 6*(3–4), 161-184, doi: http://dx.doi.org/10.1016/0743-9547(91)90065-6.

Geary, E. E., R. W. Kay, J. C. Reynolds, and S. M. Kay (1989), Geochemistry of mafic rocks from the Coto Block, Zambales ophiolite, Philippines: trace element evidence for two stages of crustal growth*, Tectonophysics, 168*(1–3), 43-63, doi: http://dx.doi.org/10.1016/0040-1951(89)90368-5.

Giggenbach, W., Y. Sano, and H. Wakita (1993), Isotopic composition of helium, and CO_2 and CH_4 contents in gases produced along the New Zealand part of a convergent plate boundary*, Geochim. Cosmochim. Acta, 57*(14), 3427-3455.

Goff, F., D. Bergfeld, C. Janik, D. Counce, and J. Stimac (2001), Geochemical Data on Waters, Gases, Rocks and Sediments from The Geysers-Clear Lake Region, California (1991-2000)*, Los Alamos National Laboratory, December*.

Goldstein, J., D. E. Newbury, D. C. Joy, C. E. Lyman, P. Echlin, E. Lifshin, L. Sawyer, and J. R. Michael (2003)*, Scanning Electron Microscopy and X-Ray Microanalysis*, 3rd ed., 689-350 pp., Springer, United States of America.

Goncharov, A., D. Ionov, L. Doucet, and L. Pokhilenko (2012), Thermal state, oxygen fugacity and C-O-H fluid speciation in cratonic lithospheric mantle: New data on peridotite xenoliths from the Udachnaya kimberlite, Siberia*, Earth Planet. Sci. Lett., 357*, 99-110.

Gonzalez-Mancera, G., F. Ortega-Gutierrez, N. Nava, and H. Arriola (2003), Mössbauer study of serpentine minerals in the ultramafic body of Tehuitzingo, southern Mexico*, Hyperfine interactions, 148*(1-4), 61-71.

Govindaraju, K. (1994), 1994 compilation of working values and sample description for 383 geostandards*, Geostandards Newsletter, 18*, 1-158, doi: 10.1046/j.1365-2494.1998.53202081.x-i1.

Groppo, C., C. Rinaudo, S. Cairo, D. Gastaldi, and R. Compagnoni (2006), Micro-Raman spectroscopy for a quick and reliable identification of serpentine minerals from ultramafics*, European Journal of Mineralogy, 18*(3), 319-329.

GUSTAFSON, W. I. (1974), The Stability of Andradite, Hedenbergite, and Related Minerals in the System Ca—Fe—Si—O—H*, J. Petrol., 15*(3), 455-496.

Hacker, V. (2003), A novel process for stationary hydrogen production: the reformer sponge iron cycle (RESC)*, J. Power Sources, 118*(1), 311-314.

Hacker, V., R. Fankhauser, G. Faleschini, H. Fuchs, K. Friedrich, M. Muhr, and K. Kordesch (2000), Hydrogen production by steam–iron process*, J. Power Sources, 86*(1), 531-535.

Hall, R., J. R. Ali, C. D. Anderson, and S. J. Baker (1995), Origin and motion history of the Philippine Sea Plate*, Tectonophysics, 251*(1), 229-250.

Harlow, G. and S. Sorensen (2005), Jade (nephrite and jadeitite) and serpentinite: metasomatic connections*, Int. Geol. Rev., 47*(2), 113-146.

Harper, G. D. (1984), The Josephine ophiolite, northwestern California*, Geological Society of America Bulletin, 95*(9), 1009-1026.

Harrison, S. and N. Rajakaruna (2011)*, Serpentine: The Evolution and Ecology of a Model System*, Univ of California Press.

Hashemi, F., S. Rowshanzamir, and M. Rezakazemi (2012), CFD simulation of PEM fuel cell performance: Effect of straight and serpentine flow fields, *Math. Comput. Model., 55*(3–4), 1540-1557, doi: http://dx.doi.org/10.1016/j.mcm.2011.10.047.

Hawkins, J. W., S. H. Bloomer, C. A. Evans, and J. T. Melchior (1984), Evolution of intra-oceanic arc-trench systems, *Tectonophysics, 102*(1), 175-205.

Hawkins, J. W. and C. A. Evans (1983), Geology of the Zambales Range, Luzon, Philippine Islands: ophiolite derived from an island arc-back arc basin pair, *Geophysical Monograph Series, 27*, 95-123.

Hawkins, J. (2003), Geology of supra-subduction zones: Implications for the origin of ophiolites, *Ophiolite Concept and the Evolution of Geological Thought: Boulder, Colorado.Geological Society of America Special Paper, 373*, 227-268.

Hayes, D. E. (1980), *The Tectonic and Geologic Evolution of Southeast Asian Seas and Islands*, vol. 23, American geophysical union.

Hazen, R. M., R. T. Downs, A. P. Jones, and L. Kah (2013), Carbon Mineralogy and Crystal Chemistry, *Rev. Mineral. Geochem., 75*, 7-46, doi: 10.2138/rmg.2013.75.2.

Hazen, R. M. and C. M. Schiffries (2013), Why Deep Carbon?, *Rev. Mineral. Geochem., 75*, 1-6, doi: 10.2138/rmg.2013.75.1.

Hellevang, H., S. Huang, and I. H. Thorseth (2011), The potential for low-temperature abiotic hydrogen generation and a hydrogen-driven deep biosphere, *Astrobiology, 11*(7), 711-724.

Hensen, B. J. and D. Green (1973), Experimental study of the stability of cordierite and garnet in pelitic compositions at high pressures and temperatures, *Contributions to Mineralogy and Petrology, 38*(2), 151-166.

Hirauchi, K. and I. Katayama (2013), Rheological contrast between serpentine species and implications for slab–mantle wedge decoupling, *Tectonophysics, 608*(0), 545-551, doi: http://dx.doi.org/10.1016/j.tecto.2013.08.027.

Hirschmann, M. M., C. Aubaud, and A. C. Withers (2005), Storage capacity of H_2O in nominally anhydrous minerals in the upper mantle, *Earth Planet. Sci. Lett., 236*(1), 167-181, doi: 10.1016/j.epsl.2005.04.022.

Hirschmann, M. M., T. Tenner, C. Aubaud, and A. C. Withers (2009), Dehydration melting of nominally anhydrous mantle: The primacy of partitioning, *Phys. Earth Planet. Inter., 176*(1–2), 54-68, doi: http://dx.doi.org/10.1016/j.pepi.2009.04.001.

Hoehler, T. M. (2005), Biogeochemistry of dihydrogen, in *Biogeochemical Cycles of Elements*, vol. 43, edited by A. Sigel, H. Sigel, and R. K. O. Sigel, pp. 9--48.

Hogarth, W. H. J., J. Steiner, J. B. Benziger, and A. Hakenjos (2007), Spatially-resolved current and impedance analysis of a stirred tank reactor and serpentine fuel cell flow-field at low relative humidity, *J. Power Sources, 164*(2), 464-471, doi: http://dx.doi.org/10.1016/j.jpowsour.2006.10.103.

Holm, N. G., M. Dumont, M. Ivarsson, and C. Konn (2006), Alkaline fluid circulation in ultramafic rocks and formation of nucleotide constituents: a hypothesis, *Geochem.Trans, 7*(7), 1-13.

Hopson, C. A. and E. A. Pessagno Jr (2005), Tehama-Colusa serpentinite mélange: A remnant of Franciscan Jurassic oceanic lithosphere, northern California, *Int. Geol. Rev., 47*(1), 65-100.

Hopson, C. A., J. E. Wright, and J. W. Shervais (2008), *Ophiolites, Arcs, and Batholiths: A Tribute to Cliff Hopson*, vol. 438, Geological Society of America.

Hopson, C. A., J. M. Mattinson, E. A. Pessagno, and B. P. Luyendyk (2008), California Coast Range ophiolite: Composite Middle and Late Jurassic oceanic lithosphere, *Geological Society of America Special Papers, 438*, 1-101, doi: 10.1130/2008.2438(01).

Horen, H., M. Zamora, and G. Dubuisson (1996), Seismic waves velocities and anisotropy in serpentinized peridotites from Xigaze ophiolite: abundance of serpentine in slow spreading ridge, *Geophys. Res. Lett., 23*(1), 9-12.

Hsueh, C., H. Chu, W. Yan, and C. Chen (2010), Transport phenomena and performance of a plate methanol steam micro-reformer with serpentine flow field design, *Appl. Energy, 87*(10), 3137-3147, doi: http://dx.doi.org/10.1016/j.apenergy.2010.02.027.

Huckenholz, H. and H. Yoder Jr (1971), Andradite stability relations in the CaSiO 3-Fe 2 O 3 join up to 30 kb, *Neues Jahrb.Mineral.Abhandl, 114*, 246-280.

Ionov, D., I. Ashchepkov, H. Stosch, G. Witt-Eickschen, and H. Seck (1993), Garnet peridotite xenoliths from the Vitim Volcanic Field, Baikal Region: the nature of the garnet—spinel peridotite transition zone in the continental mantle, *J. Petrol., 34*(6), 1141-1175.

Ionov, D. A. (2010), Petrology of mantle wedge lithosphere: new data on supra-subduction zone peridotite xenoliths from the andesitic Avacha volcano, Kamchatka, *J. Petrol., 51*(1-2), 327-361.

Jannasch, H. W. and M. J. Mottl (1985), Geomicrobiology of deep-sea hydrothermal vents, *Science, 229*(4715), 717-725, doi: 229/4715/717 [pii].

Jean, M. M., J. W. Shervais, S. Choi, and S. B. Mukasa (2010), Melt extraction and melt refertilization in mantle peridotite of the Coast Range ophiolite: an LA–ICP–MS study, *Contributions to Mineralogy and Petrology, 159*(1), 113-136.

Jeon, D. H., S. Greenway, S. Shimpalee, and J. W. Van Zee (2008), The effect of serpentine flow-field designs on PEM fuel cell performance, *Int J Hydrogen Energy, 33*(3), 1052-1066, doi: http://dx.doi.org/10.1016/j.ijhydene.2007.11.015.

Ji, F., H. Zhou, and Q. Yang (2008), The abiotic formation of hydrocarbons from dissolved CO2 under hydrothermal conditions with cobalt-bearing magnetite, *Origins of Life and Evolution of Biospheres, 38*(2), 117-125.

Jochum, K. P., U. Nohl, K. Herwig, E. Lammel, B. Stoll, and A. W. Hofmann (2005), GeoReM: a new geochemical database for reference materials and isotopic standards, *Geostandards and Geoanalytical Research, 29*(3), 333-338.

Jochum, K. P., U. Nohl, K. Herwig, E. Lammel, B. Stoll, and A. W. Hofmann (2005), GeoReM: A New Geochemical Database for Reference Materials and Isotopic Standards, *Geostandards and Geoanalytical Research, 29*(3), 333-338, doi: 10.1111/j.1751-908X.2005.tb00904.x.

Jones, G., A. Robertson, and J. Cann (1991), Genesis and emplacement of the supra-subduction zone pindos ophiolite, northwestern Greece, *Ophiolite Genesis and Evolution of the Oceanic Lithosphere*, pp. 771-799, Springer.

Juteau, T. (2003), Identification of a mantle unit in ophiolites: A major step in the evolution of the ophiolite concept, *Special Papers-Geological Society of America*, 31-54.

Juteau, T. (2003), Identification of a mantle unit in ophiolites: A major step in the evolution of the ophiolite concept, *Geological Society of America Special Papers, 373*, 31-53, doi: 10.1130/0-8137-2373-6.31.

Kang, S. and B. Zhou (2014), Numerical study of bubble generation and transport in a serpentine channel with a T-junction, *Int J Hydrogen Energy, 39*(5), 2325-2333, doi: http://dx.doi.org/10.1016/j.ijhydene.2013.11.115.

Karig, D., D. Sarewitz, and G. Haeck (1986), Role of strike-slip faulting in the evolution of allochthonous terranes in the Philippines, *Geology, 14*(10), 852-855.

Karson, J., G. Früh-Green, D. S. Kelley, E. Williams, D. R. Yoerger, and M. Jakuba (2006), Detachment shear zone of the Atlantis Massif core complex, Mid-Atlantic Ridge, 30 N, *Geochem. Geophys. Geosyst., 7*(6).

Kashefi, K. and D. R. Lovley (2003), Extending the upper temperature limit for life, *Science, 301*(5635), 934, doi: 10.1126/science.1086823 [doi].

Kelemen, P. B. and J. Matter (2008), In situ carbonation of peridotite for CO2 storage, *Proceedings of the National Academy of Sciences, 105*(45), 17295-17300.

Kelley, D. S., G. L. Fruh-Green, J. A. Karson, and K. A. Ludwig (2007), The Lost City hydrothermal field revisited, *Oceanography, 20*(4), 90-99.

Kelley, D. S. et al. (2005), A serpentinite-hosted ecosystem: the Lost City hydrothermal field, *Science, 307*(5714), 1428-1434, doi: 307/5714/1428 [pii].

Kingston Tivey, M. (1995), Modeling chimney growth and associated fluid flow at seafloor hydrothermal vent sites, *Seafloor Hydrothermal Systems: Physical, Chemical, Biological, and Geological Interactions*, 158-177.

Klein, F., W. Bach, S. E. Humphris, W. Kahl, N. Jöns, B. Moskowitz, and T. S. Berquó (2013), Magnetite in seafloor serpentinite—Some like it hot, *Geology, 42*(2), 135-138.

Klein, F., W. Bach, N. Jöns, T. McCollom, B. Moskowitz, and T. Berquó (2009), Iron partitioning and hydrogen generation during serpentinization of abyssal peridotites from 15 N on the Mid-Atlantic Ridge, *Geochim. Cosmochim. Acta, 73*(22), 6868-6893.

Koglin, N. (2008), Geochemistry, petrogenesis and tectonic setting of ophiolites and mafic-ultramafic complexes in the Northeastern Aegean Region.

Koivisto, E. (2013), *Utilization Potential of Iron Oxide By-Product from Serpentinite Carbonation*.

Kusky, T. M., L. Wang, Y. Dilek, P. Robinson, S. B. Peng, and X. Y. Huang (2011), Application of the modern ophiolite concept with special reference to Precambrian ophiolites, *SCIENCE CHINA Earth Sciences, 54*(3), 315-341.

Lafay, R., F. Deschamps, S. Schwartz, S. Guillot, M. Godard, B. Debret, and C. Nicollet (2013), High-pressure serpentinites, a trap-and-release system controlled by metamorphic conditions: Example from the Piedmont zone of the western Alps, *Chem. Geol., 343*, 38-54.

Leblanc, M. and A. Nicolas (1992), Ophiolitic chromitites, *Int. Geol. Rev., 34*(7), 653-686.

Lee, T. and L. A. Lawver (1995), Cenozoic plate reconstruction of Southeast Asia, *Tectonophysics, 251*(1), 85-138.

Lever, M. A. et al. (2013), Evidence for microbial carbon and sulfur cycling in deeply buried ridge flank basalt, *Science, 339*(6125), 1305-1308, doi: 10.1126/science.1229240 [doi].

Liou, J. G., R. Y. Zhang, and W. G. Ernst (2007), Very high-pressure orogenic garnet peridotites, *Proc. Natl. Acad. Sci. U. S. A., 104*(22), 9116-9121, doi: 0607300104 [pii].

Little, S. A., K. D. Stolzenbach, and R. P. Von Herzen (1987), Measurements of plume flow from a hydrothermal vent field, *Journal of Geophysical Research: Solid Earth (1978–2012), 92*(B3), 2587-2596.

Lodders, K. and B. J. Fegley (1998), *The Planetary Scientist's Companion*, 1st ed., 371-145-147 pp., Oxford Univeristy Press.

Lorand, J. (1987), Cu☐ Fe☐ Ni☐ S mineral assemblages in upper-mantle peridotites from the Table Mountain and Blow-Me-Down Mountain ophiolite massifs (Bay of Islands area, Newfoundland): Their relationships with fluids and silicate melts, *Lithos, 20*(1), 59-76.

MacPherson, G. J. and S. P. Phipps (1985), Comment and Reply on "Geochemical evidence for the tectonic setting of the Coast Range ophiolite: A composite island arc–oceanic crust terrane in western California" COMMENT, *Geology, 13*(11), 827-828.

Magaritz, M. and H. P. Taylor Jr (1976), Oxygen, hydrogen and carbon isotope studies of the Franciscan formation, Coast Ranges, California, *Geochim. Cosmochim. Acta, 40*(2), 215-234.

Mallmann, G. and H. S. C. O'Neill (2009), The crystal/melt partitioning of V during mantle melting as a function of oxygen fugacity compared with some other elements (Al, P, Ca, Sc, Ti, Cr, Fe, Ga, Y, Zr and Nb), *J. Petrol., 50*(9), 1765-1794.

Malvoisin, B., C. Chopin, F. Brunet, and M. E. Galvez (2012), Low-temperature Wollastonite Formed by Carbonate Reduction: a Marker of Serpentinite Redox Conditions, *J. Petrol., 53*(1), 159-176.

Marcaillou, C., M. Muñoz, O. Vidal, T. Parra, and M. Harfouche (2011), Mineralogical evidence for H2 degassing during serpentinization at 300 °C/300 bar, *Earth Planet. Sci. Lett., 303*(3–4), 281-290, doi: http://dx.doi.org/10.1016/j.epsl.2011.01.006.

Marques, J. M., P. M. Carreira, M. R. Carvalho, M. J. Matias, F. E. Goff, M. J. Basto, R. C. Graça, L. Aires-Barros, and L. Rocha (2008), Origins of high pH mineral waters from ultramafic rocks, Central Portugal, *Appl. Geochem., 23*(12), 3278-3289.

Martin, W., J. Baross, D. Kelley, and M. J. Russell (2008), Hydrothermal vents and the origin of life, *Nature Reviews Microbiology, 6*(11), 805-814.

Martins Belchor, P., M. M. Camargo Forte, and D. E. Ortiz Suman Carpenter (2012), Parallel serpentine-baffle flow field design for water management in a proton

exchange membrane fuel cell, *Int J Hydrogen Energy, 37*(16), 11904-11911, doi: http://dx.doi.org/10.1016/j.ijhydene.2012.05.091.

Masaaki, O. (1980), The Ronda Peridotite: Garnet-, Spinel-, and Plagioclase-Lherzolite Facies and the PT Trajectories of a High-Temprature Mantle Intrusion, *J. Petrol., 21*(3), 533-572.

Mayhew, L., E. Ellison, T. McCollom, T. Trainor, and A. Templeton (2013), Hydrogen generation from low-temperature water-rock reactions, *Nature Geoscience, 6*(6), 478-484.

Mazeina, L., A. Navrotsky, and D. Dyar (2008), Enthalpy of formation of sulfate green rusts, *Geochim. Cosmochim. Acta, 72*(4), 1143-1153, doi: http://dx.doi.org/10.1016/j.gca.2007.11.032.

McCanta, M. C., A. H. Treiman, M. D. Dyar, C. M. O. Alexander, D. Rumble III, and E. J. Essene (2008), The LaPaz Icefield 04840 meteorite: Mineralogy, metamorphism, and origin of an amphibole- and biotite-bearing R chondrite, *Geochim. Cosmochim. Acta, 72*(23), 5757-5780, doi: http://dx.doi.org/10.1016/j.gca.2008.07.034.

Mccollom, T. M. and J. P. Amend (2005), A thermodynamic assessment of energy requirements for biomass synthesis by chemolithoautotrophic micro-organisms in oxic and anoxic environments, *Geobiology, 3*, 135–144-35–144.

McCollom, T. M. and W. Bach (2009), Thermodynamic constraints on hydrogen generation during serpentinization of ultramafic rocks, *Geochim. Cosmochim. Acta, 73*(3), 856-875.

McCollom, T. M. (1999), Methanogenesis as a potential source of chemical energy for primary biomass production by autotrophic organisms in hydrothermal systems on Europa, *Journal of Geophysical Research: Planets (1991–2012), 104*(E12), 30729-30742.

McCollom, T. M. (2013), Laboratory simulations of abiotic hydrocarbon formation in Earth's deep subsurface, *Rev Mineral Geochem, 75*, 467-494.

McCollom, T. M., G. Ritter, and B. R. Simoneit (1999), Lipid synthesis under hydrothermal conditions by Fischer-Tropsch-type reactions, *Origins of Life and Evolution of the Biosphere, 29*(2), 153-166.

McCollom, T. M. and J. S. Seewald (2001), A reassessment of the potential for reduction of dissolved CO_2 to hydrocarbons during serpentinization of olivine, *Geochim. Cosmochim. Acta, 65*(21), 3769-3778.

McCollom, T. M. and J. S. Seewald (2006), Carbon isotope composition of organic compounds produced by abiotic synthesis under hydrothermal conditions, *Earth Planet. Sci. Lett., 243*(1), 74-84.

McCollom, T. M. and J. S. Seewald (2013), Serpentinites, hydrogen, and life, *Elements, 9*(2), 129-134.

McLaughlin, R., M. Blake Jr, A. Griscom, C. Blome, and B. Murchey (1988), Tectonics of formation, translation, and dispersal of the Coast Range ophiolite of California, *Tectonics, 7*(5), 1033-1056.

Meersman, F., I. Daniel, D. H. Bartlett, R. Winter, R. Hazael, and P. F. McMillan (2013), High-Pressure Biochemistry and Biophysics, *Rev. Mineral. Geochem., 75*, 607-648, doi: 10.2138/rmg.2013.75.19.

Metcalf, R. V. and J. W. Shervais (2008), Suprasubduction-zone ophiolites: Is there really an ophiolite conundrum?, *Special Papers-Geological Society of America, 438*, 191.

Mével, C. (2003), Serpentinisation des peridotites abysales aux dorsales oceaniques, *Comptes rendus-Geoscience, 335*(10-11), 825-852.

Michalski, J. R., J. Cuadros, P. B. Niles, J. Parnell, A. D. Rogers, and S. P. Wright (2013), Groundwater activity on Mars and implications for a deep biosphere, *Nature Geoscience, 6*(2), 133-138.

Minitti, M. E., L. A. Leshin, M. D. Dyar, T. J. Ahrens, Y. Guan, and S. Luo (2008), Assessment of shock effects on amphibole water contents and hydrogen isotope compositions: 2. Kaersutitic amphibole experiments, *Earth Planet. Sci. Lett., 266*(3–4), 288-302, doi: http://dx.doi.org/10.1016/j.epsl.2007.11.012.

Minitti, M. E., M. J. Rutherford, B. E. Taylor, M. D. Dyar, and P. H. Schultz (2008), Assessment of shock effects on amphibole water contents and hydrogen isotope compositions: 1. Amphibolite experiments, *Earth Planet. Sci. Lett., 266*(1–2), 46-60, doi: http://dx.doi.org/10.1016/j.epsl.2007.10.047.

Miranda, E. A. and Y. Dilek (2010), Oceanic core complex development in modern and ancient oceanic lithosphere: Gabbro-localized versus peridotite-localized detachment models, *J. Geol., 118*(1), 95-109.

Mitchell, A. and F. Hernandez (1986), Cenozoic evolution of the Philippine Archipelago, *Journal of Southeast Asian Earth Sciences, 1*(1), 3-22.

Monterroso, R., M. Fan, M. D. Argyle, K. Varga, D. Dyar, J. Tang, Q. Sun, B. Towler, K. W. Elliot, and D. Kammen (2014), Characterization of the mechanism of gasification of a powder river basin coal with a composite catalyst for producing

desired syngases and liquids, *Applied Catalysis A: General, 475*(0), 116-126, doi: http://dx.doi.org/10.1016/j.apcata.2014.01.007.

Moody, J. B. (1976), Serpentinization: a review, *Lithos, 9*(2), 125-138, doi: 10.1016/0024-4937(76)90030-X.

Mookherjee, M. and L. Stixrude (2009), Structure and elasticity of serpentine at high-pressure, *Earth Planet. Sci. Lett., 279*(1–2), 11-19, doi: http://dx.doi.org/10.1016/j.epsl.2008.12.018.

MOORE, D. E. (1984), Metamorphic history of a high-grade blueschist exotic block from the Franciscan Complex, California, *J. Petrol., 25*(1), 126-150.

Moores, E. M., L. H. Kellogg, and Y. Dilek (2000), Tethyan ophiolites, mantle convection, and tectonic" historical contingency": A resolution of the" ophiolite conundrum", *Special Papers-Geological Society of America*, 3-12.

Morita, R. (1999), Is H2 the universal energy source for long-term survival?, *Microb. Ecol., 38*(4), 307-320.

Morrill, P. L., J. G. Kuenen, O. J. Johnson, S. Suzuki, A. Rietze, A. L. Sessions, M. L. Fogel, and K. H. Nealson (2013), Geochemistry and geobiology of a present-day serpentinization site in California: The Cedars, *Geochim. Cosmochim. Acta, 109*, 222-240.

Morrill, P. L., N. Szponar, W. J. Brazelton, M. O. Schrenk, D. M. Bower, and A. Steele (2011), The Tablelands Ophiolite of Newfoundland: A Mars Analogue Site of Present-Day Serpentinization, *LPI Contributions, 1612*, 6017.

Morris, R. V., G. Klingelhöfer, C. Schröder, D. S. Rodionov, A. Yen, D. W. Ming, P. De Souza, T. Wdowiak, I. Fleischer, and R. Gellert (2006), Mössbauer mineralogy of rock, soil, and dust at Meridiani Planum, Mars: Opportunity's journey across sulfate-rich outcrop, basaltic sand and dust, and hematite lag deposits, *Journal of Geophysical Research: Planets (1991–2012), 111*(E12).

Mottl, M. J., S. C. Komor, P. Fryer, and C. L. Moyer (2003), Deep-slab fluids fuel extremophilic Archaea on a Mariana forearc serpentinite mud volcano: Ocean Drilling Program Leg 195, *Geochem. Geophys. Geosyst., 4*(11).

Mottl, M., S. Komer, and P. Fryer (2002), Deep fluids from the subducting pacific plate and associated extremophilic microbial activity on a mariana forearc serpentine seamount, ODP leg 195, Geochimica et Cosmochimica Acta.

Murad, E. (1998), Clays and clay minerals: what can Mössbauer spectroscopy do to help understand them?, *Hyperfine Interactions, 117*(1-4), 39-70.

Nasir, S., A. Lehlooh, I. Abu-Aljarayesh, and S. Mahmood (1993), Ferric iron in upper mantle Cr-spinel: a Mossbauer spectroscopic study, *Chemie der Erde, 53*, 265-271.

Neal, C. and G. Stanger (1983), Hydrogen generation from mantle source rocks in Oman, *Earth Planet. Sci. Lett., 66*, 315-320.

Nealson, K. H., F. Inagaki, and K. Takai (2005), Hydrogen-driven subsurface lithoautotrophic microbial ecosystems (SLiMEs): do they exist and why should we care?, *Trends Microbiol., 13*(9), 405-410.

Nesse, W. D. (2000), *Introduction to Mineralogy*, 1st ed., Oxford University Press, Inc.

Neubeck, A., N. T. Duc, D. Bastviken, P. Crill, and N. G. Holm (2011), Formation of H2 and CH4 by weathering of olivine at temperatures between 30 and 70 degrees C, *Geochem. Trans., 12*(1), 6-4866-12-6, doi: 10.1186/1467-4866-12-6 [doi].

O'Hanley, D. S., and M. D. Dyar (1993), The composition of lizardite 1T and, the formation of magnetite in serpentinites, *American Mineralogist, 78*, 391-404.

O'Hanley, D. S. and M. D. Dyar (1998), The composition of chrysotile and its relationship with lizardite, *Canadian mineralogist, 36*, 727-740.

Okland, I., S. Huang, H. Dahle, I. H. Thorseth, and R. B. Pedersen (2012), Low temperature alteration of serpentinized ultramafic rock and implications for microbial life, *Chem. Geol., 318*, 75-87.

Orphan, V. J. and T. M. Hoehler (2011), Microbiology: hydrogen for dinner, *Nature, 476*(7359), 154-155.

Osako, M., A. Yoneda, and E. Ito (2010), Thermal diffusivity, thermal conductivity and heat capacity of serpentine (antigorite) under high pressure, *Phys. Earth Planet. Inter., 183*(1–2), 229-233, doi: http://dx.doi.org/10.1016/j.pepi.2010.07.005.

Oze, C., L. C. Jones, J. I. Goldsmith, and R. J. Rosenbauer (2012), Differentiating biotic from abiotic methane genesis in hydrothermally active planetary surfaces, *Proc. Natl. Acad. Sci. U. S. A., 109*(25), 9750-9754, doi: 10.1073/pnas.1205223109; 10.1073/pnas.1205223109.

Parkinson, I. J. and J. A. Pearce (1998), Peridotites from the Izu–Bonin–Mariana forearc (ODP Leg 125): evidence for mantle melting and melt–mantle interaction in a supra-subduction zone setting, *J. Petrol., 39*(9), 1577-1618.

Parlak, O. and M. Delaloye (1996), Geochemistry and timing of post-metamorphic dyke emplacement in the Mersin Ophiolite (southern Turkey): New age constraints from 40Ar/39Ar geochronology, *Terra Nova, 8*(6), 585-592.

Parlak, O., V. Höck, and M. Delaloye (2002), The supra-subduction zone Pozanti–Karsanti ophiolite, southern Turkey: evidence for high-pressure crystal fractionation of ultramafic cumulates, *Lithos, 65*(1), 205-224.

Pasini, V., D. Brunelli, P. Dumas, C. Sandt, J. Frederick, K. Benzerara, S. Bernard, and B. Ménez (2013), Low temperature hydrothermal oil and associated biological precursors in serpentinites from Mid-Ocean Ridge, *Lithos, 178*, 84-95.

Paukert, A. N., J. M. Matter, P. B. Kelemen, E. L. Shock, and J. R. Havig (2012), Reaction path modeling of enhanced in situ CO2 mineralization for carbon sequestration in the peridotite of the Samail Ophiolite, Sultanate of Oman, *Chem. Geol., 330–331*(0), 86-100, doi: http://dx.doi.org/10.1016/j.chemgeo.2012.08.013.

Peacock, S. M. (1987), Serpentinization and infiltration metasomatism in the Trinity peridotite, Klamath province, northern California: implications for subduction zones, *Contributions to Mineralogy and Petrology, 95*(1), 55-70.

Pearson, D., F. Brenker, F. Nestola, J. McNeill, L. Nasdala, M. Hutchison, S. Matveev, K. Mather, G. Silversmit, and S. Schmitz (2014), Hydrous mantle transition zone indicated by ringwoodite included within diamond, *Nature, 507*(7491), 221-224.

Peslier, A. H., J. F. Luhr, and J. Post (2002), Low water contents in pyroxenes from spinel-peridotites of the oxidized, sub-arc mantle wedge, *Earth Planet. Sci. Lett., 201*(1), 69-86.

Peters, E. K. (1993), D-18O enriched waters of the Coast Range Mountains, northern California: Connate and ore-forming fluids, *Geochim. Cosmochim. Acta, 57*(5), 1093-1104, doi: 10.1016/0016-7037(93)90043-V.

Popa, T., M. Fan, M. D. Argyle, M. D. Dyar, Y. Gao, J. Tang, E. A. Speicher, and D. M. Kammen (2013), H2 and COx generation from coal gasification catalyzed by a cost-effective iron catalyst, *Applied Catalysis A: General, 464–465*(0), 207-217, doi: http://dx.doi.org/10.1016/j.apcata.2013.05.038.

Potter, S. L., M. A. Chan, E. U. Petersen, M. D. Dyar, and E. Sklute (2011), Characterization of Navajo Sandstone concretions: Mars comparison and criteria for distinguishing diagenetic origins, *Earth Planet. Sci. Lett., 301*(3–4), 444-456, doi: http://dx.doi.org/10.1016/j.epsl.2010.11.027.

Proskurowski, G., M. D. Lilley, D. S. Kelley, and E. J. Olson (2006), Low temperature volatile production at the Lost City Hydrothermal Field, evidence from a hydrogen stable isotope geothermometer, *Chem. Geol., 229*(4), 331-343.

Proskurowski, G., M. D. Lilley, J. S. Seewald, G. L. Fruh-Green, E. J. Olson, J. E. Lupton, S. P. Sylva, and D. S. Kelley (2008), Abiogenic hydrocarbon production at lost city hydrothermal field*, Science, 319*(5863), 604-607, doi: 10.1126/science.1151194 [doi].

Reynard, B. (2013), Serpentine in active subduction zones*, Lithos, 178*(0), 171-185, doi: http://dx.doi.org/10.1016/j.lithos.2012.10.012.

Rollinson, H. (1993)*, Using Geochemical Data: Evaluation, Presentation, Interpretation*, 1st ed., 9-16 pp., Longman Scientific & Technical.

Rossman, D. L., G. C. Castañada, and G. C. Bacuta (1989), Geology of the Zambales ophiolite, Luzon, Philippines*, Tectonophysics, 168*(1–3), 1-22, doi: http://dx.doi.org/10.1016/0040-1951(89)90366-1.

Rüpke, L. H., J. P. Morgan, M. Hort, and J. A. Connolly (2004), Serpentine and the subduction zone water cycle*, Earth Planet. Sci. Lett., 223*(1), 17-34.

Russell, M., A. Hall, and W. Martin (2010), Serpentinization as a source of energy at the origin of life*, Geobiology, 8*(5), 355-371.

Saccocia, P. J., J. S. Seewald, and W. C. Shanks III (2009), Oxygen and hydrogen isotope fractionation in serpentine–water and talc–water systems from 250 to 450 °C, 50 MPa*, Geochim. Cosmochim. Acta, 73*(22), 6789-6804, doi: http://dx.doi.org/10.1016/j.gca.2009.07.036.

Sackett, D. and K. Martin (1998), EPA method 6200 and field portable X-ray fluorescence, A presentation developed for the EPA Technology Innovation Office and On-Site In-Sights Workshops for innovative field characterization technologies.

Sakai, R., M. Kusakabe, M. Noto, and T. Ishii (1990), Origin of waters responsible for serpentinization of the Izu-Ogasawara-Mariana forearc seamounts in view of hydrogen and oxygen isotope ratios*, Earth Planet. Sci. Lett., 100*(1), 291-303.

Sánchez-Murillo, R., E. Gazel, E. M. Schwarzenbach, M. Crespo-Medina, M. O. Schrenk, J. Boll, and B. C. Gill (2014), Geochemical evidence for active tropical serpentinization in the Santa Elena Ophiolite, Costa Rica: An analog of a humid early Earth?*, Geochem. Geophys. Geosyst.*, n/a-n/a, doi: 10.1002/2013GC005213.

Sano, Y., A. Urabe, H. Wakita, and H. Wushiki (1993), Origin of hydrogen-nitrogen gas seeps, Oman*, Appl. Geochem., 8*(1), 1-8.

Schiffman, P., R. C. Evarts, A. E. Williams, and W. J. Pickthorn (1991), Hydrothermal metamorphism in oceanic crust from the coast range ophiolite of california: Fluid-rock interaction in a rifted island arc, in *Ophiolite Genesis and Evolution of the Oceanic Lithosphere*Anonymous , pp. 399-425, Springer.

Schmädicke, E., J. Gose, and T. M. Will (2011), Heterogeneous mantle underneath the North Atlantic: evidence from water in orthopyroxene, mineral composition and equilibrium conditions of spinel peridotite from different locations at the Mid-Atlantic Ridge, *Lithos, 125*(1), 308-320.

Schoonen, M. A. A., E. C. Sklute, M. D. Dyar, and D. R. Strongin (2012), Reactivity of sandstones under conditions relevant to geosequestration: 1. Hematite-bearing sandstone exposed to supercritical carbon dioxide commingled with aqueous sulfite or sulfide solutions, *Chem. Geol., 296–297*(0), 96-102, doi: http://dx.doi.org/10.1016/j.chemgeo.2011.11.013.

Schrenk, M. O., D. S. Kelley, S. Bolton, and J. D. Baross (2004), Low archaeal diversity linked to sub-seafloor geochemical processes at the Lost City Hydrothermal Field, Mid-Atlantic Ridge, *Environmental Microbiology, 6(10)*, 1,086-1,095.

Schrenk, M. O., W. J. Brazelton, and S. Q. Lang (2013), Serpentinization, carbon, and deep life, *Rev Mineral Geochem, 75*, 575-606.

Schulte, M., D. Blake, T. Hoehler, and T. McCollom (2006), Serpentinization and its implications for life on the early Earth and Mars, *Astrobiology, 6*(2), 364-376.

Schweller, W., D. Karig, and S. Bachman (1983), Original setting and emplacement history of the Zambales ophiolite, Luzon, Phillipines, from stratigraphic evidence, *The Tectonic and Geologic Evolution of Southeast Asian Seas and Islands: Part 2*, 124-138.

Scirè, S., E. Ciliberto, C. Crisafulli, V. Scribano, F. Bellatreccia, and G. D. Ventura (2011), Asphaltene-bearing mantle xenoliths from Hyblean diatremes, Sicily, *Lithos, 125*(3), 956-968.

Shallo, M. (1990), Ophiolitic mélange and flyschoidal sediments of the Tithonian–Lower Cretaceous in Albania, *Terra Nova, 2*(5), 476-483.

Shervais, J. W. (1982), Ti-V plots and the petrogenesis of modern and ophiolitic lavas, *Earth Planet. Sci. Lett., 59*(1), 101-118.

Shervais, J. W. (2001), Birth, death, and resurrection: The life cycle of suprasubduction zone ophiolites, *Geochem. Geophys. Geosyst., 2*(1).

Shervais, J. W. (2006), The significance of subduction-related accretionary complexes in early Earth processes, *Geological Society of America Special Papers, 405*, 173-192.

Shervais, J. W., S. H. Choi, W. D. Sharp, J. Ross, M. Zoglman-Schuman, and S. B. Mukasa (2011), Serpentinite matrix mélange: Implications of mixed provenance for mélange formation, *Geological Society of America Special Papers, 480*, 1-30.

Shervais, J. W. and B. B. Hanan (1989), Jurassic volcanic glass from the Stonyford volcanic complex, Franciscan assemblage, northern California Coast Ranges, *Geology, 17*(6), 510-514.

Shervais, J. W. and D. L. Kimbrough (1985), Comment and Reply on "Geochemical evidence for the tectonic setting of the Coast Range ophiolite: A composite island arc–oceanic crust terrane in western California" REPLY, *Geology, 13*(11), 828-829.

Shervais, J. W. and D. L. Kimbrough (1985), Geochemical evidence for the tectonic setting of the Coast Range ophiolite: A composite island arc–oceanic crust terrane in western California, *Geology, 13*(1), 35-38.

Shervais, J. W. and D. L. Kimbrough (1987), Alkaline and transitional subalkaline metabasalts in the Franciscan Complex melange, California, *Mantle metasomatism and alkaline magmatism: Geological Society of America Special Paper, 215*, 165-182.

Shervais, J. W., P. Kolesar, and K. Andreasen (2005), A field and chemical study of serpentinization—Stonyford, California: chemical flux and mass balance, *Int. Geol. Rev., 47*(1), 1-23.

Shervais, J. W., B. L. Murchey, D. L. Kimbrough, P. R. Renne, and B. Hanan (2005), Radioisotopic and biostratigraphic age relations in the Coast Range Ophiolite, northern California: Implications for the tectonic evolution of the Western Cordillera, *Geological Society of America Bulletin, 117*(5-6), 633-653.

Shervais, J. W., M. M. Z. Schuman, and B. B. Hanan (2005), The Stonyford volcanic complex: a forearc seamount in the northern California Coast Ranges, *J. Petrol., 46*(10), 2091-2128.

Shervais, J. W., S. K. Vetter, and B. B. Hanan (2006), Layered mafic sill complex beneath the eastern Snake River Plain: Evidence from cyclic geochemical variations in basalt, *Geology, 34*(5), 365-368.

Shervais, J. W. and D. L. Kimbrough (January, 1985), Geochemical evidence for the tectonic setting of the Coast Range ophiolite: A composite island arc–oceanic crust terrane in western California, *Geology, 13*(1), 35-38, doi: 10.1130/0091-7613(1985)13<35:GEFTTS>2.0.CO;2.

Sherwood Lollar, B., K. Voglesonger, L. Lin, G. Lacrampe-Couloume, J. Telling, T. Abrajano, T. Onstott, and L. Pratt (2007), Hydrogeologic controls on episodic H2 release from Precambrian fractured rocks-Energy for deep subsurface life on Earth and Mars, *Astrobiology, 7*(6), 971-986.

Shock, E. L., T. McCollom, and M. D. Schulte (1995), Geochemical constraints on chemolithoautotrophic reactions in hydrothermal systems, *Origins of Life and Evolution of the Biosphere, 25*(1-3), 141-159.

Sleep, N. H., D. K. Bird, and E. C. Pope (2011), Serpentinite and the dawn of life*, Philosophical Transactions of the Royal Society B: Biological Sciences, 366*(1580), 2857-2869.

Sleep, N., A. Meibom, T. Fridriksson, R. Coleman, and D. Bird (2004), H2-rich fluids from serpentinization: Geochemical and biotic implications*, Proc. Natl. Acad. Sci. U. S. A., 101*(35), 12818-12823.

Sleep, N. H., D. K. Bird, and E. C. Pope (2011), Serpentinite and the dawn of life*, Philos. Trans. R. Soc. Lond. B. Biol. Sci., 366*(1580), 2857-2869, doi: 10.1098/rstb.2011.0129; 10.1098/rstb.2011.0129.

Sobolev, A. V. and M. Chaussidon (1996), H_2O concentrations in primary melts from supra-subduction zones and mid-ocean ridges: Implications for H_2O storage and recycling in the mantle*, Earth Planet. Sci. Lett., 137*(1), 45-55.

Sobolev, N. and A. Logvinova (2005), Significance of accessory chrome spinel in identifying serpentinite paragenesis*, Int. Geol. Rev., 47*(1), 58-64.

State of California (2010), California geologic map, Copyright 2007, http://www.quake.ca.gov/gmaps/GMC/stategeologicmap.html, accessed September 2014.

Stephan, J. F., R. Blanchet, C. Rangin, B. Pelletier, J. Letouzey, and C. Muller (1986), Geodynamic evolution of the Taiwan-Luzon-Mindoro belt since the late Eocene*, Tectonophysics, 125*(1), 245-268.

Stern, R. J. (2002), Subduction zones*, Rev. Geophys., 40*(4), 1012.

Stern, R. J. and S. H. BLOOMER (1992), Subduction zone infancy: examples from the Eocene Izu-Bonin-Mariana and Jurassic California arcs*, Geological Society of America Bulletin, 104*(12), 1621-1636.

Stern, R. J. (2005), Evidence from ophiolites, blueschists, and ultrahigh-pressure metamorphic terranes that the modern episode of subduction tectonics began in Neoproterozoic time*, Geology, 33*(7), 557-560.

Suda, K. et al. (2014), Origin of methane in serpentinite-hosted hydrothermal systems: The CH4–H2–H2O hydrogen isotope systematics of the Hakuba Happo hot spring*, Earth Planet. Sci. Lett., 386*(0), 112-125, doi: http://dx.doi.org/10.1016/j.epsl.2013.11.001.

Suga, K., W. Nishimura, T. Yamamoto, and M. Kaneda , Measurements of serpentine channel flow characteristics for a proton exchange membrane fuel cell*, Int J Hydrogen Energy*(0), doi: http://dx.doi.org/10.1016/j.ijhydene.2014.01.195.

Suresh, P. V., S. Jayanti, A. P. Deshpande, and P. Haridoss (2011), An improved serpentine flow field with enhanced cross-flow for fuel cell applications, *Int J Hydrogen Energy, 36*(10), 6067-6072, doi: http://dx.doi.org/10.1016/j.ijhydene.2011.01.147.

Szponar, N., W. J. Brazelton, M. O. Schrenk, D. M. Bower, A. Steele, and P. L. Morrill (2013), Geochemistry of a continental site of serpentinization, the Tablelands Ophiolite, Gros Morne National Park: A Mars analogue, *Icarus, 224*(2), 286-296.

Takai, K., K. Nakamura, K. Suzuki, F. Inagaki, K. H. Nealson, and H. Kumagai (2006), Ultramafics-Hydrothermalism-Hydrogenesis-HyperSLiME (UltraH3) linkage: a key insight into early microbial ecosystem in the Archean deep-sea hydrothermal systems, *Paleontological research, 10*(4), 269-282.

Takai, K., C. L. Moyer, M. Miyazaki, Y. Nogi, H. Hirayama, K. H. Nealson, and K. Horikoshi (2005), Marinobacter alkaliphilus sp. nov., a novel alkaliphilic bacterium isolated from subseafloor alkaline serpentine mud from Ocean Drilling Program Site 1200 at South Chamorro Seamount, Mariana Forearc, *Extremophiles, 9*(1), 17-27.

Tamayo, R. A., R. C. Maury, G. P. Yumul, M. Polvé, J. Cotten, C. B. Dimantala, and F. O. Olaguera (2004), Subduction-related magmatic imprint of most Philippine ophiolites: implications on the early geodynamic evolution of the Philippine archipelago, *Bull. Soc. Geol. Fr., 175*(5), 443-460.

Tamura, A. and S. Arai (2006), Harzburgite–dunite–orthopyroxenite suite as a record of supra-subduction zone setting for the Oman ophiolite mantle, *Lithos, 90*(1), 43-56.

Taran, Y., N. Varley, S. Inguaggiato, and E. Cienfuegos (2010), Geochemistry of H2-and CH4-enriched hydrothermal fluids of Socorro Island, Revillagigedo Archipelago, Mexico. Evidence for serpentinization and abiogenic methane, *Geofluids, 10*(4), 542-555.

Teir, S., R. Kuusik, C. Fogelholm, and R. Zevenhoven (2007), Production of magnesium carbonates from serpentinite for long-term storage of CO_2, *Int. J. Miner. Process., 85*(1), 1-15.

Tiago, I., A. P. Chung, and A. Verissimo (2004), Bacterial diversity in a nonsaline alkaline environment: heterotrophic aerobic populations, *Appl. Environ. Microbiol., 70*(12), 7378-7387, doi: 70/12/7378 [pii].

Tiago, I., C. Pires, V. Mendes, P. V. Morais, M. S. da Costa, and A. Verissimo (2006), Bacillus foraminis sp. nov., isolated from a non-saline alkaline groundwater, *Int. J. Syst. Evol. Microbiol., 56*(Pt 11), 2571-2574, doi: 56/11/2571 [pii].

Tian, Z., W. Xiao, B. F. Windley, L. Lin, C. Han, J. Zhang, B. Wan, S. Ao, D. Song, and J. Feng (2014), Structure, age, and tectonic development of the Huoshishan–

Niujuanzi ophiolitic mélange, Beishan, southernmost Altaids*, Gondwana Research, 25*(2), 820-841.

Tsujimori, T., J. G. Liou, and R. G. Coleman (2007), Finding of high-grade tectonic blocks from the New Idria serpentinite body, Diablo Range, California: Petrologic constraints on the tectonic evolution of an active serpentinite diapir*, Special Papers-Geological Society of America, 419*, 67.

Tyburczy, J. A., T. S. Duffy, T. J. Ahrens, and M. A. Lange (1991), Shock wave equation of state of serpentine to 150 GPa: Implications for the occurrence of water in the Earth's lower mantle*, Journal of Geophysical Research: Solid Earth (1978–2012), 96*(B11), 18011-18027.

Tyburczy, J. A., R. V. Krishnamurthy, S. Epstein, and T. J. Ahrens (1990), Impact-induced devolatilization and hydrogen isotopic fractionation of serpentine: Implications for planetary accretion*, Earth Planet. Sci. Lett., 98*(2), 245-261, doi: http://dx.doi.org/10.1016/0012-821X(90)90063-4.

Ulmer, P. and V. Trommsdorff (1995), Serpentine stability to mantle depths and subduction-related magmatism*, Science, 268*(5212), 858-861, doi: 268/5212/858 [pii].

USGS (2011), tectonic plate boundary graphic, http://pubs.usgs.gov/publications/text/slabs.html, accessed September 2014.

Vance, S. (2007)*, High Pressure and Low Temperature Equations of State for Aqueous Magnesium Sulfate: Applications to the Search for Life in Extraterrestrial Oceans, with Particular Reference to Europa.*

Vaughan, A. P. M. and J. H. Scarrow (2003), Ophiolite obduction pulses as a proxy indicator of superplume events?*, Earth Planet. Sci. Lett., 213*(3), 407-416.

Wakabayashi, J. (1992), Nappes, tectonics of oblique plate convergence, and metamorphic evolution related to 140 million years of continuous subduction, Franciscan Complex, California*, J. Geol.*, 19-40.

Wakabayashi, J. and Y. Dilek (2000), Spatial and temporal relationships between ophiolites and their metamorphic soles: a test of models of forearc ophiolite genesis*, Special Papers-Geological Society of America*, 53-64.

Wallin, E. T. and R. V. Metcalf (1998), Supra-subduction zone ophiolite formed in an extensional forearc: Trinity Terrane, Klamath Mountains, California*, J. Geol., 106*(5), 591-608.

Wang, B., L. Shu, M. Faure, B. Jahn, D. Cluzel, J. Charvet, S. Chung, and S. Meffre (2011), Paleozoic tectonics of the southern Chinese Tianshan: insights from structural,

chronological and geochemical studies of the Heiyingshan ophiolitic mélange (NW China)*, Tectonophysics, 497*(1), 85-104.

Wang, X., Z. Ouyang, S. Zhuo, M. Zhang, G. Zheng, and Y. Wang (2014), Serpentinization, abiogenic organic compounds, and deep life*, Science China Earth Sciences*, 1-10.

Wang, X., Y. Huang, C. Cheng, J. Jang, D. Lee, W. Yan, and A. Su (2010), An inverse geometry design problem for optimization of single serpentine flow field of PEM fuel cell*, Int J Hydrogen Energy, 35*(9), 4247-4257, doi: http://dx.doi.org/10.1016/j.ijhydene.2010.02.059.

Wang, X., W. Yan, Y. Duan, F. Weng, G. Jung, and C. Lee (2010), Numerical study on channel size effect for proton exchange membrane fuel cell with serpentine flow field*, Energy Conversion and Management, 51*(5), 959-968, doi: http://dx.doi.org/10.1016/j.enconman.2009.11.037.

Wang, X., X. Zhang, W. Yan, D. Lee, and A. Su (2010), Non-isothermal effects of single or double serpentine proton exchange membrane fuel cells*, Electrochim. Acta, 55*(17), 4926-4934, doi: http://dx.doi.org/10.1016/j.electacta.2010.03.092.

Wedepohl, K. H. and Y. Muramatsu (1979), Proceedings of the Second International Kimberlite Conference.

Wenner, D. B. and H. P. Taylor Jr (1971), Temperatures of serpentinization of ultramafic rocks based on O18/O16 fractionation between coexisting serpentine and magnetite*, Contributions to Mineralogy and Petrology, 32*(3), 165-185.

Wenner, D. B. and H. P. Taylor (1973), Oxygen and hydrogen isotope studies of the serpentinization of ultramafic rocks in oceanic environments and continental ophiolite complexes*, Am. J. Sci., 273*(3), 207-239.

Wetzel, L. R. and E. L. Shock (2000), Distinguishing ultramafic-from basalt-hosted submarine hydrothermal systems by comparing calculated vent fluid compositions*, Journal of Geophysical Research: Solid Earth (1978–2012), 105*(B4), 8319-8340.

Whattam, S. A. and R. J. Stern (2011), The 'subduction initiation rule': a key for linking ophiolites, intra-oceanic forearcs, and subduction initiation*, Contributions to Mineralogy and Petrology, 162*(5), 1031-1045.

Wheat, C. G., P. Fryer, A. T. Fisher, S. Hulme, H. Jannasch, M. J. Mottl, and K. Becker (2008), Borehole observations of fluid flow from South Chamorro Seamount, an active serpentinite mud volcano in the Mariana forearc*, Earth Planet. Sci. Lett., 267*(3), 401-409.

Wilson, M., D. Jones, and W. McHardy (1981), The weathering of serpentinite by Lecanora atra, *The Lichenologist, 13*(02), 167-176.

Winter, J. D. (2010), *Principles of Igneous and Metamorphic Petrology*, 2nd ed., 647-652 pp., Pearson Education, Inc.

Wirth, K. and A. Barth (2012), X-Ray Fluorescence (XRF), *Science Education Resource Center (SERC) at Carleton College, 2013*.

Wunder, B. and W. Schreyer (1997), Antigorite: High-pressure stability in the system $MgO—SiO_2—H_2O$ (MSH), *Lithos, 41*(1), 213-227.

Yamamoto, S., T. Komiya, K. Hirose, and S. Maruyama (2004), Crustal zircons from the podiform chromitites in Luobusa ophiolite, Tibet, American Geophysical Union, Fall Meeting Abstract V31C-1443.

Yang, J., G. Godard, J. Kienast, Y. Lu, and J. Sun (1993), Ultrahigh-pressure (60 kbar) magnesite-bearing garnet peridotites from northeastern Jiangsu, China, *J. Geol.*, 541-554.

Yumul, G. P. (2007), Westward younging disposition of Philippine ophiolites and its implication for arc evolution, *Island Arc, 16*(2), 306-317.

Yumul, G. P., C. B. Dimalanta, and F. T. Jumawan (2000), Geology of the southern Zambales ophiolite complex, Luzon, Philippines, *Island Arc, 9*(4), 542-555.

Yumul, G. (1996), Varying mantle sources of supra-subduction zone ophiolites: REE evidence from the Zambales Ophiolite Complex, Luzon, Philippines, *Tectonophysics, 262*(1), 243-262.

Yumul, G. P. (2004), Zambales Ophiolite Complex (Philippines) Transition-Zone Dunites: Restite, Cumulate, or Replacive Products?, *Int. Geol. Rev., 46*(3), 259-272, doi: 10.2747/0020-6814.46.3.259.

Zanchetta, S., F. Berra, A. Zanchi, M. Bergomi, M. Caridroit, A. Nicora, and G. Heidarzadeh (2013), The record of the Late Palaeozoic active margin of the Palaeotethys in NE Iran: Constraints on the Cimmerian orogeny, *Gondwana Research, 24*(3), 1237-1266.

Zhang, Y., P. Zhang, Z. Yuan, H. He, Y. Zhao, and X. Liu (2011), A tapered serpentine flow field for the anode of micro direct methanol fuel cells, *J. Power Sources, 196*(6), 3255-3259, doi: http://dx.doi.org/10.1016/j.jpowsour.2010.12.012.